# Radiative Characteristics of Soil Derived Aerosols

by Steven A. Ackerman and
Stephen K. Cox

Atmospheric Science
PAPER NO.
417

DEPARTMENT OF ATMOSPHERIC SCIENCE
COLORADO STATE UNIVERSITY
FORT COLLINS, COLORADO

# RADIATIVE CHARACTERISTICS OF SOIL DERIVED AEROSOLS

by

Steven A. Ackerman

and

Stephen K. Cox

Department of Atmospheric Science

Colorado State University

Fort Collins, Colorado

July, 1987

Atmospheric Science Paper No. 417

ABSTRACT

RADIATIVE CHARACTERISTICS OF SOIL DERIVED AEROSOLS

A multiple scattering model is employed to study the impact of a dust layer on the radiative fluxes at the top of the atmosphere, at the bottom of the atmosphere and within the atmosphere. The sensitivity of the radiative fluxes to various changes in the optical properties of the dust is assessed. Model calculations of the radiative fluxes, with environmental conditions as input, are compared to the aircraft measured fluxes.

A parameterization of the extinction coefficient, the single scattering albedo and the asymmetry parameter for a dust layer in the SW spectral region is presented which accounts for the physical and chemical changes of a dust layer as it is mobilized and transported. It is demonstrated that the parameterization scheme is applicable to other aerosols, including water clouds. A scaling parameter is presented which can be used to describe the optical properties of an aerosol layer with a large effective size parameter. The parameterization of the LW radiative properties of the dust layer follows the classic emissivity approach. The effective emissivity is derived for a non-isothermal layer. The radiative parameterizations are incorporated into a radiative-convective equilibrium climate model to assess the impact of the dust microphysical properties on the steady state temperature.

## ACKNOWLEDGEMENTS

I would like to extend my thanks to my committee members, Drs. Stephen K. Cox, Graeme Stephens, Thomas B. McKee and Gerry Taylor, for their support during this and other research projects. I am also indebted to Ms. Melissa Tucker and Ms. Judy Sorbie for their assistance in the preparation of the manuscript. Special thanks are extended to my family, Anne, Erin and Laura, for their understanding, support and encouragement of my studies. This research was funded by the National Science Foundation under grant ATM-8521214 and the National Aeronautics and Space Administration under grant NAG 1-554. Computer support was provided by the National Center for Atmospheric Research which is sponsored by the National Science Foundation.

ACKNOWLEDGEMENTS

I would like to extend my thanks to my committee members, Drs. Stephen K. Cox, Graeme Stephens, Thomas B. McKee and Gerry Taylor, for their support during this and other research projects. I am also indebted to Ms. Melissa Tucker and Ms. Judy Sorbie for their assistance in the preparation of the manuscript. Special thanks are extended to my family, Anne, Erin and Laura, for their understanding, support and encouragement of my studies. This research was funded by the National Science Foundation under grant ATM-8521214 and the National Aeronautics and Space Administration under grant NAG 1-554. Computer support was provided by the National Center for Atmospheric Research which is sponsored by the National Science Foundation.

CONTENTS

LIST OF FIGURES

LIST OF TABLES

# Chapter 1

# INTRODUCTION

Soil derived aerosols are largely generated by surface wind erosion and are a major component of the total tropospheric aerosol burden (Study of Man's Impact on Climate, 1971). Today the major source regions of airborne dust are the world's deserts, particularly the Sahara. In the past the weathering processes associated with glaciers, in association with stormy and dry weather conditions, could have produced large quantities of airborne dust. In the future, human activity may be a major source as wind erosion is increased through cultivation, improper grazing, poor watershed management, deforestation and off road vehicles.

The mobilization, transportation and deposition of dust is a concern of several disciplines (e.g. climatology, ecology, geology and pedology). The presence of suspended dust has an affect on the tropospheric radiative heating rates (DeLuisi et al., 1976; Carlson and Benjamin, 1980; Ackerman and Cox, 1982; and Ellingson and Serafino, 1984) as well as the surface radiative energy budget (e.g. King et al., 1980; Cerf 1980; Brinkman and McGregor, 1983; and Ackerman and Cox, 1982). The radiative properties of the airborne dust may affect the climate of the earth (Bryson and Barreis, 1967; Randall and Carlson, 1983; Joseph, 1977; and Idso, 1981a and b). In large concentrations dust can also present a health hazard, suffocate livestock and severely limit visibility causing hazardous traffic conditions (Péwé, 1981). The mobilization and transportation of dust denudes the source region surface of needed nutrients and minerals while the deposition of dust contributes to the mineralogy of the adjacent regions (Prospero, 1981). The present study is concerned with the effects of a dust layer on the atmospheric radiative fluxes, with particular emphasis on to the parameterization of the dust radiative properties.

In the last 15 years, a variety of field experiments (see Appendix A) have been undertaken to measure the effect of a dust layer on the atmospheric radiative energy budget. All of these experiments observed a significant impact on solar fluxes while the effect on the longwave spectrum has not been as conclusive. As a result, recent modeling studies have investigated the sensitivity of General Circulation Models (GCMs) to the presence of dust. For example, Randall et al. (1984) and Joseph (1984) indicate that the GCMs response is not limited to the areas where the dust is assumed to reside. D'Almeida (1986) has undertaken the task of modeling the atmospheric transport of dust. It may take several days for a dust layer to move from one geographic region to another (Reiff et al., 1986; Rahn et al., 1981; Shaw, 1980). With such a time scale the influence of radiative processes on the thermodynamic structure of the dust layer need to be addressed. To date models of atmospheric circulations only crudely treat, if at all, the radiative properties of the aerosol and do not allow for the interaction between the aerosol optical properties and the dynamic variables. As global and regional models become more advanced, changes in the radiative properties of the dust layer during its lifecycle (mobilization, transport and deposition) need to be considered. This will require appropriate parameterization schemes.

## 1.1 Objectives of the research

The radiative forcing of a dust layer not only depends on the dust concentration and chemical composition, but also on such parameters as surface albedo, solar zenith angle, surface temperature and the thermodynamic structure of the atmosphere. In addition, the crustal aerosol can be transported out of a source region by the wind and deposited in another location. As a dust layer is transported, its radiative characteristics change as the size distribution and mineralogy are modified by sedimentation; this makes it difficult to parameterize the radiative properties on a global scale. As a prerequisite to developing useful parameterization schemes, one must understand the relationship between a dust layer radiative characteristics and its microphysical structure. Thus the present study has two major objectives:

1) to describe the interaction of an atmosphere containing soil derived aerosols with its solar and terrestrial radiative fields

2) to develop a parameterization of the dust radiative properties.

In addition, the parameterization schemes are employed to demonstrate their utility in assessing the impact of the presence of dust on simple climate systems. As an aid to the reader, an outline of the study is presented below.

### 1.1.1 Outline of dissertation

Chapter 2 discusses various observations of the thermodynamic and microphysical structure of dust laden atmospheres. These parameters are needed as input to the radiative calculations. The present study makes use of observations made over the Saudi Arabian Peninsula. Observations from other regions of the globe are presented to highlight commonalities and differences between observations. The shortwave and longwave radiative transfer models used in the study are discussed in Chapter 3. Appropriate two-stream/adding models are developed in this chapter. The chapter also discusses the more accurate doubling/adding models which are used to investigate the remote sensing applications discussed in Appendix B, and to provide a comparison between the radiative fluxes calculated with the doubling models, the two stream models and aircraft observations which are given at the end of the chapter. The two stream models are employed in chapter 4 to describe the effect of a dust layer on the atmospheric radiative fluxes. Of primary interest are changes in the fluxes at the top of the atmosphere, at the earth's surface and changes in the atmospheric radiative heating rates. Section 4.1 presents changes in the solar fluxes as a function of dust optical depth and solar zenith angle while Section 4.2 describes the changes in the longwave fluxes as a function of optical depth and surface temperature. The effects of the dust layer on the diurnal radiative energy budgets are presented at the end of chapter 4. Chapter 5 presents the more interesting aspects of the study as appropriate parameterizations for the shortwave and longwave spectral regions are developed. The parameterization of the longwave characteristics of dust layer follows the methodologies often applied to water and ice clouds. One notable exception is that the layer need not be isothermal. In the case of the shortwave spectrum, a scaling parameter is presented which can be used to describe changes in the optical properties of a dust layer. This scaling parameter accounts for much of the variations in the microphysical observations discussed in Chapter 2. In addition, the scaling parameter can be used to describe variations of the single scattering albedo of other aerosols, including water clouds, in the shortwave spectrum. Chapter 6 incorporates the parameterization schemes of Chapter 5 into a simple climate model to address the importance of dust microphysical structure on the steady state surface temperature. The major results of the study are summarized in Chapter 7.

# Chapter 2

# MODEL INPUT PARAMETERS

The simulation of the radiative characteristics of a dust laden atmosphere requires the following information: the thermodynamic structure of the atmosphere, the absorption and scattering properties of the air molecules, the absorption and scattering properties of the dust and its vertical and horizontal distribution, the spectral reflectance and emittance of the surface and the spectral distribution of extra-terrestrial solar energy. These model input parameters will be discussed in this section. Due to the availability of the aircraft measurements of Ackerman and Cox (1982) and Patterson et al. (1983) as well as the surface measurements of Smith (1986) the present study focuses on the radiative characteristics of the dust overlying the Saudi Arabian Peninsula and adjacent region. Few studies have studied the physical and radiative properties on the soil derived aerosols of this region. Comparisons between the dust observed over Saudi Arabia with dust suspended over other geographic regions will be presented.

## 2.1 Spatial and temporal variations of airborne dust

In assessing the climatic implications of dust the spatial and temporal variations of the aerosol must be addressed. Spatial frequency patterns of dust are inevitably linked to regions of available soil (e.g. Sahara, Rub al Khali, Mojave), while temporal patterns will primarily depend on meteorological parameters (e.g. wind speed and precipitation). Perhaps the most common method for studying dust episodes is the analysis of surface observations of the frequency, duration and intensity of dust storms. Dust outbreaks over the Sahara and the southwest United States have been described in detail by several investigators (see for example Orgill and Sehmel, 1976; Morels, 1979 and Pewe, 1981). Dust outbreaks associated with the geographical region of the southwest Indian monsoon have received less attention. Thus this study will attempt to focus on the characteristics of the dust in this region ($10^0N$ to $37^0N$ and $35^0E$ to $90^0E$).

The horizontal and vertical distributions of airborne dust were deduced from surface weather observations, archived by the National Center for Atmospheric Research, for the area shown in figure 1. The initial analysis covered the region $30^0E$ to $100^0E$ and $30^0S$ to $40^0N$; however due to the limited number of station observations of dust outbreaks, the study was reduced to the region $35^0E$ to $90^0E$ and $10^0N$ to $37^0N$. Meteorological observation times were 00, 06, 12 and 18 GMT. This region includes five major deserts: the Nafud and Rub al Khali deserts of the Arabian Peninsula, the Great Indian or Thar Desert, the Dasht-e Kavir in Iran and the southern regions of the Taklimakan Desert of China. Additional analysis of dust outbreaks and various meteorological parameters (e.g. wind speed and direction) are given in Appendix B.

There are several disadvantages of working with surface observations of dust. For example, data are sparse in largely uninhabited, central-desert regions. Surface observations give little quantitative description of the physical properties needed to assess the climatological impact of the dust. Although horizontal visibilities have been correlated with dust mass loading (Chepil and Woodruff 1957, Patterson and Gillette 1977), a necessary parameter for radiative transfer calculations. Surface observations also contain variations resulting from different observers.

On the other hand, surface observations have the advantage of presenting a qualitative description of the horizontal distribution of suspended dust as well as the number of occurrences of dust outbreaks; these are two important parameters for estimating the impact of dust on regional and global circulations. In addition, surface observations lend insight into the meteorological conditions associated with a dust outbreak as well as the horizontal movement of the dust.

In the text a dust day is defined as a day in which an observer noted that airborne dust was present, as reported in the present weather section of the WMO synoptic code (Table 1). Observations of haze, smoke and duststorms associated with thunderstorms are not included in the analysis. In addition to tabulating the total number of dust days,

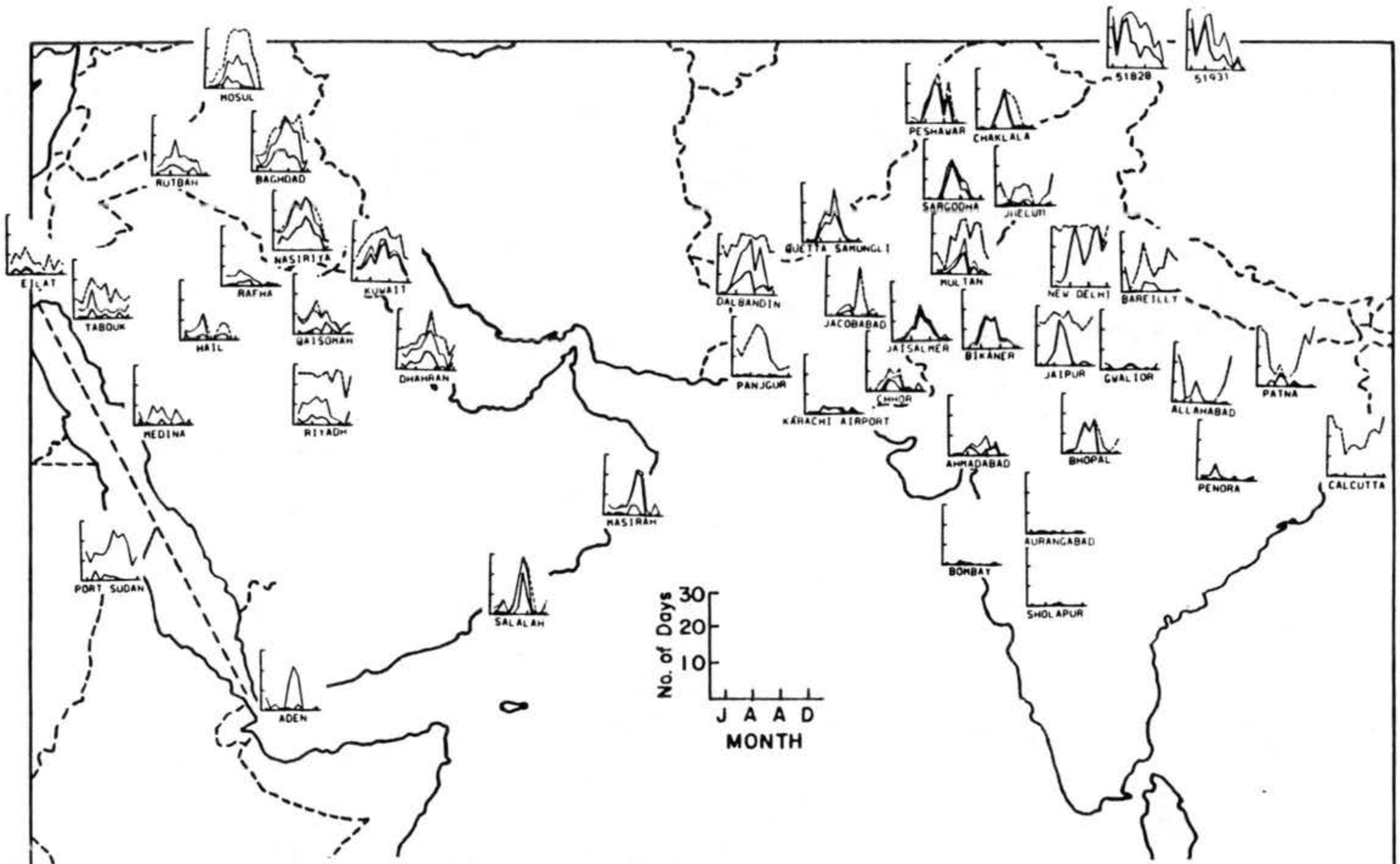


Figure 2.1 Number of dust days as a function of month for several stations in the southwest monsoon region for the year 1979. The absicissa is month where the four tic marks represent January, April, August and December. The ordinate is the numer of days where each tic mark is an increment of 10 days. The thick line represents the number of dust days for which the visibility was less than 5 km. The dashed line includes days with haze observations.

Table 2.1: Weather symbols of surface observations of airborne dust (after WMO,1974).

| CODE | SYMBOL | REMARKS | |
|---|---|---|---|
| 06 |  | Widespread dust in suspension in the air, not raised by wind at or near the station at the time of observation. | |
| 07 |  | Dust or sand raised by wind at or near the the time of observation, but no well- developed dust whirl(s) and no duststorm or sandstorm seen | |
| 08 |  | Well-developed dust whirl(s) or sand whirl(s) seen at or near the station during the preceding hour or at the time of observation, but no duststorm or sandstorm | |
| 09 | 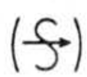 | Duststorm or sandstorm within sight at the time of observation or at the station during the preceding hour | |
| 30 |  | Slight or moderate dust-storm or sandstorm | - has decreased during the preceding hour |
| 31 |  | | - no appreciable change during the preceding hour |
| 32 | 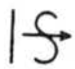 | | - has begun or has increased during the preceding hour |
| 33 | 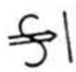 | Severe dust-storm or sandstorm | - has decreased during the preceding hour |
| 34 |  | | - no appreciable change during the preceding hour |
| 35 | 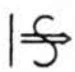 | | - has begun or has increased during the preceding hour |

the data were analyzed for heavy dust loading cases which were defined as an observation in which dust was observed and the visibility was less than or equal to 5 km. Applying the formula of Patterson and Gillette (1977) this corresponds to a dust mass loading of greater than 1 $mgm^{-3}$.

To assess the impact of soil derived aerosol on various regional and global scale problems (e.g. climate, ecology, health and traffic hazards) one needs to first assess the seasonal and geographical distribution of this type aerosol. Figure 1 depicts the number of days in which an observation of suspended dust was made as a function of month for the year 1979 for several stations in the Indian southwest monsoon region. Also shown (heavy line) are the number of dust days in which the visibility was less than 5 km. The dashed line includes dust days and days with haze observations. Tic marks on the ordinate represent 10 day increments while those along the abscissa represent the months of January, April, August and December. An apparent annual cycle in the number of days with suspended aerosols is evident at most stations with maximum occurrences in the spring and summer months.

Middleton (1986) found a similar annual cycle in dust storm frequencies for southwest Asia. Dubief (1953) also demonstrated a preference of dust storm frequency from early spring until fall for regions of the Sahara. The summer maximum in the number of dust days over the desert regions is undoubtedly correlated to the high summer insolation. The high, daytime summer, near-surface temperatures result in large turbulent eddies and a mixed layer which can extend to 600 mb (Ackerman and Cox, 1982). Once dust is injected into the atmosphere it can reach higher altitudes than in the winter months when the mixed layer and turbulent eddies are much shallower; this results in a larger residence times and greater transportation distances.

Seasonal variations in regional circulation systems also play an important role in the distribution of dust days. The summer minimum at New Delhi (figure 1) and the minimum in the occurrence of haze in the Ghangi River valley region is associated with the heavy monsoon rains. The large summer peak in dust days at Salalah and Masirah as well as haze at Aden may also relate to the summer monsoon circulation. Figure 2

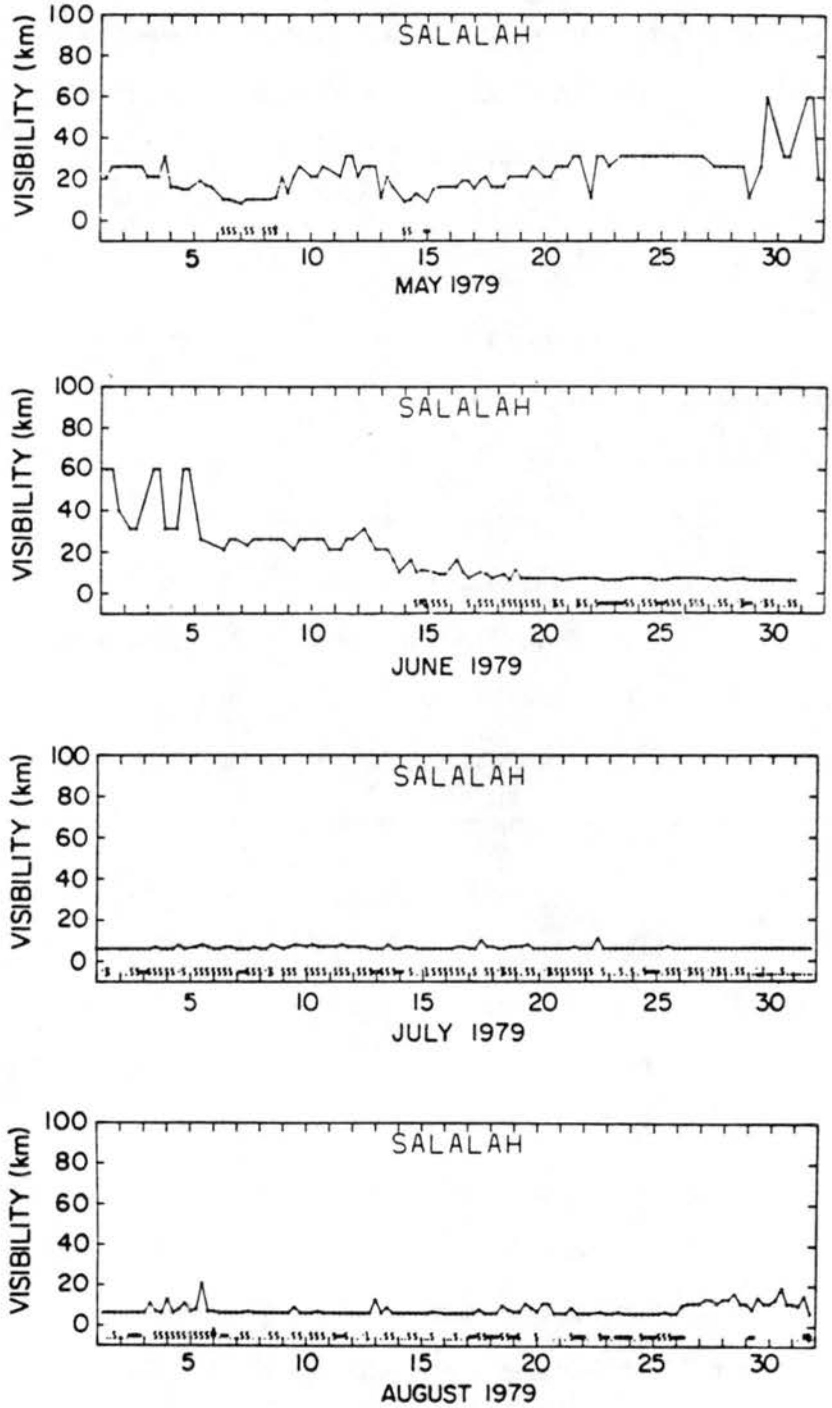


Figure 2.2: Visibility and present weather observations for Salalah for the months of May, June, July and August 1979.

depicts visibility and present weather observations for Salalah for the months of May, June, July and August 1979. During May there are only a few dust days and visibility is generally greater than 20 km. Shortly after the onset of the summer monsoon on June 11 (Krishnamurti et al., 1981), dust is observed in the atmosphere every day. As the monsoon retreats near the end of August the number of dust days decreases.

Dust outbreaks have their largest impact on the radiation budget during the summer months when the solar insolation for the region is the highest and where the dust days tend to a maxima. Das and Bedi (1981) report that during this time period dust outbreaks over the Arabian Peninsula have a large effect on the southwest summer monsoon. Because of the large impact of summer dust outbreaks a five year (1979-1983) climatology of dust outbreaks was derived for the months of May, June, and July (Table 2). Stations for which more than 10% of the observations were missing were not included in the composite. As would be expected, stations nearest to deserts tend to have the largest number of dust days. It is interesting that the majority of dust outbreaks over Northern India and Pakistan have visibilities less than 5 km; while this is not the case over the Arabian Peninsula. Most stations exhibit a diurnal variation in the occurrence of dust outbreaks with maxima during the day suggesting the importance of surface heating. As solar insolation heats the surface, turbulent eddies destroy the low level nighttime inversion, and transport momentum downwards to the surface. If greater than a threshold value, this added momentum can lift the soil off the surface and the eddies can transport the dust upward. Analyses by Orgill and Sehmel (1976) and Kalu (1979) also revealed a daytime preference in dust storm frequency. This daytime maximum is likely correlated to the period of maximum thermal instability, though observer bias may play a role.

The present day sources of dust are primarily the world's deserts, in which the greatest numbers of dust days occur during the summer months. Thus this study will focus on the atmospheric conditions and Earth-Sun geometry appropriate to summer time conditions. In addition, we shall consider those outbreaks which cover large geographical regions and assume the dust layers to be horizontally uniform.

Table 2.2: Number of observations of dust as a function of time (GMT) for various stations. For each station there are three rows; the top row is the total number of dust occurrences, the second row is for conditions with visibilities less than or equal to 5 km and the bottom row is for visibilites less than or equal to 1 km

| STATION | 00Z | 06Z | 12Z | 18Z | STATION | 00Z | 06Z | 12Z | 18Z |
|---|---|---|---|---|---|---|---|---|---|
| Riyadh | 49 | 146 | 108 | 77 | Quetta | 111 | 186 | 124 | 35 |
| | 18 | 47 | 29 | 20 | Samungli | 27 | 177 | 117 | 3 |
| | 2 | 4 | 2 | 2 | | 2 | 3 | 3 | |
| Dhahran | 53 | 189 | 164 | 40 | Dalbandin | 121 | 120 | 152 | 131 |
| | 31 | 105 | 60 | 15 | | 7 | 114 | 148 | 1 |
| | 5 | 7 | 3 | 0 | | 7 | 94 | 124 | 1 |
| Qaisomah | 38 | 61 | 82 | 53 | Hyperbad | 19 | 32 | 31 | 21 |
| | 7 | 21 | 33 | 15 | | 3 | 28 | 27 | 1 |
| | 4 | 2 | 9 | 1 | | 2 | 4 | 1 | 1 |
| Rafha | 23 | 42 | 54 | 23 | Jacobabad | 5 | 11 | 4 | 2 |
| | 13 | 15 | 18 | 12 | | 1 | 7 | 4 | 1 |
| | 0 | 2 | 3 | 1 | | 0 | 1 | 1 | 1 |
| Hail | 5 | 35 | 37 | 29 | Multan | 76 | 82 | 87 | 76 |
| | 1 | 7 | 5 | 2 | | 27 | 80 | 83 | 1 |
| | 0 | 0 | 0 | 0 | | 6 | 6 | 7 | 0 |
| Medina | 2 | 41 | 44 | 22 | Hissar | 36 | 70 | 68 | 32 |
| | 0 | 3 | 8 | 0 | | 34 | 70 | 67 | 32 |
| | 0 | 0 | 1 | 0 | | 8 | 16 | 8 | 3 |
| Tabouk | 17 | 106 | 65 | 38 | Bikaner | 171 | 174 | 183 | 153 |
| | 0 | 6 | 29 | 8 | | 169 | 174 | 181 | 152 |
| | 0 | 1 | 1 | 0 | | 25 | 28 | 37 | 35 |
| Eilat | 3 | 2 | 6 | 7 | Chhor | 20 | 56 | 51 | 22 |
| | 1 | 1 | 6 | 1 | | 3 | 54 | 48 | 0 |
| | 0 | 0 | 2 | 0 | | 3 | 2 | 2 | 0 |
| Chaklala | 86 | 151 | 142 | 55 | Karachi | 1 | 14 | 16 | 2 |
| | 79 | 145 | 136 | 2 | Airport | 0 | 13 | 16 | 1 |
| | 1 | 1 | 0 | 0 | | 0 | 0 | 0 | 1 |
| Peshawar | 136 | 228 | 187 | 27 | New Delhi | 228 | 236 | 261 | 245 |
| | 128 | 221 | 177 | 3 | | 226 | 236 | 261 | 244 |
| | 1 | 2 | 0 | 0 | | 7 | 8 | 5 | 1 |
| Jhelum | 5 | 9 | 8 | 2 | Jaipur | 172 | 194 | 161 | 143 |
| | 2 | 6 | 7 | 0 | | 170 | 194 | 161 | 143 |
| | 0 | 1 | 1 | 0 | | 10 | 8 | 9 | 2 |
| Sargodha | 170 | 182 | 110 | 69 | Gwalior | 4 | 27 | 20 | 5 |
| | 159 | 174 | 100 | 7 | | 4 | 24 | 18 | 5 |
| | 3 | 5 | 6 | 0 | | 1 | 3 | 3 | 0 |
| Fort | 3 | 3 | 9 | 5 | Bhopal | 29 | 55 | 24 | 12 |
| Sandemam | 6 | 3 | 7 | 0 | | 28 | 51 | 24 | 12 |
| | 0 | 0 | 1 | 0 | | 0 | 0 | 0 | 0 |

Table 2 continued.

| STATION | 00Z | 06Z | 12Z | 18Z | STATION | 00Z | 06Z | 12Z | 18Z |
|---|---|---|---|---|---|---|---|---|---|
| Kabul | 0 | 7 | 14 | 2 | Penora | 7 | 22 | 11 | 1 |
| Airport | 0 | 1 | 6 | 2 | | 2 | 4 | 3 | 1 |
| | 0 | 0 | 0 | 0 | | 0 | 0 | 0 | 0 |
| Ahmadabad | 2 | 13 | 29 | 1 | Patna | 1 | 25 | 26 | 1 |
| | 2 | 8 | 15 | 1 | | 1 | 24 | 26 | 1 |
| | 0 | 1 | 4 | 0 | | 0 | 2 | 0 | 0 |
| Rajkot | 2 | 14 | 16 | 1 | Calcutta | 2 | 0 | 0 | 1 |
| | 1 | 9 | 6 | 1 | | 2 | 0 | 0 | 1 |
| | 0 | 2 | 0 | 0 | | 0 | 0 | 0 | 0 |
| Bombay | 0 | 1 | 3 | 0 | Kota | 8 | 23 | 21 | 2 |
| | 0 | 1 | 3 | 0 | | 8 | 22 | 21 | 2 |
| | 0 | 0 | 2 | 0 | | 1 | 1 | 1 | 1 |
| Aurangbad | 1 | 1 | 2 | 1 | Sholapur | 1 | 3 | 2 | 0 |
| | 1 | 0 | 1 | 1 | | 0 | 1 | 1 | 0 |
| | 0 | 0 | 0 | 0 | | 0 | 1 | 0 | 0 |

## 2.2 Temperature profiles

Figure 3 displays the mean temperature profiles, plotted on a Tephigram, measured during four missions of the Convair 990 during SMONEX. Flights on 9 May and 10 May where flown over the same geographic region of the Saudi Arabian Peninsula and at approximately the same local time; while the flight on 12 May was flown early in the morning over the same region. The flight of 31 May was flown over the north central Arabian Sea. Over the desert the temperature between 850 mb and the top of the dust layer (approximately 600 mb) changes only slightly between flights. The largest temperature variations occur below 850 mb, where the effect of surface heating is strongly felt. This not only holds for the mean profiles, but for the individual dropwindsondes as well. In addition, as the dust layer is transported over the Arabian Sea (as in flight 13) it maintains its uniform temperature structure above 800 mb.

Figure 4 depicts the mean potential temperature profiles ($\theta$) associated with figure 3. There are four distinct layers of $\theta$, the surface layer (below 850 mb) where the value of $\theta$ has a diurnal structure induced by surface temperature changes. The layer between the top of the dust layer (600 mb) and 850 mb is virtually isentropic (constant $\theta$). The top of the dust layer is marked by a transition layer where $\theta$ increases with height; above the transition

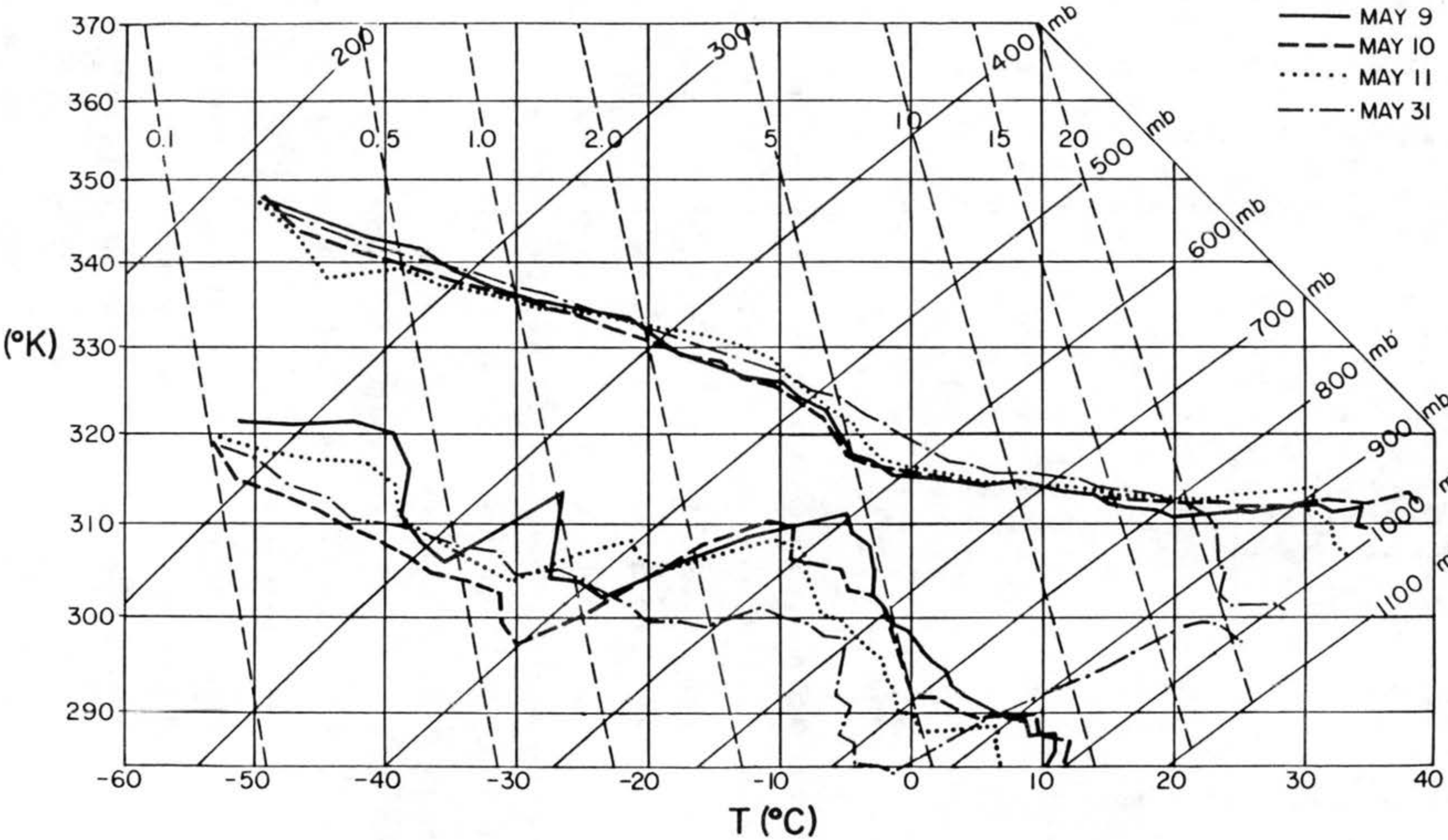


Figure 2.3 Mean temperature and moisture profiles measured during the summer monsoon experiment over the Rub al Khali Desert (9,10 and 12 May) and the Arabian Sea (18 and 31 May).

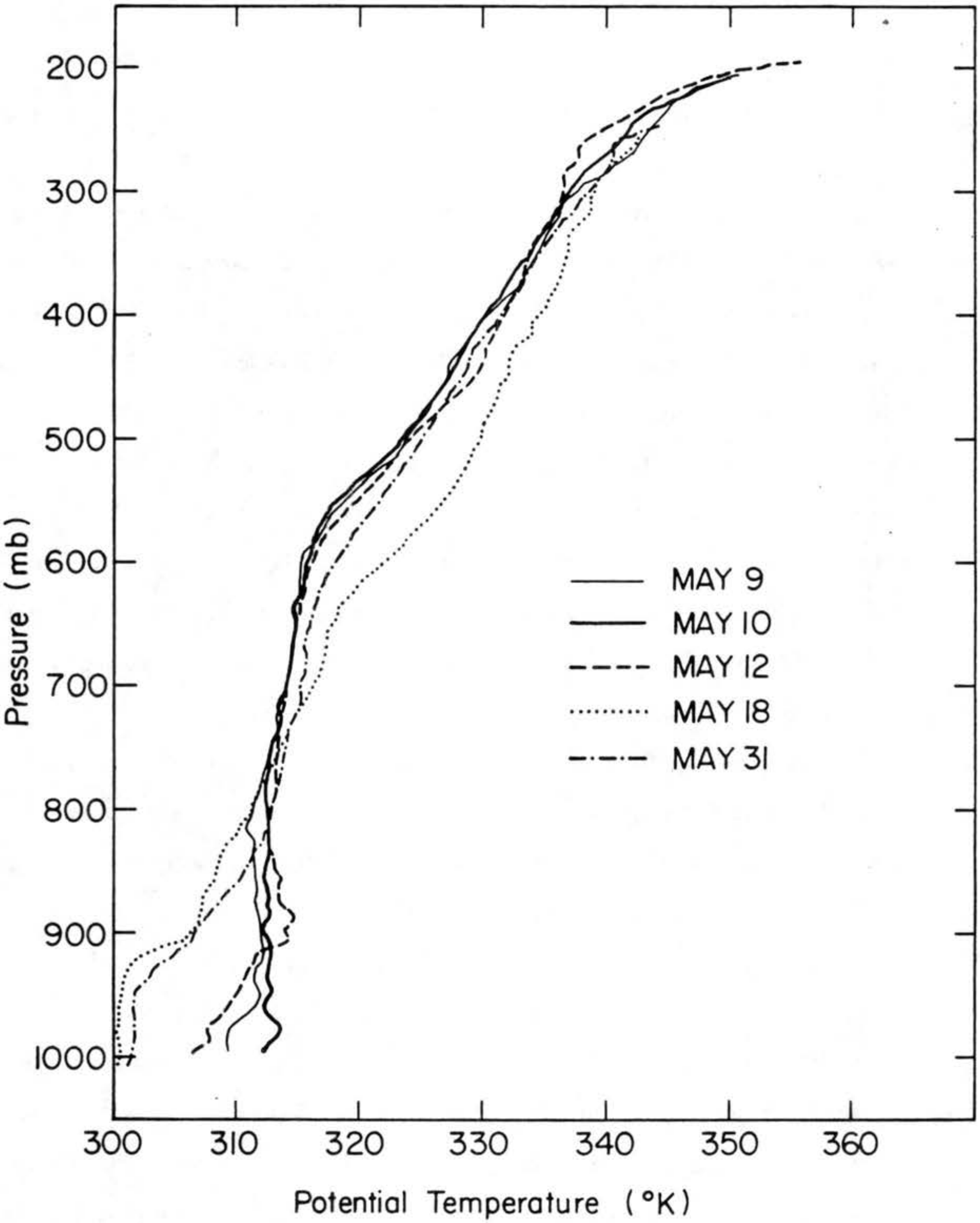


Figure 2.4: Potential temperature of the profiles shown in figure 3.

layer is a stable layer where ($\Delta\theta/\Delta Z$ remains fairly constant. The transition layer is marked by a temperature inversion at the top of the dust layer, which was consistently observed during SMONEX.

This type of temperature structure has been observed over other desert regions. Carlson and Prospero (1972) observed this capping temperature inversion in Saharan air masses crossing the Atlantic. The isentropic layer in the Saharan air mass was approximately 313 $^0K$, similar to the SMONEX observations. Carlson and Prospero (1972) note that on leaving the African continent the isentropic layer may be 3-4$^0K$ higher than when it arrives over the Caribbean. Carlson and Caverly (1977) have also discussed the similarities in the Saharan air layer as it leaves north Africa and crosses the Atlantic. A uniform $\theta$ layer was also observed by Fouquart et al. (1984) over Niger in the winter of 1980 during ECLATS. This isentropic layer was not as deep and had a lower temperature. Reiff et al. (1986) made use of this characteristic isentropic layer in tracking an African dust layer across Europe.

Rawinsonde observations (taken at 00 and 12 GMT) at Riyhad, Saudi Arabia for the year 1979 consistently displayed a temperature inversion between 400 and 600 mb during the summer months. Figure 5 displays the distribution of temperature inversions as a function of pressure and Julian Day for Riyhad for the months of May, June, July and August 1979. Temperature inversions are represented by a T and are defined as an increase in temperature with a decrease in pressure. Vertical stacking of T's indicates the depth of the inversion, thus the stratosphere is distinctly evident. The low level nighttime surface inversions are also evident in this figure. A third region of prominent temperature inversions appears in the 500-600 mb layer, associated with the top of the dust layer. This inversion layer appears in early June and is consistently observed through early October.

Large diurnal variations in surface temperature over desert and semi-desert regions are well documented. For example, Smith (1986) presents the daily mean surface temperatures of the Arabian desert. The diurnal amplitude of the surface temperature was near 40 $^0C$.

As dust outbreaks are transported from the desert to the ocean, the lower atmospheric layer undergoes an airmass transformation: cooling and moistening. An example

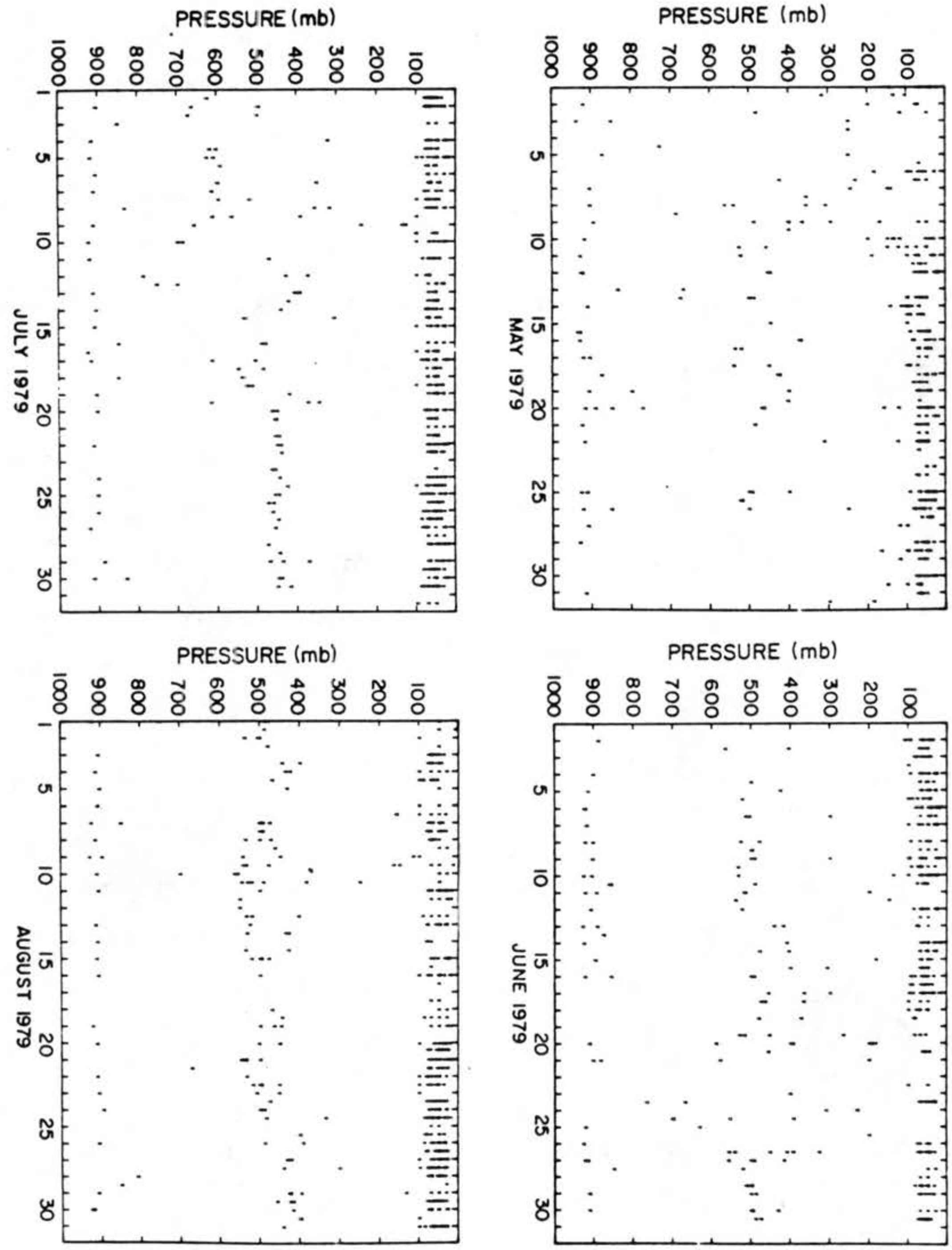


Figure 2.5: Distribution of temperature inversions as a function of pressure and Julian Day for the months of May, June July and August 1979. The location of a temperature inversion is represented by a T. Observations were taken at 00 and 12 GMT at Riyadh, Saudi Arabia.

of temperature and moisture profiles of an air mass that moved from the Saudi Arabian peninsula to the Arabian Sea is shown in figure 3 (flight 13). Similar examples of this transformation can be found in Carlson and Prospero (1972).

The observations presented above were incorporated into a representative temperature profile for desert and oceanic regimes, and are listed in tables 3 and 4. Radiative calculations in this study will use these temperature profiles unless otherwise stated.

### 2.3 Moisture profiles

Observations of the Saharan dust layer by Carlson and Prospero (1972) depict a fairly uniform mixing ratio with a mean value of 2-4 $gKg^{-1}$ within the dust layer. Mixing ratios of 4-6 $gKg^{-1}$ were measured by Fouquart et al. (1984), again uniformly mixed throughout the isentropic layer. In both studies the top of the dust layer was marked by a temperature inversion, above which the mixing ratio (q) decreased rapidly with height. The vertical distribution of q over Saudi Arabia (figure 3) displays less uniformity. Maximum values of approximately 5-9 $gKg^{-1}$ were observed near the surface with 1-2 $gKg^{-1}$ near the top of the dust layer. As in the other dust laden atmospheres, the top of the dust layer was marked by a sharp decrease in q. Variations of q are much less above the dust layer than within. The q structure observed in the mean profile is also exhibited in the individual soundings. It is apparent in figure 3 that the top of the dust layer approaches saturation; however, no clouds were observed at the time of the dropwindsonde launchs (see Smith et al., 1980).

For the desert moisture profiles we assigned a vertical profile in which q decreases with height. Similar profiles within the dust layer will be assumed for the case of a dust layer over the sea; however, for this case the lower level moisture will correspond to that of Figure 3. Both profiles are marked by a strong drying above the dust layer. Examples of the moisture profiles are given in table 3.

### 2.4 Size distributions

Size distributions of desert aerosols are generally measured with one of three methods: 1) microscopic techniques which involve electron-microscopic analysis of particles

Table 2.3: Desert and oceanic temperature and mixing ratio profiles

| | DESERT | | OCEAN | |
|---|---|---|---|---|
| Pressure (mb) | T ($^0K$) | q (g/kg) | T ($^0K$) | q (g/kg) |
| 0.0003 | 210.0 | 0.002 | 210.0 | .002 |
| 0.0579 | 219.0 | 0.002 | 219.0 | .002 |
| .854 | 270.0 | 0.006 | 270.0 | .006 |
| 1.59 | 265.0 | 0.009 | 265.0 | .009 |
| 3.05 | 254.0 | 0.010 | 254.0 | .010 |
| 6.0 | 243.0 | 0.013 | 243.0 | .013 |
| 12.2 | 232.0 | 0.020 | 232.0 | .020 |
| 25.7 | 221.0 | 0.016 | 221.0 | .016 |
| 30.0 | 219.0 | 0.012 | 219.0 | .012 |
| 35.0 | 217.0 | 0.009 | 217.0 | .009 |
| 40.9 | 215.0 | 0.008 | 215.0 | .008 |
| 48.0 | 211.0 | 0.006 | 211.0 | .006 |
| 56.5 | 207.0 | 0.005 | 207.0 | .005 |
| 66.6 | 203.0 | 0.004 | 203.0 | .004 |
| 78.9 | 199.0 | 0.004 | 199.0 | .004 |
| 93.7 | 195.0 | 0.003 | 195.0 | .003 |
| 111.0 | 197.0 | 0.003 | 197.0 | .003 |
| 132.0 | 204.0 | 0.003 | 204.0 | .003 |
| 156.0 | 210.0 | 0.004 | 210.0 | .004 |
| 200.0 | 222.2 | 0.04 | 222.2 | .07 |
| 250.0 | 230.2 | 0.07 | 231.2 | .07 |
| 300.0 | 239.2 | 0.15 | 240.2 | .15 |
| 350.0 | 248.2 | 0.25 | 248.2 | .25 |
| 400.0 | 255.2 | 0.37 | 255.2 | .44 |
| 450.0 | 260.2 | 0.60 | 263.2 | .70 |
| 500.0 | 266.2 | 0.70 | 266.2 | 1.1 |
| 550.0 | 268.4 | 2.75 | 271.2 | 1.5 |
| 600.0 | 273.2 | 3.5 | 274.7 | 2.2 |
| 650.0 | 278.2 | 4.2 | 279.2 | 3.2 |
| 700.0 | 283.2 | 4.9 | 284.2 | 3.5 |
| 750.0 | 288.2 | 5.5 | 289.2 | 3.6 |
| 800.0 | 293.2 | 6.1 | 293.2 | 3.6 |
| 850.0 | 298.2 | 6.8 | 296.2 | 4.0 |
| 900.0 | See Table 4 | 7.5 | 297.2 | 8.5 |
| 950.0 | See Table 4 | 8.1 | 298.2 | 18.1 |
| 1000.0 | See Table 4 | 8.8 | 301.2 | 20.5 |

Table 2.4: Diurnal variation of temperature for the surface and the three lowest layers of the desert atmosphere

| Local Time | Surface | 1000 mb | 950 mb | 800 mb |
|---|---|---|---|---|
| 00 | 28.4 | 27.8 | 32.7 | 28.8 |
| 01 | 26.9 | 26.7 | 32.6 | 28.7 |
| 02 | 25.3 | 25.0 | 32.4 | 28.6 |
| 03 | 24.3 | 24.0 | 32.2 | 28.5 |
| 04 | 23.7 | 23.0 | 31.8 | 28.4 |
| 05 | 23.0 | 22.5 | 31.7 | 28.3 |
| 06 | 22.7 | 22.0 | 31.5 | 28.2 |
| 07 | 26.9 | 27.0 | 31.7 | 28.3 |
| 08 | 31.6 | 30.7 | 31.9 | 28.4 |
| 09 | 38.5 | 37.8 | 32.4 | 28.4 |
| 10 | 47.2 | 39.8 | 32.6 | 28.5 |
| 11 | 53.5 | 40.5 | 32.9 | 28.6 |
| 12 | 56.4 | 41.0 | 33.2 | 28.7 |
| 13 | 57.4 | 41.4 | 33.6 | 28.8 |
| 14 | 56.9 | 41.7 | 33.8 | 28.9 |
| 15 | 55.5 | 41.5 | 34.2 | 29.0 |
| 16 | 54.0 | 41.0 | 34.6 | 29.1 |
| 17 | 50.6 | 39.9 | 34.8 | 29.2 |
| 18 | 45.8 | 38.8 | 35.0 | 29.4 |
| 19 | 39.9 | 35.5 | 34.8 | 29.3 |
| 20 | 35.7 | 33.6 | 34.3 | 29.2 |
| 21 | 33.6 | 31.7 | 33.8 | 29.1 |
| 22 | 31.9 | 30.7 | 33.5 | 29.0 |
| 23 | 30.4 | 28.7 | 33.1 | 28.9 |
| 24 | 28.4 | 27.8 | 32.7 | 28.8 |

collected on various filter membranes; 2) light scattering techniques using single particle optical counters; and 3) the mathematical inversion of radiation measurements. Extensive measurements of dust size distributions $n(r)$ are available in the literature, of which a select few are shown in figure 6. This figure is by no means an attempt to include all measurements, but rather the $n(r)$ shown were chosen to represent a variety of field experiments over different parts of the world. It is apparent from this figure that the number of particles in a given size range can vary by more that two orders of magnitude. While the variations in $n(r)$ are large several generalizations can be made. First of all the number concentrations generally decrease with increasing altitude, yet the shape of the size distributions tends to remain the same (Patterson et al., 1980; Ackerman and Cox, 1982). In addition, as a dust outbreak undergoes its life cycle, the number concentrations decrease while the shape of the size distribution remains very similar (D'Almeida and Schutz, 1983). Patterson and Gillette (1977) have characterized the size distribution of aerosols in which soil-derived particles are an important component into three modes:

A) Mode A consists of particles that have been produced from the parent soil by a process of sandblasting. It consists of aggregates of clay particles, quartz particles and other minor crustal components and is characterized by particles whose radius is less than 10 $\mu m$.

B) Mode B is composed of particles whose size distribution is characteristic of the soils from which the aerosols are derived. This mode has a dominant quartz component characterized by particles whose radii are generally greater than 10 $\mu m$.

C) Mode C is composed mostly of anthropogenic secondary aerosols.

These characteristic modes are consistently present in measurements of particle size distributions of crustal aerosols. The importance of a given mode changes as the distance from the source region increases. At a source region mode B is very pronounced while mode A becomes the more dominant component of the size distribution as the distance from the source region increases. The volume mean radius for modes A and B are approximately 3 and 30 $\mu m$ respectively. A similar bimodal structure in the particle volume distribution

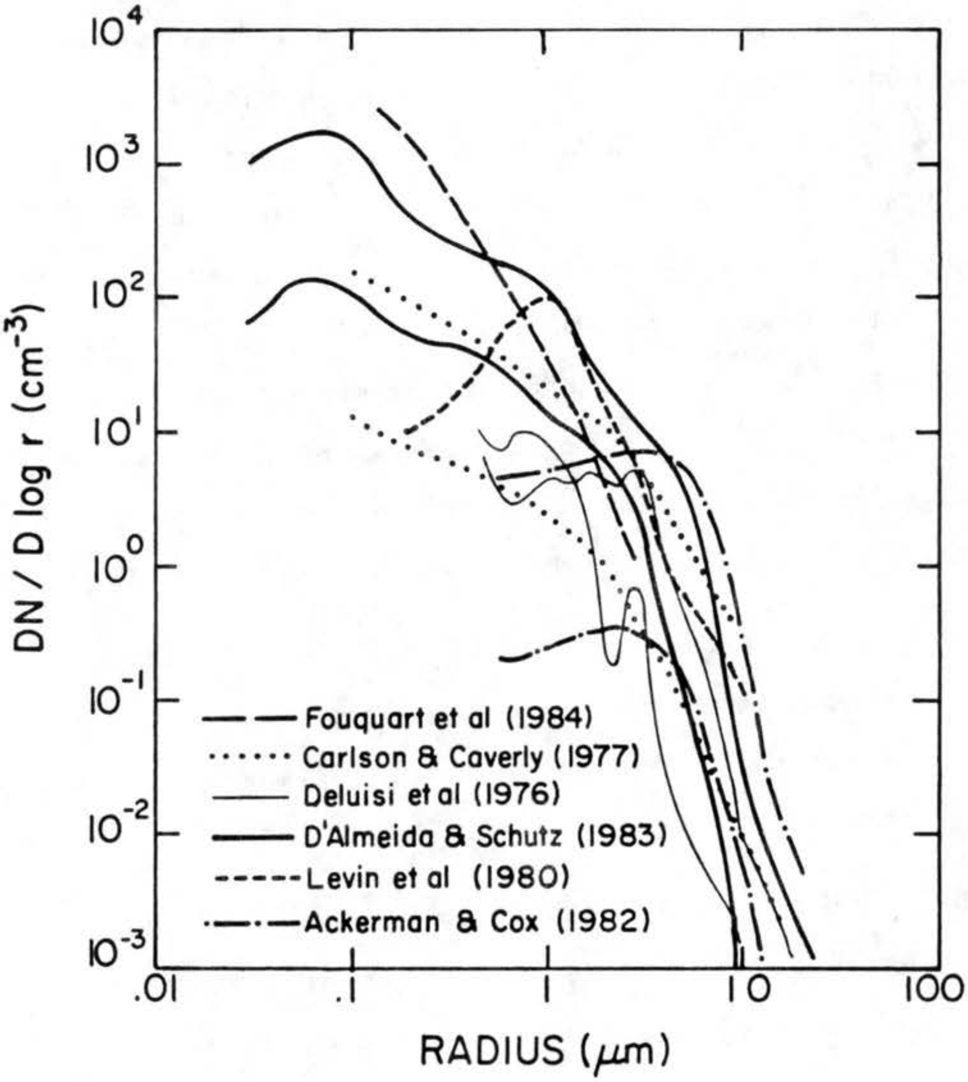


Figure 2.6: Measurements of particle size distribution for soil derived aerosols.

was observed in Saharan dust and soil by D'Almeida and Schutz (1983), however they attribute their mode C as a desert aerosol. The bimodal structure was observed in the continental boundary layer aerosol distribution of Patterson et al. (1980), with those particles with $r > 0.5\mu m$ being generally crustal aerosol particles. In a study of dust particles generated by vehicular traffic, Pinnick et al. (1985) noted that the size distribution and composition of vehicular dust were similar to those of wind blown dust.

For the purposes of this study we will use (unless otherwise stated) the analytic expressions given by Patterson and Gillette (1977) to represent the dust particle size distribution. They have fitted measured size distributions to log normal profiles of the form:

$$n(r) = \frac{N_0}{r \ln \sigma} \exp\left(\frac{-\ln^2 \frac{r}{r_n}}{2 \ln^2 \sigma}\right) \tag{1}$$

where $N_0$ is the number of particles per unit volume, $r_n$ the mean radius, and $\sigma$ the geometric standard deviation of the distribution. Each mode is represented as a separate log normal distribution. Mode A is assumed to represent the well mixed long-range transport fraction of the dust, while Mode B represents local contributions by the source region. As noted in Hansen and Travis (1974) and Ackerman and Stephens (1987), the effect of the size distribution on aerosol single scattering properties are primarily determined by the effective radius ($r_{eff}$) of the distribution, defined as

$$r_{eff} = \frac{\int_0^\infty n(r) r^3 dr}{\int_0^\infty n(r) r^2 dr} \tag{2}$$

The $r_{eff}$ of modes A and B are 2.06 and 31.85 $\mu m$ respectively.

### 2.5 Index of refraction

Measurements of the index of refraction ($m = n - i\kappa$) of a material are very difficult (Bohren and Huffman 1983). Estimates of $m$ for an aerosol are also compounded by the fact that changes in the size distribution reflect changes in the mineralogical and chemical properties of the aerosol, and thus a corresponding change in the index of refraction.

Patterson (1981) tabulated measurements of m for crustal aerosols for wavelengths between 0.25 - 20 $\mu m$. Patterson (1981) demonstrated that the index of refraction of dust is a function of the mineralogical characteristics of the aerosol and fractionation processes that occur in their generation and transport, thus explaining some of the measurement discrepancies by different authors. The results of his work imply the feasibility of parameterizing the radiative properties of crustal aerosols. For example, the relative importance of the clay particle mode (mode A) increases with distance from the source region; since clay particles from two different source regions have similar composition, dust layers far from a source region may have similar optical properties. Patterson (1981) recommends which data set is appropriate near aerosol source regions as well as for the remote case. In this study we will primarily make use of the indices of refraction presented by Patterson (1981) for the Saharan and southwest Asian dust and by Patterson et al. (1983) for Saudi Arabian dust.

### 2.6 Single scattering properties of the crustal aerosol

The single scattering properties of the aerosol are described in terms of the single scattering albedo, $\omega_0$, the scattering phase function, $P(\mu)$ (or the asymmetry parameter, $g = \frac{1}{2}\int P(\mu)\mu d\mu$); and the extinction coefficient, $\sigma_{ext}$. These parameters can be calculated (assuming spherical particles) from Mie theory given the aerosol index of refraction and the particle size distribution.

#### 2.6.1 Particle shape

Microscopic analysis reveals that the dust particles are irregular in shape. There is no general solution to the scattering by irregularly shaped particles, one normally assumes the particles to be spherical. However it is worthwhile here to note some of the similarities and differences that exist between the scattering by spherical and nonspherical particles. In general large nonspherical particles scatter in the forward direction ( angles less than $60^0$) in a manner similar to area-equivalent spheres (Hodkinson and Greenleaves, 1963; Hodkinson, 1963 and Ellison, 1957). In these large particles the forward scattering is primarily a result of diffraction, external reflection and twice refracted transmission. Greatest differences in the phase function between nonspherical and spherical particles is at angles greater than about $90^0$. The phase function is much flatter for the nonspherical particles, which do not exhibit a sharp increase in the backward direction. Quartz particles tend to scatter more in the $60^0 - 140^0$ range than their spherical counterparts. Measurements by Proctor and Harris (1974) indicated that large irregular quartz particles scatter light at wider angles than do spheres of the same size.

Generalizations regarding the asymmetry parameter differences between spherical and nonspherical particles are difficult to make. For example, Pollack and Cuzzi (1980) calculated asymmetry parameters for nonspherical particles which were less than the spherical counterparts. While Asano and Sato (1980) calculated values which were less than for the irregular particle shape, Pollack and Cuzzi (1980) also calculated single-scattering albedos that were larger . Mugnai and Wiscombe (1980) demonstrated that agreement between nonspherical particles and equivalent spheres improves with increased absorption and size averaging.

Mugnai and Wiscombe (1980) also noted that the agreement between equivalent spheres and moderately nonspherical particles was best for the absorption cross section. Hodkinson (1963) reported than for large size parameters measurements of extinction by irregularly shaped quartz particles, indicates that the extinction efficiency approaches a constant value. Thus for a size distribution of dust particles the single scattering albedo may be well approximated by Mie theory at visible wavelengths where the absorption is high and the size parameter large. Bohren and Huffman (1981) demonstrate the importance of shape effects in the vicinity of strong infrared and absorption bands, for small particles with a uniform size distribution. They showed that assuming a continuous distribution of ellipsoids was a better approximation than assuming a spherical shape when the size parameter was much less than 1.

### 2.6.2 Spectral dependency

Several studies have estimated $\omega_0$ at solar wavelengths, either from direct measurements or from Mie calculations. $\omega_0$ is often reported as a function of wavelength. Figure 7 gives an example of the wide variety of the estimates of $\omega_0$ given by different authors.

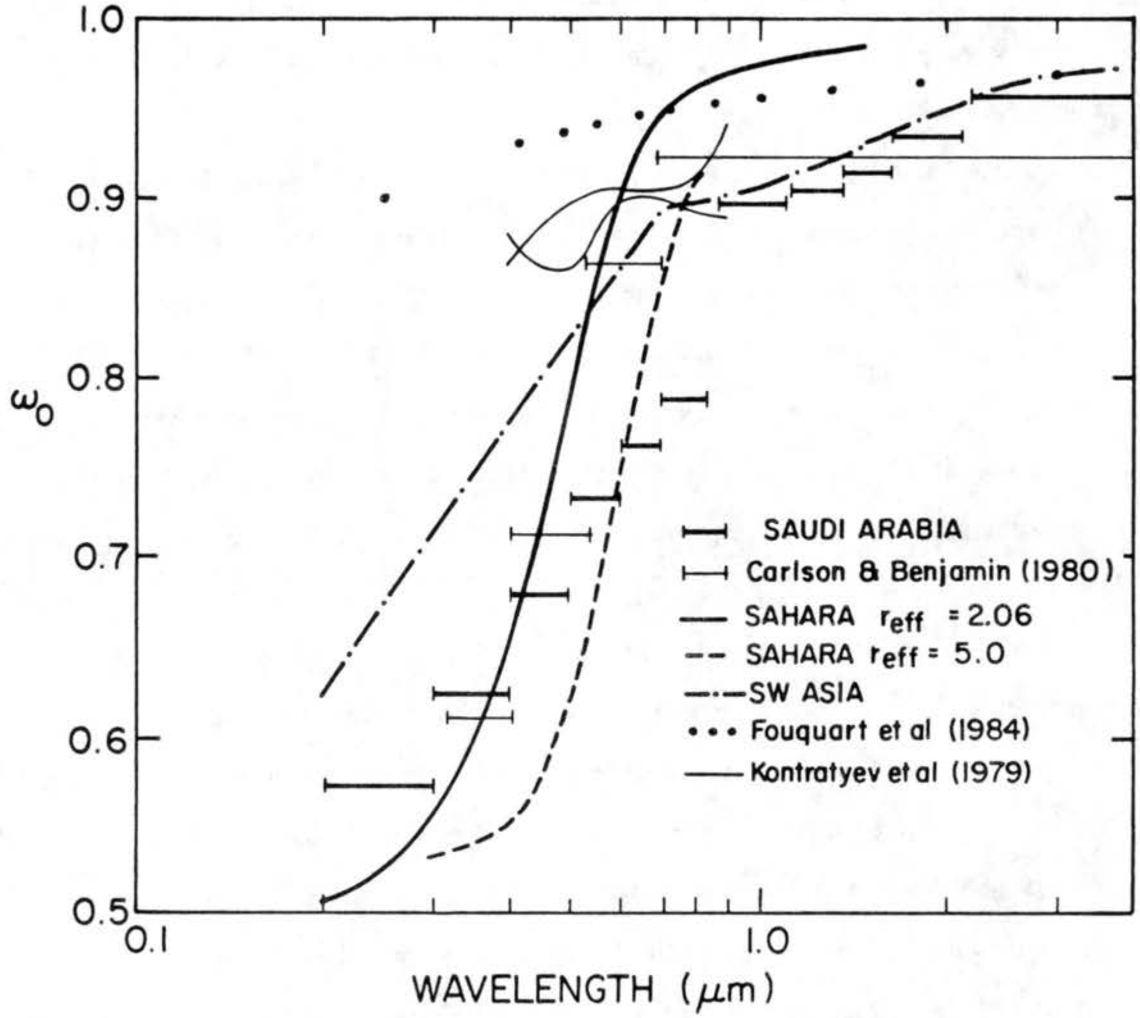


Figure 2.7: The single scattering albedo as a function of wavelength for different crustal aerosols.

All of the values shown in figure 7 were determined from Mie calculations for given size distributions and indices of refraction. Fouquart et al. (1983) assume a constant index of refraction of $1.55 - 0.005i$ and Kondratyev et al. (1979) assume a constant value of $m = 1.65 - 0.005i$ over the wavelength shown. Thus the wavelength variation exhibited by these two studies is due solely to a changing size parameter. The remaining studies allow the index of refraction to vary with wavelength ($\lambda$) and therefore display a more pronounced wavelength dependency. The effect on $\omega_0$ of changing the index of refraction on can be seen by comparing the SW Asian and Saharan dust calculation. The effect of changing size distribution can be seen by comparing the two Saharan profiles, one has an effective radius of $2.06\mu m$ while the second has an effective radius of 5 $\mu m$. A change in size distribution and/or index of refraction has a substantial impact on $\omega_0$.

Table 5 presents calculations of $\omega_0$ at several infrared (IR) wavelengths. Two gamma function size distributions with effective radii of 2.06 and 5 $\mu m$ where used with indices of refraction taken from Patterson (1981). The fourth column assumes a gamma size distribution with a 5 $\mu m$ effective radius and index of refraction measured by Voltz (1973). This table demonstrates that the $\omega_0$ in the LW spectrum is also very sensitive to the dust layer microphysics.

Few studies report values of the asymmetry parameter ($g$) or the scattering phase function appropriate for the SW or LW spectra. Since $g$ is much less variable than $\omega_0$ or $\sigma_{ext}$ it is usually assumed to remain constant for a given wavelength. This may not be appropriate as shown in figure 8 which depicts $g$ as a function of $\lambda$ for the SW spectrum. A comparison of $g$ for the SW Asian and Sahara dust demonstrates the effect of changing the index of refraction while retaining identical size distributions; the effect of changing size distribution can be seen by comparing the two Saharan dust calculations. Table 6 lists values of the asymmetry parameter as a function of IR wavelength for the same dust microphysics given in Table 5. For the SW, $g$ is a strong function of both the size distribution and index of refraction.

The most widely measured optical parameter is the dust optical depth ($\tau_d$). A popular technique for measuring $\tau_d$ is with a photometer or pyrheliometer, from which the total optical depth ($\tau$) or atmospheric turbidity is obtained from Beer's law, i.e.,

Table 2.5: Single scattering albedo for various wavelengths ($\mu m$) and dust microphysics

| $\lambda$ | $n(r)$ / $m$ | Gamma $r_{eff} = 2.06$ Patterson | Gamma $r_{eff} = 5$ Patterson | Gamma $r_{eff} = 2.06$ Volz | Log normal light Patterson | Log normal heavy Patterson |
|---|---|---|---|---|---|---|
| 4.71 | | .84203 | .77560 | .94669 | .81934 | .80280 |
| 5.00 | | .83224 | .77501 | .89827 | .81000 | .79301 |
| 5.26 | | .81777 | .76876 | .88731 | .79594 | .77881 |
| 5.56 | | .79435 | .75559 | .83768 | .77315 | .75629 |
| 5.88 | | .75141 | .72625 | .77070 | .73100 | .71570 |
| 6.25 | | .67714 | .67444 | .74626 | .65860 | .64740 |
| 6.67 | | .53267 | .59455 | .70363 | .52542 | .52365 |
| 7.14 | | .53143 | .60585 | .53140 | .52937 | .52703 |
| 7.69 | | .52330 | .63875 | .52651 | .53853 | .53528 |
| 8.70 | | .22330 | .40999 | .25400 | .23653 | .27182 |
| 9.70 | | .37945 | .45830 | .37130 | .36228 | .37253 |
| 10.50 | | .56121 | .53117 | .43709 | .53545 | .53578 |
| 11.75 | | .57557 | .61188 | .50756 | .56855 | .56349 |
| 12.9 | | .31021 | .48631 | .31021 | .34295 | .36479 |
| 15.0 | | .28489 | .17073 | .06385 | .07532 | .13974 |
| 18.5 | | .14310 | .34762 | .13644 | .18984 | .25659 |
| 22.2 | | .49866 | .63056 | .47277 | .55015 | .54404 |
| 28.6 | | .39154 | .62368 | .36730 | .50265 | .50791 |
| 40.0 | | .37250 | .65290 | .34863 | .54459 | .54419 |
| 66.6 | | .12566 | .55602 | .11494 | .29437 | .47239 |

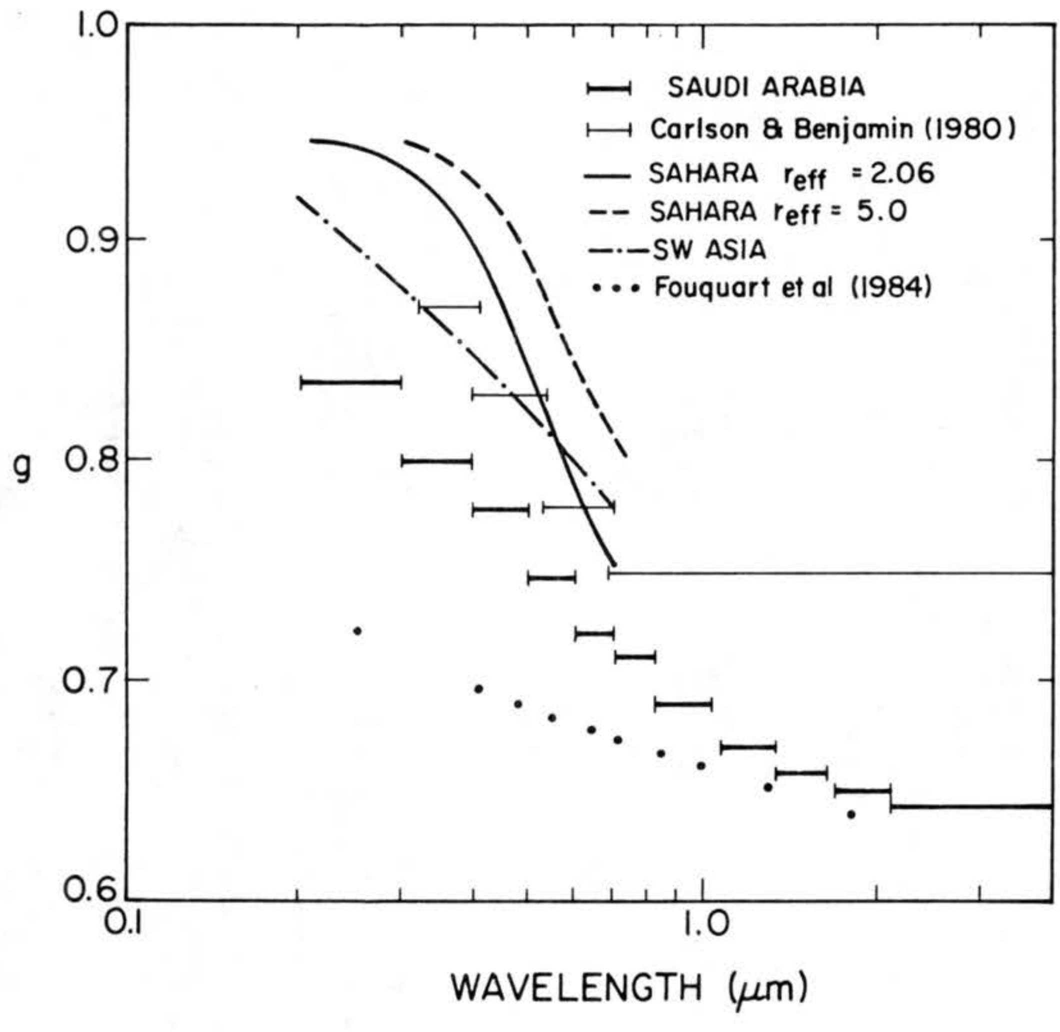


Figure 2.8: The asymmetry parameter as a function of wavelength for the solar spectrum for various soil derived aerosols.

Table 2.6: Asymmetry parameter for various wavelengths ($\mu m$) and dust microphysics

| $\lambda$ | $n(r)$ | Gamma | Gamma | Gamma | Log normal | Log normal |
|---|---|---|---|---|---|---|
| | | $r_{eff} = 2.06$ | $r_{eff} = 5$ | $r_{eff} = 2.06$ | light | heavy |
| | $m$ | Patterson | Patterson | Volz | Patterson | Patterson |
| 4.71 | | .76456 | .81009 | .75394 | .75244 | .76008 |
| 5.00 | | .75764 | .81128 | .75184 | .74846 | .75676 |
| 5.26 | | .75136 | .81355 | .74592 | .74524 | .75423 |
| 5.56 | | .74395 | .81711 | .74111 | .74185 | .75168 |
| 5.88 | | .73622 | .82360 | .73524 | .73892 | .74987 |
| 6.25 | | .72680 | .83310 | .72429 | .73526 | .74801 |
| 6.67 | | .72139 | .85845 | .72094 | .74284 | .76063 |
| 7.14 | | .70351 | .85166 | .70351 | .73341 | .75320 |
| 7.69 | | .68813 | .85689 | .68819 | .73848 | .76380 |
| 8.70 | | .56062 | .81200 | .53446 | .63187 | .69736 |
| 9.70 | | .50477 | .72530 | .46506 | .52679 | .55452 |
| 10.50 | | .51225 | .67238 | .48830 | .52932 | .55085 |
| 11.75 | | .52083 | .69780 | .51628 | .57042 | .59832 |
| 12.9 | | .47913 | .76088 | .47913 | .59712 | .66156 |
| 15.0 | | .88280 | .73574 | .35992 | .53787 | .77259 |
| 18.5 | | .30745 | .67892 | .30585 | .49830 | .68127 |
| 22.2 | | .322941 | .53448 | .32005 | .43710 | .49891 |
| 28.6 | | .23310 | .49055 | .23112 | .39440 | .49950 |
| 40.0 | | .17270 | .39428 | .17128 | .33174 | .46571 |
| 66.6 | | .0555 | .29707 | .05545 | .16026 | .50157 |

$$I_\lambda = I_{0\lambda} \exp\left(-\frac{\tau}{\mu_0}\right) \tag{3}$$

where $\mu_0$ is the solar zenith angle and

$$\tau = \tau_R + \tau_{oz} + \tau_w + \tau_d \tag{4}$$

with the subscripts $R$, $oz$, $w$ and $d$ referring to Rayleigh scattering, ozone absorption, water vapor absorption and dust respectively. In general the wavelength regimes are chosen to avoid water vapor absorption bands. By subtracting out the effects of Rayleigh scattering and ozone absorption one can then determine the optical depth of the aerosol. If the depth of the dust layer ($\Delta Z$) is known and the aerosol size distribution is independent of height then the extinction coefficient ($\sigma_{ext}$) can be obtained from

$$\tau_d = \sigma_{ext} \Delta Z. \tag{5}$$

The extinction coefficient may also obtained from Mie calculations given a measured size distribution and a measured (more often assumed) index of refraction. A comparison of $\sigma_{ext}$ determined from Mie calculations with that determined from extinction measurements is given in De Luisi et al. (1976).

In addition to estimating $\sigma_{ext}$, measurements of $\tau_d$ at different wavelengths are often depicted on a log-log plot, and a power dependence of the form $\tau_d \approx \lambda^\gamma$ is often observed. The slope of the line ($\gamma$) is the negative of the Angström turbidity coefficient (Angström, 1931). For an inverse power distribution a simple relationship exists between the power of the size distribution and $\gamma$. For example, in Junge size distribution where $dN/d\log r = Cr^{-\beta}$, and

$$\tau_d = \pi \int_0^z \int_0^\infty r^2 Q_{ext}(m, \chi) n(r) dr dz \qquad (6).$$

If the refractive index ($m$) varies little with wavelength over the spectral region of interest, than $Q_{ext}$ is primarily a function of the size parameter. If the size distribution remains constant with height, then

$$\tau_d \approx C\lambda^{2-\beta}\int_0^\infty Q_{ext}(U)U^{1-\beta}dU \qquad (7)$$

where $U = \frac{r}{\lambda}$. The turbidity has often been observed to be proportional to $\lambda^\gamma$, where $\lambda$ is the Angström turbidity coefficient. The $\lambda^\gamma$ dependence of $\tau_d$ on $\lambda$ in equation (7), thus implying an inverse power distribution with $\beta = 2 + \gamma$. Observations of$\gamma$ range between -0.5 and -1.5. In the case where $Q_{ext}$ varies little with size parameter, then from (7), we see that $\tau_d$ is independent of wavelength, $(\gamma = 0)$.

Measurements of Carlson and Caverly (1977) observed this neutral extinction $(\gamma = 0)$ in visible wavelengths. $\sigma_{ext}$ of course depends on the aerosol concentration, and Carlson and Caverly (1977) found a nearly linear relationship between mass loading, $u, (\mu g m^{-3})$ and $\sigma_{ext}$ $(km^{-1})$; $u = 8 * 10^3\sigma_{ext}^{1.25}$. Similar relationships were observed by Patterson and Gillette (1976), and by D'Almeida (1986). Neutral extinction was also observed by Patterson (1977) between 0.55 $\mu m$ and 10.6 $\mu m$. DeLuisi et al. (1976) observed neutral extinction across the visible for the cases in which the particle distribution had a large particle mode; however for the size distributions having only a few large particles, optical depth decreased with increasing wavelength. Fouquart et al. (1984) also measured a monotonically decreasing $\tau_d$ with increasing $\lambda$, as did King et al. (1980).

### 2.6.3 Vertical variation

Figure 9 depicts the vertical variation of $\omega_0$ and $g$ for six spectral intervals determined from measurements made during SMONEX. Both $\omega_0$ and $g$ are constant with height, within instrument error.

Vertical variations of $\sigma_{ext}$ are not as well documented as the integrated values discussed above. Fouquart et al. (1984) found $\sigma_{ext}$ to be uniform with height within the dust layer. For high dust concentrations, Kashima (1965) found that the dust content of the surface layer varies exponentially with height. DeLuisi et al.(1976) measured a highly variable vertical structure in aerosol concentration. Shaw (1980) measured a vertical structure in $\sigma_{ext}$ which was bimodal in an Asian dust layer that was transported over Hawaiian Islands. The primary peak occurred near the top of the layer, while the second

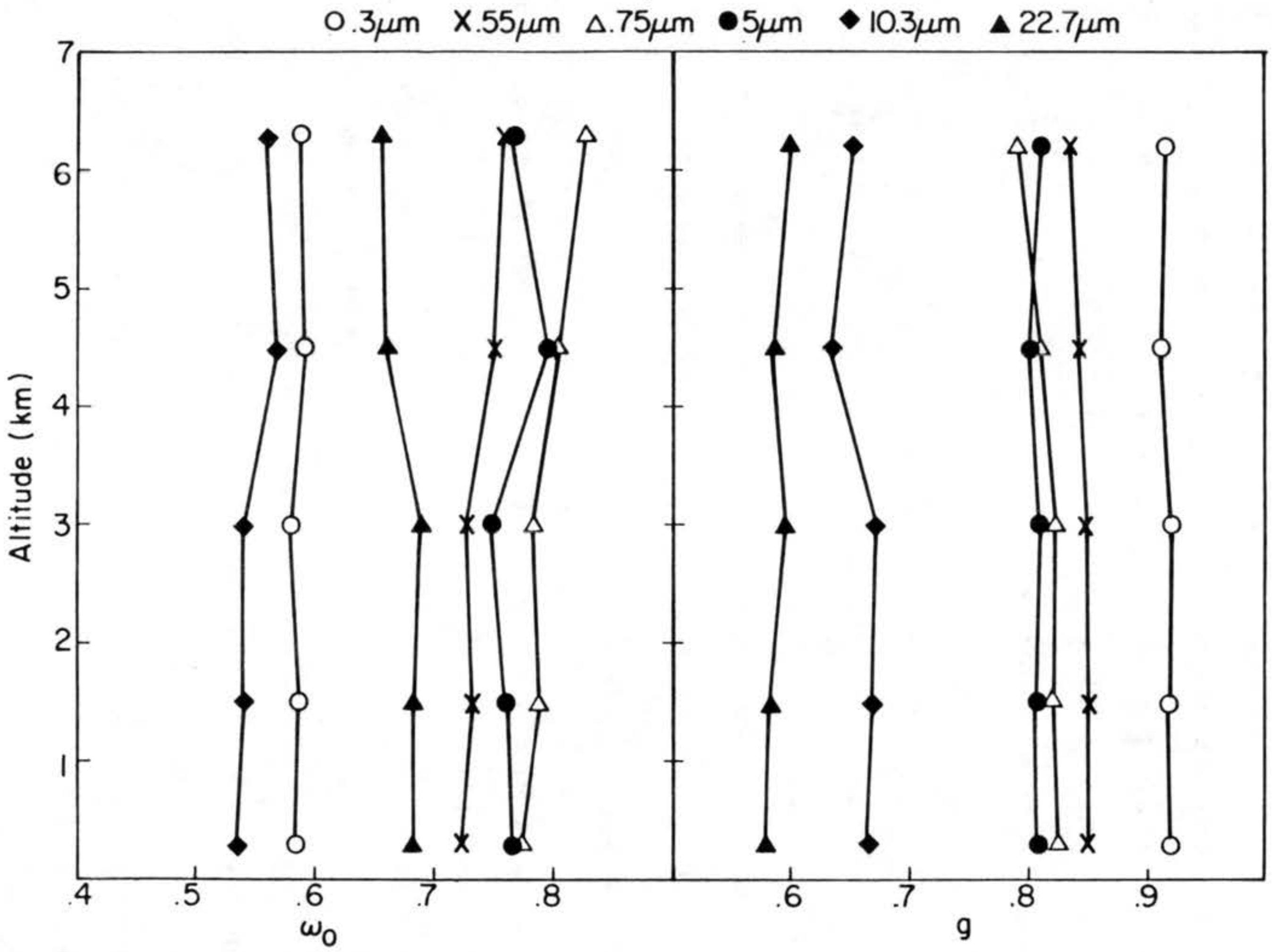


Figure 2.9: Vertical variation of single scattering albedo and asymmetry parameter for six wavelengths as determined by measurements made during SMONEX.

smaller peak existed at or just below the trade inversion. This second peak was attributed to the growth of hygroscopic particles. In their study of the radiative heating rates of Saharan dust, Carlson and Benjamin (1980) assumed that $\sigma_{ext}$ was nearly constant for their desert case, but use a vertical variation in $\sigma_{ext}$ based on the measurements of Prospero and Carlson (1972) for their ocean case. Figure 10 depicts the vertical structure of $\sigma_{ext}$ over the Saudi Arabian peninsula determined from the measurements of Ackerman and Cox (1982) and Patterson et al. (1983). The measurements indicate a strong vertical variation of $\sigma_{ext}$ with maximum values near the surface. This result is relatively independent of wavelength.

For the purposes of this study we employ the single scattering properties determined from the measurements of Ackerman and Cox (1982) and Patterson et al. (1983). The $\omega_0$ and $g$ are assumed to be independent of height. The $\tau_d$ will either be constant with height or decrease with height in a manner similar to that observed by Ackerman and Cox (1982). The total dust optical depth at 0.55 $\mu m$ will be varied between 0 and 3.

### 2.7 Surface radiative properties

Surface reflectivity is a function of surface composition and moisture content as well as the angular and spectral distribution of the incident radiation. This study assumes the desert surfaces to be dry; a wetting of the surface would decrease the surface albedo. Desert surfaces tend to display a distinct difference between visible and near-infrared albedos (Ackerman and Cox, 1982; Smith, 1986 and Smith et al., 1986) with the latter being much higher. The dependence of surface albedo on solar zenith angle also varies between the visible and near-infrared wavelengths; figure 11 depicts the measurements of Smith (1986), denoted by circles, as well as a least square fit to the measurements. This study assumes the solar zenith angle dependence depicted in figure 11. The visible curve is adopted for wavelengths less than 0.7 $\mu m$, while the near-infrared curve is applied to the larger wavelengths. Measurements by Coulson (1966) indicate that specular reflection from desert sand is small and it is therefore assumed that the reflected energy is entirely diffuse.

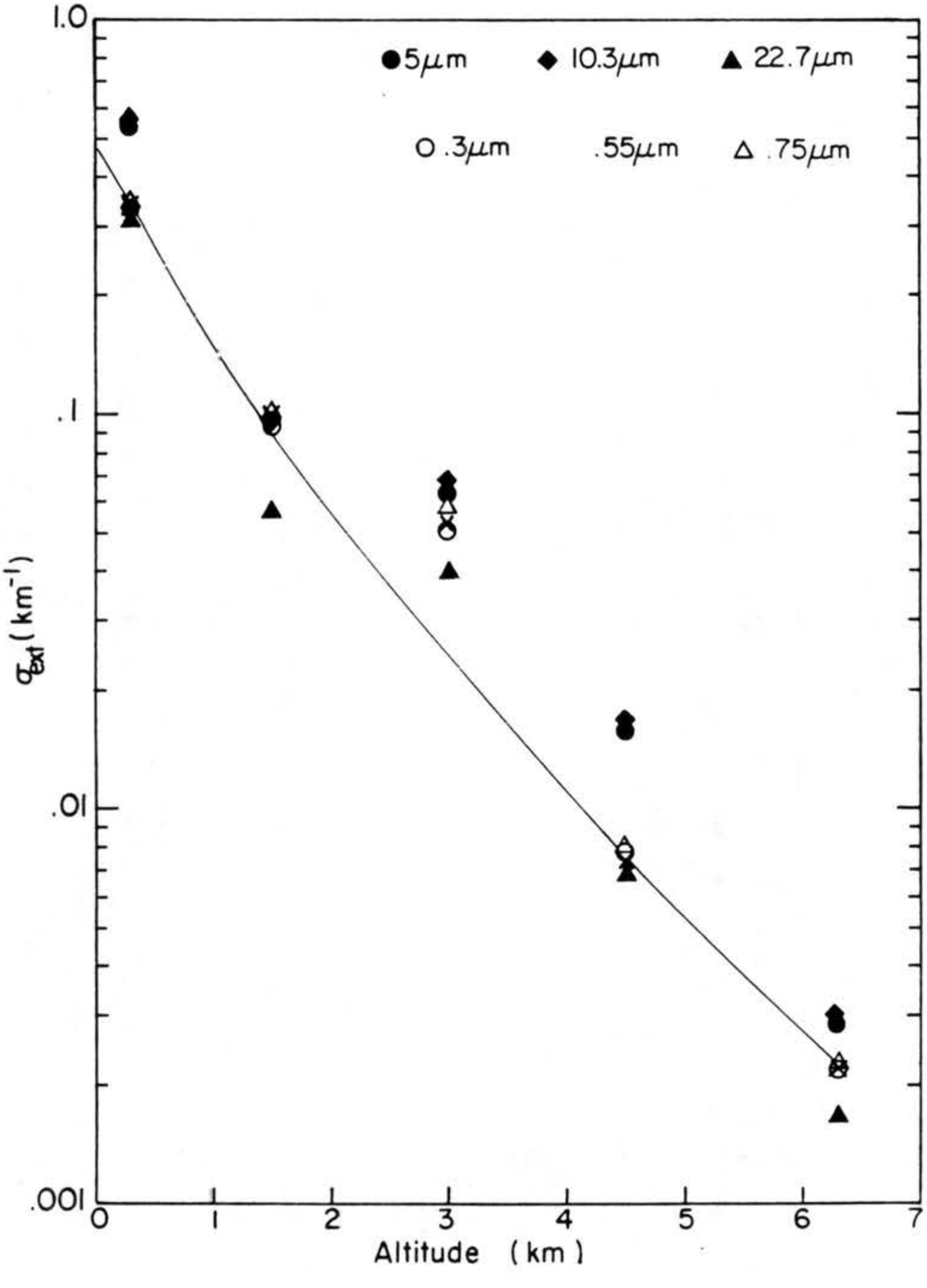


Figure 2.10: Vertical structure of the extinction coefficient over the Saudi Arabian Peninsula at six wavelengths as determined from the measuremens of Ackerman and Cox (1982) and Patterson et al. (1984).

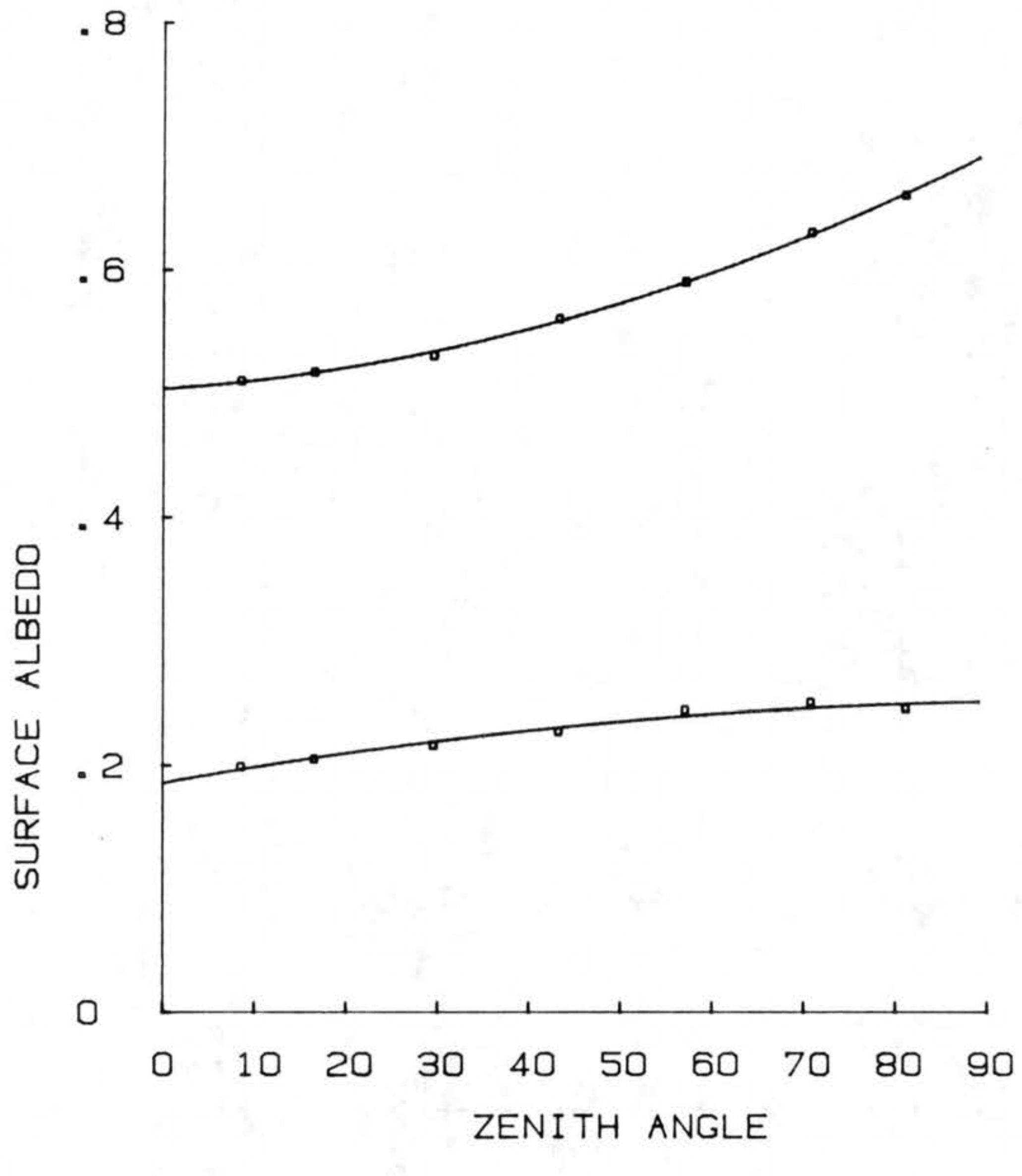


Figure 2.11: Surface albedo as a function of solar zenith angle for the visible (bottom) and near-infrared wavelengths (top). Circles depict measurements of Smith (1986).

Emissivities integrated over the spectral region 8 to 12 $\mu m$ for sandy soils generally vary between 0.9 and 0.98 (Gayevsky 1951, Buettner and Kern 1965). In the present study a surface emissivity of 0.95 is assumed for the LW window regime and a value of 1.0 is assumed for the remaining LW spectral intervals. An emissivity of 1.0 is assigned for water surfaces.

# Chapter 3

## DESCRIPTION OF THE RADIATIVE TRANSFER MODELS

The azimuthally averaged monochromatic radiative transfer equation for diffuse radiation, $I(\tau,\mu)$, in a plane-parallel, horizontally homogeneous medium which scatters, emits and absorbs is

$$\mu\frac{dI(\tau,\mu)}{d\tau} = I(\tau,\mu) - \sigma(\tau,\mu) - \frac{\omega_0}{2}\int_{-1}^{1} P(\tau,\mu,\mu')I(\tau,\mu')d\mu' \qquad (8)$$

where

- $\tau$ optical depth
- $\omega_0$ single scattering albedo
- $I(\tau,\mu,)$ azimuthally averaged intensity
- $P(\tau,\mu,\mu')$ azimuthally averaged phase function
- $\mu = \cos(\theta)$ where $\theta$ is measured from the downward normal direction
- $\sigma(\tau,\mu)$ source term $(\sigma_T + \sigma_D)$
- $\sigma_T = (1-\omega_0)B(T)$ = thermal source
- $\sigma_D = \frac{\omega_0 F_0}{4\pi}P(\tau,\mu,\mu_0)e^{-\tau\mu_0}$ =direct solar source
- $B(T)$ Planck function at temperature $T$
- $F_0$ solar flux incident on the top of the atmosphere
- $\mu_0$ cosine of solar zenith angle

Various mathematical methods have been developed to solve this intergro-differential equation (see for example Irvine, 1975 and Lenoble 1980). In this section two methods of solving equation (8) are presented. The first is the doubling/adding technique, and is discussed in section 3.1. The second and most often used model in this study is a two-stream/adding model. This model is less accurate but more computationally expedient than the doubling method. The derivation of the two-stream model is presented in section 3.2. A comparison between the two models and aircraft observations is presented in section 3.3.

## 3.1 The doubling/adding model

An accurate technique to solve equation (8) is the doubling method. This type of model has been discussed in detail in previous atmospheric studies (e.g. Grant and Hunt, 1969; Wiscombe, 1976a and b; and Stephens, 1979). The doubling method is an application of the interaction principle which can be written as

$$I_1^+ = t_{01} I_0^+ + r_{10} I_1^- + J_{01}^+ \tag{9}$$

$$I_0^- = r_{01} I_0^+ + t_{10} I_1^- + J_{10}^+ \tag{10}$$

where $t_{01}$, $r_{01}$, $t_{10}$ and $r_{10}$ represent the transmittance and reflectance operators of the layer and the positive direction is downward (increasing $\tau$). The $I$'s represent diffuse intensities while the $J$'s are source terms. A schematic representation is given in figure 3.1.

### 3.1.1 Matrix equation of transfer

For the case of different directional radiances the downward ($I^+(\tau)$) and upward ($I^-(\tau)$) radiances are expressed in matrix form

$$I^{\pm}(\tau, \mu) = \begin{bmatrix} I^{\pm}(\tau, \mu_1) \\ I^{\pm}(\tau, \mu_2) \\ \vdots \\ I^{\pm}(\tau, \mu_n) \end{bmatrix} \tag{11}$$

where $I^+(\tau,\mu_i)$ is the radiance traveling in the direction $\theta_i = \cos^{-1}\mu_i$ , while $I^-(\tau,\mu_i)$ is traveling in the opposite direction. To apply the doubling method to the equation (8), the radiance vectors are divided into $2n$ ($n$ up and $n$ down) discrete beams and the the integral term is discretized into $2n$ angles. The discretized radiative transfer equation becomes

$$\mu_i \frac{dI(\tau,\mu_i)}{d\tau} = I(\tau,\mu_i) - \sigma(\tau,\mu_i) - \frac{\omega_0}{2}\sum_{j=1}^{n} c_j\left[P(\tau,\mu_i,\mu_j)I(\tau,\mu_j) + P(\tau,\mu_i,-\mu_j)I(\tau,-\mu_j)\right] \tag{12}$$

$$\mu_i \frac{dI(\tau,\mu_i)}{d\tau} = I(\tau,\mu_i) - \sigma(\tau,\mu_i) - \frac{\omega_0}{2}\sum_{j=1}^{n} c_j(P_{ij}^{++}I^+ + P_{ij}^{+-}I^-) \tag{13}$$

Or in matrix form

$$\pm M\frac{dI_i^{\pm}}{d\tau} = I_i^{\pm} - \sigma_i^{\pm} - \frac{\omega_0}{2}C(P_{ij}^{++}I_j^{\pm} + P_{ij}^{+-}I_j^{\mp}) \tag{14}$$

where

$$M = [\mu_i\delta_{ij}] \tag{15}$$

$$C = [c_j\delta_{ij}] \tag{16}$$

### 3.1.2 Initialization

Wiscombe (1976a) has discussed a number of initialization schemes for the doubling method. The present study employs the Infinitesimal Generator Initialization (IGI). Defining the following average quantities over a a thin layer,$\Delta\tau$

$$I_{1/2}^{\pm} = \frac{1}{\Delta\tau}\int_{\tau_0}^{\tau_1} I^{\pm}d\tau \tag{17}$$

$$\sigma_{1/2}^{\pm} = \frac{1}{\Delta\tau}\int_{\tau_0}^{\tau_1} \sigma^{\pm}d\tau \tag{18}$$

yields

$$\pm M(I_1^{\pm} - I_0^{\pm}) = I_{1/2}^{\pm}\Delta\tau - \frac{\omega_0}{2}C\Delta\tau\left[P_{ij}^{++}I_{1/2}^{\pm} + P_{ij}^{+-}I_{1/2}^{\mp}\right] - \sigma_{1/2}^{\pm} \tag{19}$$

To solve (19) the central intensities ($I_{1/2}^{\pm}$)are expressed as a linear function of the the two boundary intensities

$$I_{1/2}^{+} = X^{+}I_0^{+} + \left[\Im - X^{+}\right]I_1^{+} \tag{20}$$

$$I_{1/2}^{-} = X^{-}I_1^{-} + \left[\Im - X^{-}\right]I_0^{-} \tag{21}$$

Where $\Im$ is the identity matrix. The IGI assumes $X^{+} = X^{-} = \Im$. So that $I_{1/2}^{+} = I_0^{+}$ and $I_{1/2}^{-} = I_1^{-}$ which results in

$$I_1^{+} = I_0^{+}(\Im - \hat{T}\Delta\tau) + \hat{R}\Delta\tau I_1^{-} + \sigma_{1/2}^{+}\Delta\tau \tag{22}$$

$$I_0^{-} = I_1^{-}(\Im - \hat{T}\Delta\tau) + \hat{R}\Delta\tau I_0^{+} + \sigma_{1/2}^{-}\Delta\tau \tag{23}$$

where

$$\hat{T} = M^{-1}(\Im - \frac{\omega_0}{2}P_{ij}^{++}C) \tag{24}$$

$$\hat{R} = M^{-1}\frac{\omega_0}{2}CP_{ij}^{+-} \tag{25}$$

Equations (22) and (23) are statements of the interaction principle with the operators

$$t_{01} = (\Im - \hat{T}\Delta\tau) \tag{26}$$

$$r_{01} = \hat{R}\Delta\tau \tag{27}$$

$$J_{01}^{+} = \sigma_{1/2}^{+}\Delta\tau \tag{28}$$

$$J_{10}^{-} = \sigma_{1/2}^{-}\Delta\tau \tag{29}$$

Bounds are placed on the initial optical thickness ($\Delta\tau$) to insure that the initial reflectance and transmittance matrices are non-negative. For the IGI the upper limit is (Wiscombe, 1976a)

$$\Delta\tau_{max} \approx \mu_1/10 \tag{30}$$

### 3.1.3 Phase function

The phase function $P(\mu,\mu')$ in equation (8) describes the angular distribution of scattered energy. The phase function can be expanded with a finite number of terms using Legendre Polynomials ($P_\ell(\mu)$). For the azimuthally averaged phase function

$$P(\mu,\mu') = \sum_{\ell=0}^{2N-1} \chi_\ell P_\ell(\mu) P_\ell(\mu') \tag{31}$$

where

$$\chi_\ell = \frac{2\ell+1}{2}\int_{-1}^{1} P(\mu)P_\ell(\mu)d\mu \tag{32}$$

Energy conservation requires that the azimuthally averaged phase function satisfy

$$\frac{1}{2}\int_{-1}^{1} P(\mu,\mu')d\mu' = \frac{1}{2}\sum_{j=1}^{N} c_j\left[P(\mu,\mu_j) + P(\mu,-\mu_j)\right] = 1 \tag{33}$$

This equality is satisfied with the use of Gaussian quadrature. While energy conservation is obtained it is possible to get negative values of $P(\mu,\mu_j)$ for small values of $N$. To overcome this problem the $\delta - M$ method of Wiscombe (1977) is employed in which $\chi_\ell$ is replace with

$$\chi_\ell^* = \frac{\chi_\ell - f}{1-f} \tag{34}$$

where

$$f = \chi_{2N} \tag{35}$$

and $\tau$ and $\omega_0$ are replace with $\tau'$ and $\omega_0'$ where

$$\tau' = (1 - \omega_0)\tau \tag{36}$$

$$\omega_0' = \frac{(1-f)\omega_0}{(1-f\omega_0)} \tag{37}$$

### 3.1.4 Doubling/adding

For the case in which only the emergent radiance of the layer are of interest, the problem is one of defining the diffuse reflection and transmission operators and the source vectors for the total layer. The diffuse reflection and transmission operators are derived from the interaction principle and are

$$t_{n+1} = t_n(\Im - r_n r_n)^{-1} t_n \tag{38}$$

$$r_{n+1} = r_n + t_n(\Im - r_n r_n)^{-1} r_n t_n \tag{39}$$

The doubling method determines these operators by iterating from $n = 0$ to $n = N - 1$ to yield $r_N$ and $t_N$ of the entire layer.

Wiscombe (1976b) has derived the doubling rules for several inhomogeneous sources whose spatial and angular dependencies separate. In the case of the exponential source (e.g direct solar component) the source doubling rules are

$$J_{n+1}^{+} = t_n \Gamma_n(\sigma_n r_n J_n^{-} + J_n^{+}) + \sigma_n J_n^{+} \tag{40}$$

$$J_{n+1}^{-} = t_n \Gamma_n(r_n J_n^{+} + \sigma_n J_n^{-}) \tag{41}$$

where

$$\Gamma_n = (\Im - r_n r_n)^{-1} \tag{42}$$

$$e_n = \exp\left(-2^n \frac{\Delta\tau}{\mu_0}\right) \tag{43}$$

For the case of the thermal source, the Planck function is assumed to be linear in optical depth

$$B(\hat{\tau}) = B(\tau_0) + \frac{B(\tau_N) - B(\tau_0)}{\tau_N}\hat{\tau} \quad 0 \leq \hat{\tau} \leq \tau_N \tag{44}$$

The doubling relations are then

$$J_n^{\pm} = \frac{1}{2}[B(\tau_0) + B(\tau_N)]Y_n \pm \left[\frac{B(\tau_N) - B(\tau_0)}{\tau}\right] Z_n \tag{45}$$

where

$$Z_{n+1} = Z_n + g_n Y_n + (t_n \Gamma_n - t_n \Gamma_n r_n)(Z_n - g_n Y_n) \tag{46}$$

$$g_n = 2^{n-1}\Delta\tau \tag{47}$$

$$Z_0 = 0 \tag{48}$$

$$t_n = t_0^{2n} \tag{49}$$

$$Y_{n+1} = (t_n \Gamma_n r_n + t_n \Gamma_n + \Im)Y_n \tag{50}$$

$$Y_0 = (1 - \omega_0)M^{-1}\Delta\tau \tag{51}$$

The doubling method is applicable to a layer in which the single scattering properties are uniform. For the case of an inhomogeneous atmosphere, it is divided into $N$ homogeneous layers. The doubling procedure is used to derive the diffuse reflection operator, $r(n, n+1)$, the diffuse transmittance operator, $t(n, n+1)$, and the source terms $J^+(n, n+1)$ and $J^-(n, n+1)$ for the homogeneous layer bounded by levels $n$ and $n+1$. To combine these homogeneous layers requires the use of an adding scheme in which the reflectance and transmittance operators and source terms for the homogeneous layers are combined to yield the appropriate operators for the inhomogeneous layer. According to the interaction principle (see Chandrasekhar, 1950), the radiances $I_1^+$ and $I_0^-$ emerging from a layer (see figure 3.1) are linear functions of the incident radiances $I_0^+$ and $I_1^-$ in addition to contributions from sources within the layer, $J_{01}^+$ and $J_{10}^-$. Thus the radiances exiting the layer between $\tau_0$ and $\tau_1$ are

$$I_1^+ = t_{01} I_0^+ + r_{10} I_1^- + J_{01}^+ \tag{52}$$

$$I_0^- = r_{01} I_0^+ + t_{10} I_1^- + J_{10}^- \tag{53}$$

where $t_{01}$ and $r_{01}$ are the diffuse transmittance and reflectance operators of the layer. Similarly, for the radiance emerging from the layer $\tau_1$ to $\tau_2$

$$I_2^+ = t_{12} I_1^+ + r_{21} I_2^- + J_{12}^+ \tag{54}$$

$$I_1^- = r_{12} I_1^+ + t_{21} I_2^- + J_{21}^- \tag{55}$$

and for $\tau_0$ to $\tau_2$

$$I_2^+ = t_{02} I_0^+ + r_{20} I_2^- + J_{02}^+ \tag{56}$$

$$I_0^- = r_{02} I_0^+ + t_{20} I_2^- + J_{20}^- \tag{57}$$

Solving for $I_1^+$ and $I_1^-$ we have

$$I_1^+ = (1 - r_{10} r_{12})^{-1} (t_{01} I_0^+ + r_{10} t_{21} I_2^- + J_{01}^+ + r_{10} J_{21}^-) \tag{58}$$

$$I_1^- = (1 - r_{12} r_{10})^{-1} (t_{21} I_{-}^{+} + r_{12} t_{01} I_0^+ + J_{21}^- + r_{12} J_{01}^+) \tag{59}$$

From the above set of equations one can derive the transmittance, reflectance and source operators for the combined layers. They are

$$t_{02} = t_{12}(1 - r_{10}r_{12})^{-1}t_{01} \tag{60}$$

$$r_{20} = r_{21} + t_{12}(1 - r_{10}r_{12})^{-1}r_{10}t_{21} \tag{61}$$

$$J_{02} = J_{12} + t_{12}(1 - r_{10}r_{12})^{-1}(J_{01} + r_{10}J_{21}) \tag{62}$$

and

$$J_{20} = J_{10} + t_{10}(1 - r_{12}r_{10})^{-1}(J_{21} + r_{12}J_{01}) \tag{63}$$

Thus the radiances exiting the layer bounded by the level $\tau_n$ and $\tau_{n+1}$ can be determined for $n = N, N-1, \ldots 2, 1$ by the recursive formulae

$$I_{n+1}^{+} = r_{n,n+1}I_{n+1}^{-} + J_{n,n+1} \tag{64}$$

$$I_{n+1}^{-} = t_{n,n+1}I_{n+1}^{+} + J_{n,n+1} \tag{65}$$

In the case of a reflecting surface at $\tau_{N+1}$,

$$I_{N+1}^{-} = r_g I_{N+1}^{+} \tag{66}$$

where $r_g$ is a suitable defined reflection operator. Substituting equation (66) into (64) yields

$$I_{N+1}^{+} = \left[\Im - r_{1,N+1}r_g\right]^{-1} J_{n,n+1} \tag{67}$$

from which $I_{N+1}^{-}$ follows from equation (66), and the remaining intensities are computed from the recursive relations (64) and (65).

The upward and downward fluxes at each level are then computed from

$$F^{+}(\tau) = 2\pi \sum_{i=1}^{n} c_i \mu_i I^{+}(\tau, -\mu_i) + \sigma_s \tag{68}$$

$$F^-(\tau) = 2\pi \sum_{i=1}^{n} c_i \mu_i I^-(\tau, \mu_i) \tag{69}$$

To apply the doubling/adding model, the atmosphere is divided into $N$ homogeneous layers. The single scattering properties of the dust, which may reside in any given layer, are assigned according to the previous chapter. A Rayleigh scattering phase function is used when no dust is present with in the layer.

### 3.1.5 Molecular Absorption

Molecular absorption is incorporated by expressing the transmittance function averaged over the spectral interval as a sum of exponentials (Wiscombe and Evans, 1977). That is

$$t = \sum_n w_n e^{k_n u} \tag{70}$$

where $w_n$ and $k_n$ are the exponential fit parameters and $u$ is the absorber amount. In the case of a layer in which both gases and aerosol are present the asymmetry parameter and the single scattering albedo of the layer are expressed as

$$g = \frac{g_d \tau_d}{\tau_d + \tau_g} \tag{71}$$

and

$$\omega_0 = \frac{\omega_{0d}\tau_d + \omega_{0g}\tau_g}{\tau_d + \tau_g} \tag{72}$$

where the subscripts $g$ and $d$ refer to the gas and dust respectively.

The SW version of the doubling/adding model has 11 spectral bands; six water vapor absorption bands (.94, 1.1, 1.38, 1.87, 2.7 and $3.2\mu m$) and four bands for the spectral region $.2 - .8\mu m$. A solar constant of $1368 W m^{-2}$ is assumed. The energy distribution of each spectral interval is assigned according to the data of Thekaekara and Drummond, 1971. The scaling approximation

$$k_\nu(P,T) = k_\nu(P_0, T_0) \int \left(\frac{P}{P_0}\right)^n du \tag{73}$$

is employed to account for the nonhomogeneous water vapor pathlength. $k_\nu$ is the absorption coefficient and $n = 0.9$. The sensitivity of atmospheric heating profiles to the value of $n$ is discussed in Chou and Arking (1980). No path length correction is made for ozone. The surface is assumed to be Lambertian, so that

$$r_g = \frac{a_{sfc}}{\sum_{j=1}^{n} c_i \mu_i} \begin{bmatrix} c_1\mu_1 & \cdots & c_n\mu_n \\ \vdots & \ddots & \vdots \\ c_1\mu_1 & \cdots & c_n\mu_n \end{bmatrix}. \tag{74}$$

The longwave model consists of 20 spectral bands, in which the transmittance is expressed as a sum of exponentials. Nonhomogeneous gaseous pathlengths are accounted for by approximating the optical depth as

$$\tau = k_\nu(P_0, T_0) \int \left(\frac{P}{P_0}\right)^n \left(\frac{T_0}{T}\right)^m du \tag{75}$$

where $P_0$ and $T_0$ are reference pressure and temperature and $u$ is the absorber amount. In addition $n = 0.9(1.75)$ and $m = 0.5(8)$ for water vapor $(CO_2)$. This scaling approximation is a commonly employed simplification whose accuracy is discussed in Chou and Arking (1980). No scaling approximation is required for the e-type continuum absorption as this can be expressed directly as a function of $P$ and $T$ (Roberts et al., 1976).

The transmission of two different gases that absorb in the same spectral bandpass is determined from

$$t(u_1, u_2) = t(u_1)t(u_2) \tag{76}$$

Ohring and Joseph (1978) discuss the cooling result due to overlapping gases.

## 3.2 The two-stream/adding model

Repeated calculations of a doubling/adding model are computationally expensive and, when fluxes are concerned, often unwarranted since simpler radiative transfer models are adequate. Thus a two-stream/adding model was used to calculate radiative fluxes for a large range of atmospheric conditions. Two-stream models consider only the upward and downward irradiances at a given level and can be derived from equation (8) in the following manner. The first step is to integrate equation (8) over the upward (-) and downward (+) direction. For the downward direction $0 \le \mu \le 1$, equation (8) becomes

$$\int_0^1 \mu \frac{dI(\tau,\mu)}{d\tau} d\mu = -\int_0^1 I(\tau,\mu)d\mu + \int_0^1 \sigma(\tau,\mu)d\mu + \frac{\omega_0}{2}\int_0^1 \int_{-1}^1 P(\tau,\mu,\mu')I(\tau,\mu')d\mu' d\mu \quad (77)$$

while for the upward radiance

$$\int_0^1 \mu \frac{dI(\tau,-\mu)}{d\tau} d\mu = \int_0^1 I(\tau,-\mu)d\mu - \int_0^1 \sigma(\tau,-\mu)d\mu - \frac{\omega_0}{2}\int_0^1 \int_{-1}^1 P(\tau,\mu,\mu')I(\tau,\mu')d\mu' d\mu \quad (78)$$

The left hand side of equations (77) and (78) are $dF^+(\tau)/d\tau$ and $dF^-(\tau)/d\tau$ respectively where the positive sign denotes the downward direction. The first term on the right hand side of equations (77) and (78) becomes

$$\int_0^1 I(\tau,\mu)d\mu = D^+(\tau)F^+(\tau) \quad (79)$$

$$\int_0^1 I(\tau,-\mu)d\mu = D^-(\tau)F^-(\tau) \quad (80)$$

where

$$D^+(\tau) = \frac{\int_0^1 I(\tau,\mu)d\mu}{\int_0^1 I(\tau,\mu)\mu d\mu} \quad (81)$$

$$D^-(\tau) = \frac{\int_0^1 I(\tau,-\mu)d\mu}{\int_0^1 I(\tau,-\mu)\mu d\mu} \quad (81)$$

The factors $D^+(\tau)$ and $D^-(\tau)$ are often referred to as diffusivity factors and, in general, are not necessarily equal. For an isotropic radiance field $D^+(\tau) = 2$ while for a collimated beam $D^+(\tau) = \mu_0^{-1}$

The last term of equation (77) can be written as

$$\frac{\omega_0}{2}\int_0^1 \left[\int_0^1 P(\tau,\mu,\mu')I(\tau,\mu')d\mu' + \int_{-1}^0 P(\tau,\mu,\mu')I(\tau,\mu')d\mu'\right] d\mu \quad (83)$$

and similarly for the last term of equation (78). Thus the development of a two stream model requires assumptions regarding the angular distribution of the radiance fields and the phase function, so that the integrals in equation (77) and (78) can be evaluated.

For the shortwave, the $\Delta$-Eddington approximation (Joseph et al., 1973) is commonly employed, where

$$I(\tau, \pm\mu) = \frac{1}{2}\left[(2 \pm 3\mu)F^{+}(\tau) + (2 \mp 3\mu)F^{-}(\tau)\right] \qquad \mu \geq 0 \tag{84}$$

and

$$P(\mu, \mu') = 2f\delta_{\mu,\mu'} + (1-f)(1+g'\mu\mu') \tag{85}$$

where

$$f = g^2 \tag{86}$$

$$g' = (g-f)(1-f). \tag{87}$$

In the present study, the hybrid model of Meador and Weavor (1980) is employed, in which the radiance distribution is approximated as

$$I(\tau, \pm\mu) = \frac{1}{1-g^2(1-\mu_0)}\left\{(1-g^2)\frac{1}{2}\left[(2 \pm 3\mu)F^{+}(\tau) + (2 \mp 3\mu)F^{-}(\tau)\right] + g^2\delta_{\mu,\mu_0}F^{\pm}(\tau)\right\} \tag{88}$$

The source function for the transfer of shortwave radiation is

$$\sigma(\tau, \mu) = \frac{\omega_0}{2}F_0 e^{-\tau/\mu_0}P(\mu, \mu') \tag{89}$$

so

$$\begin{aligned}\int_0^1 \sigma(\tau, -\mu)d\mu &= \frac{\omega_0}{2}F_0 e^{-\tau/\mu_0}\int_0^1 P(-\mu, mu_0)d\mu \\ &= \frac{\omega_0}{2}F_0 e^{-\tau/\mu_0}\beta_0\end{aligned} \tag{90}$$

and

$$\int_0^1 \sigma(\tau,\mu)d\mu = \frac{\omega_0}{2}F_0 e^{-\tau/\mu_0}(1-\beta_0) \tag{91}$$

Several two-stream models have been used in a variety of atmospheric studies (for review see Meador and Weaver, 1980; King and Harshvardhan, 1986). The SW two-stream model of the present study assigns layer reflectances and transmittances according to the two-stream approximation of Meador and Weavor (1980). The accuracy of various two-stream models has been discussed by King and Harshvarden (1986) and the reader should refer to this paper for a detailed comparison of several two-stream models with a doubling model.

In the case of the LW radiative transfer equation, a two point quadrature method is often employed in which

$$F^+(\tau) = 2\pi I(\tau,\bar{\mu}) \tag{92}$$

For Gaussian quadrature $\bar{\mu} = \sqrt{3}^{-1}$, and equations (77) and (78) become

$$\bar{\mu}\frac{dI^+}{d\tau} = -I^+ + I^+\frac{\omega_0}{2}P(\bar{\mu},\bar{\mu}) + I^-\frac{\omega_0}{2}P(\bar{\mu},-\bar{\mu}) + (1-\omega_0)B(\tau) \tag{94}$$

$$\bar{\mu}\frac{dI^-}{d\tau} = I^- - I^-\frac{\omega_0}{2}P(-\bar{\mu},\bar{\mu}) - I^+\frac{\omega_0}{2}P(\bar{\mu},-\bar{\mu}) - (1-\omega_0)B(\tau) \tag{95}$$

The phase function is then written

$$P(\pm\bar{\mu},\pm\bar{\mu}) = (1-\beta) \tag{96}$$

$$P(\mp\bar{\mu},\mp\bar{\mu}) = \beta \tag{97}$$

$\beta$ is the backward scattering coefficient and can be approximated as (Wiscombe and Grams, 1976)

$$\beta = \frac{1}{2} - \frac{3}{8}g - \frac{7}{128}g^3 - \frac{9}{128}g^5 \tag{98}$$

These approximations result in a coupled pair of ordinary differential equations;

$$\frac{dF^-(\tau)}{d\tau} = \bar{\mu}^{-1}(1-\omega_0(1-\beta_0))F^- - \bar{\mu}^{-1}\omega_0\beta F^+ - \bar{\mu}^{-1}(1-\omega_0)B(\tau) \tag{99}$$

$$\frac{dF^+(\tau)}{d\tau} = \bar{\mu}^{-1}(1-\omega_0(1-\beta_0))F^+ - \bar{\mu}^{-1}\omega_0\beta F^- + \bar{\mu}^{-1}(1-\omega_0)B(\tau) \tag{100}$$

To solve this coupled system of equations one needs to make an assumption regarding the depth dependency of the Planck function,$B(\tau)$. It is generally assumed to vary linearly with optical depth (Wiscombe, 1976), that is;

$$B(\tau) \approx B(\tau_b) + \frac{B(\tau_t) - B(\tau_b)}{\tau}\Delta\tau \tag{101}$$

where the subscripts $b$ and $t$ refer to the bottom and top of the layer respectively. The appropriate boundary condition for the top of the atmosphere is

$$F^+(0) = 0 \tag{102}$$

while at the bottom of the atmosphere

$$F^-(\tau) = (1-\varepsilon_{sfc})F^+(\tau_{sfc}) + \varepsilon_{sfc}B(T_{sfc}) \tag{103}$$

where the subscribe *sfc* denotes at the surface. The solution to the system of equations (99) and (100) is then

$$\begin{bmatrix} F^+(\tau_b) \\ F^-(\tau_t) \end{bmatrix} = \begin{bmatrix} t & r \\ r & t \end{bmatrix} \begin{bmatrix} F^+(\tau_t) \\ F^-(\tau_b) \end{bmatrix} + \begin{bmatrix} s-t & 1-s-r \\ 1-s-r & s-t \end{bmatrix} \begin{bmatrix} B(\tau_t) \\ B(\tau_b) \end{bmatrix} \tag{104}$$

where

$$r = \frac{\rho(1-e^{-2\tau_{eff}})}{1-\rho^2 e^{-2\tau_{eff}}} \tag{105}$$

$$t = \frac{e^{-\tau_{eff}}(1-\rho^2)}{1-\rho^2 e^{-2\tau_{eff}}} \tag{106}$$

$$s = \frac{(1 - t + r)}{\bar{\mu}(1 - \omega_0 + 2\omega_0\beta)\tau} \tag{107}$$

$$K = \sqrt{1 - 2\omega_0 + \omega_0^2 + 2\omega_0\beta - 2\omega_0^2\beta} \tag{108}$$

$$\tau_{eff} = \bar{\mu}K\tau \tag{109}$$

$$\rho = \frac{\omega_0\beta}{1 - \omega_0 + \omega_0\beta + K} \tag{110}$$

To investigate the errors associated with the LW two-stream model, a comparison is made with the results from the LW doubling model. Figure 3.2a depicts the ratio of the flux out the top of a layer to the incident flux at the base of the layer ($\frac{FLUXUP}{FLUXIN}$) from a doubling model as a function of optical depth and the ratio $\frac{B_{cld}}{B_{sfc}}$ where $B_{cld}$ is the Planck emission of the layer. The single scattering and asymmetry parameter for these calculations are 0.5 and 0.6 respectively, values typical of dust at a wavelength of $10\mu m$. A similar plot for the ratio of the flux out the bottom of the layer to $FLUXIN$ is shown in figure 3.2b. The two-stream longwave model errors are depicted in figure 3.3, contour interval is 0.025 (or 2.5%). As one would expect, the two stream model has its smallest errors for the upward flux at both large and small optical depths (Figure 3.3a). At large optical depths the upward flux is primarily composed of the emission of the layer, while for the thin optical depths the surface emission constitutes the majority of the upward flux. Largest errors in the upward flux occur at moderate optical depths when the layer temperature is much colder than the surface temperature. The errors are greater for the $\frac{FLUXDN}{FLUXIN}$ case (figure 3.3b), with the largest errors occurring at moderate optical depths for the case of a layer temperature which is greater than the surface temperature.

## 3.3 Comparison of the doubling, two-stream models and aircraft observations

In this section the doubling and two-stream models discussed above are compared with aircraft radiative flux measurements made during SMONEX. Results for the shortwave models and longwave models are discussed separately.

### 3.3.1 Shortwave intercomparison

A comparison of model calculated shortwave fluxes and aircraft measured fluxes from two aircraft flights is depicted in figure 3.4. The flux measurements were made during the SMONEX over the Saudi Arabian peninsula (Ackerman and Cox, 1982). The mean temperature and moisture profiles used in the radiation calculations are shown in figure 2.3. Ackerman and Cox (1982) also present measured particle size distributions. These measured size distributions along with indices of refraction reported by Patterson et al. (1983) were used to determine the single scattering parameters of the dust layer. The resulting $\omega_0$, $\sigma_{ext}$ and $g$ were discussed in Chapter 2. The solar zenith angle of the 10 May flight was $25.9^0$ while that of 12 May was approximately $75^0$. The surface albedos used in the model corresponded to either the visible ($.28 - .7\mu m$) or NIR ($.7 - 2.8\mu m$) albedo measured by the aircraft at it lowest altitude (approximately 0.3 km). In figure 3.4 the solid lines represent the upward or downward total SW fluxes, the dotted line represents the direct component of the downward flux while the net SW flux is shown as the longer dashed line. The thick lines, and the dotted line, represent calculations made with the doubling model, while the thin lines depict the two stream calculations. The A's represent the measured upward and downward fluxes, while the N's are the measured net fluxes. In general there is excellent agreement between the model and measured downward fluxes. Agreement is not as good for the upward fluxes and might be influenced by an incorrect specification of the surface boundary conditions. The two stream model tends to overestimate the upward fluxes. The models reproduce the magnitude and tendencies of the net flux measured by the aircraft pyranometers.

It is worthwhile here to point out some of the interesting features shown in these figures which will be the focus of the next section. Solar absorption by the dust is large and occurs primarily in the visible portions of the spectrum. The presence of the dust layer not only reduces the total incoming flux, but also reapportions the energy between the direct and diffuse components. This redistribution is a strong function of the solar zenith angle. Within the dust layer the upward fluxes tend to decrease with height for the smaller solar zenith angle case and increase with height for the larger zenith angle case. In both cases the net flux and the downward flux decrease with height.

### 3.3.2 Longwave intercomparison

Longwave (LW) flux comparisons of observations and the model calculations for a dust laden atmosphere are shown in figure 3.5. The aerosol size distributions discussed above along with the index of refraction of Patterson (1981) were used to specify the single scattering properties of the dust. Surface temperature was assigned according to aircraft measurements of a downward facing spectral radiometer (Smith et al, 1980) at the lowest flight altitude. Except for the downward fluxes at the lowest two aircraft flight levels, model calculations are generally within 4% of the measurements. Changing the size distribution or index of refraction does not substantially improve the agreement at these lowest levels. According to the model calculations, the dust primarily affects the $8-13\mu m$ region. For example, the dusty-clear difference between the downward flux at the surface for the model atmosphere of flight 8 is $61Wm^{-2}$; of this difference $56Wm^{-2}$ is accounted for in the $8-13\mu m$ spectral interval. Similar behavior has been observed in the transmittance measurements of Pinnick et al. (1985). The aircraft observations suggest that the dust has only a small effect on the longwave fluxes.

This discrepancy between aircraft broadband measurements and calculations has lead to disagreement in the literature about the effects of soil derived aerosols on the longwave spectral region. Aircraft measurements of broadband longwave fluxes find it difficult to detect the effect of crustal aerosols (Minnis and Cox, 1978; Ackerman and Cox, 1982; Ellingson and Serafino, 1984). On the other hand model calculations (Carlson and Benjamin, 1980; Harshvardhan and Cess, 1978 and the present study) and spectral measurements (Pueschel and Kuhn, 1975; Pinnick et al., 1985) suggest a moderate effect on the IR fluxes. Surface LW flux measurements by Idso (1975) showed a 10% increase in the downward LW flux at the surface with passage of a dust storm in Arizona. Harshvardhan and Cess (1978) concluded, based on model calculations, that the presence of a dust layer results in a 10% increase in the IR radiative cooling. Ellingson and Serafino (1984) obtained better agreement between measured and calculated LW downward fluxes when model calculations included aerosols, however, the large uncertainties associated the pyrgeometer measurements left the aerosols effect undeterminable. The largest uncertainties associated with the model calculations are the index of refraction and the size distribution of the dust. While large uncertainties exist in the measurements of the index of refraction, all studies indicate a large absorption coefficient in the $9-11\mu m$ band. This is supported by laboratory measurements of the index of refraction of quartz (Peterson and Weinman, 1969). Merely changing the index of refraction in the calculations cannot account for the discrepancies noted in figure 3.5. Model calculations of the present study indicate that the dust primarily affects the $8-13\mu m$ spectral interval; this agrees with the spectral measurements of Pinnick et al. (1985). In Appendix C it is shown that the presence of a dust layer can strongly affect satellite radiance measurements in the LW window region; this agrees with the observations of Martin (1975). Spectral transmittance measurements, model calculations and satellite observations suggest that dust has an effect on the LW radiative energy budgets. Thus we turn our attention to possible errors in the broadband radiation measurements.

The instrument commonly used to measure LW radiative fluxes from an aircraft is an Eppley pyrgeometer. The incoming flux is determined from the energy budget of the pyrgeometer (Albrecht and Cox, 1974 and 1977)

$$E = K_1 V_0 + \sigma\varepsilon T_s^4 - K_2\sigma(T_d^4 - T_s^4) \tag{111}$$

where

- $E$ = incident longwave radiation
- $V_0$ = output of the pyrgeometer thermopile in mv
- $\sigma$ = Stephan-Boltzman constant
- $\varepsilon$ = emittance of the thermopile
- $T_d$ = temperature of pyrgeometer dome ($^0K$)
- $T_s$ = temperature of thermopile cold junction or sink ($^0K$)
- $K_1, K_2$ = calibration constants

The largest term is the sink temperature term and under conditions of large dome-sink temperature gradients, the thermopile term can be the smallest contributor to the measurement. The largest uncertainty in the measurements is the dome-sink energy term. Determination of the coefficient $K_2$ in the lab can, under environmental conditions, lead to errors as large as $40Wm^{-2}$ (Ackerman and Cox, 1980). Recent studies have focused on the calibration techniques which attempt to account for the dome-sink temperature difference term. Ackerman and Cox (1980) employed an infield calibration technique to determine $K_2$ by flying a stepped racetrack pattern over an ocean under clear skies. Brogniez et al. (1986) also present a calibration technique. Griffith (1982) and Foot (1986) note that $K_2$ is a function of airspeed and Griffith (1982) suggests a method of changing airspeed to perform the calibration of $K_2$. Foot (1986) redesigned the pyrgeometer in an attempt to eliminate this dome-sink temperature difference term. Based on the spectral measurements, model calculations and satellite observations; it appears that the pyrgeometer measurements are in error. Future aircraft measurements would likely benefit from LW spectral measurements.

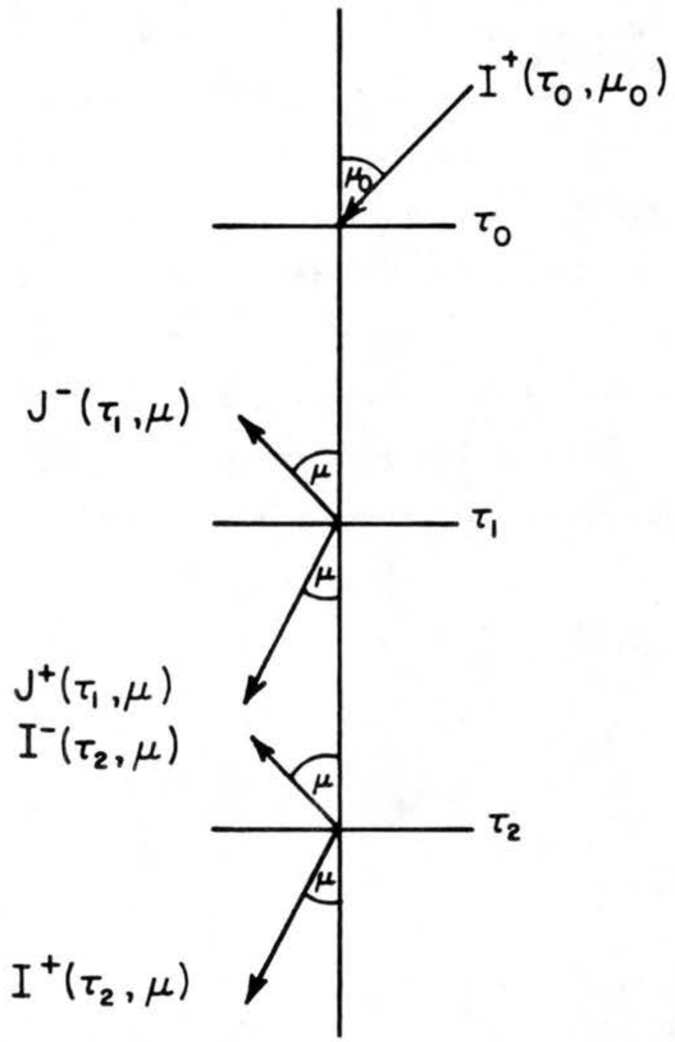


Figure 3.1: Schematic representation of the diffuse radiances($I$) and source functions($J$) in a two layer atmosphere.

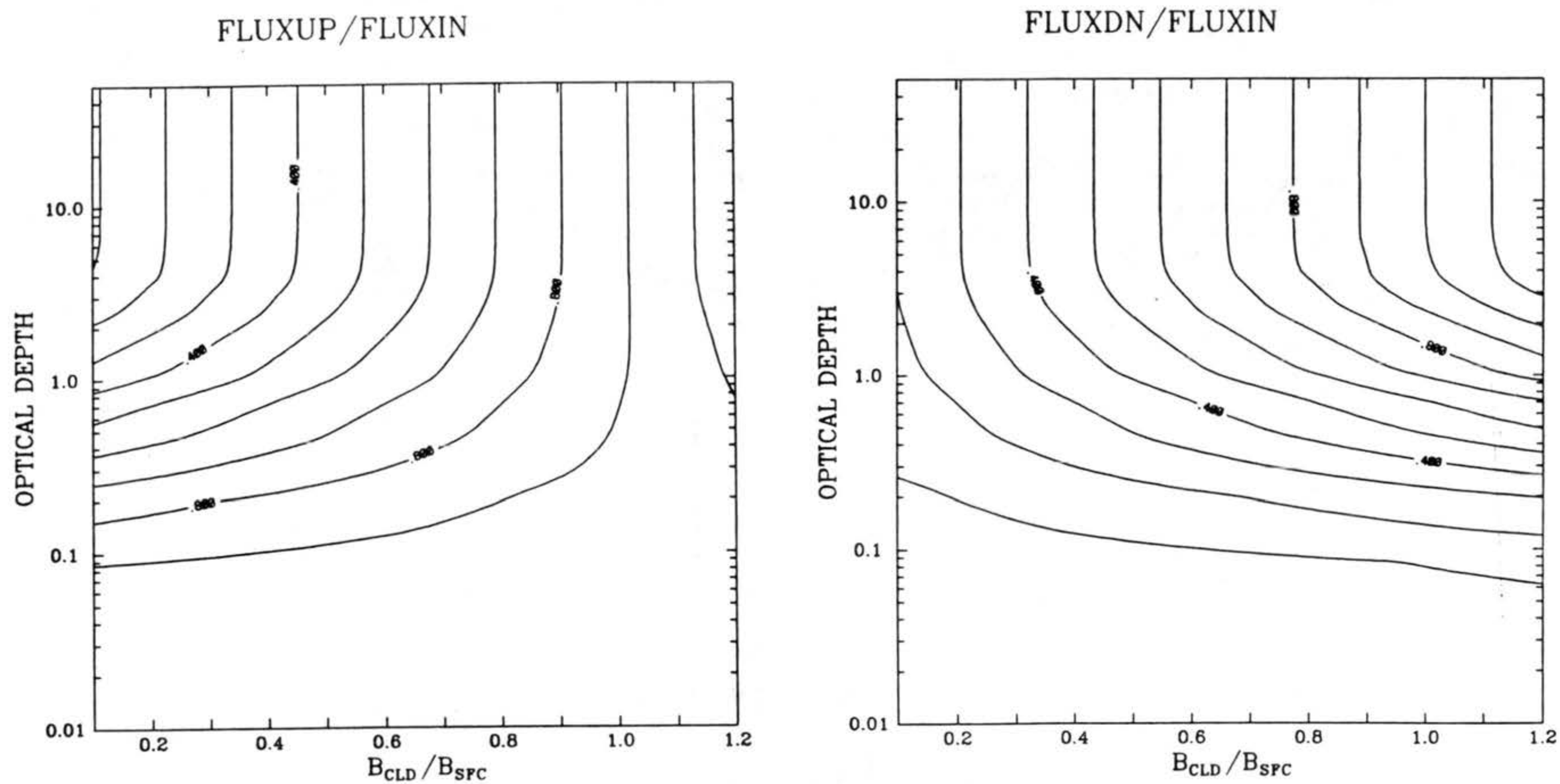


Figure 3.2 Ratio of the flux out the top of a layer to the surface Plankian emisssion (left) as a function of optical depth and the ratio of the layer emission to the surface emission. Contour intervals are 0.1. Right hand panel depicts the ratio of the flux out the bottom of the layerr to the surface Plankian emission. Single scatter albedo and asymmetry parameter used in the doubling model calculation were 0.5 and 0.6 respectively.

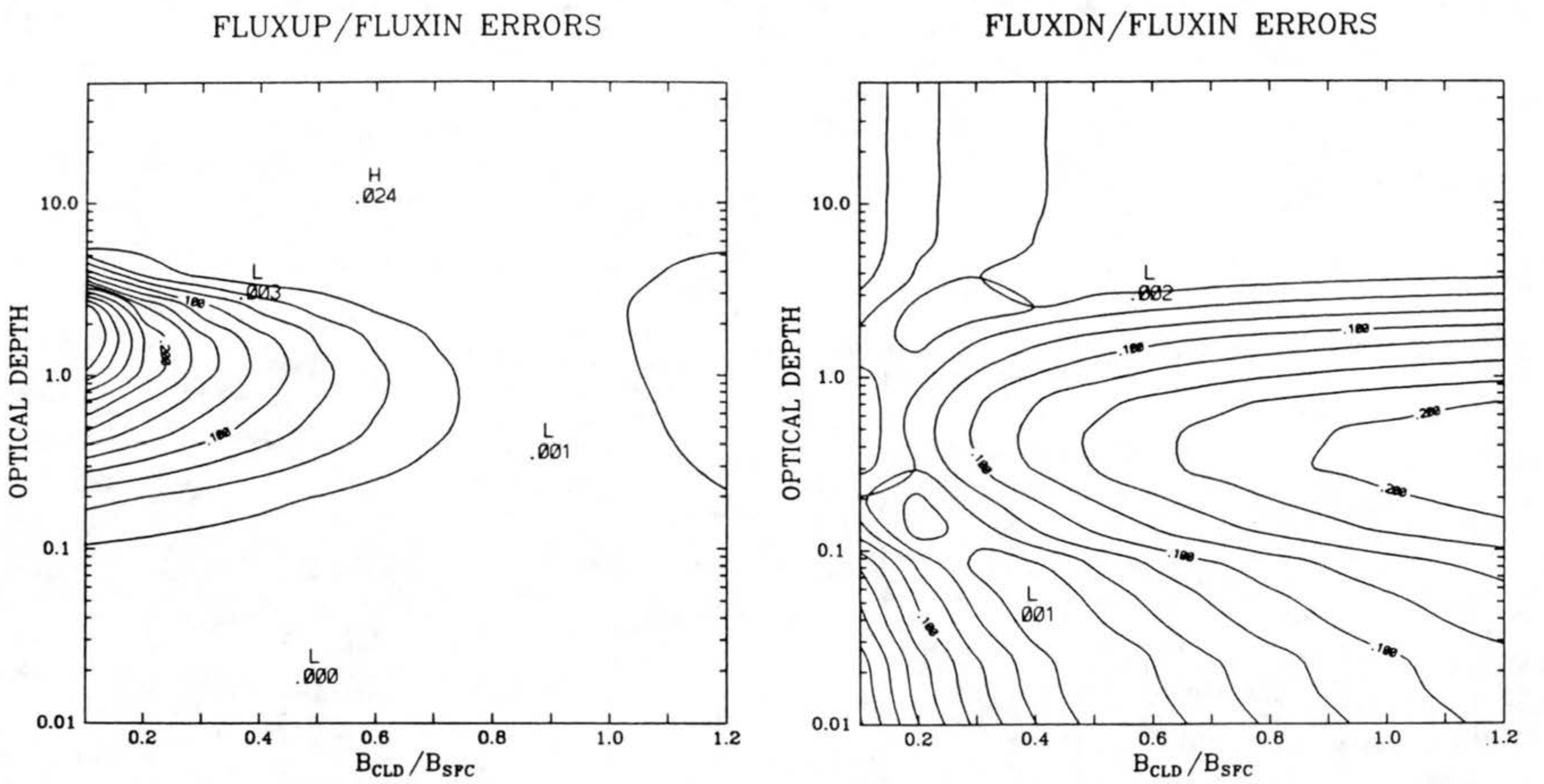


Figure 3.3 Errors associated with the two-stream LW model in determining the ratios of the fluxes out of the layer to the fluxes incident on the bottom of the layer.

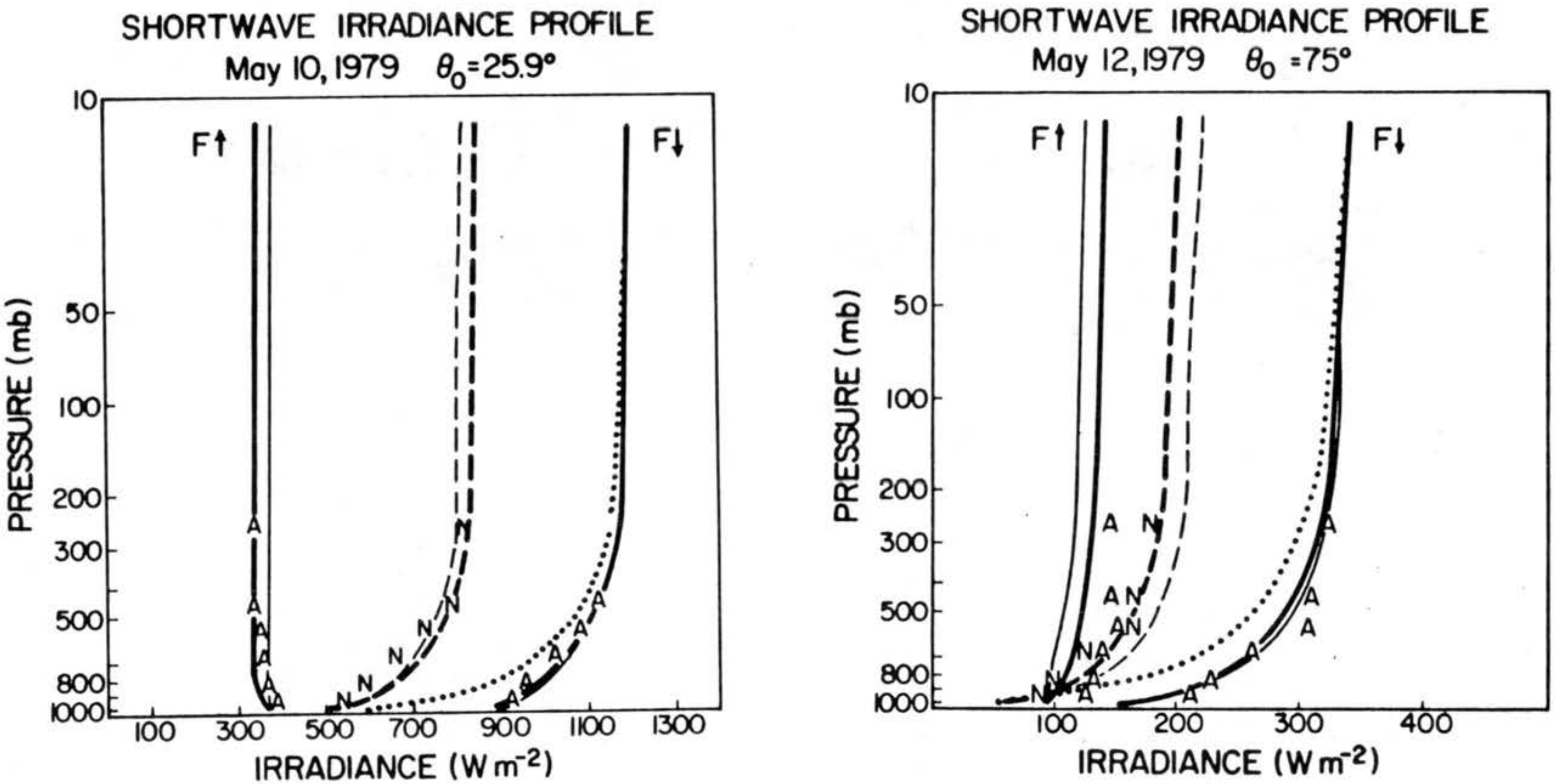


Figure 3.4 Comparison of model calculated shortwave fluxes to aircraft measured fluxes made during the SMONEX over the Saudi Arabian peninsula. Solid lines represent the model calculated upward or downward total SW fluxes, the dotted line represents the direct component of the downward flux while the net SW flux is shown as the dashed line. The thick lines represent the calculations using the doubling model, while the thin lines depict the two-stream model results. The A's represent the measured upward and downward fluxes, while the N's are the measured net fluxes.

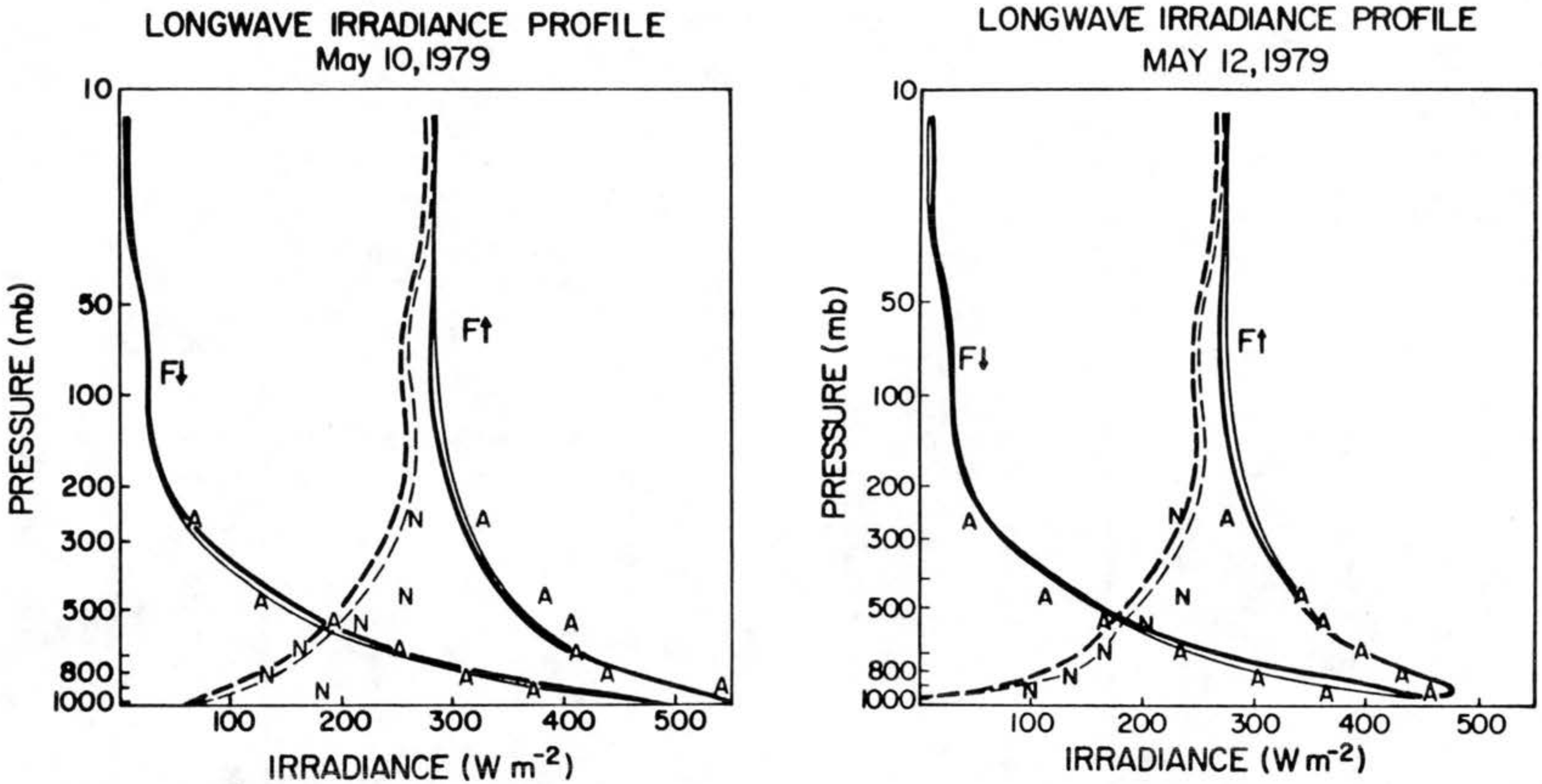


Figure 3.5 Comparison of model calculated longwave fluxes to aircraft measured fluxes made during the SMONEX over the Saudi Arabian peninsula. Solid lines represent the model calculated upward or downward total LW fluxes and the net LW flux is shown as the dashed line. The thick lines represent the calculations using the doubling model, while the thin lines depict the two-stream model results. The A's represent the measured upward and downward fluxes, while the N's are the measured net fluxes

# Chapter 4

## MODEL RESULTS

A major objective of this study is to assess the effects of dust on the changes in the net flux at the top of the atmosphere, the changes in the net flux at the earth's surface, and the changes in the net flux as a function of height (atmospheric heating) arising from the presence of a dust layer. Large variations in the single scattering properties of a dust layer were presented in Chapter 2. In this chapter, representative dust layer characteristics are chosen to quantify the changes in the radiative fluxes due to the presence of a dust layer. Four different atmospheric conditions are presented. These are

**DESERTL** This model assumes an atmospheric temperature and moisture profiles corresponding to the desert case of Table 3 along with the surface albedos and emittances of section II. The microphysical properties of the dust layer are assumed to be constant with altitude with a size distribution corresponding to the light dust loading distribution of Patterson and Gillette (1977). Thus an increase in optical depth is attained by an increase in the number of particles. The index of refraction corresponds to that of Patterson et al. (1983) for the shortwave spectrum and Patterson (1981) for the longwave spectrum. The top of the dust layer is located near 5 km with a base at the surface.

**DESERTH** This case is similar to DESERTL with the exception that the dust particle size distribution corresponds to the heavy dust loading case of Patterson and Gillette (1977). Thus differences between DESERTL and DESERTH are in the single scattering properties of the dust layer resulting from a change in size distribution.

**DESERTV** The difference between DESTERV and the previous models is that this case allows for the vertical variation of $\sigma_{ext}$ according to the observations of Ackerman and Cox (1982). The single scattering albedo and asymmetry parameter are the same as in the DESERTL case.

**OCEANL** This model assumes an atmospheric temperature and moisture profiles corresponding to the ocean case of Table 3. The microphysical properties of the dust layer are assumed to be constant with altitude within the layer $850mb - 550mb$. The particle size distribution corresponds to the light dust loading distribution of Patterson and Gillette (1977). The index of refraction corresponds to that of Patterson et al. (1983) for the SW and Patterson (1981) for the LW.

The effect on the total fluxes (SW+LW) will be considered after addressing the aerosol's impact on the solar and terrestrial spectrae separately. In all cases, the fluxes were computed with the two-stream model discussed in the previous chapter.

## 4.1 Shortwave model results

Measurements from a variety of field experiments (see Appendix A) reveal that crustal aerosols have a large impact on the shortwave energy budget of the earth-atmosphere system. Aerosols scatter and absorb solar radiation and as a result can cool or warm the earth-atmosphere system depending on the magnitudes of $\omega_0$ and $g$. In addition to reducing the incoming solar flux at the earth's surface, the aerosol layer modifies the distribution of radiative heating within the atmosphere. Several studies have reported comparisons of model calculations and measurements (e.g. DeLuisi et al. 1976; Ackerman and Cox 1982; and Ellingson and Serfino, 1984). In this section the SW two-stream/adding model presented in Chapter 3 is employed to examine the radiative properties of a dust laden atmosphere.

### 4.1.1 Changes in the SW flux at the top of the atmosphere

Differences between the SW upward flux at the top of the atmosphere (TOA) for a dust laden and dust free environment of the DESERTL (solid) case are shown in figure 4.1 as a function of solar zenith angle and dust optical depth at $0.55\mu m$ ($\tau_d$). The optical depth at a wavelength of $0.55\mu m$ is used since this is the most common wavelength for

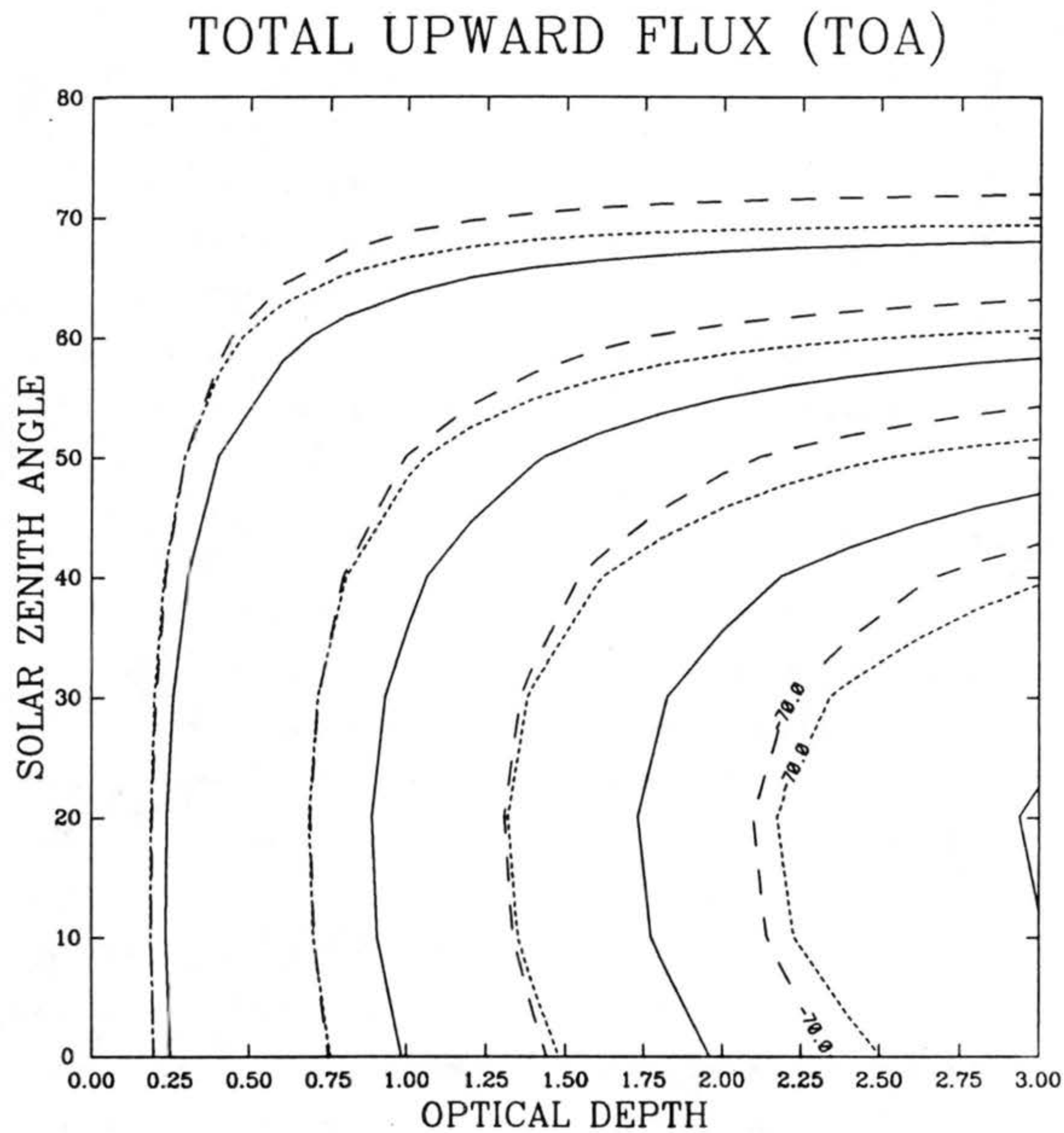


Figure 4.1: Differences in the SW upward flux at the top of the atmosphere between a dust laden and dust free environment for the DESERTL (solid), DESERTH (long dashed) and DESERTV (short dashed) cases as a function of solar zenith anle and dust optical depth at $0.55\mu m$. Contour intervals are $20 W m^{-2}$.

inferring dust optical depths from surface measurements. Contour intervals are $20Wm^{-2}$. Negative values indicate a greater upward flux for the clear sky case, thus the presence of the dust layer results in a darkening of the surface. The largest changes resulting from an increasing $\tau_d$ are for the smallest zenith angles where the upward flux decreases and the net flux increases due to absorption by the dust. The presence of a dust layer results in a net SW energy gain by the Earth-atmosphere system. Results for the DESERTH (dashed) and DESERTV (dotted) cases are also shown. Changing the size distribution (DESERTL vs. DESERTH) or the vertical structure of $\sigma_{ext}$ (DESERTL vs. DESERTV) results in differences of no more than about $15Wm^{-2}$. The DESERTH case is darker than the DESERTL case due to the smaller single scattering albedo and the larger asymmetry parameter. For $\tau_d$ of 1.2 there is little solar zenith angle dependence for $\theta_0 < 40^0$. As $\tau_d$ becomes greater than 1 and $\theta_0 > 60^0$ very little additional absorption occurs.

### 4.1.2 Changes in the SW heating of the atmosphere

Figure 4.2 depicts differences in the total SW flux convergence ($Wm^{-2}$ per $1000mb$) of the atmosphere obtained by subtracting the dust laden and clear sky conditions, for the three desert cases. Again the largest effect is for smaller zenith angles where there is a nearly linear relationship between energy gain and optical depth for a given solar zenith $< 20^0$. For the larger solar zenith angles, the largest energy gains due to the presence ot the dust layer occurs when going from no dust to a dust loading of approximately $\tau_d = 1$. For zenith angles greater than $65^0$ increases in the optical depth beyond 1 do not substantially increase the total atmospheric heating. The heavy dust loading case has a larger effective radius than the light loading case, this results in a smaller single scattering albedo explaining the increase in absorption over the lighter loading. The effect of changing size distribution is less than changing the vertical distribution of the dust as seen in the figure. Differences between the three desert loading cases are a maximum at large $\tau_d$ and low $\theta_0$, being greater than $50Wm^{-2}$ per $1000mb$ ($.42^0C/Day$). For the lower values of optical depth the absorption is nearly independent of $\theta_0$ up to about $\theta_0 = 60^0$.

The majority of the increased atmospheric heating occurs in the dust layer. Figure 4.3 presents the differences in the radiative heating profile of the dust free atmosphere

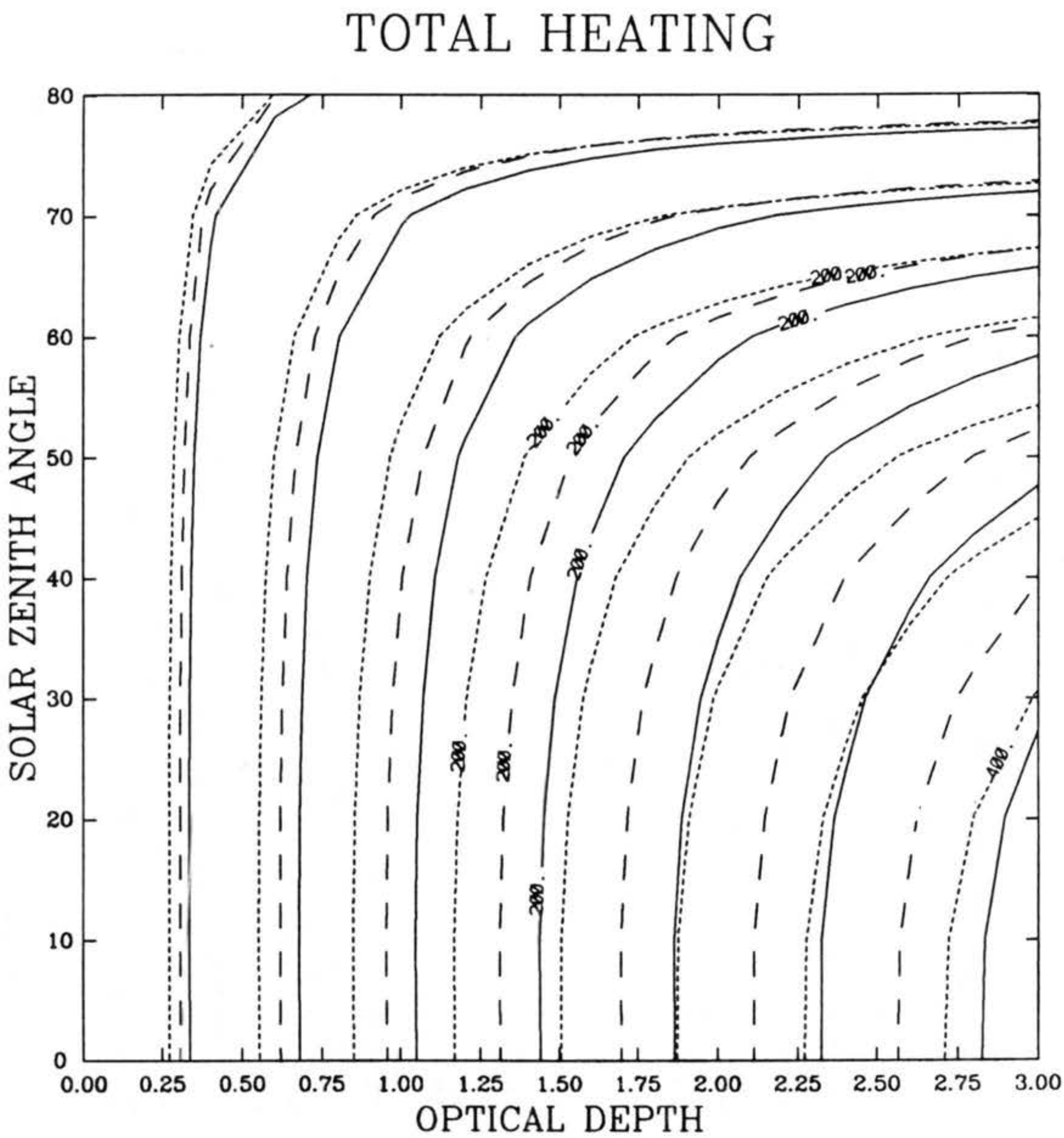


Figure 4.2: Dust laden minus clear sky differences in the total SW heating of the atmosphere for the three desert cases; DESERTL (solid), DESERTH (long dashed) and DESERTV (short dashed) Contour intervals are $50Wm^{-2}$ per 1000 mb.

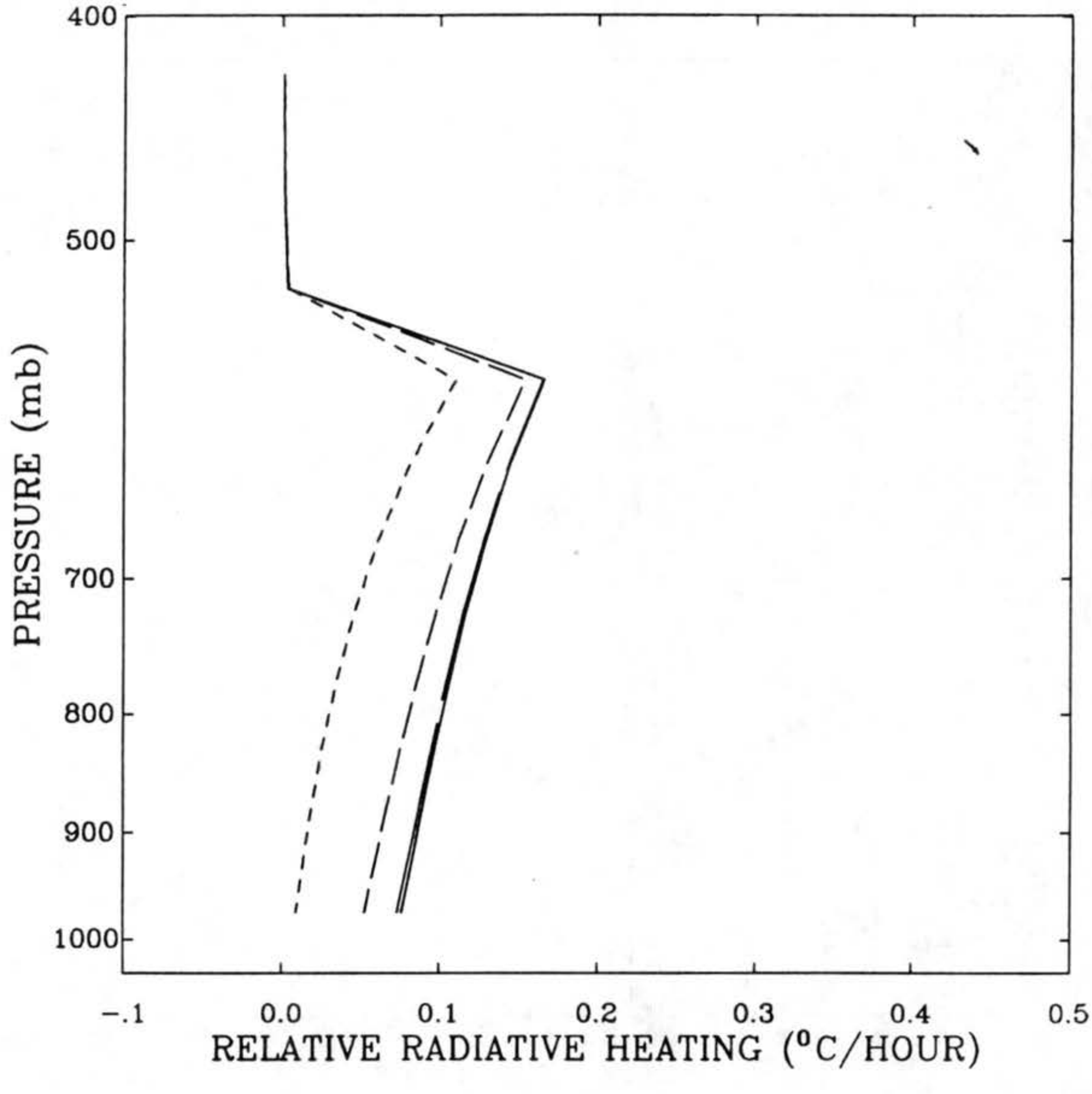


Figure 4.3: Differences in the radiative heating profile of the dust free atmosphere and the dust laden one for the DESERTL case with $\tau_d = 1$. The differences at four solar zenith angles $0^0$ (solid), $30^0$ (long dashed), $60^0$ (dashed) and $80^0$ (short dashed) are shown.

and the dust laden one for the DESERTL case. The differences for an optical depth of 1 and for four solar zenith angles ($0^0, 30^0, 60^0$ and $80^0$) are shown. The increased radiative heating due to the presence of a dust layer is similar for solar zenith angles of $0^0$ and $30^0$, in agreement with figure 4.2. As the $\theta_0$ increases differences between the dust laden and dust free atmosphere decrease. In all cases the maximum difference between the clear and dusty atmospheres is at the top of the dust layer in agreement with the calculations of Carlson and Benjamin (1980) and the measurements of Ackerman and Cox (1982) and DeLuisi et al (1976). That the vertical distribution of the heating changes little with $\theta_0$ is seen in figure 4.4 which depicts the radiative heating rates for an optical depth of 0.6 for the four solar zenith angles.

Unlike clouds (Stephens, 1978), the depth dependency of the heating varies only slightly with increasing $\theta_0$. The reasons for this can be seen by considering a two-stream approximation to the radiative transfer equation. For example, replacing the integral in (8) by a two point gaussian quadrature with the boundary conditions $F^- = 0$ at $\tau = 0$ and $F^- - F^+ \to 0$ as $\tau_d \to \infty$ then

$$F^+ - F^- = C_1 \exp -k\tau + C_2 \exp -\tau/\mu_0 \tag{112}$$

where

$$k = (3(1-\omega_0)(1-g))^{1/2} \tag{113}$$

$$C_1 = \frac{\sqrt{3}\omega_0 F_0 \mu_0 k \left(\mu_0 + \frac{\sqrt{3}\mu_0^2 g k^2}{3\omega_0(1-g)^2} + \frac{\mu_0(g/\omega_0+\sqrt{3})}{(1-g)}\right)}{2(k^2\mu_0^2 - 1)(1 + \frac{k}{\sqrt{3}(1-g)})} \tag{114}$$

$$C_2 = \frac{\sqrt{3}kF_0\mu_0\omega_0}{2(1-k^2\mu_0^2)(1-\sqrt{3}(1-g))} \tag{115}$$

For simplicity we consider a uniformly mixed dust layer with $\omega_0$, $g$ and $\sigma_{ext}$ constant with height. The scale depth, defined as the depth at which the heating $d(F^+ - F^-)/d\tau$ is reduced by a factor of $e^{-1}$, is a function of $\mu_0$ and $k$. Typical values of $k^{-1}$ as a function of $\lambda$ are shown in figure 4.5 for the Saharan, SW Asian and Arabian dust types. In all cases $k^{-1} > \mu_0$, thus the diffuse scale depth is greater than the scale depth of the direct component. The nearly constant heating distribution within the dust layer with changing

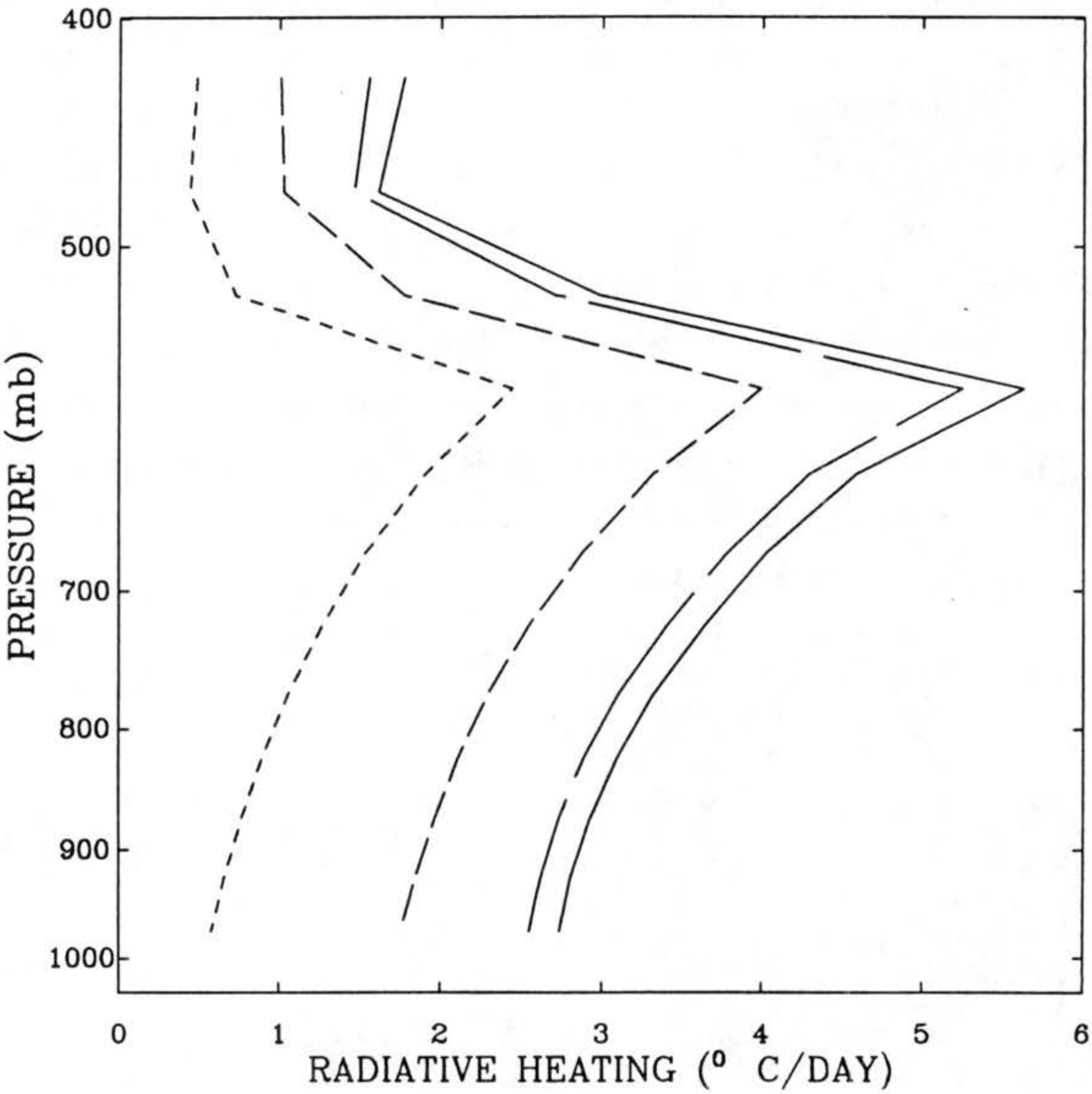


Figure 4.4: Radiative heating rates for the DESERTL case with $\tau_d = 0.6$ at four solar zenith angles; $0^0$ (solid), $30^0$ (long dashed), $60^0$ (dashed) and $80^0$ (short dashed).

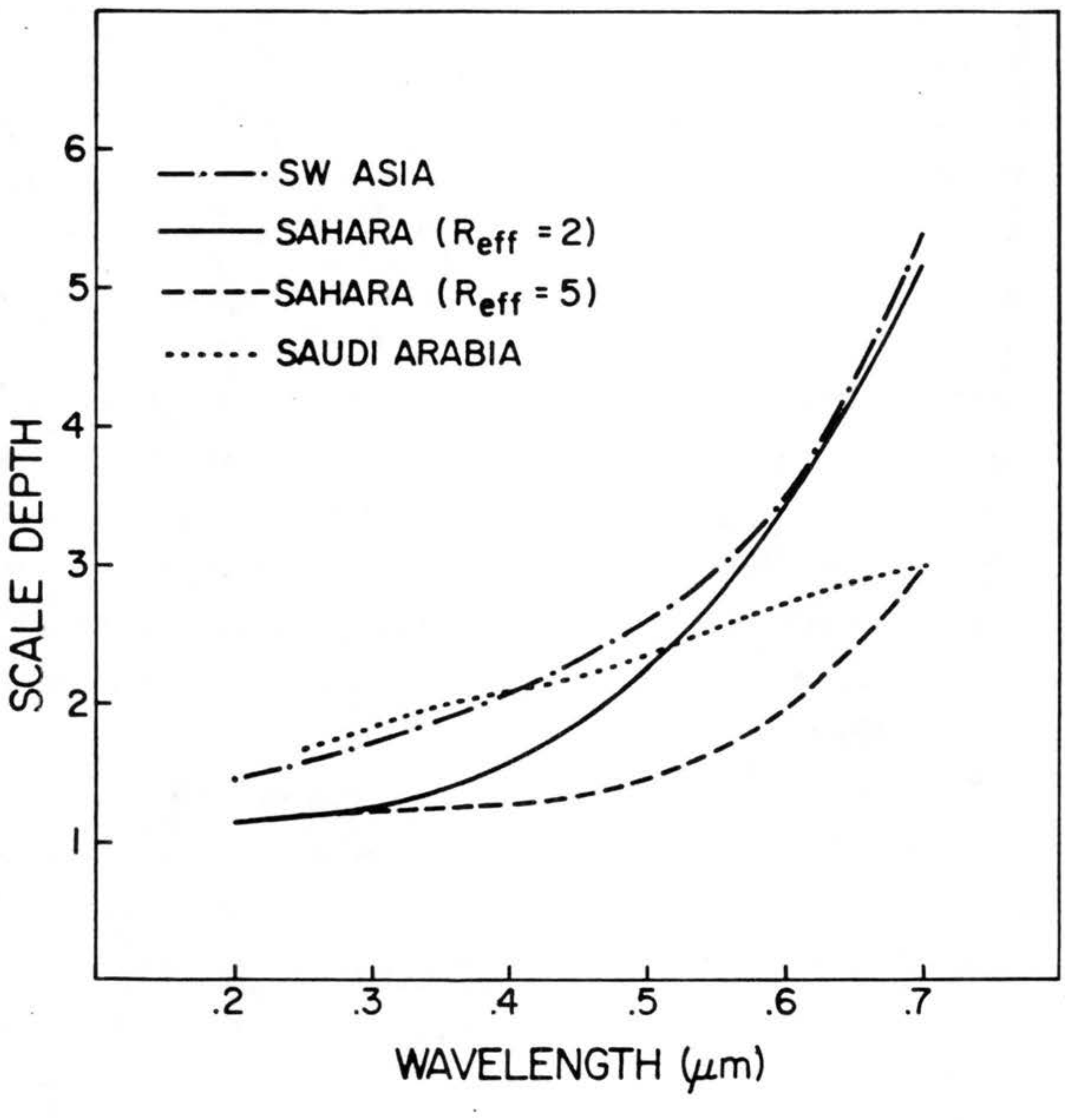


Figure 4.5: Scale depth for diffuse radiation as a function of wavelength for different soil derived aerosols depicted in the legend

$\theta_0$, results from the large diffuse component which allows the SW radiation to penetrate further into the dust layer due to the larger scale depth.

The increase in the atmospheric heating in the presence of dust is largely due to the absorption of radiative energy in the .2-.8 $\mu m$ spectral interval. Figure 4.6 depicts the dusty-clear heating profiles for the spectral intervals 0.2-0.86 $\mu m$ (visible) and 0.86-3.85 $\mu m$ (near IR or NIR) intervals for an optical depth of 2. In addition to absorbing in the NIR region, multiple scattering in the dust layer can increase the absorption by the water vapor within the layer. To investigate the effect of enhanced water vapor absorption, we considered the effects of a dust layer with DESERTL characteristics except that no water vapor is present within the dust layer. The differences between this case, the dust free atmosphere and the DESERTL case depicts the increase in water vapor absorption due to multiple scattering. Figure 4.7 compares the dust laden minus clear heating profiles for the DESERTL case with and without water vapor in the dust layer. If the dust single scattering and asymmetry parameters were 1 in the water vapor absorption bands then the heating rate differences depicted in figure 4.7 would be the same. However, the DESERTL case with water vapor shows a smaller dusty-clear difference than the case without water vapor. The difference between these two cases (shaded) results from an enhanced water vapor absorption due to multiple scattering by the dust.

The primary gaseous atmospheric constituent which absorbs in the region .2-.7 $\mu m$ is stratospheric $O_3$. The presence of a tropospheric dust layer may also have an impact on stratospheric heating rates through the modification of the upwelling radiation at the tropopause. For the desert cases dust does have a slight impact on the stratospheric heating rates (figure 4.8). For small solar zenith angles the presence of a dust layer inhibits stratospheric heating by absorbing the upwelling flux reflected from the surface. As $\theta_0$ increases the reflectivity of the dust layer increases and by $\theta_0 = 80^0$ the presence of a dust layer causes an increase in the radiative heating of the stratosphere. The small magnitude and the change of sign of layer heating indicates that the dust layer would have minimal impact on the stratospheric radiative heating rates, even when integrated over a period as long as 3 months.

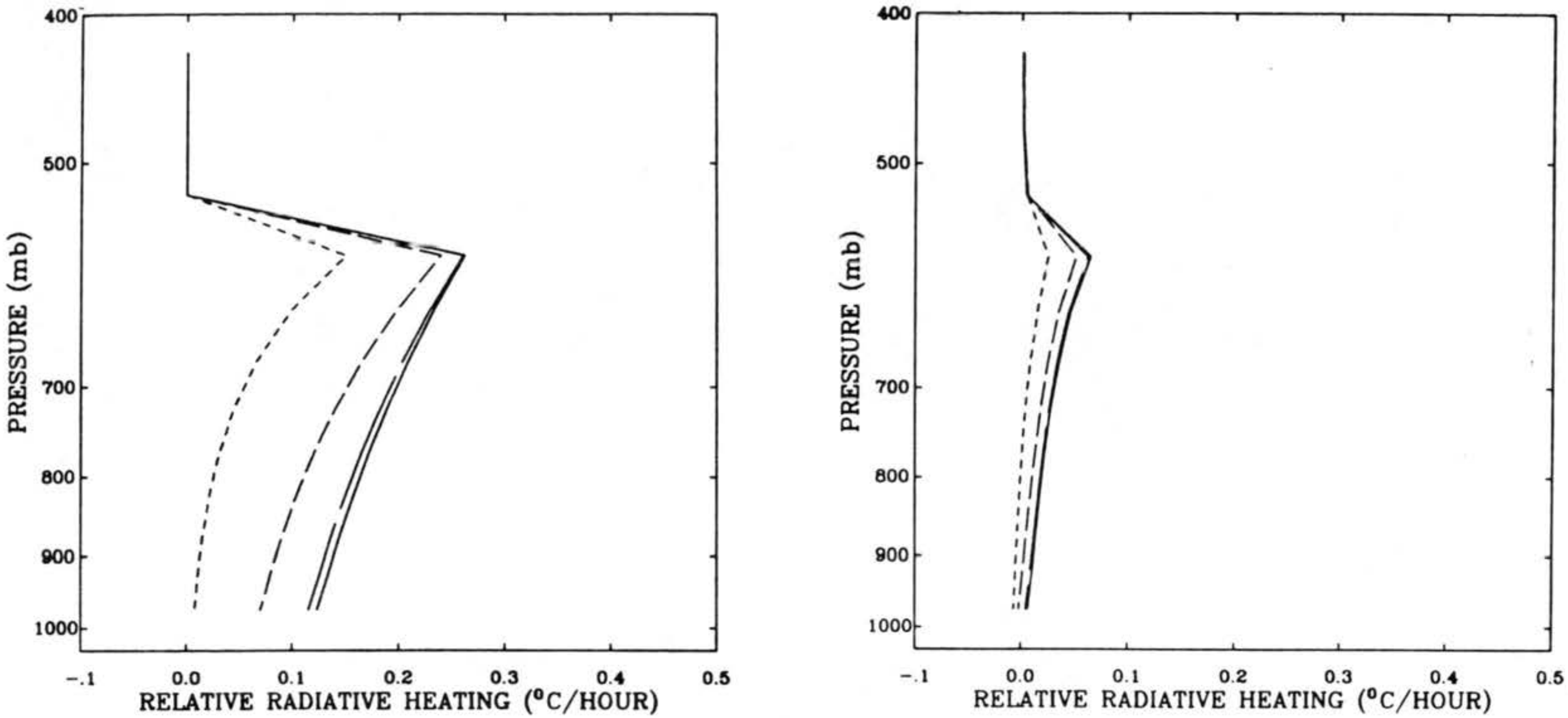


Figure 4.6 Dusty-clear radiative heating profiles for the spectral intervals 0.2–0.86$\mu m$ (left) and 0.86–3.95$\mu m$ (right) for an optical depth of 2.0.

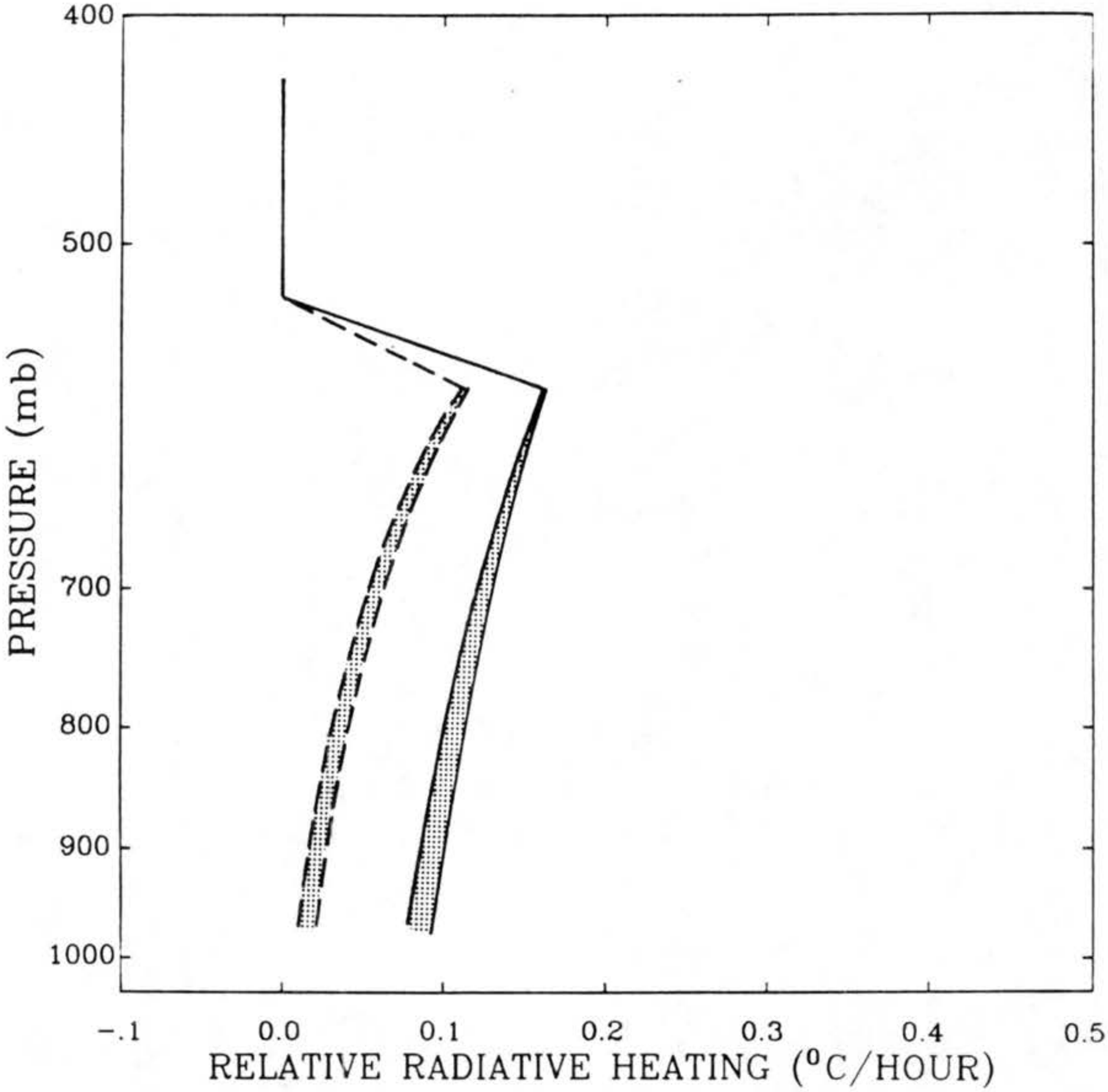


Figure 4.7: Dust laden minus clear radiative heating profiles for the DESERTL case with and without water vapor in the dust layer. Solid line represents a solar zenith angle of $0^0$, while the dotted line represents a solar zenith angle of $80^0$. The shaded portions highlight the differences between the calculations.

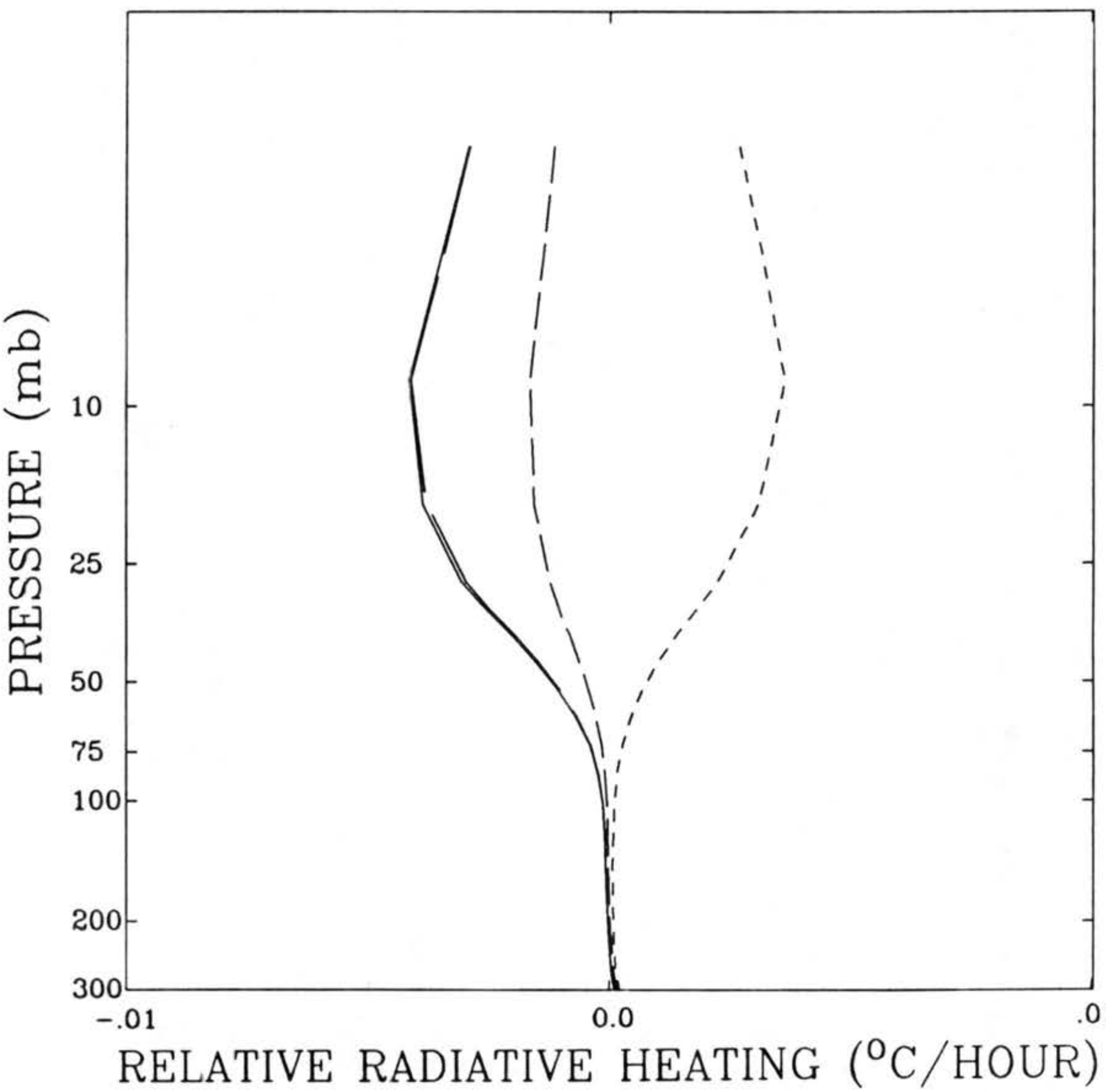


Figure 4.8: Stratospheric radiative heating rate differences between the dust laden (DESERTL) and the clear atmosphere at four solar zenith angles; $0^0$ (solid), $30^0$ (long dashed), $60^0$ (dashed) and $80^0$ (short dashed).

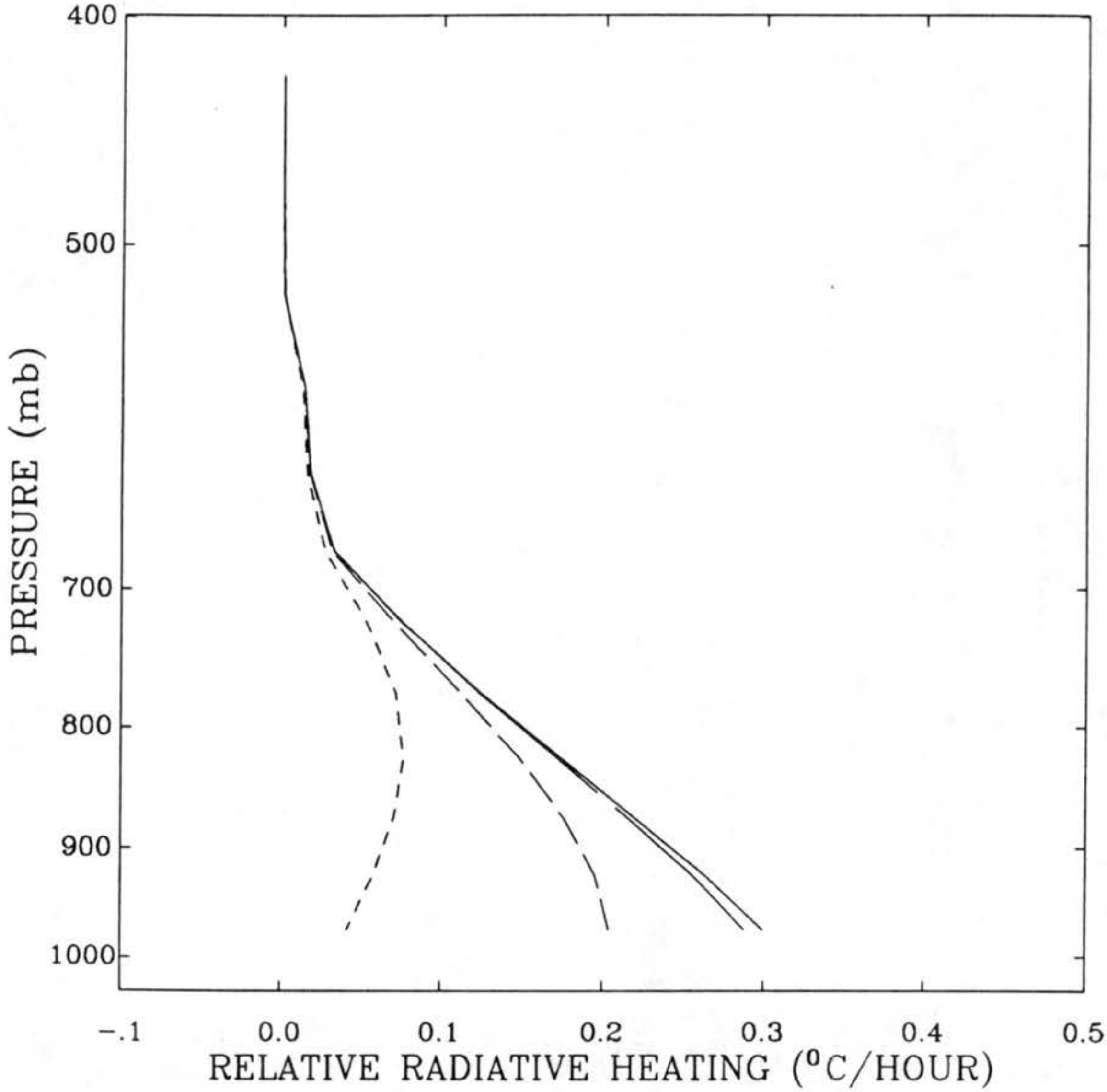


Figure 4.9: Differences in the radiative heating profile of the dust free atmosphere and the dust laden one for the DESERTV case with $\tau_d = 1$. The differences at four solar zenith angles $0^0$ (solid), $30^0$ (long dashed), $60^0$ (dashed) and $80^0$ (short dashed) are shown.

Figure 4.9 shows that changing the vertical distribution of the dust can have a large impact on the vertical structure of atmospheric heating. The smaller optical depth at the top of the dust layer allows radiation to penetrate deeper into the dust layer where the energy is more likely to be absorbed before escaping from the layer.

### 4.1.3 Changes in the SW fluxes at the surface

The effect of a dust layer on the net SW flux at the surface is depicted in figure 4.10. Contour intervals are $50Wm^{-2}$. For all solar zenith angles the net surface SW flux decreases as the optical depth increases. Again, the dust layer has its greatest impact at the lower zenith angles. The increased $\omega_0$ associated with the DESERTH case results in a larger reduction of the downward shortwave component. The largest reduction occurs in the DESERTV case. The relationships between $\theta_0$ and $\tau_d$ are similar to that observed for the total heating field.

The SW energy reaching the earth's surface is comprised of a direct and a diffuse component. The partitioning of energy between the direct and diffuse radiation is demonstrated in figure 4.11 which depicts the ratio of the direct component at the surface to the total (direct + diffuse) downward flux at the surface for the DESERTL case. Values close to one represent a field that is primarily comprised of direct solar radiation while a value of zero is for a totally diffuse field. An increase in the turbidity results in a large increase in the amount of diffuse radiation, while an increase in solar zenith angle leads to a smaller increase. The diffuse radiation constitutes up to 40% of the total surface flux for optical depths as low as 0.5, and contributes significantly to the daily energy gain of the surface. The wavelength dependence of the direct to total ratio is shown in figure 4.12 for the spectral bands 0.5-0.6 $\mu m$ (solid line) and 2.3-3.8 $\mu m$ (dashed line). The shorter wavelength region depicts a strong dependence in both optical depth and solar zenith angle, while the 2.7 $\mu m$ band shows only a weak dependence on solar zenith for the small optical depths. The heavy solid line demarks equivalent ratios for the two wavelengths, with values to the left of this line representing regions where, for a given optical depth and solar zenith, the 2.7 $\mu m$ band has a larger relative direct component. The smaller ratios in the 2.7 $\mu m$ band results from the smaller asymmetry parameter. This changing

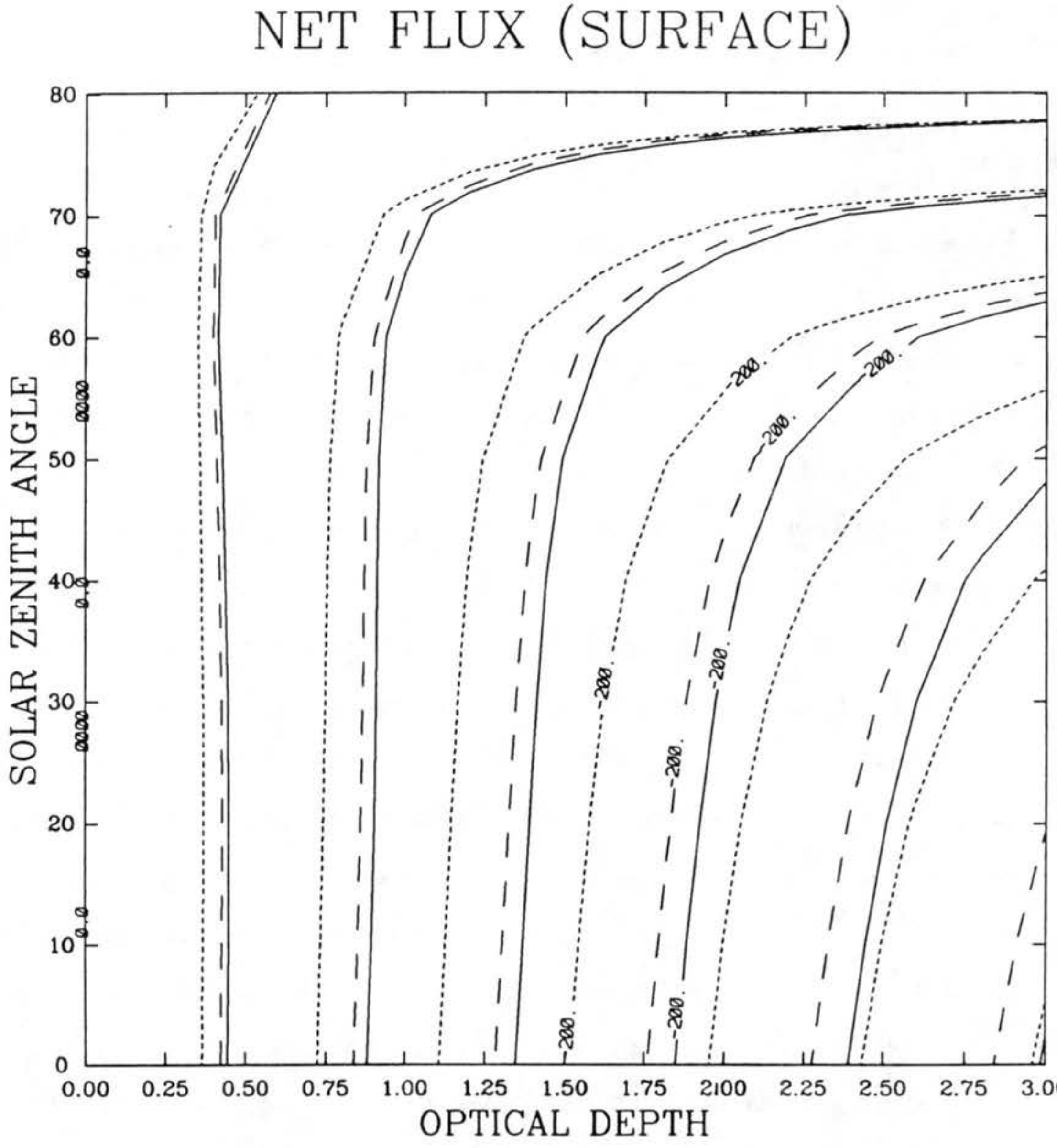


Figure 4.10: Dust laden minus clear sky differences in the net SW flux at the surface as a function of solar zenith angle and turbidity for the three desert cases; DESERTL (solid), DESERTH (long dashed) and DESERTV (short dashed) Contour intervals are $50 W m^{-2}$.

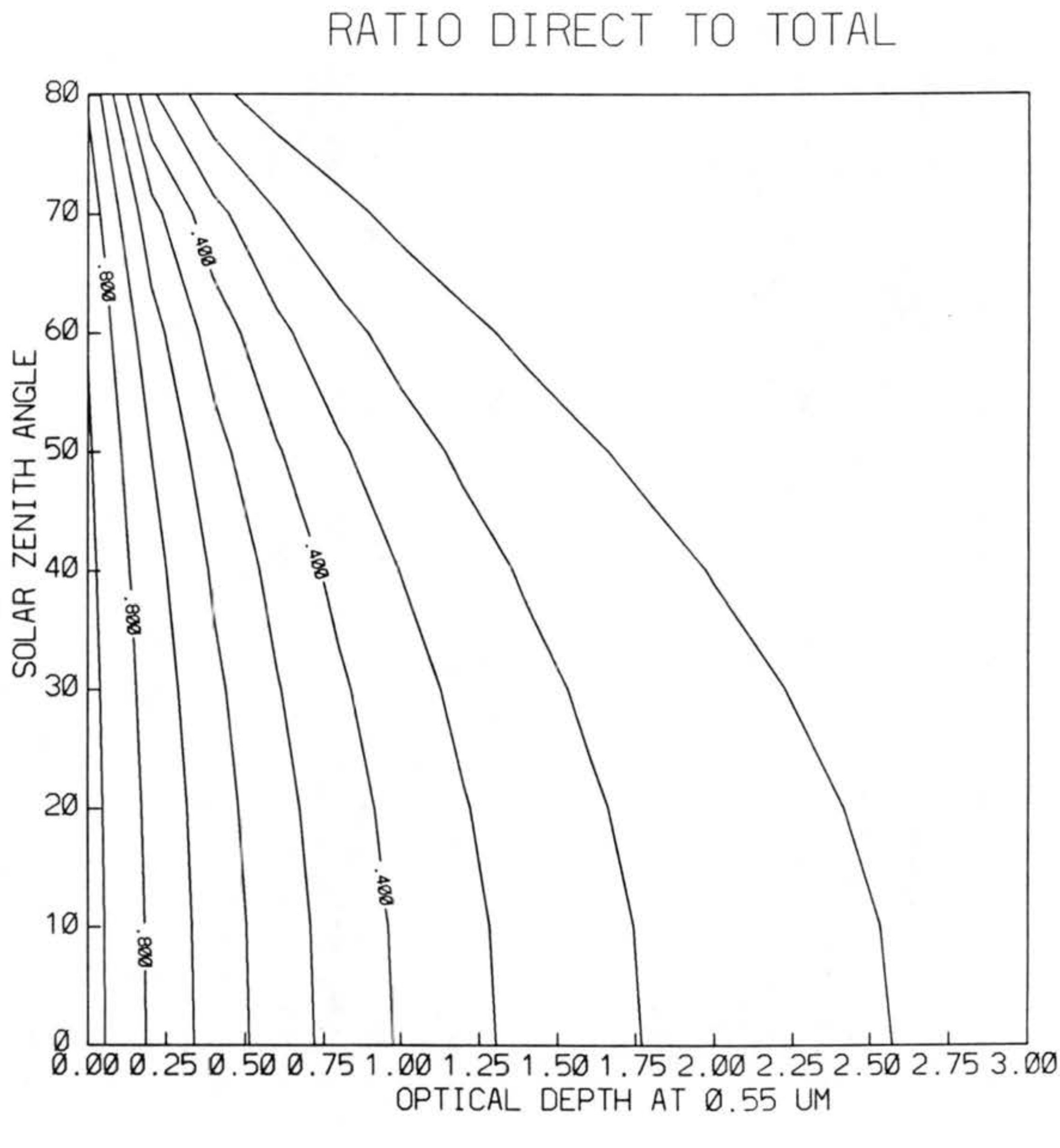


**Figure 4.11: Ratio of the direct component at the surface to the total downward flux at the surface for the DESERTL case.**

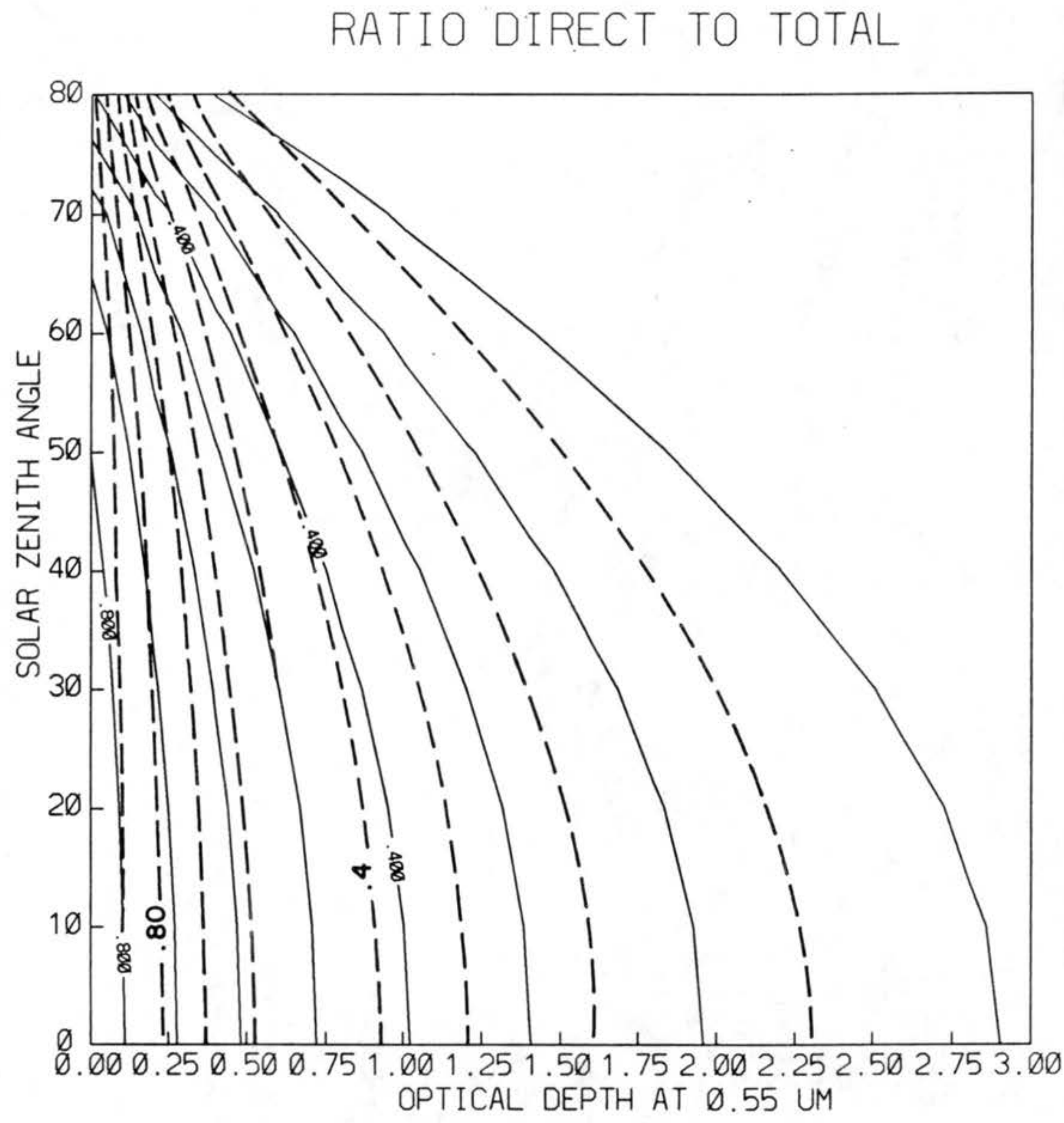


Figure 4.12: Direct to total ratio for the spectral bands $0.5 - 0.5\mu m$ (solid line) and $2.3 - 3.8\mu m$ (dashed).

energy distribution is of interest in considering the aerosols' potential climatic impact. In addition, the large diffuse component will degrade horizontal visibility across the entire 0.2 to 4 $\mu m$ spectral interval. The amount of diffuse flux also affects surface measurements of dust optical thickness as discussed in the next section.

### 4.1.4 Changes in the SW fluxes over the ocean

Dust-laden minus dust-free differences in the upward SW flux at the TOA for the OCEANL case are shown in figure 4.13. Contrary to the desert cases the impact of the low surface albedo of the ocean is to increase (decrease) the upward (net) flux with increasing turbidity, for a given solar zenith angle. Thus the presence of the dust layer over a low albedo surface decreases the SW energy gain of the earth-atmosphere system. In addition, the ocean case displays a greater sensitivity of the upward flux to changes in solar zenith angle and turbidity. The total atmospheric heating for the OCEANL case (figure 4.14) displays trends similar to the desert cases with the exception of smaller heating due to the lower surface albedo. Differences between the dusty-clear radiative heating profiles (figure 4.15) are similar to the DESERTL case, though smaller in magnitude. As a result of the lower surface albedo the presence of the dust layer increases the upward visible flux resulting in larger stratospheric heating than the desert cases (figure 4.16). Changes in the net surface flux (figure 4.17) are larger for the ocean case than the desert cases owing again to the smaller surface albedo. The total downward flux for the ocean case also shows trends similar trends to the desert cases except with smaller magnitudes.

### 4.1.5 Summary of the effects of dust on the SW fluxes

We can summarize the above discussion with the following points:

- The absorption of solar energy by a soil derived aerosol is large and produces significant atmospheric heating. For optical depths of 0.2, the presence of a dust layer can increase the radiative heating of the troposphere by $0.02^0C/hour$, while for larger optical depths the heating rates can increase 0.16 $^0C/hour$. The majority of this heating is by the aerosol itself in the 0.2-0.86 $\mu m$ spectral region. The shape of the radiative heating profile is a strongly depends on the vertical distribution of dust

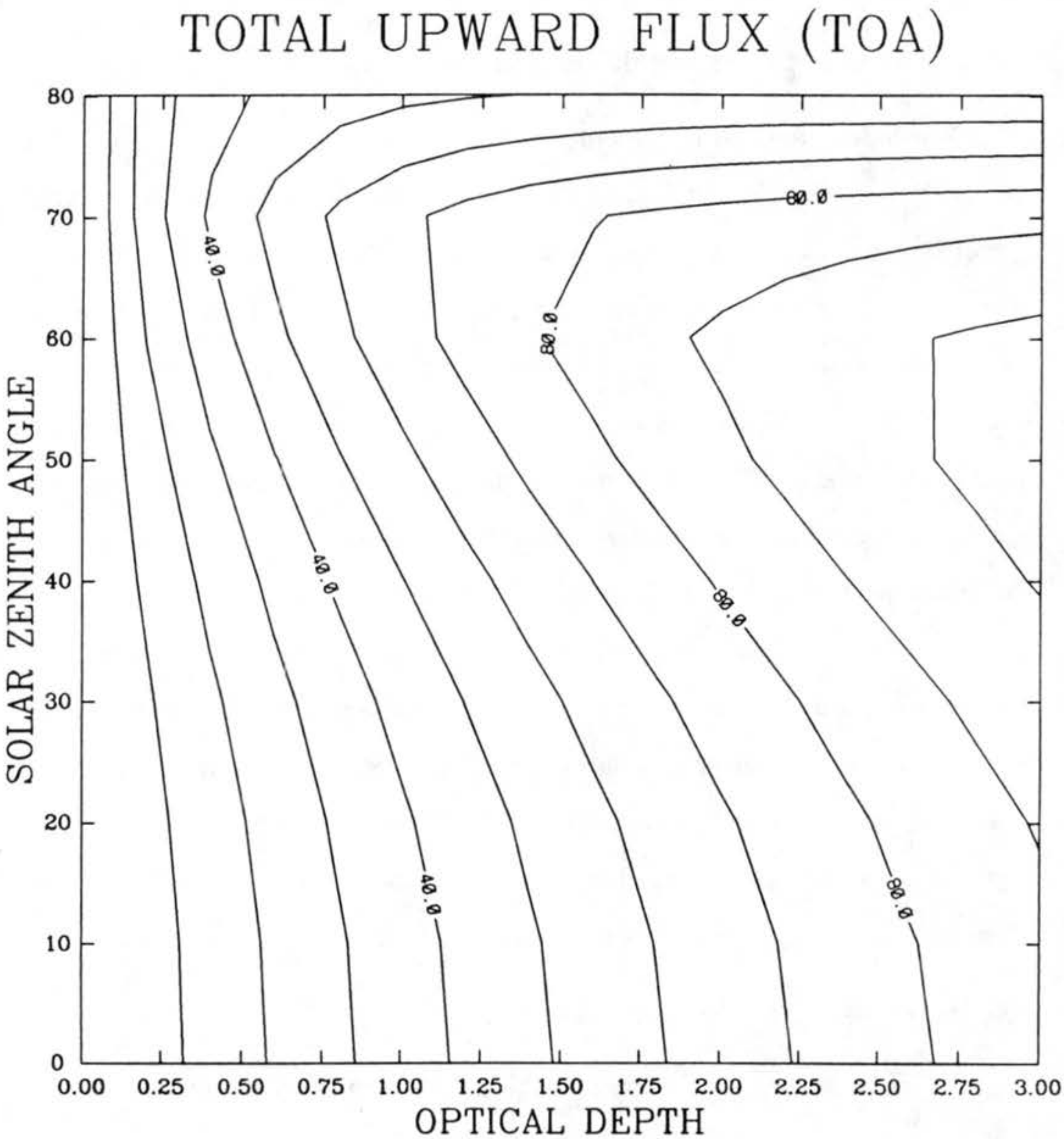


Figure 4.13: Dust laden-dust free differences in the upward SW flux at the top of the atmosphere for the OCEANL case.

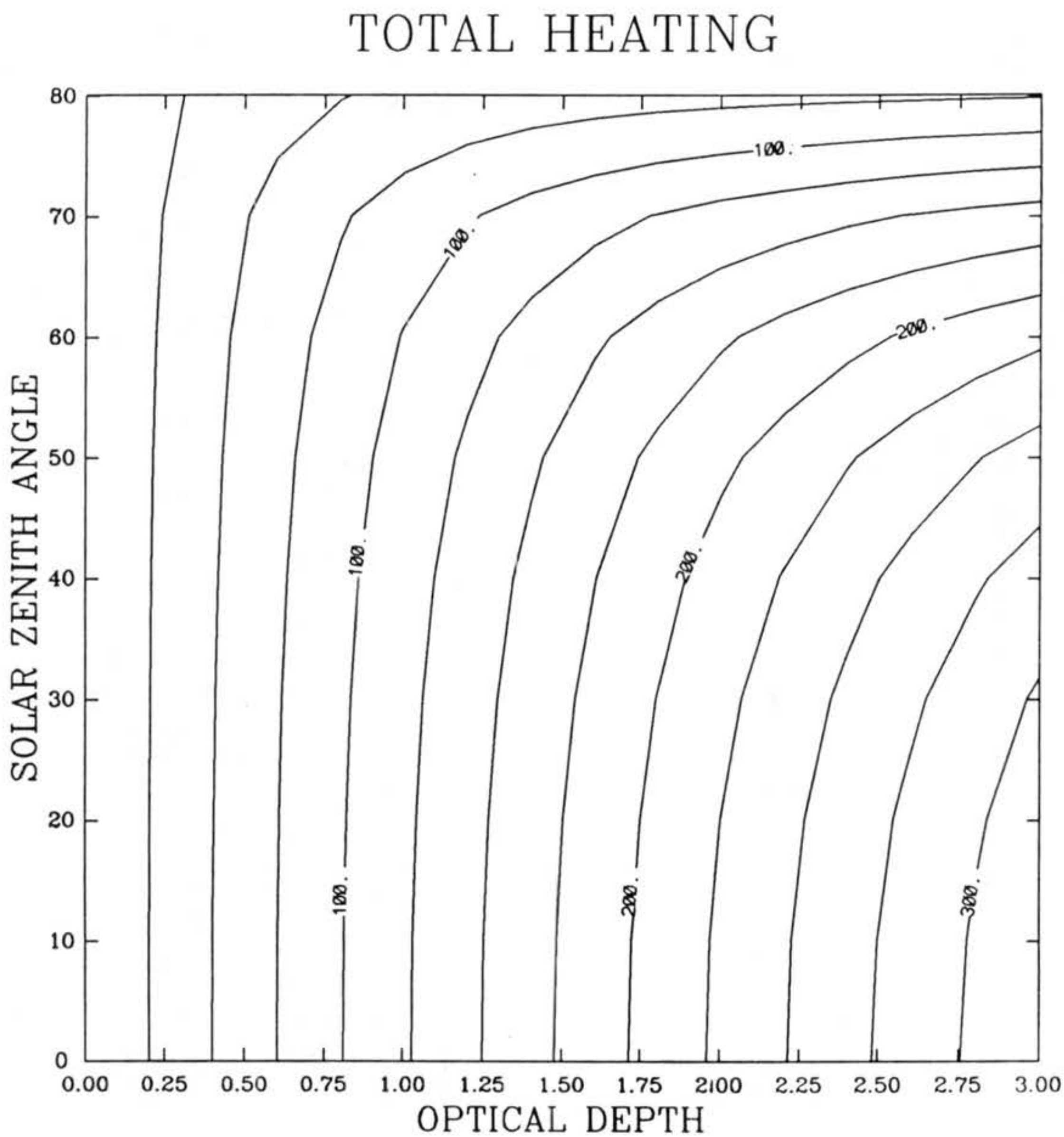


Figure 4.14: Differences in the dusty minus clear SW atmospheric radiative heating for the OCEANL case. Contour intervals are $50 W m^{-2}$ per 1000 mb.

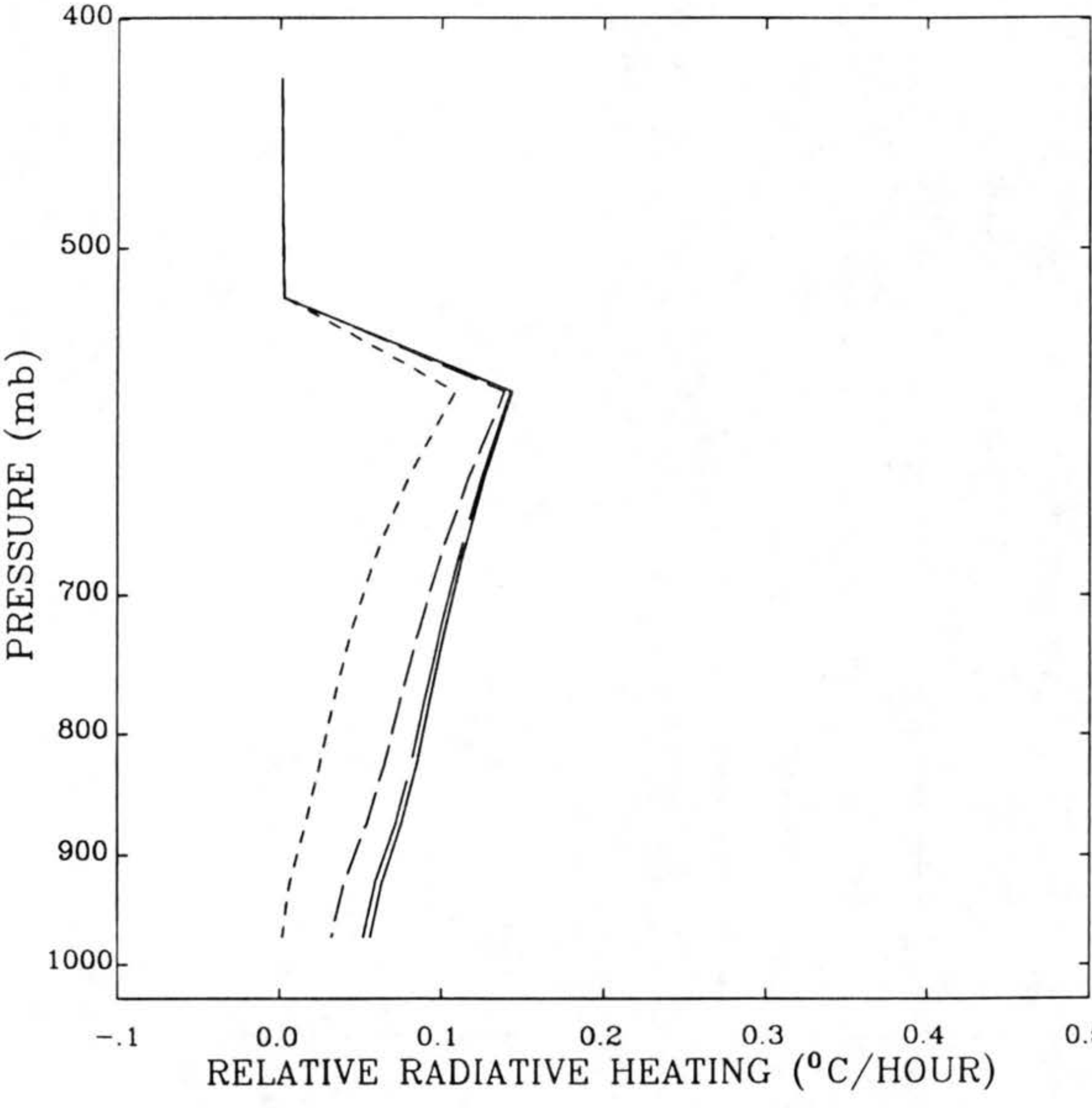


Figure 4.15: Tropospheric radiative heating differences between the dust laden and clear atmospheres for the OCEANL case at four solar zenith angles;$0^0$ (solid), $30^0$ (long dashed), $60^0$ (dashed) and $80^0$ (short dashed).

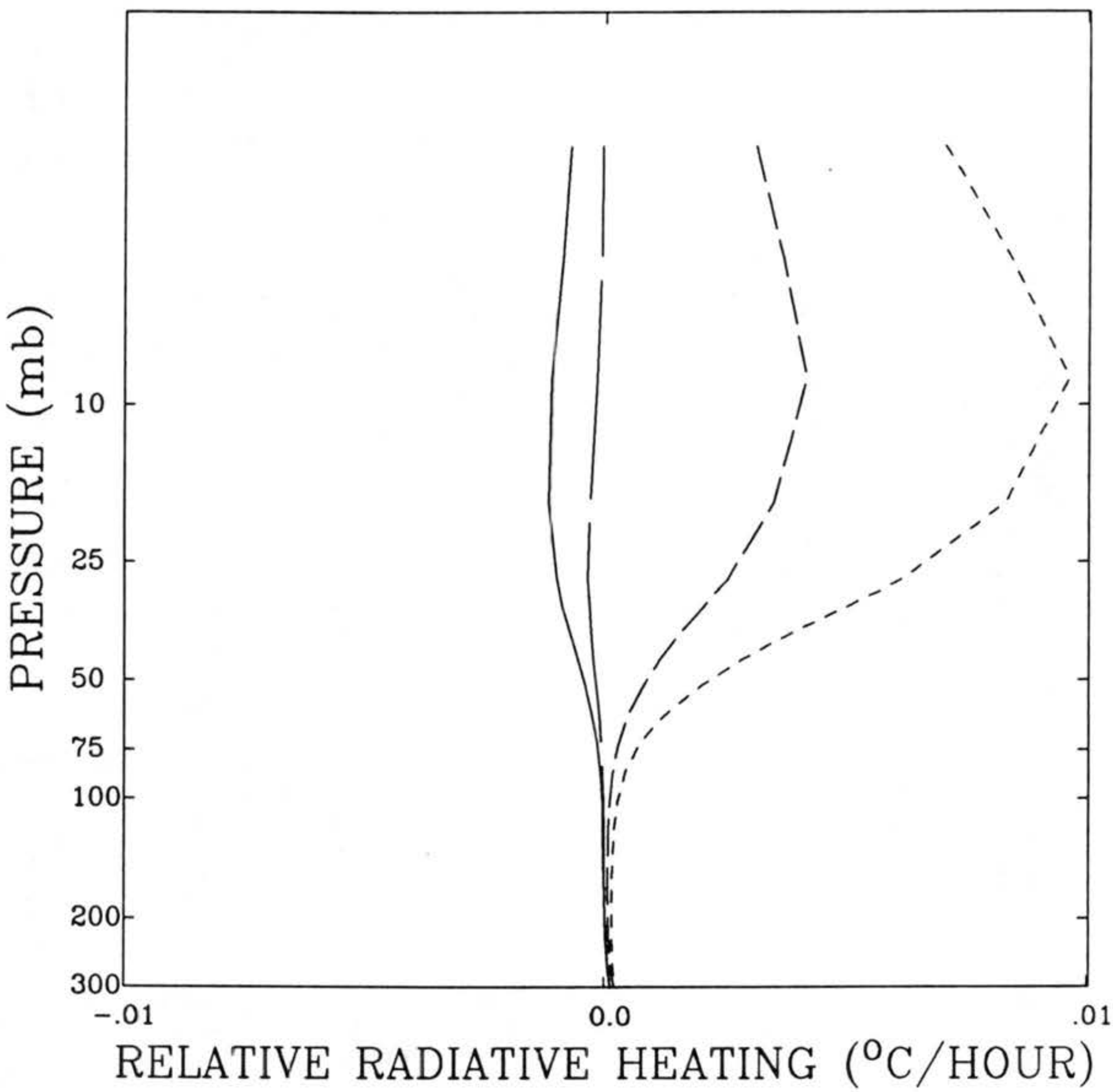


Figure 4.16: Stratospheric radiative heating differences between the dust laden and clear atmospheres for the OCEANL case at four solar zenith angles;$0^0$ (solid), $30^0$ (long dashed), $60^0$ (dashed) and $80^0$ (short dashed).

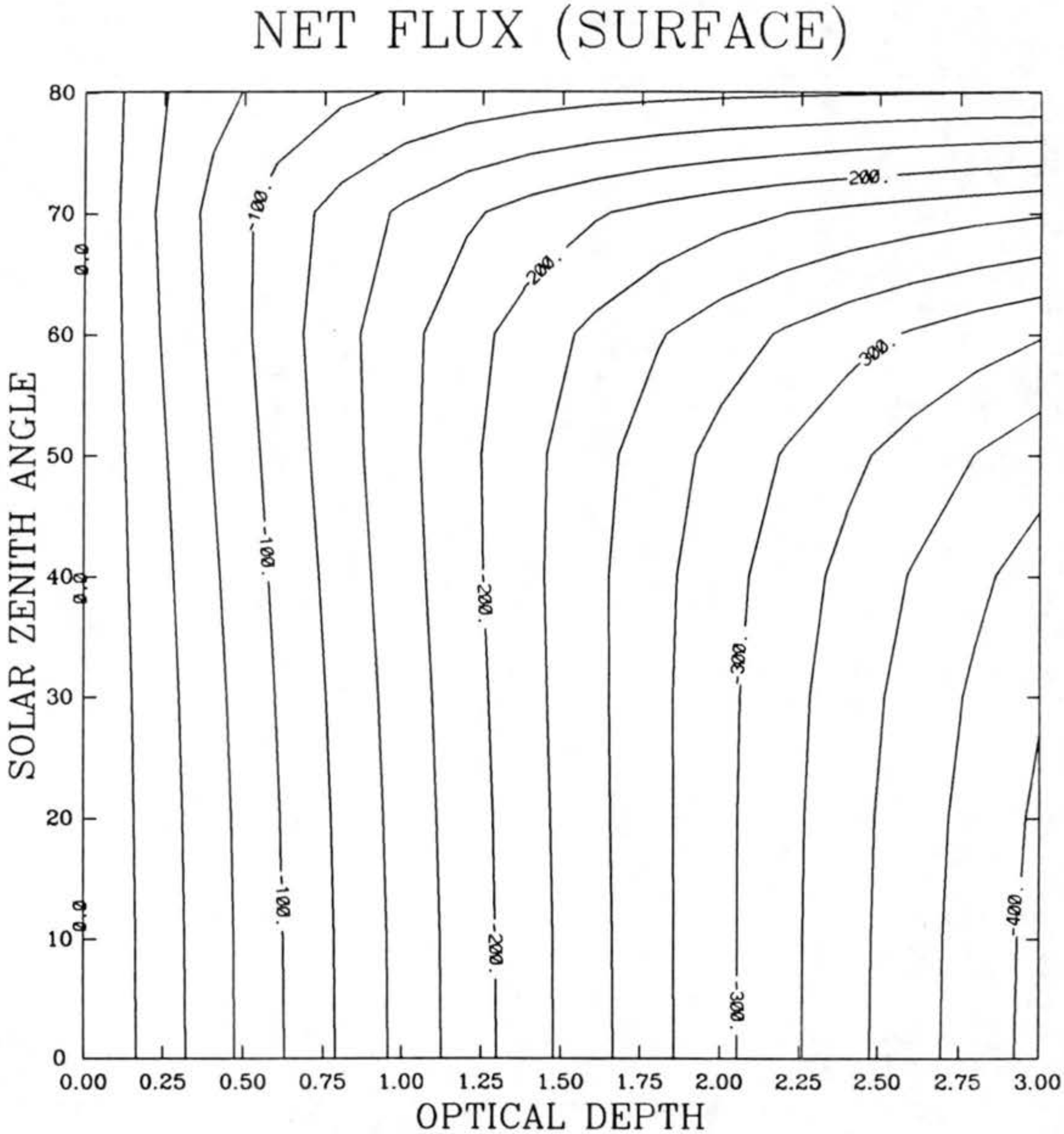


Figure 4.17: Changes in the net SW surface flux due to the presence of a crustal aerosol for the OCEANL case. Contour intervals are $25 W m^{-2}$.

optical depth with changes in the size distribution playing a secondary role. The altitude at which the largest heating occurs is a function of solar zenith angle and the vertical distribution of the dust.

- While dust and water vapor have their strongest absorption in different spectral regions in the solar spectrum, the presence of the dust enhances the water vapor absorption through multiple scattering. This enhancement is 10% of the absorption by the aerosol itself. Soil derived aerosols and $O_3$ both absorb in the visible wavelengths and thus the presence of a dust layer can affect stratospheric radiative heating rates by modifying the upward visible fluxes at the tropopause. This effect can lead to increased or decreased heating for the desert cases depending on the solar zenith angle. For the ocean case, the presence of the dust layer increases the radiative heating of the stratosphere, except at the small solar zenith angles.

- The radiative fluxes at the top of the atmosphere display a smaller sensitivity to the dust optical properties than the surface fluxes or atmospheric absorption. Thus the presence of a dust layer primarily results in a redistribution of the radiative energy between the atmosphere and the Earth's surface. In the case of the desert environment where ground storage is small (Smith, 1986a), the dust layer results in an increased radiative heating of the atmosphere while the sensible heat flux from the surface is reduced. For the ocean case, the absorption of SW energy by the dust layer results in a direct heating of the atmosphere at the expense of surface energy budget of the ocean.

## 4.2 Longwave model results

In this section the LW two-stream model is employed to study the sensitivity of the LW fluxes to the presence of a dust layer. The four dust loading atmospheres presented at the beginning of this chapter are also used in this section. Atmospheric temperatures above 850 mb are held fixed based on observations discussed in the beginning of Chapter 2. Temperature profiles from the surface to 850 mb are assumed to decrease linearly with height. Thus for surface temperature less than approximately 25 $^0C$ a temperature inversion exists.

### 4.2.1 Changes in the LW flux at the top of the atmosphere

Differences in the LW flux at TOA between clear sky calculations and dusty atmosphere as a function of turbidity and surface temperature are shown in figure 4.18. Negative values indicate that the clear sky values are greater than those for the dust laden case. The DESERTL (solid) and DESERTH (dashed) cases are similar showing decreases in the upward flux with increasing optical depth. This is due to the fact that the presence of the dust layer reduces the surface LW radiative energy losses to space; the impact is greater for higher surface temperatures. For the DESERTV case (dotted) where most of the dust is concentrated in the lowest atmospheric levels, the presence of the dust can lead to an increase in the TOA upward flux for lower surface temperatures and turbidities greater than about 0.4. This results from the lower level temperature inversion in conjunction with the large dust concentrations near the surface.

### 4.2.2 Changes in the LW heating of the atmosphere

Changes in the atmospheric LW radiative convergence induced by the presence of the dust layer are shown in figure 4.19. Contour intervals are 5 $Wm^{-2}$ per 1000 $mb$ (0.04 $^0C/Day$ in heating rate units), and negative values indicate that the dust laden atmosphere is cooling more than the clear atmosphere. The presence of the dust layer results in a net cooling of the atmosphere which increases with dust loading. Again the DESERTL and DESERTH cases are similar while the DESERTV is not only different in magnitude but also in its dependency on surface temperature. Concentrating the dust in the lower and warmer layers of the atmosphere results in considerably more cooling than when the dust is uniformly distributed. In addition, the LW radiative heating for the vertically distributed dust (DESERTV) case displays much less sensitivity to the surface temperature and a greater sensitivity to optical depth than do the other two cases.

The vertical profiles of radiative heating differences between the dusty and clear atmospheres are shown in figure 4.20 for the DESERTL case for four surface temperatures. Negative values indicate a greater cooling in the presence of the dust layer. Maximum cooling occurs near the top of the dust layer, and increases with decreasing surface temperature. The increased surface temperature allows more radiative energy to be absorbed

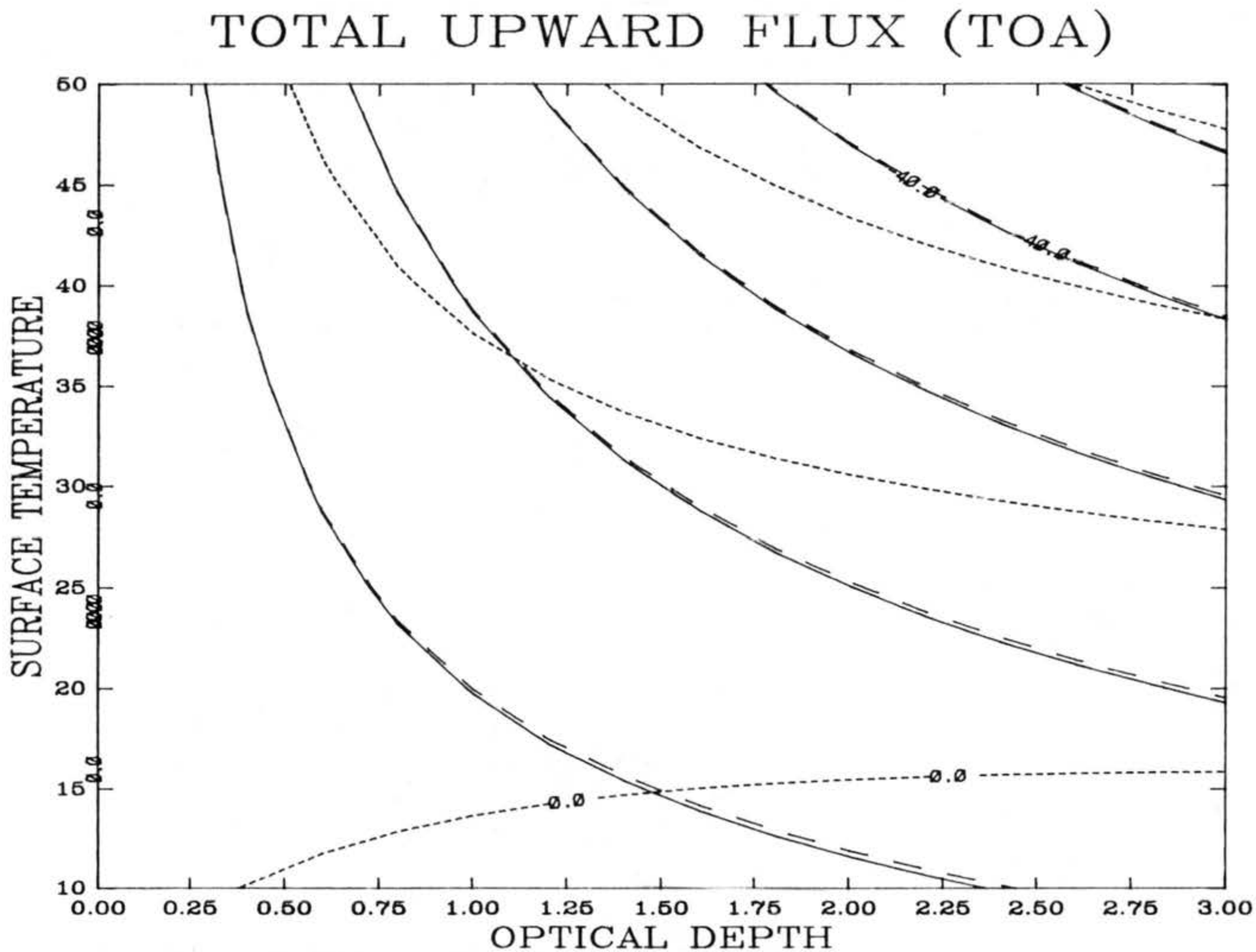


Figure 4.18 Differences in the LW flux at the top of the atmosphere between a clear and a dusty atmosphere as a function of turbidity and surface temperature for the DESERTL (solid), DESERTH (dashed) and DESERTV (dotted) cases. Contour intervals are $10 W m^{-2}$, where negative values indicate a greater clear sky value.

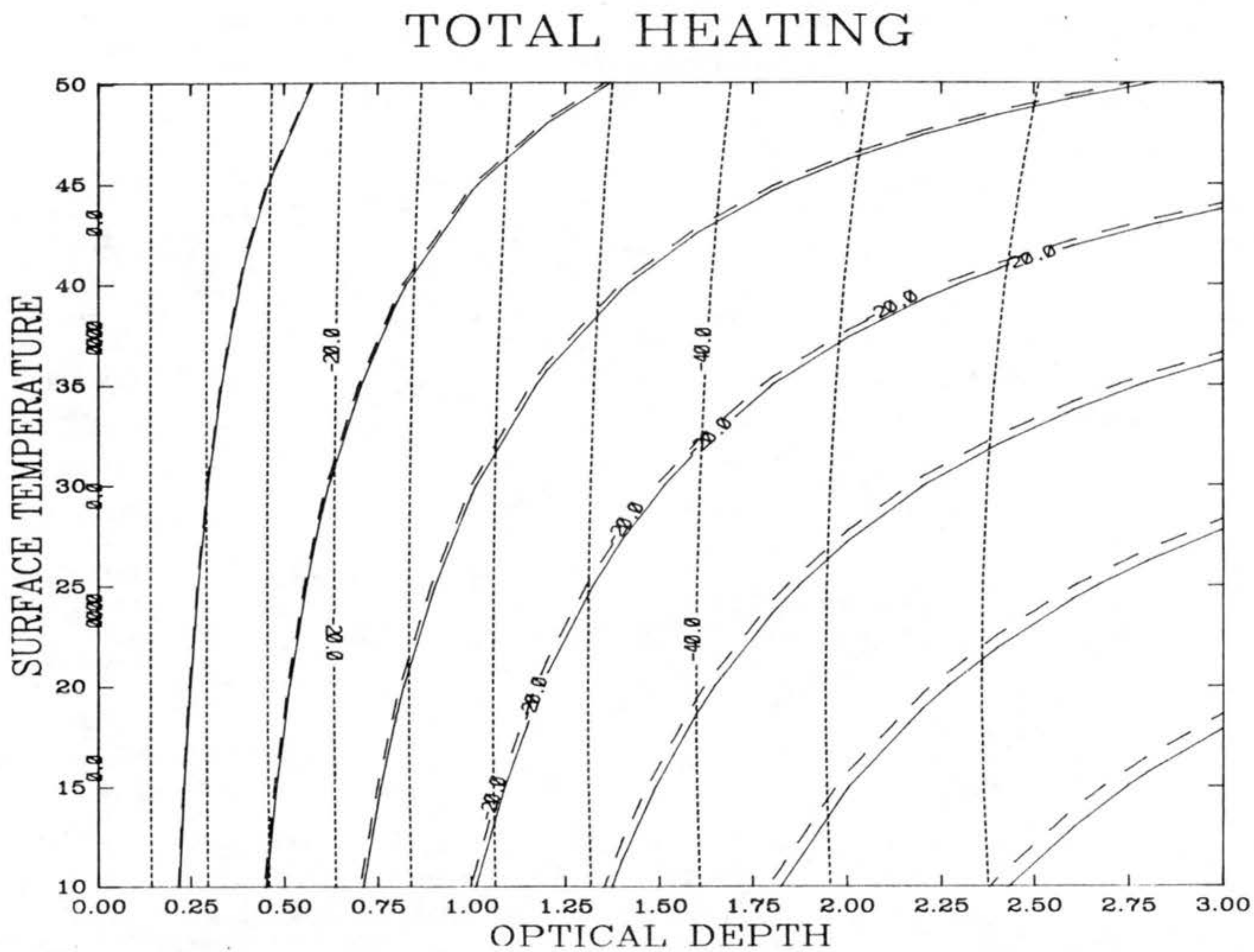


Figure 4.19: Changes in the LW radiative heating of the atmosphere due to the presence of a dust layer. Contour intervals are $5 W\,m^{-2}$ per 1000 mb with negative values indicating a greater cooling for the dust laden atmosphere.

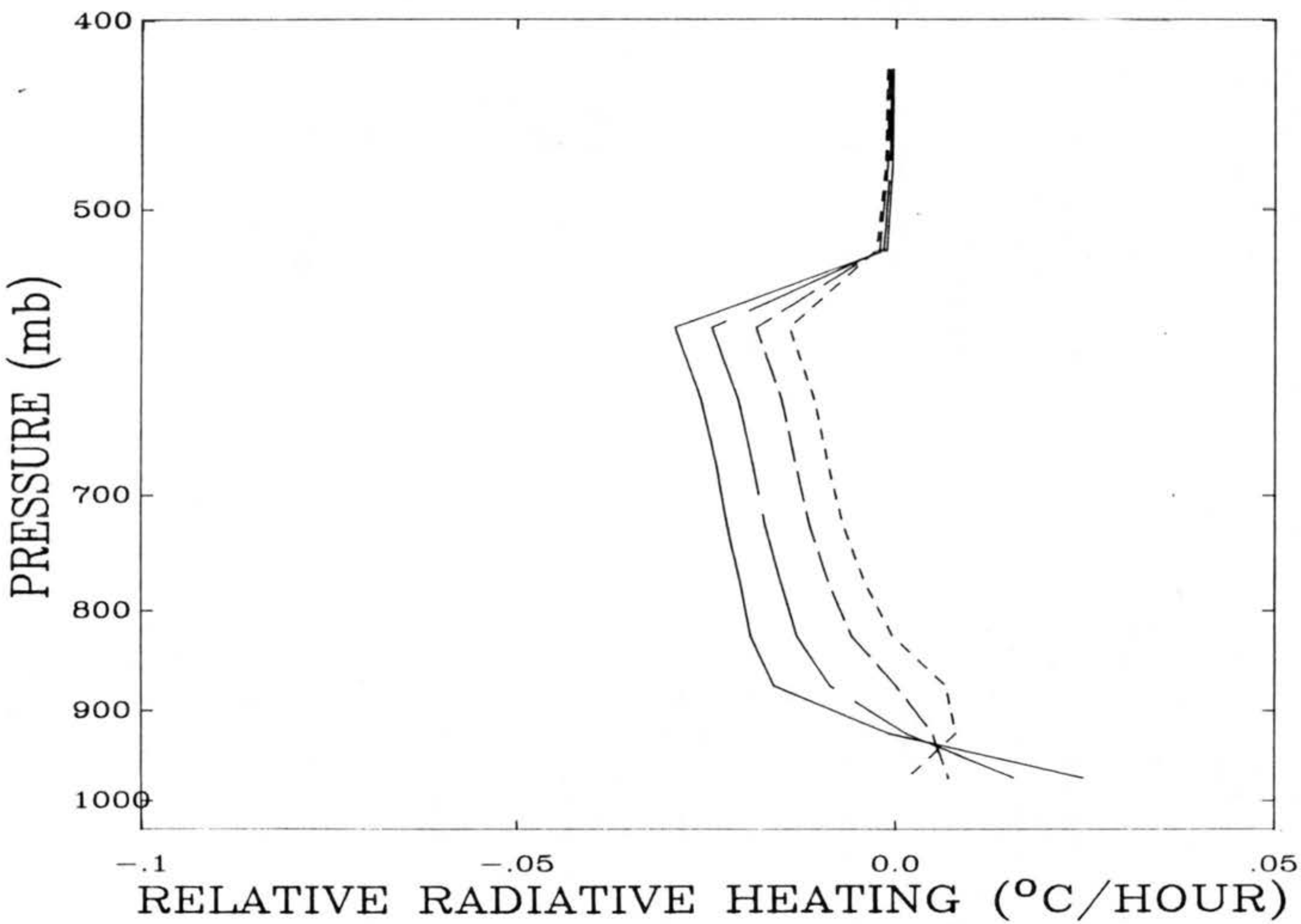


Figure 4.20: Differences in the tropospheric radiative heating profile of the dusty and clear atmospheres for the DESERTL case for surface temperatures of $10^0$ (solid), $25^0$ (long dashed), $40^0$ (dashed) and $50^0C$ (short dashed).

by the dust to offset the additional atmospheric cooling. The lower layers of the atmosphere show less cooling than the clear sky values. While maximum heating occurs in the $10^0C$ surface temperature it occurs through a shallower depth. For the $50^0C$ surface temperature, there is no low level temperature inversion and the warm surface temperatures result in a radiative warming over a deeper layer. The radiative heating profiles for the DESERTV case are shown in figure 4.21. The maximum cooling is now lower in the atmosphere, near 850 mb, where maximum cooling is again associated with minimum surface temperature. In the middle troposphere, between the top of the dust layer (550 $mb$) and 700 $mb$, the cooling increases with increasing surface temperature. The large concentration of dust below 700 mb reduces the upward flux at the 700 $mb$ layer, thereby reducing the radiative energy convergence within this middle tropospheric layer. In addition, the cooling of this layer is enhanced by the presence of the dust. Unlike the uniform $\sigma_{ext}$, the presence of the dust layer always results in an increased cooling over the dustless case.

Changes in the stratospheric radiative heating profiles arising from the presence of a DESERTL loading are depicted in figure 4.22. The presence of the dust layer reduces the upward flux in the 9.6 $\mu m$ ozone band which, in turn, reduces the stratospheric heating. As expected the effect increases with increased surface temperature.

### 4.2.3 Changes in the LW fluxes at the surface

The change in the net LW surface flux due to presence of a dust layer is shown in figure 4.23 where positive values indicate a greater surface energy loss under dust free conditions. The presence of a dust layer causes an increase in the LW downward component at the surface and thereby a decrease in the net flux. An increase in the temperature of the lower layers of the atmosphere increase the LW energy gain at the surface. The maximum increase (greater than 80 $Wm^{-2}$) occurs at large optical depths and large surface temperatures of the DESERTV case. Since the vertically structured DESERTV case has more dust at warmer temperatures it has a greater effect on the net flux, and is more sensitive to the surface temperature. The DESERTL and DESERTH have similar effects on the net surface flux.

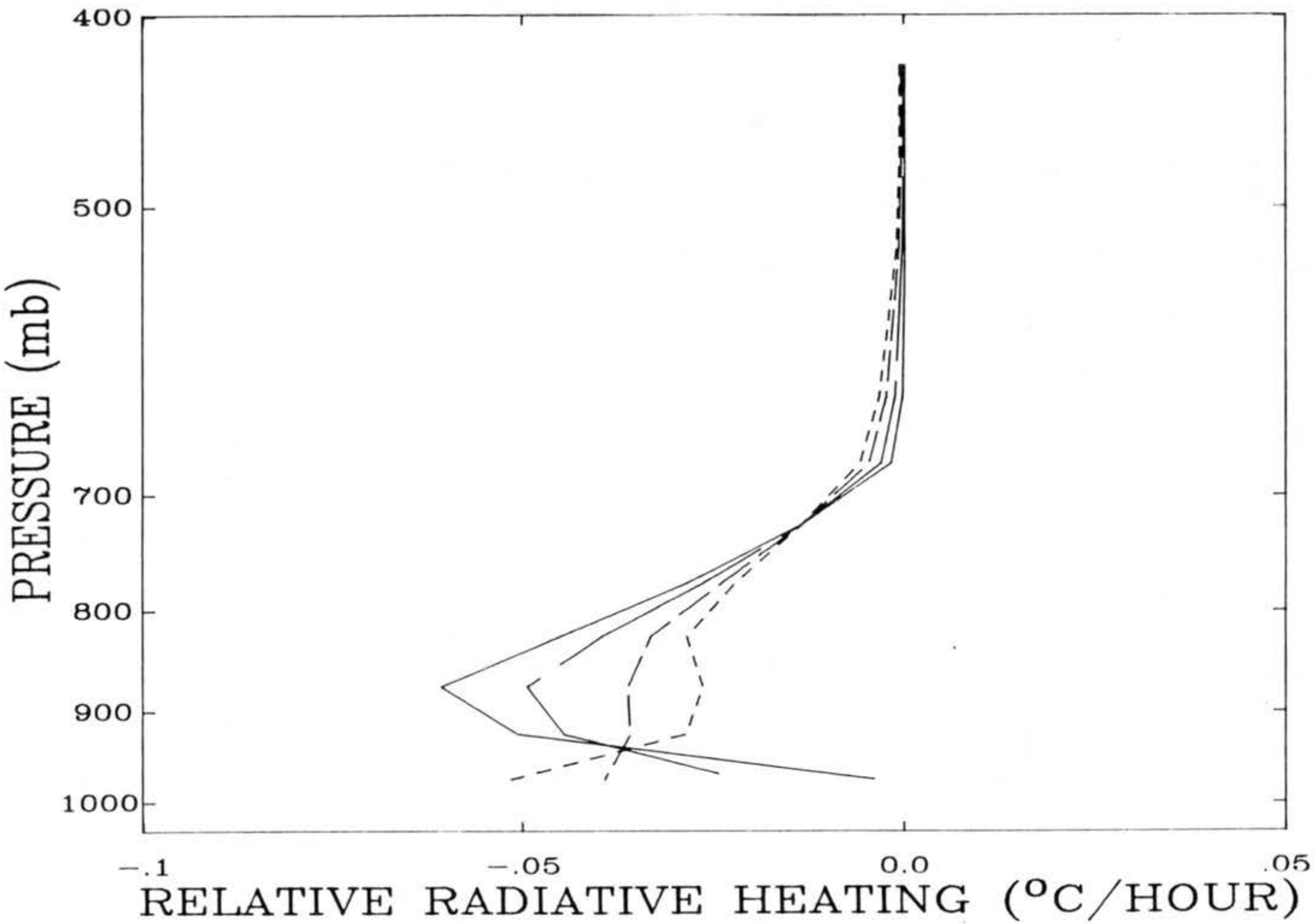


Figure 4.21: Differences in the tropospheric radiative heating profile of the dusty and clear atmospheres for the DESERTV case for surface temperatures of $10^0$ (solid), $25^0$ (long dashed), $40^0$ (dashed) and $50^0C$ (short dashed).

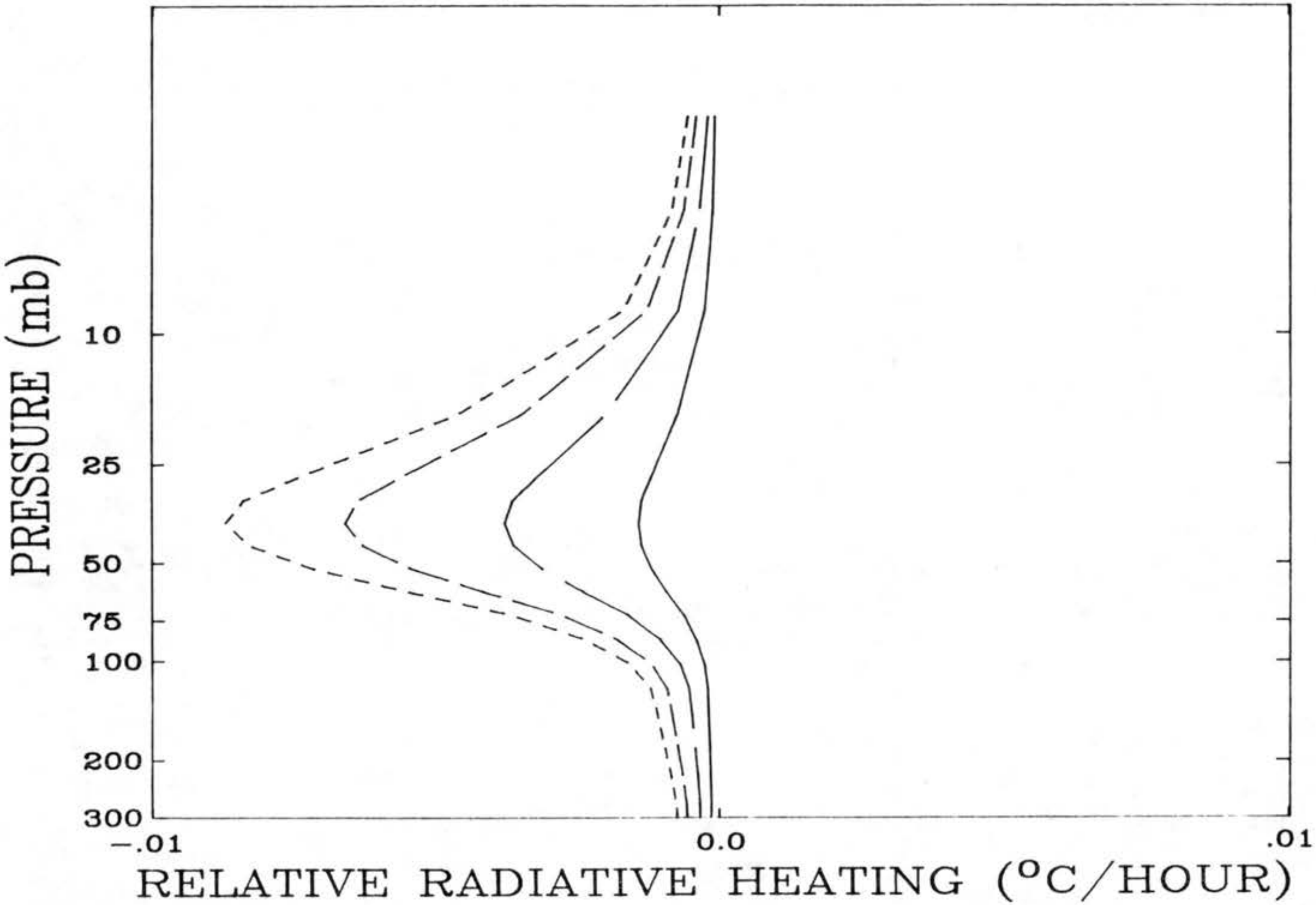


Figure 4.22 Differences in the stratospheric radiative heating profile of the dusty and clear atmospheres for the DESERTL case for surface temperatures of $10^0$ (solid), $25^0$ (long dashed), $40^0$ (dashed) and $50^0C$ (short dashed).

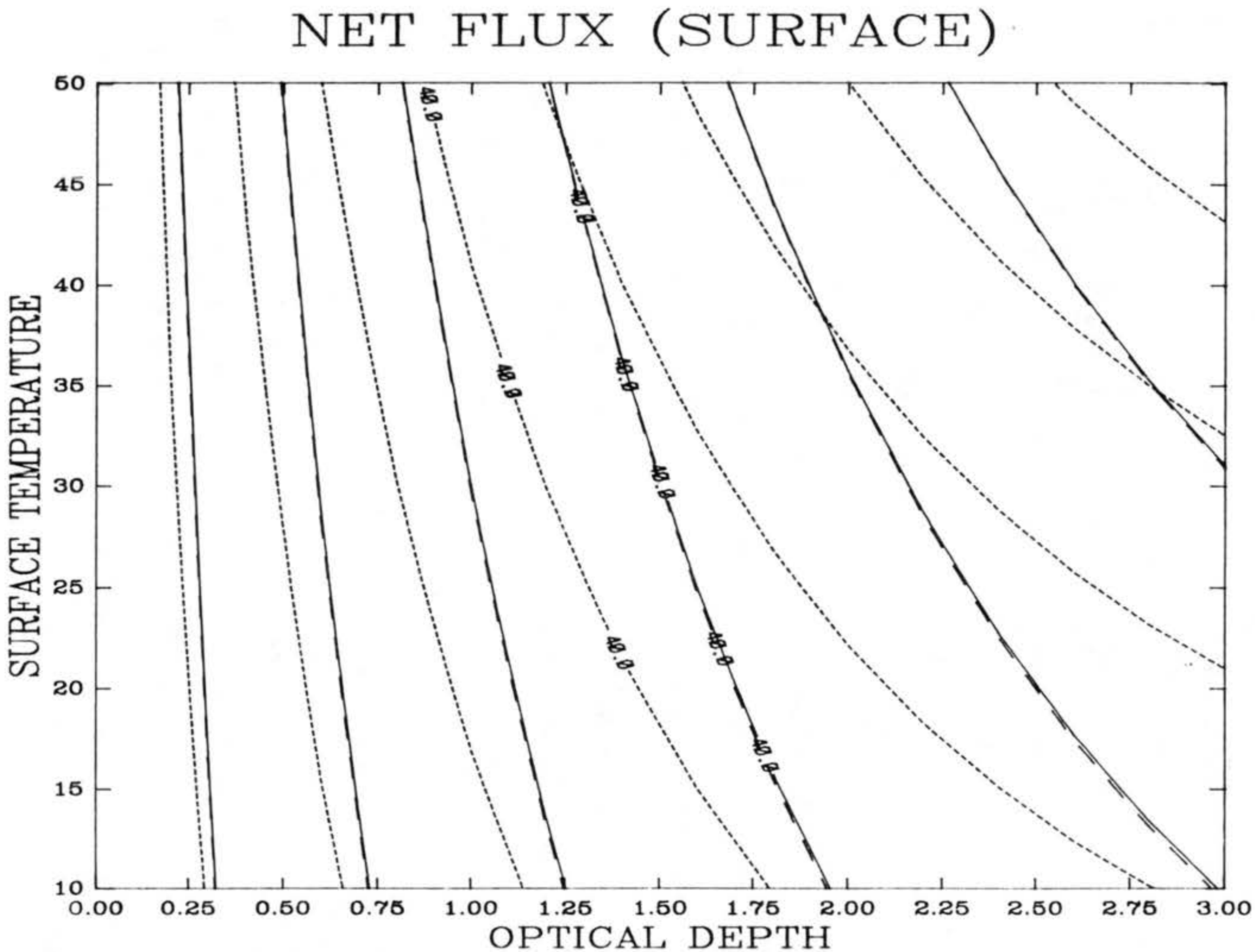


Figure 4.23 Changes in the net surface LW flux due to the presence of a dust layer. Solid line depicts the DESERTL case, the DESERTH case is dashed while the DESERTV case is represented as a dotted line.

### 4.2.4 Summary of the effects of dust on the LW fluxes

The LW model calculations can be summarized as follows;

- The presence of a dust layer results in an increased radiative cooling in both the troposphere and stratosphere. This increase in the total tropospheric cooling is, at most, $0.5^0C/Day$. The majority of this cooling occurs in the 8-13 $\mu m$ spectral interval. The magnitude of the enhanced cooling is strongly dependent on the vertical distribution of the dust, and is less sensitive to the light and heavy dust loading cases considered.

- Changes in the upward flux at the top of the atmosphere are also a function of the vertical distribution of the dust. Where the dust loading decreases exponentially with height, an increase in the upward LW can occur in the presence of lower level inversions. In most instances inclusion of a dust layer results in a decrease in the LW flux exiting the top of the atmosphere.

- The presence of the dust layer results in an increase in the downward LW flux at the surface, and thus a decrease in the surface radiative energy deficit. As expected the increase in the downward flux is a function of the vertical distribution of the dust loading as well as the lower level temperature structure.

## 4.3 Daily radiative energy budgets

The temperature profiles and moisture profiles of tables 3 and 4 were used in radiative transfer calculations to consider the effect of the dust layer on the combined shortwave and longwave radiative energy budgets. The Earth-Sun geometry corresponds to the summer solstice at $20^0N$ latitude. The diurnal radiative heating for the DESERTL case is depicted in figure 4.24. The solid line represents the clear sky values, the long dashed (short dashed) line represents a turbidity of 0.2 (1.0). As discussed earlier the dust results in an increase in the planetary SW heating and LW cooling. The symmetry about local noon results from diurnally varying solar zenith angle, while the asymmetric pattern in the LW flux is a consequence of the temperature profiles assumed. The presence of the dust layer

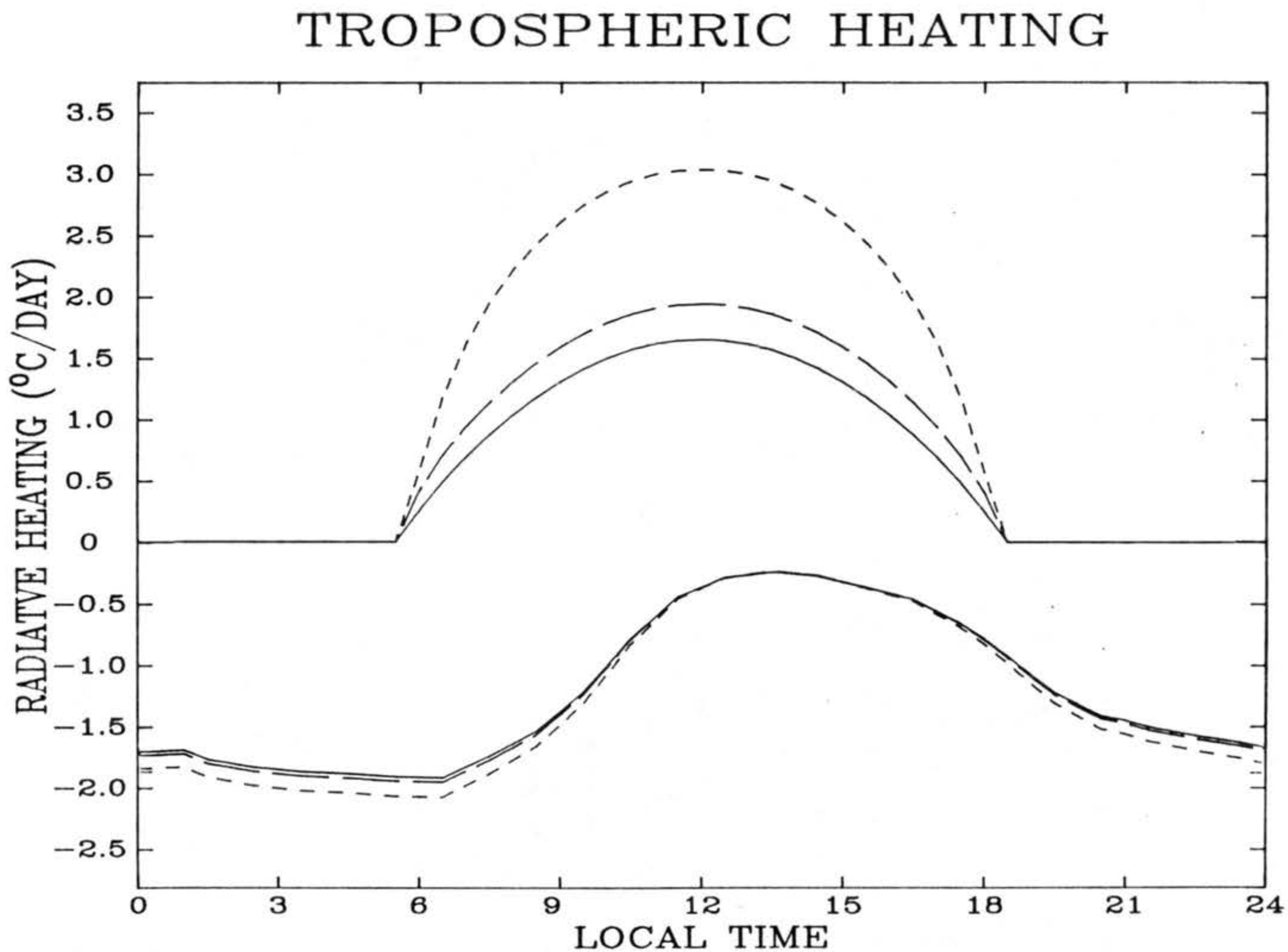


**Figure 4.24 Daily variations in the shortwave and longwave radiative heating for clear sky (solid) and dust laden atmospheres with turbidities of 0.2 (dashed) and 1.0 (dotted). Results for the DESERTL case are shown.**

enhances tropospheric heating; this enhancement effect increases with solar zenith angle and optical depth. The presence of the dust layer increases the tropospheric LW cooling by an amount that is proportional to the dust loading and atmospheric temperature structure. The largest effect on the LW cooling is at night with minimum effects between 12 and 18 LST. The diurnally averaged dust free atmosphere is cooling $-0.62^0C/Day$ (see Table 7); a dust layer of optical depth 0.2 decreases this cooling by 0.12 $^0C/Day$ due to the dominating effect of SW absorption over LW cooling. The heavier dust loading case results in a doubling of the SW atmospheric heating while the LW cooling only increases by $0.08^0C/Day$.

The diurnal structure of the net surface flux is shown in figure 4.25. The presence of the dust decreases both the LW energy losses and the SW energy gain. The 24 hour mean surface radiative energy gain is $80Wm^{-2}$ for the clear atmosphere case. For a turbidity of 0.2, the SW gain is reduced by $12Wm^{-2}$ while the LW energy loss is reduced by $8Wm^{-2}$. Thus the total net surface flux is reduced to $76Wm^{-2}$, a difference of $4Wm^{-2}$. The difference is $21Wm^{-2}$ for an optical depth of 1.0

The net flux at the top of the atmosphere is shown in figure 4.26 as a function of local time. The presence of the dust layer results in an increased planetary heating for both the LW and SW components. In the case of the troposphere or surface, an increase in one budget component was accompanied by a decrease in the other. In the mean the earth-atmosphere system is gaining $9Wm^{-2}$. A small increase in dust loading to an optical depth of 0.2 results in a doubling of this total energy gain. A dust optical depth of 1.0 causes an increase of $30Wm^{-2}$.

The 24 hour mean radiative energy budgets for the DESERTV case are given in Table 8. The SW and LW energy budgets change in comparison with the DESERTL case, yet the total change in the radiative budgets is approximately the same as in the DESERTL case. The vertical profile of tropospheric radiative heating is much different as discussed previously.

The tropospheric, surface and TOA radiative energy budgets for the OCEANL case are given in table 9. Changes in the total tropospheric heating due to the presence of the

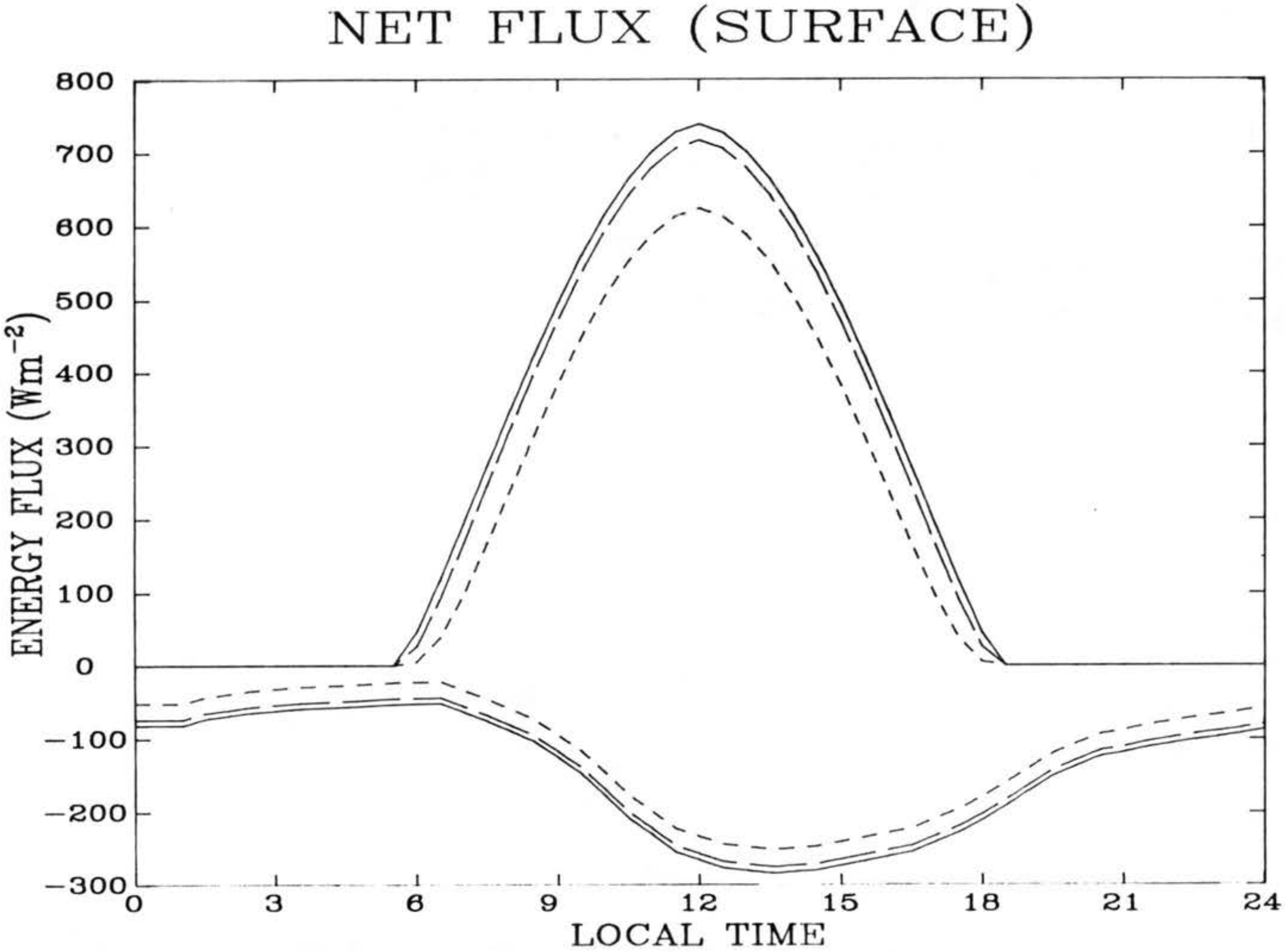


Figure 4.25 Daily variations in the shortwave and longwave surface radiative fluxes for clear sky (solid) and dust laden atmospheres with turbidities of 0.2 (dashed) and 1.0 (dotted). Results for the DESERTL case are shown.

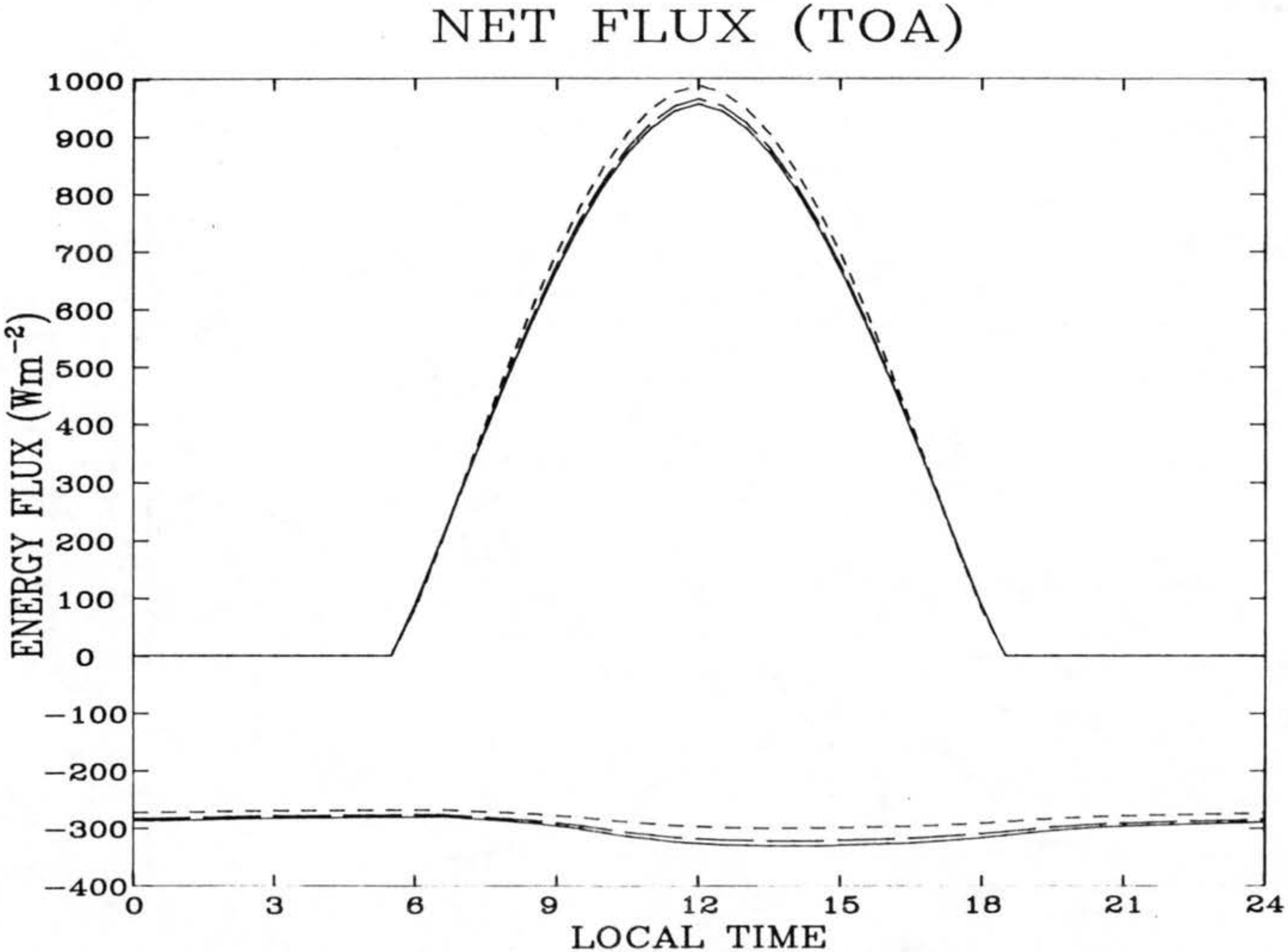


Figure 4.26 Daily variations in the shortwave and longwave fluxes at the top of the atmosphere for clear sky (solid) and dust laden atmospheres with turbidities of 0.2 (dashed) and 1.0 (dotted). Results for the DESERTL case are shown.

Table 4.1: Daily mean radiative energy budgets for DESERTL case. Units are $Wm^{-2}$ for the fluxes, and $^0C/day$ for the heating rates.

| | Tropospheric heating | | | Net surface flux | | | Net flux TOA | | |
|---|---|---|---|---|---|---|---|---|---|
| TURBIDITY | SW | LW | TOTAL | SW | LW | TOTAL | SW | LW | TOTAL |
| 0 | .6 | -1.22 | -.62 | 230 | -150 | 80 | 311 | -302 | 9 |
| 0.2 | .74 | -1.24 | -.50 | 218 | -142 | 76 | 313 | -296 | 17 |
| 1.0 | 1.20 | -1.30 | -.10 | 178 | -119 | 59 | 321 | -282 | 39 |

Table 4.2: Daily mean radiative energy budgets for DESERTV case. Units are $Wm^{-2}$ for the fluxes, and $^0C/day$ for the heating rates.

| | Tropospheric heating | | | Net surface flux | | | Net flux TOA | | |
|---|---|---|---|---|---|---|---|---|---|
| TURBIDITY | SW | LW | TOTAL | SW | LW | TOTAL | SW | LW | TOTAL |
| 0 | .6 | -1.22 | -.62 | 230 | -150 | 80 | 311 | -302 | 9 |
| 0.2 | .78 | -1.27 | -.50 | 215 | -140 | 75 | 314 | -298 | 16 |
| 1.0 | 1.33 | -1.45 | -.12 | 165 | -113 | 52 | 325 | -291 | 34 |

Table 4.3: Daily mean radiative energy budgets for OCEANL case. Units are $Wm^{-2}$ for the fluxes, and $^0C/day$ for the heating rates.

| | Tropospheric heating | | | Net surface flux | | | Net flux TOA | | |
|---|---|---|---|---|---|---|---|---|---|
| TURBIDITY | SW | LW | TOTAL | SW | LW | TOTAL | SW | LW | TOTAL |
| 0 | .6 | -1.68 | -1.08 | 347 | -86 | 261 | 428 | -288 | 140 |
| 0.2 | .71 | -1.68 | -0.97 | 326 | -81 | 245 | 419 | -283 | 136 |
| 1.0 | 1.12 | -1.70 | -0.60 | 261 | -64 | 197 | 397 | -271 | 126 |

dust layer are similar to the results of the DESERTL case. The SW heating tends to be less for the OCEANL case, this however is offset by smaller increases in LW cooling. Greatest differences are seen in changes in the net surface flux of the OCEANL case. A dust loading with $\tau_d = 0.2$ reduces the total radiative energy budget of the surface by $16Wm^{-2}$. This decrease results from a decrease in SW downward component and a smaller increase in the LW component. The climatic implications of this energy reduction will be discussed in the next section. The presence of the dust layer over the ocean increases the upward shortwave flux at the TOA which results in a decrease in the earth-atmosphere system heating. This is opposite to the desert cases where an increase in the earth-atmosphere was seen.

## Chapter 5

## RADIATIVE PARAMETERIZATION

A particular problem arises in the study of the interaction of solar and terrestrial radiation with a soil derived aerosol (and aerosols in general). As a dust outbreak goes through its life history, its physical and chemical properties change, thus changing the radiative characteristics of the aerosol layer. In discussing approaches to parameterizing the radiative characteristics of a medium it is useful to follow the nomenclature of Preisendorfer (1960) and define two classes of optical properties,

*An optical property is* **inherent** *if its operational value at a given point in a given medium is invariant under all changes of the radiance distribution at that point. An optical property is* **apparent** *if its operational value at a given point in a given medium is not invariant under all changes of the radiance distribution at that point.*

Examples of inherent optical properties are $\omega_0$, $g$ and $\sigma_{ext}$, while examples of apparent optical properties are the layer reflectance, transmittance and absorptance. A major advantage in parameterizing the inherent optical properties is that the schemes are very portable, while parameterizations of the apparent optical properties are tied to the radiative transfer model used in the parameterizations. Thus the most useful parameterization schemes are based on the modeling of the aerosols inherent optical properties. Where this is not possible one must resort to approximating the apparent optical properties.

### 5.1 Shortwave radiative parameterization

The exact solution of the electromagnetic wave equation for scattering by spheres has been developed for some time (Mie, 1908), while more recent solutions have been obtained for prolate and oblate spheroids (Asano and Yamamoto, 1975), and for infinitely long cylinders (Wait, 1955; Liou, 1972). These theories are both mathematically cumbersome and computationally tedious. A number of approximations to these complex solutions have been developed, particularly for spherical scatterers. (Gans, 1912; van de Hulst 1957; Nussenzvieg and Wiscombe,1980). These approximate theories provide two distinct advantages to the more rigorous formula;

- they are less mathematically cumbersome and thus offer more physical insight into the relationship between an aerosols' microphysical properties and its single scattering properties; and

- they are a parameterization of the inherent optical properties of the aerosol. As such, they are based on the physics of the problem and are thus model independent.

In studying the solar radiative properties of SDA, an appropriate approximation to the Mie theory is the anomalous diffraction theory (ADT) of van de Hulst (1957). This theory is based on the assumption that the size parameter $\chi = 2\pi r \gg 1$ where $r$ is the particle radius and $\lambda$ is the wavelength of the incident radiation. This assumption allows ray tracing through the particle. The second requirement is that the refractive index, $m$, must be very close to 1 (i.e. $m - 1 \ll 1$), implying that the ray suffers only a slight deviation as it crosses the two boundaries of the particle and that the energy reflected at these boundaries is negligible. Under these assumptions, van de Hulst derived analytical expressions for the efficiency factors of extinction and absorption

$$Q_{ext} = 2 - 4e^{(-\rho\tan\beta)}\frac{\cos\beta}{\rho}\left[\sin(\rho-\beta) + -\frac{\cos\beta}{\rho}\cos(\rho-2\beta)\right] + 4\left(\frac{\cos\beta}{\rho}\right)^2\cos 2\beta \quad (116)$$

$$Q_{abs} = 1 + \frac{e^{-4\chi\kappa}}{2\chi\kappa} + \frac{e^{-4\chi\kappa}-1}{8\chi^2\kappa^2} \quad (117)$$

where

$$\rho = \frac{4\pi r(m-1)}{\lambda} \quad (118)$$

$$\tan\beta = \frac{\kappa}{n-1} \quad (119)$$

While ADT is based on the assumptions $m - 1 \ll 1$ and $\chi \gg 1$, it has often been demonstrated that the theory can successfully be applied to cases outside these limits.

This simple theory can be improved upon by including edge effects and refraction of the transmitted ray (Ackerman and Stephens, 1987). For the case of the modified ADT which includes refraction (MADT) the efficiency factors for extinction and absorption are

$$Q_{ext} = 2 - \frac{4m^2}{\rho} e^{-\rho \tan\beta} \cos\rho \left[ \sin(\rho - \beta) - \frac{\cos\beta}{\rho} \cos(\rho - 2\beta) \right] \tag{120}$$

$$+ \frac{4m^2}{\rho} e^{-\rho\sqrt{1-m^{-2}} \tan\beta} \cos\beta \left[ \sqrt{1-m^{-2}} \sin(\rho\sqrt{1-m^{-2}} - \beta) + \frac{\cos\beta}{\rho} \cos(\rho\sqrt{1-m^{-2}} - 2\beta) \right]$$

$$Q_{abs} = 1 + \frac{m^2}{2\chi\kappa} e^{-4\chi\kappa} \left( 1 + \frac{1}{4\chi\kappa} \right) - \frac{m}{2\chi\kappa} e^{-4\chi\kappa\sqrt{1-m^{-2}}} \left( \sqrt{m^2 - 1} + \frac{m}{4\chi\kappa} \right) \tag{121}$$

The accuracy of these approximations has been discussed by Ackerman and Stephens (1987). By expressing the particle size distribution $n(r)$ in some analytical form (e.g. power law, log-normal or gamma distribution) one can derive analytical expressions for the volume extinction and absorption coefficients ($\sigma_{ext}$ and $\sigma_{abs}$ respectively). For a gamma distribution

$$\sigma_{ext} = 2\pi N_0 \left[ (\ell-1)(\ell-2)(ab)^2 - \frac{2(\ell-2)\cos\beta\cos\gamma}{(ab)^{\ell-2} k_1 Z^{(\ell-1)/2}} - \frac{2\cos^2\beta\cos\delta}{(ab)^{\ell-2} k_1^2 Z^{(\ell-1)/2}} + \frac{2}{k_1^2}\cos^2\beta\cos 2\beta \right]$$

$$+ 2\pi N \left( \frac{\lambda}{2\pi} \right)^{(\ell-2/3)} \Gamma\left[ \ell - \frac{2}{3} \right] \tag{122}$$

$$\sigma_{abs} = \pi N_0 \left[ (\ell-1)(\ell-2)(ab)^2 + \frac{m^2}{k} \Lambda^{1-\ell} \left( (\ell-2)ab + \frac{\Lambda}{2k} \right) \right]$$

$$+ \frac{m}{k} \gamma^{1-\ell} \left( (2k)^{-1}\gamma + m\sqrt{m^2-1}(\ell-2)ab \right) \tag{123}$$

where

$$k_1 = \frac{4\pi(n-1)}{\lambda} \tag{125}$$

$$Z = (k_1 \tan\beta + (ab)^{-1})^2 + k_1^2 \tag{126}$$

$$\cos\gamma = \cos\beta\sin\phi - \sin\beta\cos\phi \tag{127}$$

$$\cos\delta = \cos 2\beta\sin\psi - \sin 2\beta\cos\psi \tag{128}$$

$$\phi = \frac{1-b}{b}\tan^{-1}\left(\frac{k_1}{k_1\tan\beta + (ab)^{-1}}\right) \tag{129}$$

$$\psi = \frac{1-2b}{b}\tan^{-1}\left(\frac{k_1}{k_1\tan\beta + (ab)^{-1}}\right) \tag{130}$$

$$N = \frac{N_0(ab)^{(2b-1)/b}}{\Gamma\left[\frac{1-2b}{b}\right]} \tag{131}$$

$$\ell = b^{-1} \tag{132}$$

$$\Lambda = 2kab + 1 \tag{133}$$

$$\gamma = 2k\sqrt{1-m^{-2}}ab + 1 \tag{134}$$

$$k = \frac{4\pi\kappa}{\lambda} \tag{135}$$

Figure 43 depicts the errors associated with calculating the single scatter albedo using ADT or MADT as a function of $|m|$ and $\chi_{eff}$ for a $\beta$ of $0.2^0$ and $10^0$. For crustal type aerosols at solar wavelengths, $\omega_0$ can generally be estimated to within 5% using MADT. A specific application to soil derived aerosols is shown in figure 44 where estimates of $\omega_0$ are compared with Mie calculations as a function of wavelength. MADT estimates $\omega_0$ to within 3% and accurately captures the trends in $\omega_0$ as a function of wavelength for the two aerosols.

In the case of dust, the size parameters are large enough so that we may consider $Q_{ext} \approx 2$. In this limiting case, we see from equation (116), that $\omega_0$ should primarily be

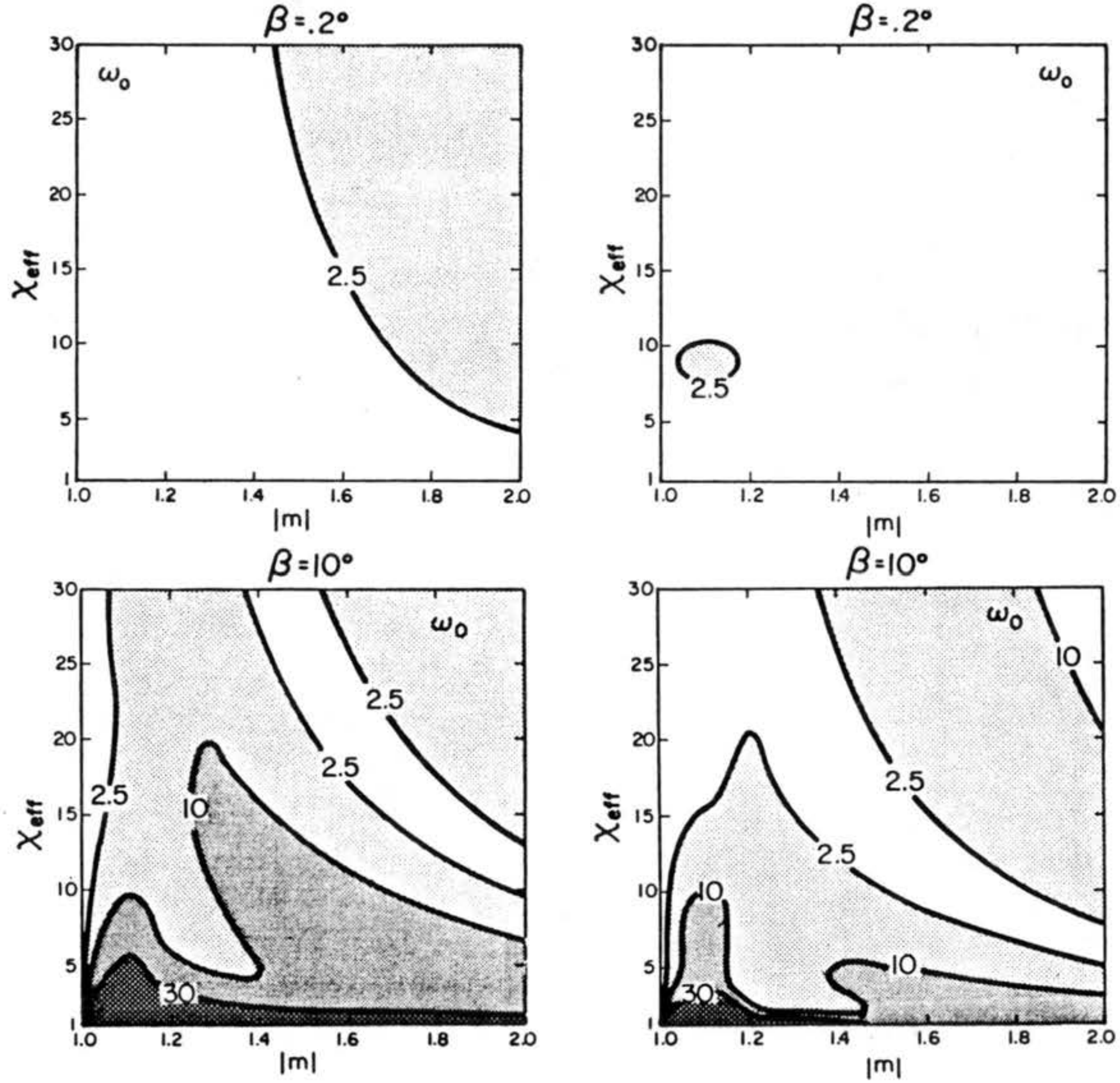


Figure 5.1 Errors associated with calculating the single scattering albedo from anomalous diffraction theory (left) and the modified theory as a function of $|m|$ and $\chi_{eff}$ for a $\beta$ of $0.2^0$ and $10^0$.

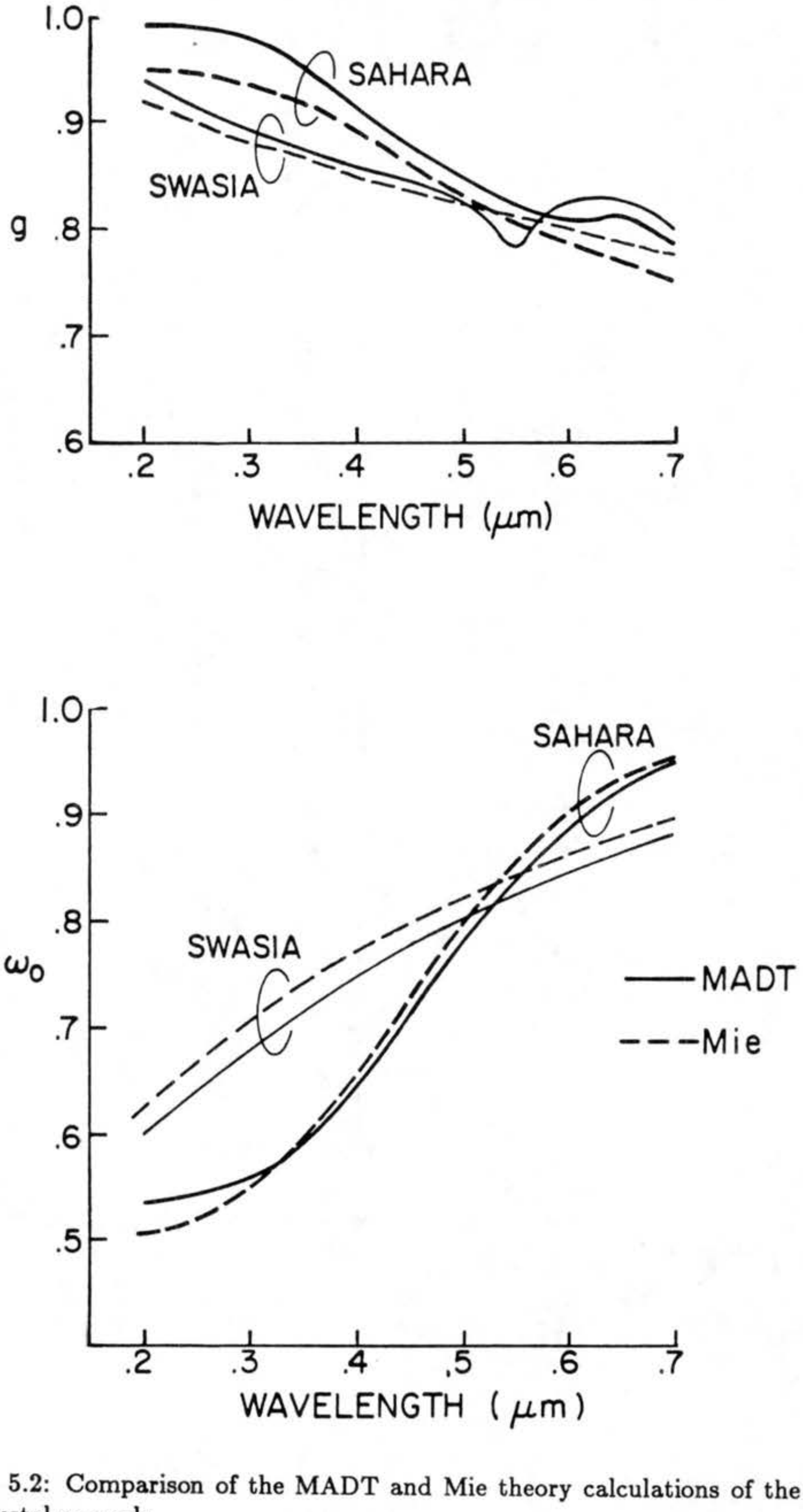


Figure 5.2: Comparison of the MADT and Mie theory calculations of the $\omega_0$ and $g$ for two crustal aerosols.

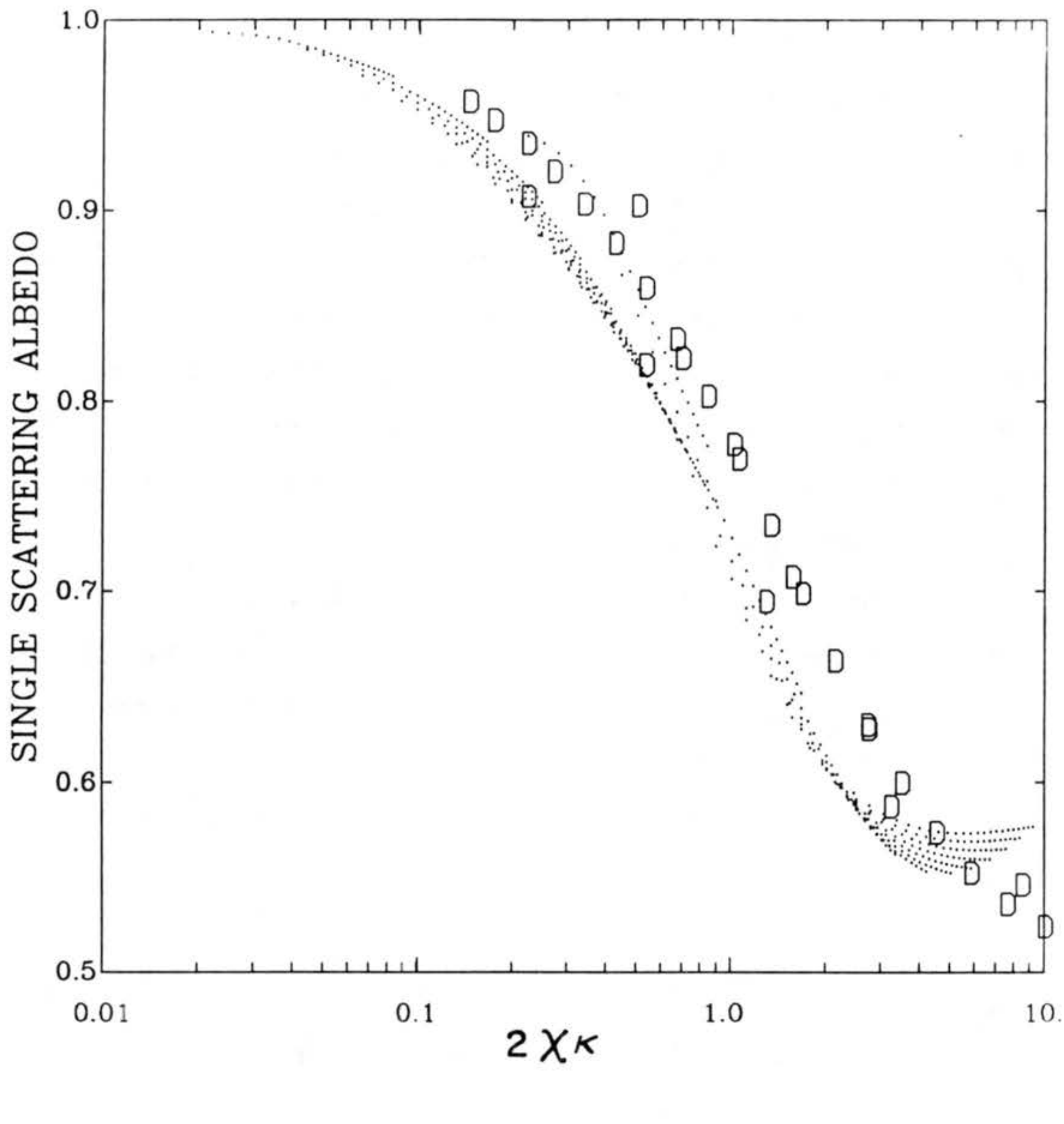


Figure 5.3: Single scattering albedo as a function of $4\chi_{eff}\kappa$. See text for details.

a function of the parameter $4\chi_{eff}\kappa$. An example of this relationship is shown in figure 45. The points represent Mie calculations with $\beta = 0.2^0$ and $10^0$, $1.1 \leq\mid m \mid\geq 2.0$ and $10 \leq \chi \geq 60$, . The D's represent Mie calculations for the Saharan and SW Asian aerosol over the wavelength region $.2 - .8\mu m$ and assuming a gamma size distribution with an effective radius of $2.06\mu m$ and $5\mu m$. Figure 45 presents a useful table look-up scheme for $\omega_0$ for atmospheric aerosols and provides a physical insight into the relationship between $\omega_0$ and the microphysical properties of the aerosol. As expected if $\chi_{eff}$ increases or $\kappa$ increases then $\omega_0$ decreases, thus the absorption of the layer increases. Large values of $4\chi\kappa$ are determined by large particles in which case $\omega_0 \rightarrow 0.5$. The small values of the scaling parameter are determined from small values of $\kappa$, thus $\omega_0 \rightarrow 1$. Thus there are three regimes, two where $\omega_0$ changes only slightly as $4\chi\kappa$ changes ($4\chi\kappa < 0.05$ and $4\chi\kappa > 3$) and one regime where $\omega_0$ changes rapidly with changes in $4\chi\kappa$. These three regimes are classified as weakly absorbing, moderately absorbing and strongly absorbing regimes. This diagram demonstrates that the relationship between a cloud (or aerosol) absorption, or reflectivity, and $r_{eff}$ changes with the different absorption regimes. Finally figure 45 demonstrates that the important parameter which defines the $\omega_0$ for atmospheric aerosols in the shortwave spectrum is the product of $r_{eff}$ (or size distribution) and $\kappa$. Therefore it may be useful to develop measurement techniques which retrieve the product $r_{eff}\kappa$ as opposed to estimating them separately.

The anomalous diffraction theory can also be employed to represent the intensity functions. Following van de Hulst (1957)

$$i_1 = i_2 = \chi^4 \mid A(\rho^*, z) \mid^2 \tag{136}$$

where $z = \chi\vartheta$ and $\vartheta$ is the scattering angle measured from the forward direction. Also

$$A(\rho^*, z) = \int_0^{\frac{\pi}{2}} (1 - \exp[-\rho(i + \tan\beta)\sin\tau]) J_0(z\cos\tau)\cos\tau\sin\tau d\tau \tag{137}$$

where $J_0$ is the Bessel function of order zero. The phase function $P(\vartheta)$ is written

$$P(\vartheta) = \frac{\frac{1}{2}[i_1(\vartheta) + i_2(\vartheta)]}{Q_{sca}} \left(\frac{\lambda}{2\pi}\right)^2 \tag{138}$$

Thus the asymmetry parameter can be approximated using (137) and (138) as

$$g = \frac{\int_0^\pi P(\vartheta)\cos\vartheta\sin\vartheta d\vartheta}{\int_0^\pi P(\vartheta)\sin\vartheta d\vartheta} \tag{139}$$

$$g = \frac{\int_0^\pi \mid A(\rho^*, z)\mid^2 \cos\vartheta\sin\vartheta d\vartheta}{\int_0^\pi \mid A(\rho^*, z)\mid^2 \sin\vartheta d\vartheta} \tag{140}$$

A comparison between the phase function calculated with Mie theory and anomalous diffraction theory is shown in figure 46, for a gamma size distribution with an effective size parameter of 20 and an effective variance of 0.2. As seen in the figure, the approximate theory is much flatter in the backward direction. However, it is a good approximation in the forward direction where the largest contributions to the asymmetry parameter occur. This is demonstrated in the inset where the cumulative contribution to $g$ is shown as a function of $\vartheta$ for the Mie calculation. Most of the contribution to $g$ occurs in the forward direction with $\vartheta < 60$, suggesting that the ADT may provide a good approximation to the asymmetry parameter.

Figure 47 depicts the errors in the ADT approximation to $g$ for $\beta = 0.2^0$. For size parameters and indices of refraction associated with crustal aerosols, ADT is generally within 5% of the Mie calculations. Figure 45 compares ADT approach to Mie theory for two different soil derived aerosols. The ADT approximation captures the dependency of $g$ on wavelength to within 5%, largest errors occur in the $0.6 - 0.7\mu m$ regime. The need to numerically integrate equation (140) over scattering angle makes the ADT less attractive and it would be advantage to find a scaling parameter as with $\omega_0$. Such a scaling parameter is not straight forward as $g$ is a strong function of the size parameter and both the imaginary and real parts of the index of refraction. An advantage of crustal aerosols is that the real part of the index of refraction is nearly constant ($n = 1.5 \leftrightarrow 1.6$). Examination of equation (137) suggests the scaling parameter $4\chi\kappa$. Figure 48 depicts $g$ as a function of $4\chi\kappa$ for different crustal aerosols as calculated from Mie theory. For non-absorbing sphere with $n = 1.5$, as $\chi \rightarrow \infty$, $g \rightarrow 0.82$ (van de Hulst, 1957). The values shown in figure 48 approach a value of 0.95 due to the absorption of the refracted rays. While the relationship is not consistent for different values of $n$, it is appropriate for the indices of refraction and size distributions encountered with dust.

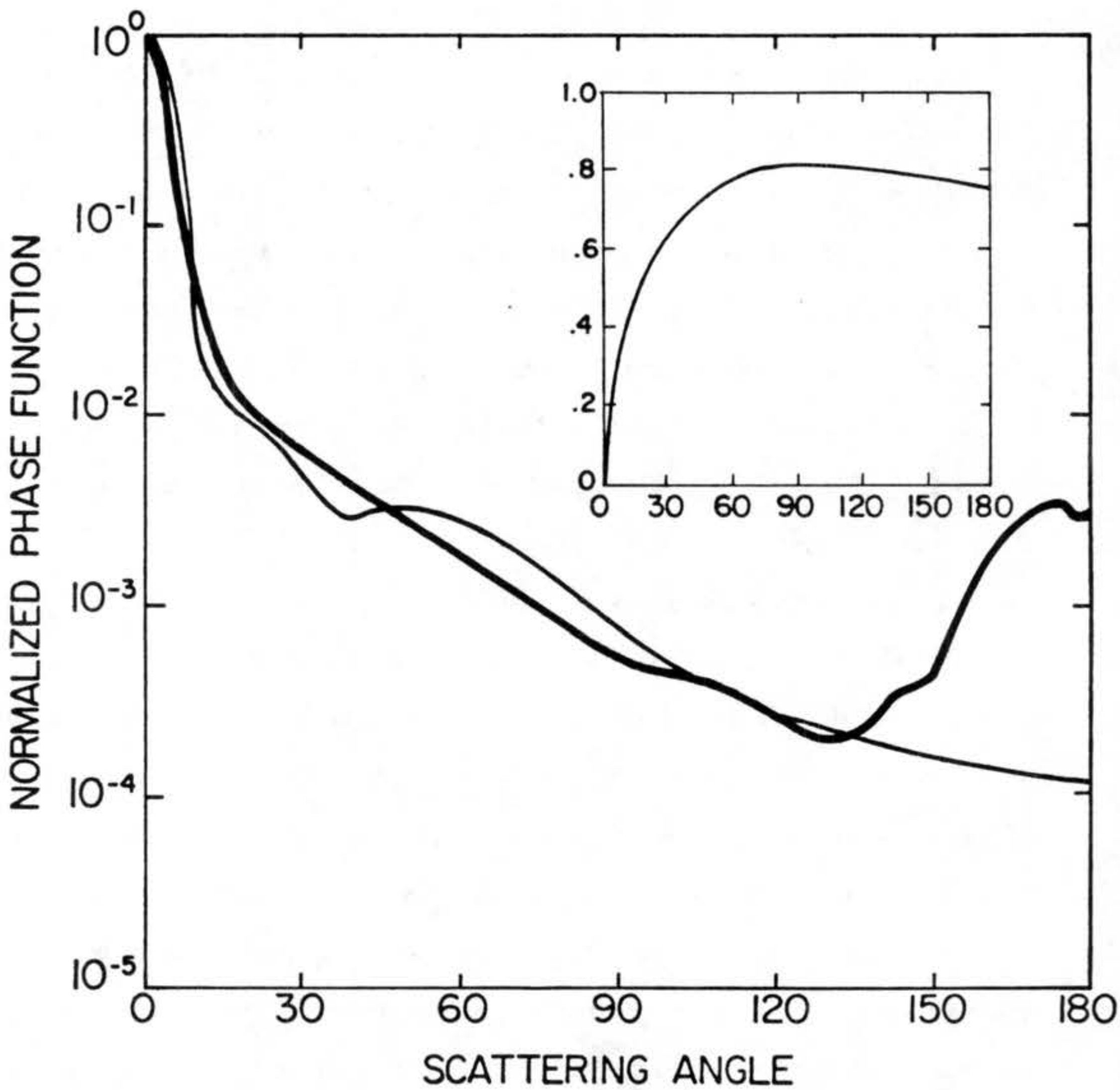


Figure 5.4: Comparison between the phase function calculated with Mie theory (thick line) and MADT (dashed). The inset depicts the cumulative contribution to $g$ as a function of scattering angle for the Mie calculation.

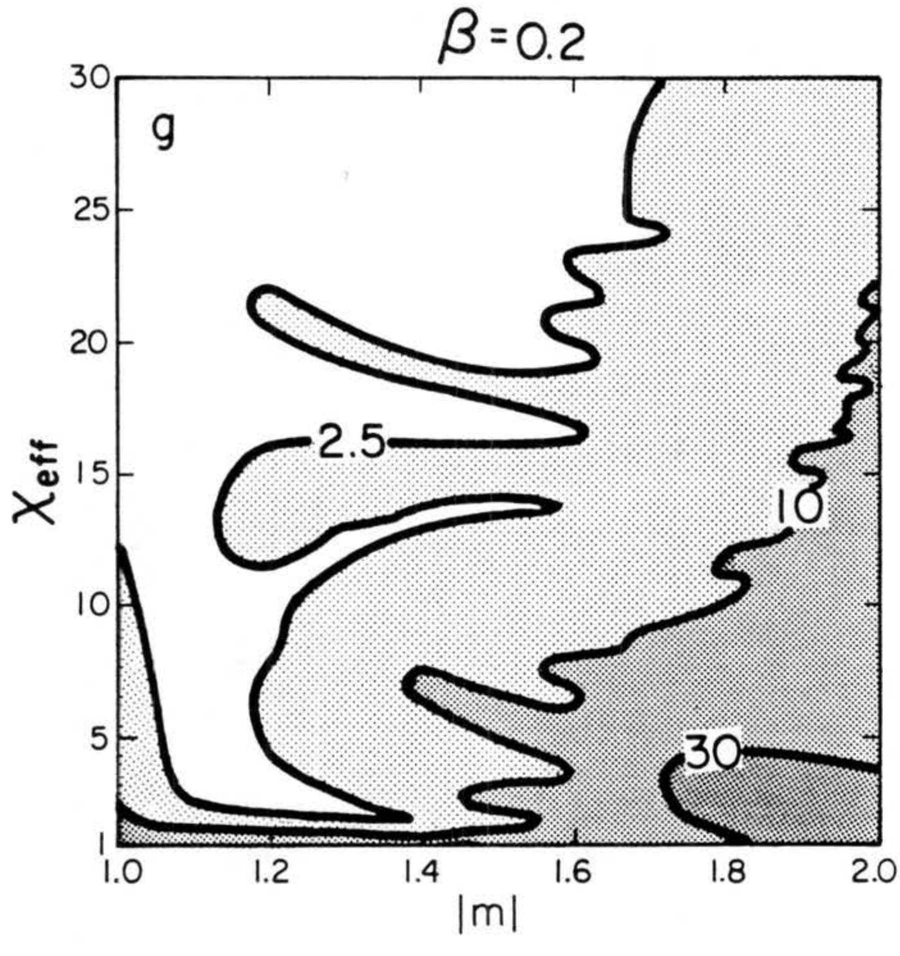


Figure 5.5: Errors in the MADT approximation to $g$ for $\beta = 0.2^0$ as a function of $|m|$ and effective size parameter.

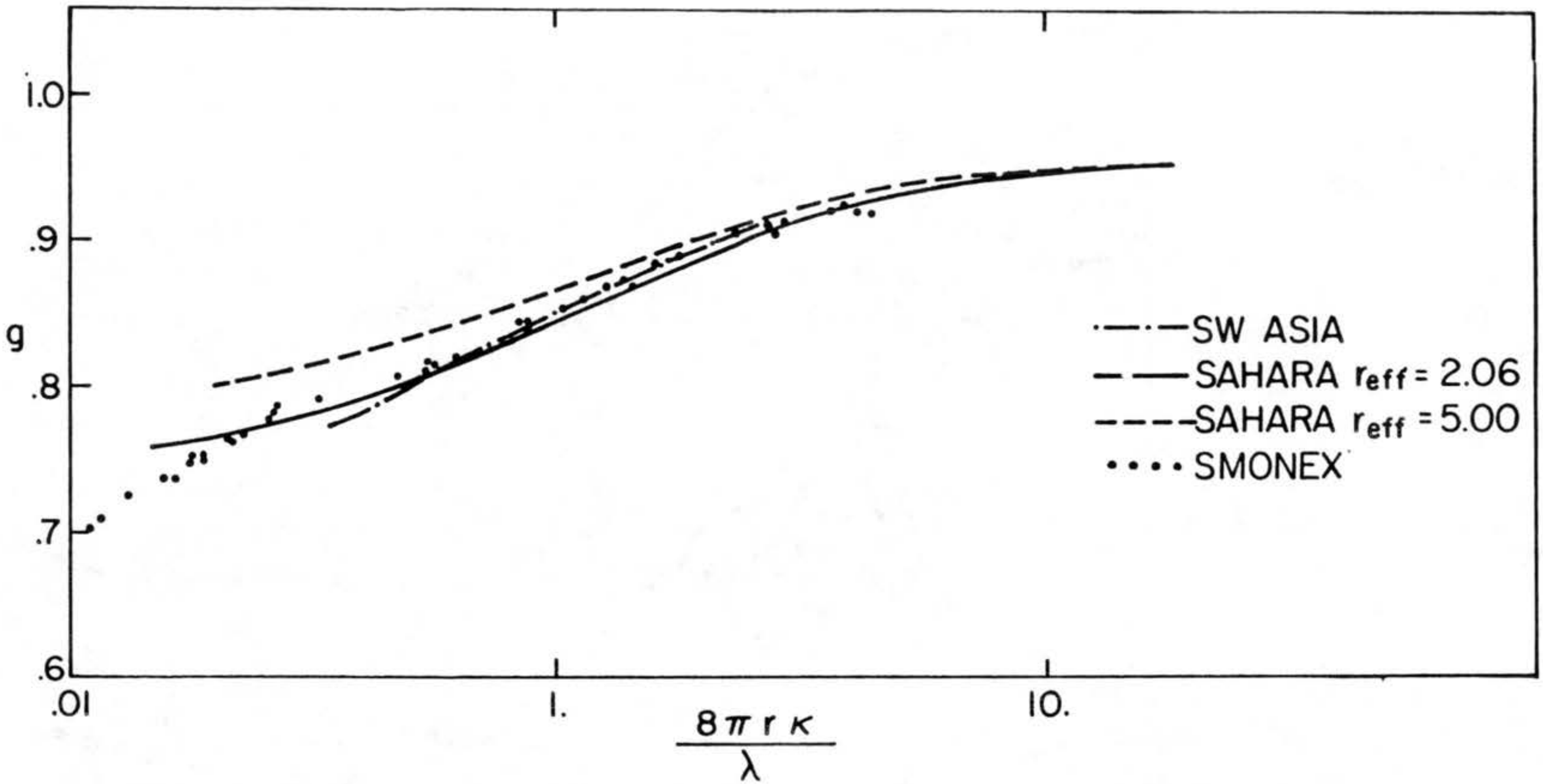


Figure 5.6 Asymmetry parameter as a function of $4\chi\kappa$ for different crustal aerosols as calculated from Mie theory.

## 5.2 Longwave radiative parameterization

As discussed previously the major effect of dust on the LW regime is in the spectral region of $8-13\mu m$. Therefore the parameterization focuses on this spectral interval, where the size parameter $.8 < \chi < 5$ and $\tan\beta$ ranges from about $10^0$ to $15^0$. No approximate theories have been developed for this type of condition. Attempts to derive a scaling parameter based on the small particle approximation were unsuccessful. Parameterization schemes therefore focused on modeling the apparent optical properties of the dust layer. A common parameterization employed for clouds in the LW is the effective emissivity (Cox, 1976). The effective emissivity follows directly from the LW two-stream model, equations (104)-(110). Assuming the reflectance of the dust layer to be zero (e.g. 1=0 in eq. (110)), then

$$\varepsilon = 1 - t = 1 - \exp(-K\tau/\mu). \tag{141}$$

This is the mathematical formulation often applied to parameterizing the LW radiative properties of water clouds (Cox, 1971; Stephens,1978 and Chýlek and Ramaswamy, 1982), and can be employed given appropriate values of the single scattering albedo and the asymmetry parameter. Alternatively, the effective emissivity can be written in terms of equation (104). That is

$$\varepsilon^* \downarrow = \frac{F\downarrow(\tau_b) - F\downarrow(\tau_t) + B(\tau_t) - B(\tau_b)}{B(\tau_t) - F\downarrow(\tau_t) + s(B(\tau_t) - B(\tau_b))} \tag{142}$$

and

$$\varepsilon^* \uparrow = \frac{F\uparrow(\tau_t) - F\uparrow(\tau_b) + B(\tau_b) - B(\tau_t)}{B(\tau_b) - F\uparrow(\tau_b) + s(B(\tau_b) - B(\tau_t))} \tag{142}$$

where

$$s = \frac{\bar{\mu}}{(1 - \omega_0 + 2\omega_0\beta)\tau}. \tag{143}$$

The emissivity defined by equations (142) and (143) allow for a non-isothermal structure of the layer. For the case of an isothermal layer, the effective emissivities take the more familiar form

$$\varepsilon^* \downarrow = \frac{F \downarrow (\tau_b) - F \downarrow (\tau_t)}{B(\tau_t) - F \downarrow (\tau_t)} \tag{145}$$

and

$$\varepsilon^* \uparrow = \frac{F \uparrow (\tau_t) - F \uparrow (\tau_b)}{B(\tau_b) - F \uparrow (\tau_b)} \tag{146}$$

Given a vertical distribution of temperature and aerosol loading, and the boundary fluxes, layer fluxes can be computed from equation (141) in conjunction with equation (104). However, most climate models employ effective emittance in a broadband flux emissivity model (Stephens, 1984), which requires the use of equations (142) and (143), or equations (145) and (146).

Figure 49 depicts the relationship between $\varepsilon^* \downarrow$ and turbidity for the DESERTL case with no water vapor absorption. Also shown is a least square fit to the data of the form $\varepsilon^* \downarrow = 1 - \exp(-a_o \tau)$. A similar approach to retrieving $\varepsilon^* \uparrow$ fails due to the equivalence of the surface temperature and the temperature of the lowest atmospheric layer ($B(\tau_b) = F \uparrow (\tau_b)$), which can cause unrealistic emissivities. However, one might expect $\varepsilon^* \uparrow \approx \varepsilon^* \downarrow$. Observation (Cox, 1971) and calculations (Stephens, 1979) indicate that for water clouds $\varepsilon^* \downarrow > \varepsilon^* \uparrow$. Rodgers (1967) discussed the need for two different effective emissivities for gases.

There are two physical explanations for this inequality, both of which depend on the incident fluxes at the layer boundaries. The first concerns the angular distribution of the irradiance, the diffusivity factor. For collimated radiance $D = 1$, while for an isotropic field $D = 2$. Thus the value of $D$ can be different for the upward and downward fluxes. In the present two stream formulation it is assumed that $D$ is independent of direction. Based on doubling calculations this approximation is reasonable for dust.

The second factor which may contribute to $\varepsilon^* \downarrow > \varepsilon^* \uparrow$ is related to differences in the spectral distribution of the energy at the layer boundaries (Cox, 1976). The upward flux at the layer base is related to the surface temperature via the spectrally integrated Planck function and surface emissivity. The downward irradiance originates from a $O_3$ contribution near $9.6\mu m$ and is much smaller. The effect an aerosol layer has on the

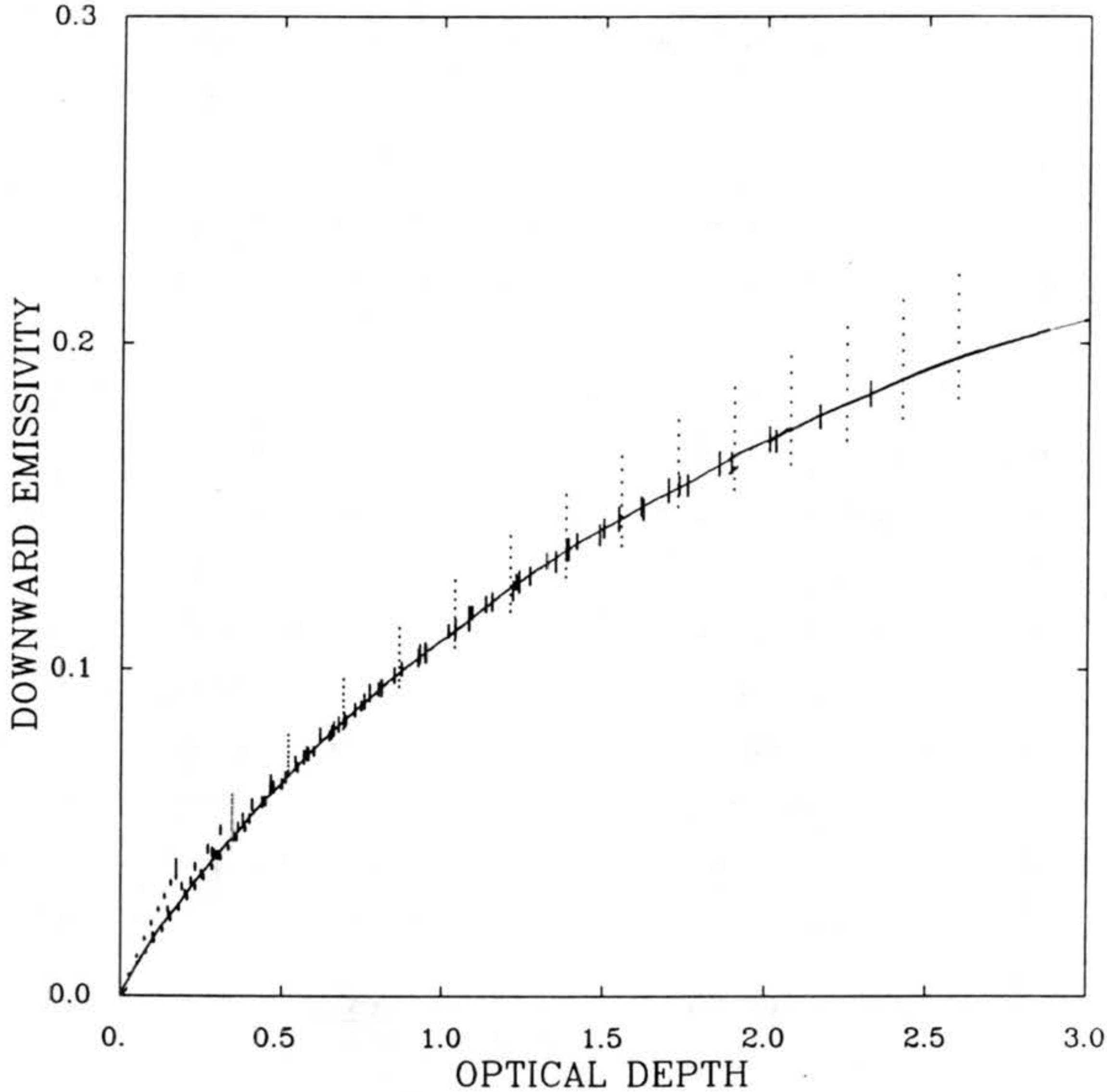


Figure 5.7: $\varepsilon^* \downarrow$ as a function of turbidity for the DESERTL case with no water vapor absorption. Also shown is a least square fit to the data.

radiative fluxes is a function of its emissivity and the layer temperature. In the case of the upward flux the warm surface temperature is replaced by a warm dust layer, only slightly modifying the energy. However, the downward incident flux at the top of the dust layer is nearly zero and the presence of the dust layer can cause a large change in the downward flux through the Planck function. In the case of a non-isothermal layer, the effective emissivities will also be a function of the temperature and aerosol vertical distribution.

Figure 50 compares the upward fluxes calculated from equation (142) with $\varepsilon^* \downarrow$ replacing $\varepsilon^* \uparrow$. Figure 50 indicates that differences in the upward and downward emissivities are small. The incident flux at the top of the dust layer is small, and for practical purposes we shall considerate to be zero, thus the downward effective emissivity is independent of any boundary fluxes. As the surface temperature and the lowest atmospheric layer temperature are equivalent, the upward effective emissivity is also independent of the boundary fluxes. Thus $\varepsilon^* \uparrow$ and $\varepsilon^* \downarrow$ should be approximately equal.

As discussed at the beginning of the chapter, the apparent optical properties of the layer are dependent on the radiance distribution at the layer boundaries and within the layer. We therefore expect the absorption coefficients to change for the DESERTV and DESERTH case. These changes are depicted in Table 13. As expected there is little difference between the DESERTL and DESERTH cases. The smaller value of $a_o$ for the DESERTV case illustrates the importance of the vertical distribution of the dust.

Table 5.1: The absorption coefficient for effective emissivity for the three desert cases.

| DUST LOADING | $a_o$ |
|---|---|
| DESERTL | -.093 |
| DESERTH | -.094 |
| DESERTV | -.073 |

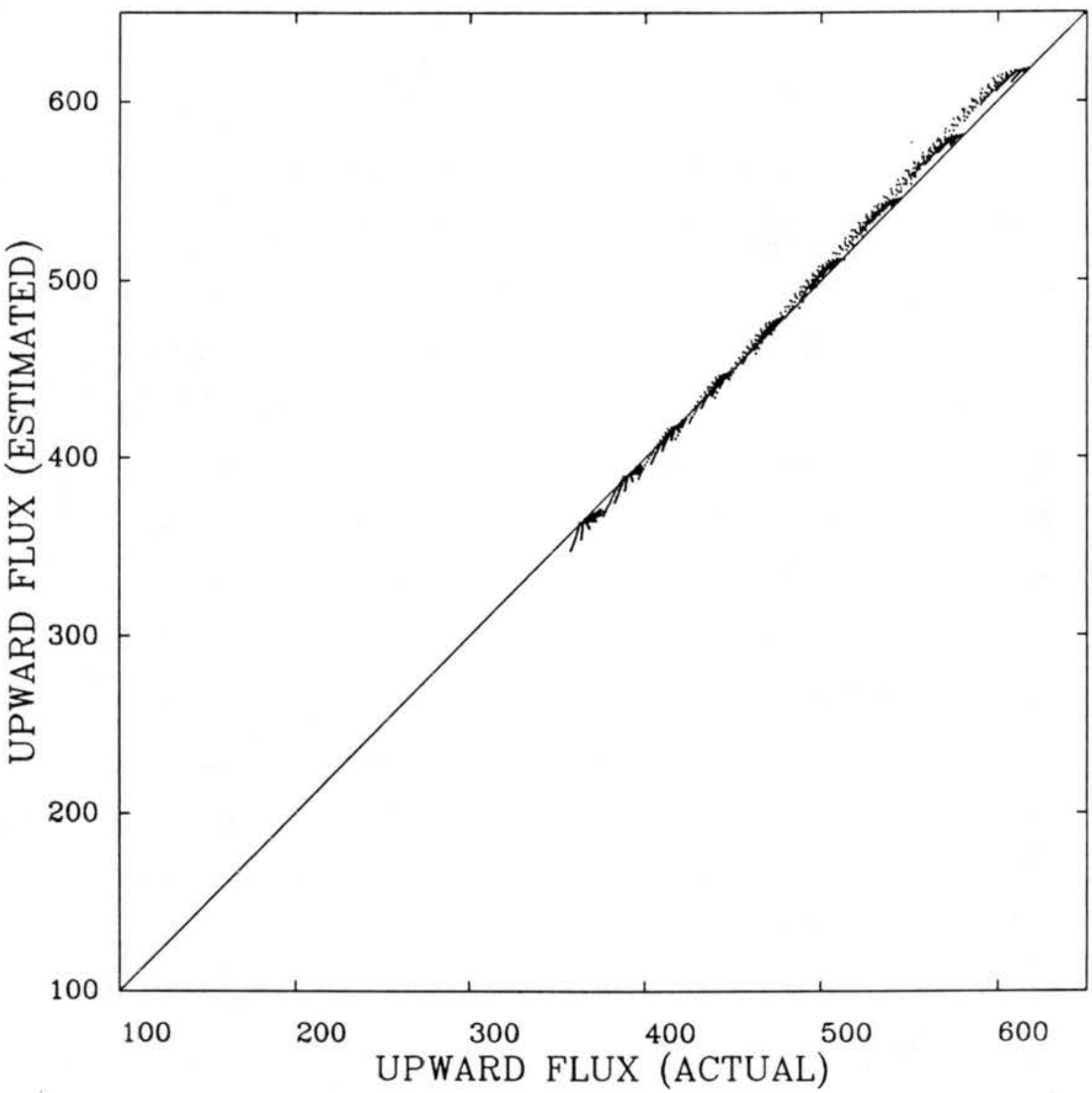


Figure 5.8: A comparison of the upward fluxes calculated from the emissivity model with $\varepsilon^*\downarrow$ replacing $\varepsilon^*\uparrow$.

## Chapter 6

## CLIMATIC IMPLICATIONS

Chapter 4 demonstrated that the presence of a dust layer changes the solar and terrestrial radiative fields within the atmosphere and at its boundaries. The primary effect of the dust layer was to modify the fluxes in the visible (0.3-0.7 $\mu$m) and in the IR window (8-13 $\mu$m) spectral regions. As a result, soil derived aerosols may have a large impact on global and regional scale climates. The radiative perturbations discussed in Chapter 4 are instantaneous and represent the initial thermodynamic response of the atmosphere to the presence of the dust layer. The relaxation of this fixed state constraint requires the use of climate models. In this chapter the parameterization schemes presented on chapter 5 are incorporated into a radiative-convective equilibrium model to address the importance of the dust layer microphysical structure on a simple climate system.

One can envision several scenarios in which a dust layer may impact the climate of the Earth. For example, the last glacial period ended with large deposits of loess in central Europe, providing a potential source of dust. The wide spread geographical distribution of dust during this period is suggested by glacial core samples in Greenland (Junge, 1979). If the radiative properties of a dust laden atmosphere result in a warming of the atmosphere, then the ending of the ice age may have been enhanced by the presence of dust. Dust may also play a role in desertification processes. It has been proposed that denuding a surface of vegetation results in an increased surface albedo and a net radiative energy loss of the earth-atmosphere system. To compensate for this energy loss, the atmosphere sinks and adiabatically warms, suppressing convection and further restricting vegetation growth. Initial studies of this feedback effect of surface albedo on desert formation by Charney (1975) tended to confirm this hypothesis. Subsequent studies have included surface moisture with similar results. None of the desertification studies have considered the effects of dust, which can be produced as the vegetative cover is removed. The presence of dust may offset or enhance this feedback interaction depending if its presence results in a net radiative cooling or warming.

Increases in atmospheric dust loading are likely to be regional, thereby limiting the usefulness of the radiative-convective model which is global in nature. Nevertheless, the radiative-convective model can be a useful tool in studying the sensitivity of the surface temperature and atmospheric temperature profile to a particular aerosol. While source regions may become more active in producing dust, it is unlikely that the dust will encompass the entire globe. Thus, the results in this section should be considered as qualitative rather than quantitative.

Reck (1974) and Wang and Domoto (1974) employed a radiative-convective equilibrium model to find a critical surface albedo in which an inclusion of an aerosol resulted in a surface cooling (warming) when the surface albedo was smaller (larger) than the critical value. Reck (1975) studied the importance of the vertical distribution of the aerosol on the equilibrium state. In this chapter the radiative-convective equilibrium model is used to investigate the importance of the inherent optical properties of the aerosol in determining the equilibrium state of the model. The inherent optical properties are defined using the scaling parameter $4\chi\kappa$, and can represent different dust layers or a single dust layer whose physical and chemical properties change due to sedimentation.

The radiative-convective equilibrium model is discussed in section 6.1. The results of model calculations are presented primarily in terms of changes in the surface equilibrium temperature, and are given in section 6.2.

## 6.1 Radiative-convective equilibrium model

Given the vertical distribution of radiatively active gases and aerosols as well as the boundary conditions at the top and bottom of the atmosphere, a radiative-convective equilibrium model (RCM) computes the vertical distribution of temperature under steady state conditions. While RCMs represent simple climate systems, they can be used to study the sensitivity of the surface and the atmospheric temperature profile to model perturbations. RCMs have been widely used in this type of study (e.g. the effects of changes in atmospheric trace gases or clouds on climate). A major disadvantage of RCMs is that no information about regional temperature changes is available.

The RCM is formulated from the thermodynamic energy equation

$$\frac{\partial \rho c_p T}{\partial t} + \nabla \rho c_p \vec{V} T + \frac{\partial \rho c_p w T}{\partial t} + \rho g w = Q \tag{146}$$

where

- $\rho$ atmospheric density
- $T$ temperature
- $Q$ net radiative heating $(Q_{lw} + Q_{sw})$
- $c_p$ specific heat at constant pressure
- $\vec{V}$ horizontal velocity vector
- $w$ vertical velocity

Averaging equation (146) with respect to latitude and longitude yields

$$\frac{\partial \langle \rho c_p T \rangle}{\partial t} = -\frac{d}{dz}(F_{lw} + F_{sw} + F_c) \tag{147}$$

where $F_c = \langle SH c_p T w \rangle$ is a latitudinal mean convective flux due to sensible heat processes. To satisfy conservation of mass, $\langle \rho g w \rangle = 0$. The above model applies to the annually averaged conditions. With the boundary conditions

$$F_{lw}(top) + F_{sw}(top) = 0 \tag{148}$$

$$F_c(top) = 0 \tag{149}$$

the steady state solution yields

$$F_{lw}(z) + F_{sw}(z) + F_c(z) = 0 \tag{150}$$

Thus the RCM assumes that on an annually and globally averaged basis, the vertical structure of the planet is determined solely by radiative and convective processes. The equilibrium temperature profile is solved using the time-stepping method of Manabe and Strickler (1964).

The radiative transfer model used to calculate the shortwave fluxes follows that of Lacis and Hansen (1974) for the clear sky conditions. As shown in Chapter 4 the primary effect on the shortwave heating by the dust layer is in the visible spectral region (0.3-0.7 $\mu$m). For the purposes of the present study it is therefore assumed that the shortwave absorption by the aerosol only occurs in the visible. The single scattering albedo and asymmetry parameter are assigned based on figures (45) and (48) respectively. The reflectance and transmittance of the dust layer are calculated based on the two-stream model of Coakley and Ch/'ylek (1975).

The longwave fluxes are calculated from

$$F \uparrow = B(\tau_{sfc})t_{sfc} + \int B(\tau_z)dt_z \tag{151}$$

$$F \downarrow = \int B(\tau_z)dt_z \tag{152}$$

where $B(T_z)$ is the blackbody radiation at temperature $T$ at height $z$. $t_z$ is the atmospheric transmittance between the height $z$ and the top, or bottom, of the atmosphere. The water vapor and $CO_2$ transmittances are modeled after the greybody emissivity approach of Rodgers (1967). The water vapor-$CO_2$ overlap region is treated in the manner of Rodgers and Walshaw (1966). The continuum absorption in the 8-13 $\mu$m region is parameterized following Cox (1974). The 9.6 $\mu$m $O_3$ band transmission is modeled after Stephens and Webster (1979). The parameterization of Chapter 5 is used to describe the LW radiative properties of the dust layer. The overlap between the dust layer and water vapor follows that of Griffith et al. (1980).

For the sensitivity studies discussed below, a constant $CO_2$ mixing ratio of 0.5 $g/kg$ is assumed along with the standard ozone profile of McClatchy et al. (1972). A surface albedo of 0.102 is assumed. A solar constant of 1368 $Wm^{-2}$ is used along with a 12 hour daylight period and a mean solar zenith angle of $0.5^0$. The model links the water vapor distribution to the temperature profile by assuming constant relative humidity. Following Manabe and Wetherald (1967) the water vapor distribution is assigned according to the formula

$$RH = 0.77 \left[ \frac{\left( \frac{p}{p_{sfc}} - 0.02 \right)}{(1 - 0.02)} \right] \tag{153}$$

The convective fluxes are parameterized using the convective adjustment scheme of Manabe and Wetherald (1967). The critical lapse rate for convective adjustment is the moist adiabatic lapse rate, which is approximated as (Iribarne and Godson, 1981)

$$\Gamma_w \approx 9.8 \frac{1 + 5.42 * 10^3 e_w/TP}{1 + 8.39 * 10^6/T^2 P} \frac{{}^0K}{Km} \tag{154}$$

## 6.2 Model results

In this section, the RCM presented above is used to asses the impact of a dust layer on the equilibrium surface temperature. The surface temperature of the no aerosol control case is $292.4^0K$. For the sensitivity studies a dust layer occupies the 2-3 km layer with an optical depth of 0.2 or 1.0. The effect of the dust layer on the downward LW and SW fluxes at the surface is shown in figure 51 as a function of the scaling parameter $4\chi\kappa$ for an optical depth of 0.2. As expected, the dust layer reduces the SW flux at the surface, with maximum reduction occurring for the strongly absorbing aerosol (large $4\chi\kappa$). The LW downward flux at the surface increases in the presence of the dust layer. This increase is due to the direct emission of the aerosol itself and the feedback of the increased water vapor amount which results from a warmer troposphere.

For the case of small optical depths and a weakly, or strongly, absorbing aerosol there is little sensitivity of the surface fluxes to small changes in $4\chi\kappa$. For scaling parameters between 0.1 and 2, a small change in the dust size distribution or chemical composition can lead to a large change in the equilibrium state. This is demonstrated in figure 52 which depicts the changes in the surface temperature as a function of the scaling parameter. A surface warming of less that $.5^0K$ occurs for a scaling parameter less than about 0.2, while

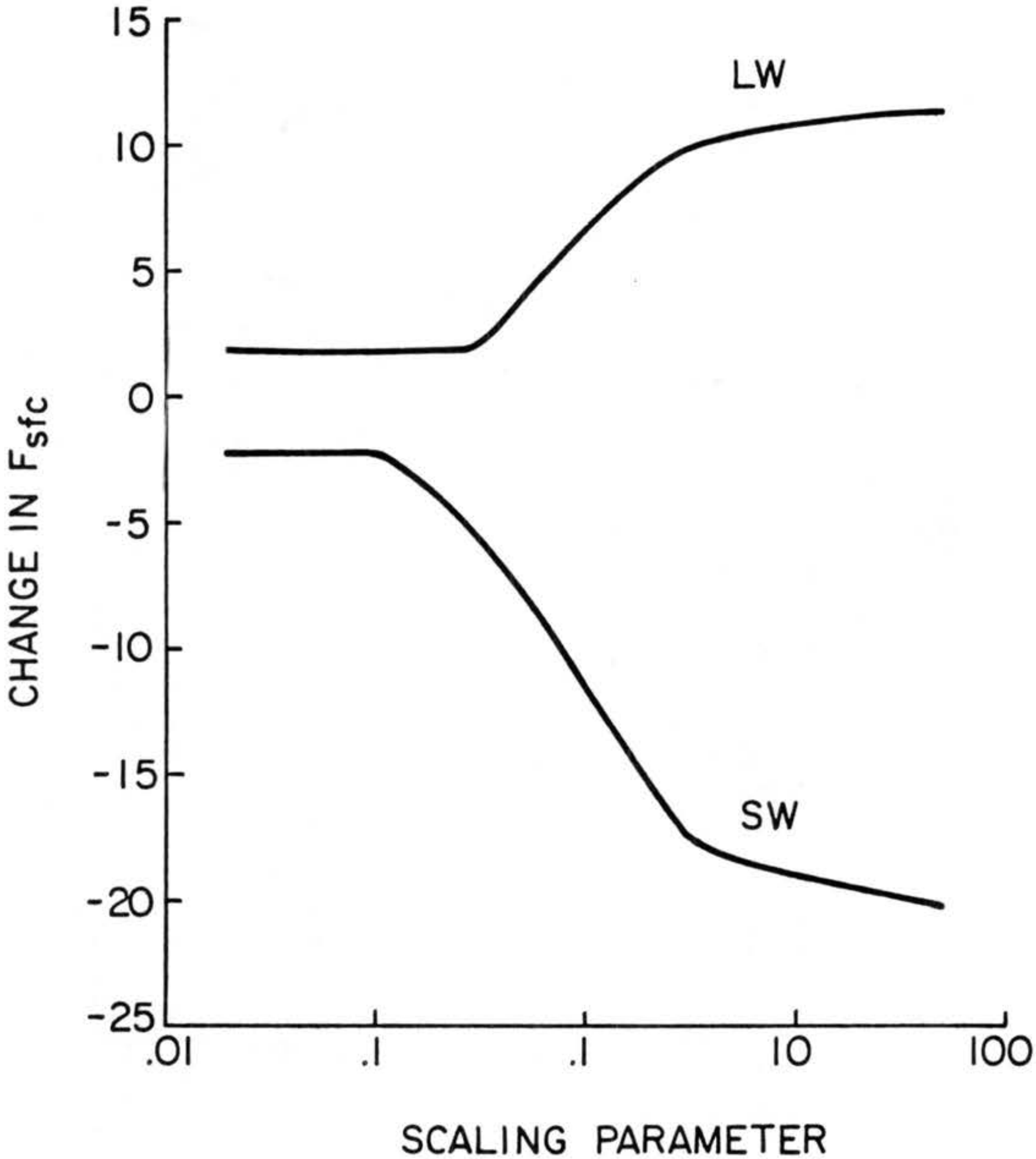


Figure 6.1: Changes in the steady state downward LW and SW fluxes at the surface as a function of $4\chi\kappa$ for an optical depth of 0.2.

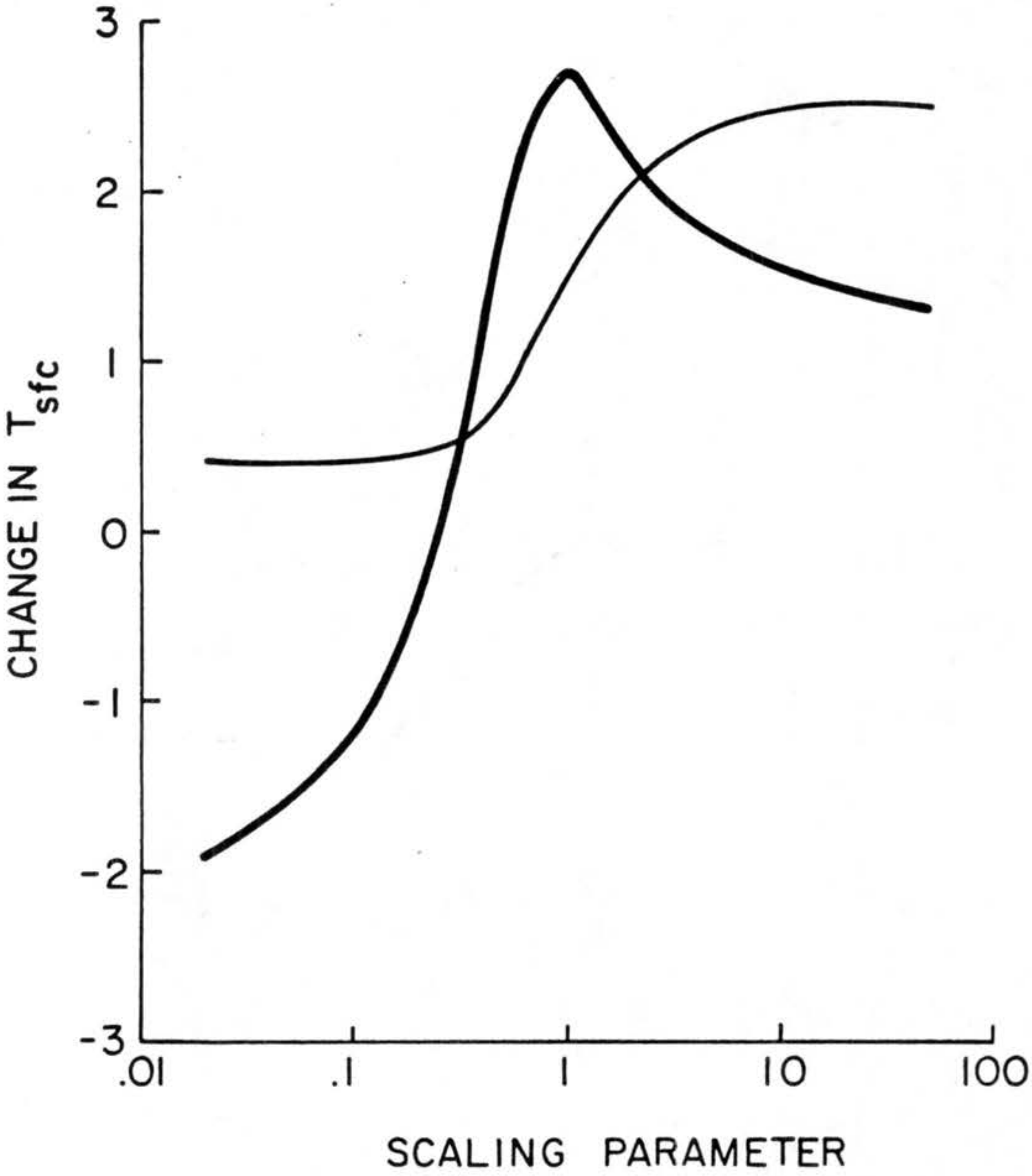


Figure 6.2: Changes in the equilibrium surface temperature as a function of $4\chi\kappa$ for optical depths of 0.2 (thin line) and 1 (thick line).

a surface warming greater than $2.5^0K$ occurs for large values of $4\chi\kappa$. The warming occurs even though there is a decrease in the surface radiation budget. The surface temperature is calculated by first assuming radiative equilibrium at the surface and is then modified by the convective adjustment scheme. With a warmer lower troposphere there is less convective adjustment, and a warmer surface results. Thus the dust layer reduces the convection needed to maintain a stable atmosphere.

The changes in surface temperature due to the presence of an aerosol is also a function of the aerosol optical depth. This is shown in figure 52 which shows the changes in the equilibrium surface temperature as a function of $4\chi\kappa$ for a dust optical depth of 1. Unlike the smaller optical depth of 0.2, an optical depth of 1 results in a surface cooling of $2^0C$ for the weakly absorbing aerosol. This cooling rapidly approaches a warming of $3^0K$ as $4\chi\kappa$ is increased to 1. Increasing $4\chi\kappa$ beyond a value of 1 results in a smaller increase in the surface temperature. At this larger optical depth and large values of the scaling parameter the convective fluxes are reduced to a point where a convective decoupling of the surface and atmosphere begins to occur. Further increases in the optical depth would stabilize the lowest layer of the atmosphere for the strongly absorbing aerosol.

Previous studies have demonstrated the importance of accurately assigning the surface albedo and the vertical distribution of the aerosol in assessing the climatic impact of an aerosol layer. Figure 52 demonstrates that the sensitivity of a climate to changes in the dust SW inherent optical properties is a function of the dust optical depth. For small optical depths, the sensitivity is likely to be small for weakly or strongly absorbing aerosols. On the other hand, at moderate optical depths the radiative forcing is a strong function of the dust inherent optical properties. This climate sensitivity makes the SW parameterizations presented in Chapter 5 very useful as they can account for the changes in the optical properties of the dust layer.

# Chapter 7

## SUMMARY AND CONCLUSIONS

Field experiments which have estimated the radiative effects of a dust layer have all concluded that the presence of a dust layer has a large impact on the shortwave (SW) radiative fluxes. Indeed, the heating due to the presence of the dust layer can be as large as the heating due to the absorption by water vapor. Broadband longwave (LW) measurements have been less conclusive, yet LW spectral measurements suggest that a dust layer reduces the atmospheric transmittance in the $8 - 13\mu m$ window region.

While field measurements are essential to the study of the radiative properties of the atmosphere their use is limited in assessing the sensitivity of the radiative fluxes to various changes in the optical properties of the dust. Thus the first objective of this study was to quantify the impact of a dust layer on the radiative fluxes at the top of the atmosphere, at the bottom of the atmosphere and within the atmosphere. To accomplish this objective appropriate radiative transfer models were developed and compared with aircraft observations. As a dust layer undergoes mobilization, transportation, and deposition, its physical and chemical properties change. Thus the radiative characteristics of four representative dust loadings were studied. These representative cases were chosen based on measurements discussed in Chapter 2. The heavy dust loading case (DESERTH) was chosen to represent a dust layer which had recently undergone mobilization. The light dust loading cases (DESERTL, DESERTV and OCEANL) were selected to represent dust layers which were undergoing transportation and deposition. The model calculations can be summarized as follows

- The presence of a dust layer results in a large increase in the atmospheric SW radiative heating. An optical depth of 1 at a wavelength of 0.55 (hereafter referred to as turbidity) can increase the desert SW atmospheric heating rate from $0.6^0C/Day$ to $1.2^0C/Day$. The heating rates of the DESERTH case are slightly greater than the DESERTL case due to the larger single scattering albedo. The majority of the increased heating is in the visible spectrum, and is due to the absorption of solar energy by the dust itself. The increased layer heating due to the enhancement of water vapor absorption by multiple scattering is small. The shortwave heating changes are sensitive to the dust loading (e.g. DESERTL, DESERTH or DESERTV). The heating rates of the DESERTH case are slightly greater than those of the DESERTL case due to the larger single scattering albedo. The greatest tropospheric heating rates occur for the DESERTV case.

- The presence of the dust layer increases the LW cooling of the atmosphere by an amount that is a function of the surface temperature. For the desert cases, a turbidity of 1 results in an increased tropospheric cooling of approximately $0.2^0C/Day$. The increased cooling resulting from a dust layer over the ocean is much less ($< .1^0C/Day$). Nearly all of the additional cooling occurs in the $8 - 13\mu m$ region. The increased cooling is similar for the DESERTL and DESERTH cases. Maximum cooling occurs in the DESERTV case due to the larger dust loading in the lower troposphere.

- When integrated over a 24 hour period, the LW cooling is only about a third of the increased SW heating by the dust. For a turbidity of 0.2, the presence of a dust layer can decrease the tropospheric radiative cooling of the desert atmosphere by 15%. For turbidities greater than 1.5, the SW heating by the dust layer can result in a radiative heat source within the atmosphere.

- The SW heating and LW cooling profiles are very sensitive to the vertical distribution of the dust. In the uniformly mixed case, maximum SW heating and LW cooling occurs near the top of the dust layer. The presence of the dust layer results in a LW warming near the base of the dust layer. In the case were the maximum dust loading is near the surface, the location of the maximum SW heating is a function of the solar zenith angle, while for the LW, all layers experience an enhanced cooling.

- The presence of the dust layer reduces the net SW surface flux while decreasing the LW radiative energy losses. The SW effect dominates so that in the daily mean the surface looses energy. For a turbidity of 1, the desert surface looses between $20 - 30Wm^{-2}$ while the ocean surface energy budget can be reduced by as much as $60Wm^{-2}$. Changes in the SW net surface flux are a function of the type of loading assumed, with greatest losses occurring for the DESERTV case. Changes in the surface LW energy budget of the DESERTH and DESERTL are within $2Wm^{-2}$. Differences in the DESERTL and DESERTV case are on the order of $5Wm^{-2}$, with the DESERTV exhibiting a greater downward LW flux.

- For the desert cases, the increased atmospheric warming dominates the surface cooling so that at the top of the atmosphere the presence of a dust layer increases the energy gain of the planet. Over the ocean the presence of the dust layer results in a cooling of the earth-atmosphere system. Changes at the top of the atmosphere are not as pronounced as changes at the surface or within the atmosphere.

- In addition to affecting the radiative energy balance of the troposphere, the presence of the dust layer can affect the stratospheric heating rates by modifying the upward flux at the troposphere. For the LW the effect of a dust layer over the desert is to cool the stratosphere by an amount which is proportional to the surface temperature as well as the optical depth of the dust layer. The cooling increases with larger surface temperatures. For the desert cases the effect of the dust layer on the SW stratospheric heating rates is a strong function of the solar zenith angle; in the daily mean it is near zero. On the other hand, a dust layer over the ocean increases the stratospheric SW heating rates by approximately $.5^0C/Day$ for a turbidity of 1.

The model calculations indicate that changes in the radiative characteristics of the atmosphere are a function of the physical and chemical properties of the dust layer, particularly in the case of the SW radiative fields. A general parameterization of the SW radiative properties of a dust layer is presented in Chapter 5 which accounts for the physical and chemical changes of a locally generated aerosol as it is mobilized and transported.

The parameterization scheme is based on the anomalous diffraction theory of van de Hulst (1957), with some modification. Estimates of the extinction coefficient, single scattering albedo and the asymmetry parameter are within 3% for conditions representative of a crustal aerosol. In addition, it is demonstrated that the parameterization scheme is applicable to other aerosol types, including water clouds. Finally the scaling parameter, $4\chi\kappa$, is presented which can be used to describe the optical properties of an aerosol layer. A plot of $\omega_0$ or of $g$ versus $4\chi\kappa$ demonstrates the sensitivity of the aerosol optical properties to changes in the size distribution or changes in the index of refraction.

The parameterization of the LW radiative properties of the dust layer follows the classic emissivity approach (e.g. Cox, 1976). However, in the present study the aerosol layer need not be isothermal. The parameterization is derived in terms of the dust turbidity, as the turbidity is often used to describe the dust loading of the atmosphere.

The radiative parameterizations are incorporated into a radiative-convective equilibrium climate model to assess the impact of the dust microphysical properties, defined in terms of $4\chi\kappa$, on the steady state temperature. Model calculations demonstrate that the sensitivity of a climate to changes in the dust SW inherent optical properties is a function of the dust optical depth. For weakly or strongly absorbing aerosols, the equilibrium surface temperature is insensitive to changes in the scaling parameter when the optical depth is small. On the other hand, at moderate optical depths the steady state temperature of the surface is a strong function of the dust inherent optical properties. The presence of the dust layer reduces the amount of convective flux needed to maintain a stable atmosphere.

## REFERENCES


Ackerman, S. A. and S. K. Cox, 1980: Colorado State University Radiation Instrumentation and Data Reduction Procedures for the Convair 990 During Summer MONEX. Atmos. Sci. Paper No. 325, Colorado State University, Ft. Collins, 72 pp.

Ackerman, S. A. and S. K. Cox, 1982: The Saudi Arabian heat low: aerosol distribution and thermodynamic structure. *J. Geophys. Res.*, **87**, 8991-9002.

Ackerman, S. A. and G. L. Stephens, 1987: The absorption of solar radiation by cloud droplets: an application of anomalous diffraction theory. To appear in *J. Atmos. Sci.*, 15 June issue.

Albrecht, B. and S. K. Cox, 1977: Procedures for improving pyrgeometer performance. *J. Appl. Meteor.*, **16**, 188-197.

Asano, S., and M. Sato, 1980: Light scattering by randomly oriented spheroidal particles. *Appl. Opt.*, **19**, 963-974.

Asano, S., and G. Yamamoto, 1975: Light scattering by a spheroidal particle. *Appl. Opt.*, **14**, 29-49.

Berkofsky, L., 1976: The effect of variable surface albedo on the atmospheric circulation in desert regions. *J. Appl. Meteor.*, **15**, 1139-1144.

Blake, D. W., T. N. Krishnamurti, S. V. Low-Nam and J. S. Fein, 1983: Heat low over the Saudi Arabian Desert during May 1979 (Summer MONEX). *Mon. Wea. Rev.*, **111**, 1759-1775.

Blanchet, J. P., 1981: The influence of the refractive index and size spectrum on atmospheric heating due to aerosols. *Atmos. Phys.*, **54**, 143-157.

Bohren, G. F. and D. R. Huffman, 1981: Absorption cross-section maxima and minima in IR absorption bands of small ionic ellipsoidal particles. *Appl. Opt.*, **20**, 959-962.

Bohren, G. F. and D. R. Huffman, 1983: /it Absorption and Scattering of Light by Small Particles. J. Wiley and Sons, Inc., 530 pp.

Box, M. A. and A. Deepak, 1978: Single and multiple scattering contributions to circumsolar radiation, *Appl. Opt.*, **17**, 3784-3797.

Box, M.A., and A. Deepak, 1979: Atmospheric scattering corrections to solar radiometry, *Appl. Opt.*, **18**, 1941-1949.

Box, M. A., 1981: Finite bandwidth and scattered light effects on the radiometric determination of atmospheric turbidity and the solar constant, *Appl. Opt.*, **20**, 2215-2219.

Brinkman, A. W., J. McGregor, 1983: Solar radiation in dense Saharan aerosol in Northern Nigeria. *Quart. J. R. Met. Soc.*, **109**, 831-847.

Bryson, R. A., and I. A. Barreis, 1967: Possibilities of major climatic modifications and their implications: Northwest India, a case for study. *Bul. Ams. Met. Soc.*, **48**, p. 136-142.

Brogniez, G., J-C. Buriez, J-C. Vanhoutte and Y. Fouquart, 1986: An improvement of the calibration of the Eppley pyrgeometer for the case of airborne measurements. *Beitr. Phys. Atmosph.*, **59**, 538-551.

Buettner, K. J. K. and C. D. Kern, 1965: The determination of infrared emissivities of terrestrial surfaces. *J. Geophys. Res.*, **70**, 1329-1337.

Carlson, T. N., and J. M. Prospero, 1972: The large scale movement of Saharan air outbreaks over the equatorial North Atlantic. *J. Appl. Meteor.*, **11**, 289-297.

Carlson, T. N., and R. S. Caverly, 1977: Radiative characteristics of Saharan dust at solar wavelengths. *J. Geophys. Res.*, **82**, 3141-3152.

Carlson, T. N., and P. Wendling, 1977: Reflected radiance measured by NOAA and VHRR as a function of optical depth for Sahara dust. *J. Appl. Meteor.*, **16**, 1368-1371.

Carlson, T. N., and S. G. Benjamin, 1980: Radiative heating rates for Saharan Dust. *J. Atmos. Sci.*, **37**, 193-213.

Cerf, A., 1980: Atmospheric turbidity over West-African. *Cont. Atmos. Phys.*, **53**, 414-428.

Chandrasekhar, S., 1960: *Radiative Transfer*. Dover, New York. 393 pp.

Charney, J., 1975: Dynamics of deserts and drought in the Sahel. *Quart. J. R. Met. Soc.*, **101**, 193-202.

Charney, J., W. J. Quirk, S. H. Chow and J. Kornfield, 1977: A comparative study of the effects of albedo change on drought in semi-arid regions. *J. Atmos. Sci.*, **34**, 1366-1385.

Chepil, W. S. and N. P. Woodruff, 1957: Sedimentary characteristics of dust storms - II. Visibility and dust concentration. *Am. J. Sci.*, **255**, 104-114.

Chou, M. and A. Arking, 1980a: An efficient method for computing the absorption of solar radiation by water vapor, *J. Atmos. Sci.*, **38**, 798-807.

Chou, M. and A. Arking, 1980b: Computation of infrared cooling rates in the water vapor bands, *J. Atmos. Sci.*, **38**, 855-867.

Coakley, J. A., Jr., and Petr Chýlek, 1975: The two-stream approximation in radiative transfer: including the angle of the incident radiation. *J. Atmos. Sci.*, **32**, 409-418.

Coakley, J. A., and R. D. Cess, 1983: The effect of tropospheric aerosols on the earth's radiation budget: a parameterization for climate models. *J. Atmos. Sci.*, **40**, 116-138.

Coakley, J. A., and R. D. Cess, 1985: Response of the NCAR community climate model to the radiative forcing by the naturally occurring tropospheric aerosol. *J. Atmos. Sci.*, **42**, 1677-1692.

Coulson, K. L., 1966: Effects of reflection properties of natural surfaces in aerial reconnaissance. *Appl. Opt.*, **5**, 905-917.

Courel, M. F., R. S. Kandel and S. I. Rasool, 1984: Surface albedo and the Sahel drought. *Nature*, **307**, 1-3.

Cox, S. K., 1973: Infra-red heating calculations with a water vapor pressure broadened continuum. *Quart. J. Roy. Meteor. Soc.*, **99**, 669-679.

Cox, S. K., 1976: Observations of cloud infrared effective emissivity. *J. Atmos. Sci.*, **33**, 287-289.

Cunnington, W. M. and P. R. Rowntree, 1986: Simulations of the Saharan atmosphere - dependence on moisture and albedo. *Quart. J. R. Met. Soc.*, **112**, 971-999.

Chýlek, P. and V. Ramaswamy, 1982: Simple approximation for infrared emissivity of water clouds, *J. Atmos. Sci.*, **39**, 171-177.

D'Almeida, G. A., and L. Schutz, 1983: Number, mass and volume distribution of mineral aerosol and soils of the Sahara. *J. Climat. Appl. Meteor.*, **22**, 233-243.

D'Almeida, G. A., R. Jaenicke, R. Roggendorf and D. Richter, 1983: New sunphotometer for network operation. *Appl. Opt.*, **22**, 3796-3801.

D'Almeida, G. A., 1986: A model for Saharan dust transport. *J. Climat. and Appl. Meteor.*, **25**, 903-916.

Das, P. K. and H. S. Bedi, 1981: The Role of Topography and Heat Sources on the Summer Monsoon. Volume of Extended Abstracts, International Conference on Early Results of FGGE and Large-Scale Aspects of its Monsoon Experiments, Tallahassee, FL. January 12-17, 1981.

Davis, J. M. and S. K. Cox, 1982: Reflected solar radiances from regional scale scenes. *J. Appl. Meteor.*, **21**, 1698-1712.

Deepak, A. and E. S. Green, 1970: Second and higher order scattering of light in a settling polydisperse aerosol, *Appl. Opt.*, **9**, 2362-2371.

Deepak, A., and M. A. Box, 1978a: Forwardscattering corrections for optical extinction measurements in aerosol media. 1: Monodispersions, *Appl. Opt.*, **17**, 2900-2908.

Deepak, A., and M. A. Box, 1978b: Forwardscattering corrections for optical extinction measurements in aerosol media. 1: Polydispersions, *Appl. Opt.*, **17**, 3169-3176.

Deirmendjian, D., 1969: *Electromagnetic scattering on spherical polydispersions.* Elsevier, New York. 290 pp.

DeLuisi, J. J., P. M. Furukawa, D. A. Gillette, B. G. Schuster, R. J. Charlson, W. M. Parch, R. W. Fegley, B. M. Herman, R. A. Rabinoff, J. T. Twitty, and J. A. Weinman, 1976: Results of a comprehensive atmospheric aerosol-radiation experiment in the Southwestern United States. Part I: Size distribution, extinction optical depth and vertical profiles of aerosols suspended in the atmosphere. *J. Appl. Meteor.*, **15**, 455-463.

DeLuisi, J. J., P. M. Furukawa, D. A. Gillette, B. G. Schuster, R. J. Charlson, W. M. Parch, R. W. Fegley, B. M. Herman, R. A. Rabinoff, J. T. Twitty, and J. A. Weinman, 1976: Results of a comprehensive atmospheric aerosol-radiation experiment in the Southwestern United States. Part II: Radiation flux measurements and theoretical interpretation. *J. Appl. Meteor.*, **15**, 455-463.

Dubief, J., 1953: Les vents de sable ay Sahara Francais. *Collog. Int. CNRS*, **35**, 45-70.

Ellingson, R. G. and G. N. Serafino, 1984: Observations and calculations of aerosol heating over the Arabian Sea during MONEX. *J. Atmos. Sci.*, **41**, 575-589.

Elterman, L. Wexler, R. and Chang, D. T., 1969: Features of tropospheric and stratospheric dust. *Appl. Opt.*, **8**, 893-903.

Foot, J. S., 1986: A new pyrgeometer. *J. Atmos. and Oceanic Technol.*, **3**, 363-370.

Fouquart, Y., B. Bonnel, G. Brogniez, A. Cerf, M. Chaoui, L. Smith and J.C. Nanhoutte, 1984: Size distribution and optical properties of Saharan aerosols during ECLATS. Aerosols and their climatic effects, ed. H. Gerber and A. Deepak. A. Deepak Publishing.

Fouquart, Y., B. Bonnel, M. C. Roquai and R. Santer, 1987: Observations of Saharan aerosols: results of ECLATS Field experiment. Part I: Optical thicknesses and aerosol size distributions. *J. Climat. and Appl. Meteor.*, **26**, 28-37.

Fouquart, Y., B. Bonnel, G. Brogniez, J. C. Buriez, L. Smith and J. J. Morcrette, 1987: Observations of Saharan aerosols: results of ECLATS field experiment. Part II: Broadband radiative characteristics of the aerosols and vertical radiative flux divergence. *J. Climat. and Appl. Meteor.*, **26**, 38-52.

Gayevsky, V. L., 1951: Surface temperature of large territories. *Proc. Main Geophys. Obs.*, **26** (**88**).

Goudie, A. S., 1978: Dust storms and their geomorphological implications. *J. Arid Environ.*, **1**, 291-310.

Grams, G. W., I. H. Blifford Jr., D. A. Gillette and P. B. Russel, 1974: Complex index of refraction of airborne particles. *J. Appl. Meteor.*, **13**, 459-471.

Grant, I. P., and G. E. Hunt, 1969: Discrete space theory of radiative transfer I. Fundamentals. *Proc. Roy. Soc. Lond. A.*, **313**, 183-197.

Hansen, J. E. and L. D. Travis, 1974: Light scattering in planetary atmospheres. *Space Science Reviews*, **16**, 527-610.

Harshvardhan and R. D. Cess, 1978: Effect of tropospheric aerosols upon atmospheric infrared cooling rates, *J. Quant. Spectrosc. Transfer*, **19**, 621-632.

Hodkinson, J. R., 1963: Light scattering and extinction by irregular particles larger than the wavelength, in *Electromagnetic Scattering*, M. Kerker (Ed.), Macmillan, New York, 87-100.

Hodkinson, J. R. and I. Greenleaves, 1963: Computations of light-scattering and extinction by spheres according to diffraction and geometrical optics and some comparisons with the Mie theory. *J. Opt. Soc. Am.*, **53**, 577-588.

Idso, S. B., 1975: Low-level aerosol effects on earth's surface energy balance, *Tellus*, **27**, 318-320.

Idso, S. B., 1981a: Climatic change: The role of atmospheric dust. *Geological Society of America Special Paper 186.*

Idso, S. B., 1981b: An experimental determination of the radiative properties and climatic consequences of atmospheric dust under nonduststorm conditions. *Atmos. Env.*, **15**, 1251-1259.

Iribarne, J. V. and W. L. Godson, 1981: *Atmospheric Thermodynamics*, Geophysics and Astrophysics Monographs, D. Reidel Publishing Company. 259 pp.

Irvine, W. M., 1975: Multiple scattering in planetary atmospheres, *Icarus*, 25, 175-204.

Joseph, J. H., A. Manes and D. Ashbel, 1973: Desert aerosols transported by Khamsinic and their climatic effects. *J. Appl. Meteor.*, **12**, 792-797.

Joseph, J. H., W. J. Wiscombe and J. A. Weinman, 1976: The delta-eddington approximation fro radiative flux transfer, *J. Atmos. Sci.*, **33**, 2452-2459.

Joseph, J. H., 1984: The sensitivity of a numerical model of the global atmosphere to the presence of desert aerosol. ***Aerosols and their climatic effects***, ed. H. Gerber and A. Deepak. A. Deepak Publishing.

Joseph, J. H., 1977: The effect of desert aerosol on a model of the general circulation. Proceedings of the Symposium on Radiation in the Atmosphere, J. J. Bolle ed. Science Press, 487-492 pp.

Junge, C. E., 1953: Die Rolle der Aerosole und der gasformigen Beimengungen der Luft im Spurenstoffhaushalt der Troposphare. *Tellus*, **5**, 1-26.

Kalu, A. E., 1979: The African dust plume: its characteristics and propagation across west Africa in winter. *Saharan Dust*, SCOPE 14, John Wiley & Sons, C. Morales, ed. pp 297.

Kashina, V. I., 1961: Dust content of the atmospheric surface layer in desert and semidesert regions of central Asia and Kazakhstan. Conference on the scattering and polarization of light in the atmosphere, October 1961. Israel Program for Scientific Translations, Jerusalem, 1965.

Katsnelson, J., 1970: Frequency of duststorms at B'er Shev a. Israel J. Earth Sci., **19**, 69.

King, M. D., P. M. Byrne, J. A. Reagan and B. M. Herman, 1980: Spectral variation of optical depth at Tucson, Arizona between August 1975 and December 1977. *J. Appl. Meteor.*, **19**, 723-732.

King, M. D. and Harshvardhan, 1986: Comparative accuracy of selected multiple scattering approximations. *J. Atmos. Sci.*, **43**, 784-801.

Kondratyev, K. Ya., O. D. Barteneva, L. I. Chapursky, A. P. Chernenko, V. S. Grishechkin, L. S. Ivlev, V. A. Ivanov, V. I. Korzov, V. B. Lipatov, M. A. Prokofyev, V. K. Tolkatchev, O. B. Vasiliev and V. F. Zhvalev, 1976: Aerosol in the GATE area and its radiative properties. Colorado State University Atmospheric Science Paper No. 247, Fort Collins, CO 80523.

Kondratyev, K. Ya., R. M. Welch, O. B. Vasiliev, V. F. Vasiliev, L.S. Ivlev, and V. F. Rodionov, 1976: Comparison between the measured and calculated spectral characteristics of shortwave radiation in the free atmosphere over the desert (from the data of the CAENEX-70 expeditions), Colorado State University Atmospheric Science Paper No. 247, Fort Collins, CO 80523.

Kondratyev, K. Ya., R. M. Welch, O. B. Vasiliev, V. F. Vasiliev, L.S. Ivlev, and V. F. Rodionov, 1979: Calculations of free atmospheric shortwave spectral characteristics over the desert (from the CAENEX-70 data), *Tellus*, **31**, 13-27.

Krishnamurti, T. M., P. Greiman, Y. Ramanathan, R. Pasch, and P. Ardanuy, 1980: Quick look Summer MONEX atlas, Part I: Saudi Arabian phase. FSU Report No. 80-4, Dept. of Meteor., Florida State Univ., Tallahassee, FL., 71 pp.

Krishnamurti, T. M., P. Ardanuy, Y. Ramanathan and R. Pach, 1981: On the onset vortex of the Summer Monsoon. *Mon. Wea. Rev.*, **109**, 344-363.

Lacis, A. A. and J. E. Hansen, 1974: A parameterization for the absorption of solar radiation in the earth's atmosphere. *J. Atmos. Sci.*, **31**, 118-133.

Laulainen, N. S. and B. J. Taylor: The precision and accuracy of Volz sunphotometry. *J. Appl. Meteor.*, **13**, 298-302.

Lenoble, J. (ed.), 1977: Standard procedures to compute atmospheric radiative transfer in a scattering atmosphere. International Association of Meteorology and Atmospheric Physics. National Center for Atmospheric Research, Boulder, CO, 80307.

Lenoble, J., and C. Brogniez, 1984: A comparative review of radiation aerosol models. *Beit. Phys. Atmosph.*, **57**, 1-20.

Levin, Z., J. H. Joseph and Y. Mekler, 1979: Properties of Sharav (Khamsin) dust - comparison of optical and direct sampling data. *J. Atmos. Sci.*, **37**, 882-891.

Liou, K. N., 1972: Light scattering by ice clouds in the visible and infrared: A theoretical study. *J. Atmos. Sci.*, **29**, 524-536.

Martin, D. W., 1975: Identification, tracking and sources of Saharan dust - an inquiry using Synchronous Meteorological Satellite (SMS). In WMO GATE Rep., 2, 217-219.

Manabe, S., and F. Moller, 1961: On the radiative equilibrium and heat balance of the atmosphere. *Mon. Wea. Rev.*, **89**, 503-532.

Manabe, S. and R. Strickler, 1964: Thermal equilibrium of the atmosphere with a convective adjustment. *J. Atmos. Sci.*, **21**, 361-385.

Manabe, S., and R. T. Wetherald, 1967: Thermal equilibrium of the atmosphere with a given distribution of relative humidity. *J. Atmos. Sci.*, **24**, 241-259.

McNaughton, D. L., 1986: Possible connection between anomalous anticyclones and sandstorms. *Weather*, **42**, 9-13.

Meador, W. E., and W. R. Weaver, 1980: Two stream approximations to radiative transfer in planetary atmospheres: A unified description of existing methods and a new improvement. *J. Atmos. Sci.*, **37**, 630-643.

Middleton, N. J., 1986: A geography of dust storms in south-west Asia. it J. Climat., **6**, 183-196.

Mie, G., 1906: Contributions to the optics of turbid media, especially colloidal metal solutions. *Ann. Physik.*, **25**, 377-445.

Minnis, P. and S. K. Cox, 1978: Magnitude of the radiative effects of the Saharan dust layer. Atmospheric Science Paper No. 283, Colorado State University, Fort Collins, CO.

Mohamed, A. B., and J. P. Frangi, 1983: Humidity and turbidity parameters in Sahel: A case study of Niamey (Niger). *J. Climat. and Appl. Meteor.*, **22**, 1820-1823.

Mohamed, A. B. and J. P. Frangi, 1986. Results from ground-based monitoring a spectral aerosol optical thickness and horizontal extinction: some specific characteristics of dusty Sahelian atmospheres. *J. Climat. and Appl. Meteor.*, **25**, 1807-1815.

Morales, C., Ed., 1979: *Saharan Dust: Mobilization, Transport, Deposition.* J. Wiley & Sons.

Morcrette, J.-J., L. Smith and Y. Fouquart, 1986: Pressure and temperature dependence of the absorption in longwave radiation parameterizations. *Beitr. Phys.Atmosph.*, **59**, 455-469.

Mugnai, A. and W. J. Wiscombe, 1980: Scattering of radiation by moderately nonsherical particles, *J. Atmos. Sci.*, **37**, 1291-1307.

Nickling, W. G. and A. J. Brazel, 1984: Temporal and spatial characteristics of Arizona dust storms (1965-1980). *J. Climat.*, **4**, 645-660.

Norton, C. C., F. R. Mosher and B. Hinton, 1979: An investigation of surface albedo variations during the recent Sahel drought. *J. Appl. Meteor.*, **18**, 1252-1262.

Nussenzveig, H. and W. Wiscombe, 1980: Efficiency factors in Mie scattering. *Phys. Rev. Lett.*, **45**, 1490-1494.

Ohring, G., and J. H. Joseph, 1978: On the combined infrared cooling of two absorbing gases in the same spectral region. *J. Atmos. Sci.*, **35**, 317-322.

Orgill, M. M., and G. A. Sehmel, 1976: Frequency and rupture variation of dust storms in the contiguous USA. *Atmos. Environ.*, **10**, 813-825.

Otterman, J., 1974: Baring high-albedo soils by overgrazing: A hypothesized desertification mechanism. *Science*, **186**, 531-533.

Patterson, E. M. and D. A. Gillette, 1977: Commonalities in measured size distributions for aerosols having a soil-derived component. *J. Geophys. Res.*, **82**, 2074-2082.

Patterson, E. M., and D. A. Gillette, 1977: Measurements of visibility vs. mass-concentration for airborne soil particles. *Atmos. Environ.*, **11**, 193-196.

Patterson, E. M., D. A. Gillette and B. H. Stockton, 1977: Complex index of refraction between 300 nm and 700 nm for Saharan aerosols. *J. Geophys. Res.*, **82**, 3153-3160.

Patterson, E. M., 1977: Atmospheric extinction between $0.55\mu m$ and $10.6\mu m$ due to soil-derived aerosols. *Appl. Opt.*, **16**, 2414-2418.

Patterson, E. M., C. S. Kiang, A.C. Delany, A. F. Warburg, A.C.D. Leslie and B.J. Huebert, 1980: Global measurements of aerosols in remote continental and marine regions: Concentrations, size distributions, and optical properties. *J. Geophys. Res.*, **85**, 7361-7375.

Patterson, E. M., 1981: Optical properties of the crustal aerosol: Relation to chemical and physical characteristics. *J. Geophys. Res.*, **86**, 3236-3246.

Patterson, E. M., G. W. Grams, and C. O. Pollard, 1983: Aircraft measurements of aerosol optical properties during the MONEX program. Final Technical Report, 28 pp.

Peterson, J. T. and J. A. Weinman, 1969: Optical properties of quartz dust particles at infrared wavelengths. *J. Geophys. Res.*, **74**, 6947-6952.

Peterson, S. T., and C. E. Junge, 1971: Sources of particulate matter in the atmosphere. *Man's Impact on the Climate.* W. W. Kellog and G. D. Robinson, Eds., MIT Press, 310-320.

Péwé, T., (ed.) 1981: *Desert Dust: Origin, Characteristics, and Effect on Man*, Special Paper No. 186, The Geological Society of America, Boulder, CO, 303 pp.

Pinnick, R. G., G. Fernandez, B. D. Hinds, C. W. Bruce, R. W. Schaefer, and J. D. Pendleton, 1985: Dust generated by vehicular traffic on unpaved roadways: Sizes and infrared extinction characteristics. *Aerosol Science and Technology*, **4**, 99-121.

Pollack, J. B., O. B. Toon, and B. N. Khare, 1973: Optical properties of some terrestrial rocks and glasses. *Icarus*, **19**, 372-389.

Pollack, J. B., and J. N. Cuzzi, 1980: Scattering by nonspherical particles of size comparable to a wavelength: a new semi-empirical theory and its application to tropospheric aerosols. *J. Atmos. Sci.*, **37**, 868-881.

Pollack, J. B., and C. P. McKay, 1985: The impact of polar stratospheric clouds on the heating rates of the winter polar stratosphere. *J. Atmos. Sci.*, **42**, 245-262.

Preisendorfer, R. W., 1960: Application of radiative transfer theory to light measurements in the sea. *International Association of Physical Oceanography*, 11-31.

Proctor, T. D. and G. W. Harris, 1974: The turbidity of suspensions of irregular quartz particles. *Aerosol Science*, **5**, 81-90.

Prospero, J. M., and T. N. Carlson, 1972: Dust concentration in the atmosphere of the equatorial North Atlantic Ocean. *J. Geophys. Res.*, **77**, 5255-5265.

Prospero, J. M., 1981: Arid regions as sources of mineral aerosols in the marine atmosphere. Geological Society of America Special Paper 186.

Pueschel, R. F. and P. M. Kuhn, 1975: Infrared absorption of tropospheric aerosols: Urban and rural aerosols of Phoenix, Arizona, *J. Geophys. Res.*, **21**, 2960-2962.

Rahn K.A., R.D. Borys, G.E. Shaw, L. Schutz and R. Jaenicke 1979: Long range impact of desert aerosol on atmospheric chemistry: two examples. *Saharan Dust*, SCOPE 14, J. Wiley & Sons, C. Morales, ed. pp 297.

Randall, D. A. and T. N. Carlson, 1983: The sensitivity of a general circulation model to Saharan Dust heating. Fifth Conference on Atmospheric Radiation, Baltimore, MD, October 31 - 4 November, 137-140 pp.

Raschke, R. A. and S. K. Cox, 1983: Instrumentation and technique for deducing cloud optical depth. *J. Climat. and Appl. Meteor.*, **22**, 1887-1893.

Reck, R. A., 1974: Influence of surface albedo on the change in the atmospheric radiation balance due to aerosols. *Atmos. Environ.*, **8**, 823-833.

Reck, R. A., 1975: Influence of aerosol cloud height on the change in atmospheric radiation balance due to aerosols. *Atmos. Environ.*, **9**, 89-99.

Reiff, J. and G. S. Forbes, 1986: African dust reaching Northwestern Europe: A case study to verify trajectory calculations. *J. Climat. and Appl. Meteor.*, **25**, 1543-1567.

Roberts, R. E., J. E. Selby and L. M. Biberman, 1976: Infrared continuum absorption by atmospheric water vapour in the $8 - 12\mu m$ window. *Appl. Opt.*, **15**, 2085-2090.

Rodgers, C. D., 1967: The use of emissivity in atmospheric radiation calculations. *J. Atmos. Sci.*, 43-54.

Schutz, L. and R. Jaenicke, 1974: Particle number and mass distribution above 10-4 cm radius in sand and aerosol of the Sahara Desert. *J. Appl. Meteor.*, **13**, 863-870.

Shaw, G. E., 1980: Transport of Asian desert aerosol to the Hawaiian Islands, *J. Appl. Meteor.*, **19**, 1254-1259.

Shettle, E. P. and R. W. Fenn, 1979: Models for the aerosols of the lower atmosphere and the effects of humidity variations on their optical properties. AFGL TR 790214, Environ. Res. Papers No. 676.

Smith, E. A., S. A. Ackerman, S. K. Cox and T. H. Vonder Haar, 1980: Summer MONEX high altitude aircraft radiation measurements. Atlas of MONEX Aircraft Measurements. Dept. of Atmos. Sci., Colorado State University, Fort Collins, CO, 80523, 84 pp.

Smith, E. A., 1986a: The structure of the Arabian heat low. Part I: surface energy budget. *Mon. Wea. Rev.*, **114**, 1067-1083.

Smith, E. A., 1986b: The structure of the Arabian heat low. Part II: bulk tropospheric heat budget and implications. *Mon. Wea. Rev.*, **114**, 1084-1102.

Smith, E. A., 1986: Transition of surface energy budget in the Gobi Desert between spring and summer seasons. *J. Clim. and Appl. Meteor.*, **25**, 1725-1740.

Stephens, G. L., 1978a and b: Radiative properties of extended water clouds. Parts I and II. *J. Atmos. Sci.*, **35**, 2111-2132.

Stephens, G. L. and P. J. Webster, 1979: Sensitivity of radiative forcing to variable cloud and moisture, *J. Atmos. Sci.*, **36**, 1542-1556.

Stephens, G. L., G. G. Campbell, and T. H. Vonder Haar, 1981: Earth radiation budgets. *J. Geophys. Res.*, **86**, 9739-9760.

Stephens, G. L., S. Ackerman, E. A. Smith, 1984: A shortwave parameterizaton revised to improve cloud absorption, *J. Atmos. Sci.*, **41**, 687-690.

Stephens, G. L., 1984: The parameterization of radiation for numerical weather prediction and climate models, *Mon. Wea. Rev.*, **112**, 826-867.

Tam, W. G. and A. Zardecki, 1982: Multiple scattering corrections to the Beer-Lambert law. 1: Open detector. *Appl. Opt.*, **21**, 2405-2412.

Thekaekara, M. P., and A. J. Drummond, 1971: Standard values of the solar constant and its spectral components. Nature (London), Phys. Sci., **229**, 6-9.

Tucker, C. J., J. R. G. Townshend, T. E. Goff, 1985: African land-cover classification using satellite data. *Science*, **227**, 369-375.

Toon, O. B. and Pollack, J. B., 1976: A global average model of atmospheric aerosols for radiative transfer calculations. *J. Appl. Meteor.*, **15**, 225-246.

Volz, F. E., 1973: Infrared optical constants of ammonium sulfate, Saharan dust, volcanic pumice and flyash. *Appl. Opt.* **12**, 564-567.

Volz, F. E., 1974: Economical multispectral sun photometer for measurements of aerosol extinction from 0.44 $\mu m$ to 1.6 $\mu m$ and precipitable water. *Appl. Opt.* **13**, 1732-1733.

Wait, J. R., 1955: Scattering of a plane wave from a circular dielectric cylinder at oblique incidence. *Can. J. Phys.*, **33**, 189-195.

Wang, W. and G. A. Domoto, 1974: The radiative effect of aerosols in the Earth's atmosphere, *J. Appl. Meteor.*, **13**, 521-534.

Widger, W. K., Jr., and M. P. Woodall, 1976: Integration of the Planck blackbody radiation function. *Bull. Amer. Meteor. Soc.*, **57**, 1217-1219.

Wiscombe, W., 1976a: Extension of the doubling method to inhomogeneous sources. *J. Quant. Spectrosc. Radiat. Transfer*, **16**, 477-489.

Wiscombe, W., 1976b: On initialization, error and flux conservation in the doubling method. *J. Quant. Spectrosc. Radiat. Transfer*, **16**, 637-658.

Wiscombe, W., and G. W. Grams, 1976: The backscattered fraction in two-stream approximations. *J. Atmos. Sci.*, **33**, 2440-2451.

Wiscombe, W., 1977: The delta-m method: Rapid yet accurate radiative flux calculations for strongly asymmetric phase functions, *J. Atmos. Sci.*, **34**, 1408-1422.

Wiscombe, W., and J. W. Evans, 1977: Exponential-sum fitting of radiative transmission functions. *J. Comput. Phys.*, **24**, 416-444.

WMO, 1974: International Codes, WMO-306, Manual on Codes, Vol. 1.

Zardecki, A. and W. G. Tam, 1982: Multiple scattering corrections to the Beer-Lambert law. 1: Detector with a variable field of view. *Appl. Opt.*, **21**, 2413-2420.

Zardecki, A., A. and A. Deepak, 1983: Forward multiple scattering corrections as a function of detector field of view. *Appl. Opt.*,**22**, 2970-2976.

## Appendix A

## SUMMARY OF FIELD EXPERIMENTS

This appendix gives a brief description of several major field experiments that have measured the radiative properties of a dust layer. The location and time of the experiment are given along with appropriate references that discuss the radiative measurements.

**Complex Atmospheric Energetics Experiment (CAENEX)** This experi- ment took place and was a multi-year experiment in the early 1970's. A portion of the experiment took place over the Kara Kum desert in the Repetek region of the USSR in 1970, (CAENEX-70). Aerosol number density, size distribution and chemical composition were measured. In addition, measurements were also made of the broadband upward and downward longwave and shortwave fluxes as well as narrow band spectral measurements within the spectral range $0.4 - 2.5\mu m$. Aircraft was used for vertical profiling. Results regarding the radiation measurements of CAENEX-70 can be found in Kondratyev et al. (1976).

**Comprehensive Atmospheric Aerosol-Radiation Experiment (CAAR)** This experiment was the First GAARS field test and was located in the southwestern United States. The experiment took place from 14-25 May, 1972. Measurements included aerosol optical extinction, aerosol size distributions and SW and LW broadband radiation flux measurements. Aircraft were used to obtain vertical profiles. Results of the experiment have been published by DeLuisi et al. (1976 a and b).

**GARP Atlantic Tropical Experiment (GATE)** This international experiment was conducted out of Dakar, Senagal in the summer of 1974. Radiation measurements at the surface and in the atmosphere (made from aircraft platform) were made over the eastern tropical Atlantic and western Africa. Measurements included aerosol size distributions and index of refraction, aerosol extinction measurements as well as broadband flux measurements. Satellite data was also available for analysis. Publications pertaining to the radiation measurements include; Kondratyev et al. (1976), Carlson and Caverly (1977), Minnis and Cox (1978) and Carlson and Benjamin (1980)

**Summer Monsoon Experiment (SMONEX)** This field program was the second special observation period (SOP II) of the First GARP Global Experiment (FGGE) and was conducted in the summer of 1979. Aircraft observations of aerosol size distribution, aerosol index of refraction and broadband radiative flux measurements were made over the Saudi Arabian Peninsula, the Arabian Sea, India and the Bay of Bengal. Results regarding the radiative properties of the soil derived aerosol can be found in Ackerman and Cox (1982), Patterson et al. (1983) and Ellingson and Serafino (1984).

**Etude de la Couche Limite Atmospherique Tropicale Seche (ECLATS)** This field experiment was conducted in Niamey, Niger in November-December 1980 and included measurements of broadband radiative fluxes, aerosol concentration and size distributions at the surface and from an aircraft platform. Observation of solar extinction were also made. The interested reader should refer to Fouquart et al. (1987a and b) for a summary of the radiation measurements.

## Appendix B

# SURFACE WEATHER OBSERVATIONS OF DUST OUTBREAKS ASSOCIATED WITH THE SOUTHWEST SUMMER MONSOON REGION

Problems associated with dust outbreaks can be broken down into three processes: the mobilization, the transport and the deposition of the dust. Surface station observations can be very helpful in describing these processes; for example, an estimate of the direction in which dust, once mobilized, will be transported is obtained by compositing wind direction as a function of dust suspended in the atmosphere for heavy dust conditions (cases in which the visibility was less than or equal to 5 km) for May, June and July for the years 1979-1983. The results are shown in figure B1. Stations for which more than 25% of observations were missing are not included in the analysis. Each ring represents an increment of 50 dust occurrences. The number to the left of the station name is the number of cases of dust loading for calm winds.

Figure B1 indicates that, for most of the stations, there is a preferred wind direction of outbreak occurrences for heavy dust. Comparison of figure B1 with a similar figure depicting the frequency of occurrence of a given wind direction indicates that for most of the stations, the preferred wind direction for a heavy dust outbreak is aligned with the climatological wind direction. This suggests that the mobilization and transport is accomplished by the mean wind; however, synoptic systems may play a significant role as seen below. Prediction of dust outbreaks based on wind direction for these stations would fail due to the number of non-occurrences of dust outbreaks for a given wind

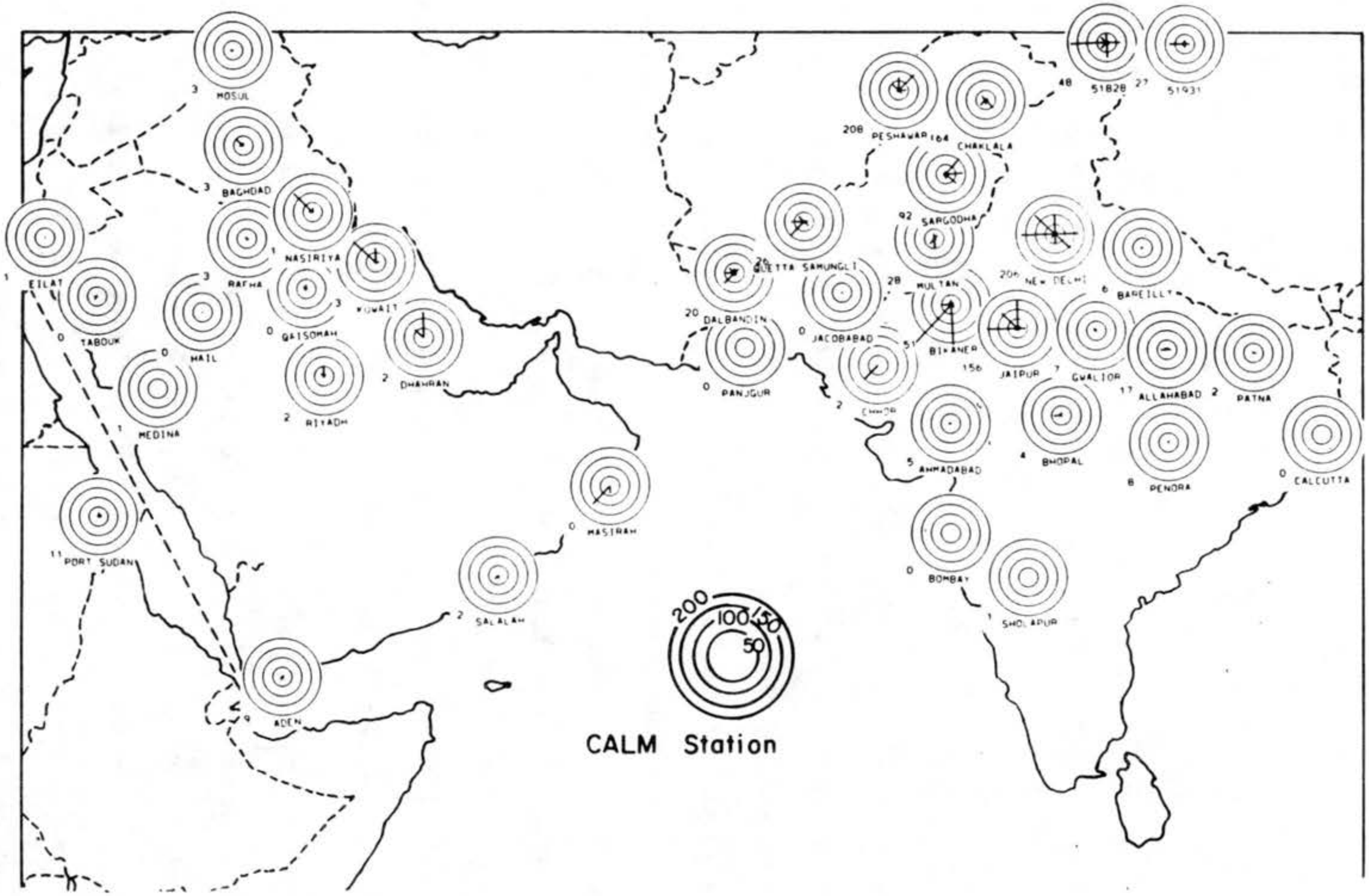


Figure B.1 Five year composite (1979-1983) of wind direction associated with a dust observation in which the visibility was less than 5 km. Each ring represents an increment of 50 days. The number to the left of the station name corresponds to the number of occurrances with calm winds.

direction. However this preferred direction is certainly helpful if one is concerned with the atmospheric transport of the dust. Regions of high dust deposition can also be inferred from this type analysis. For example, northern India and northern Pakistan stations have large occurrences of heavy dust loading with calm winds, allowing gravitational settling.

The importance of synoptic disturbances in generating and transporting dust is seen in figures B2-B5 which depicts a large scale dust outbreak observed over the Saudi Arabian Peninsula. Each station plot includes information on wind speed and direction, temperature, dew point depression, cloud cover, present and past weather, visibility, pressure and 24 hour pressure tendency, (WMO, 1974). Isopleths of low visibility are also depicted (note that these regions of low visibility do not include all observations of suspended dust). On the 22 June 0 GMT, approximately 3 LST, there were few observations of suspended dust over the region; however, by 18 GMT (figure B2) wind speeds increased raising up dust and reducing visibility. On the 23 June 0 GMT (figure B3) the dust was concentrated in southern Iraq and was associated with a low level jet maximum. This low level jet extends to 700 mb as seen in the analysis of Krishnamurti et al. (1980). The region of low visibility increases in area by 6 GMT and begins spreading down the Persian Gulf (figure B4). By 6 GMT on the 24 June (figure B5), the outbreak engulfs the entire peninsula and then appears to drift eastward. Some of this dust was transported over the Arabian Sea and was observed in large quantities during the Summer Monsoon Experiment on 26 June (Smith et al. , 1980). The dust over the Arabian Sea was observed in conjunction with large amounts of low level cloud. Figure B6 depicts various weather observations at

Kuwait during the period covering the dust outbreak. The outbreak at Kuwait began between 6 and 12 GMT on 23 June. Low visibilities are associated with large wind speeds and while there is little diurnal variation in the visibility during the outbreak there is still a strong diurnal component in the wind speed. The outbreak is associated with a pressure surge (positive 24 hour pressures changes) signifying the intensification of a low level anticyclone. Similar pressure surges have been noted by McNaughton (1987). During the peak of the outbreak, (23 and 24 of June) there was a reduction in the daytime temperature which may either be associated with a cooler air mass, or reduced heating

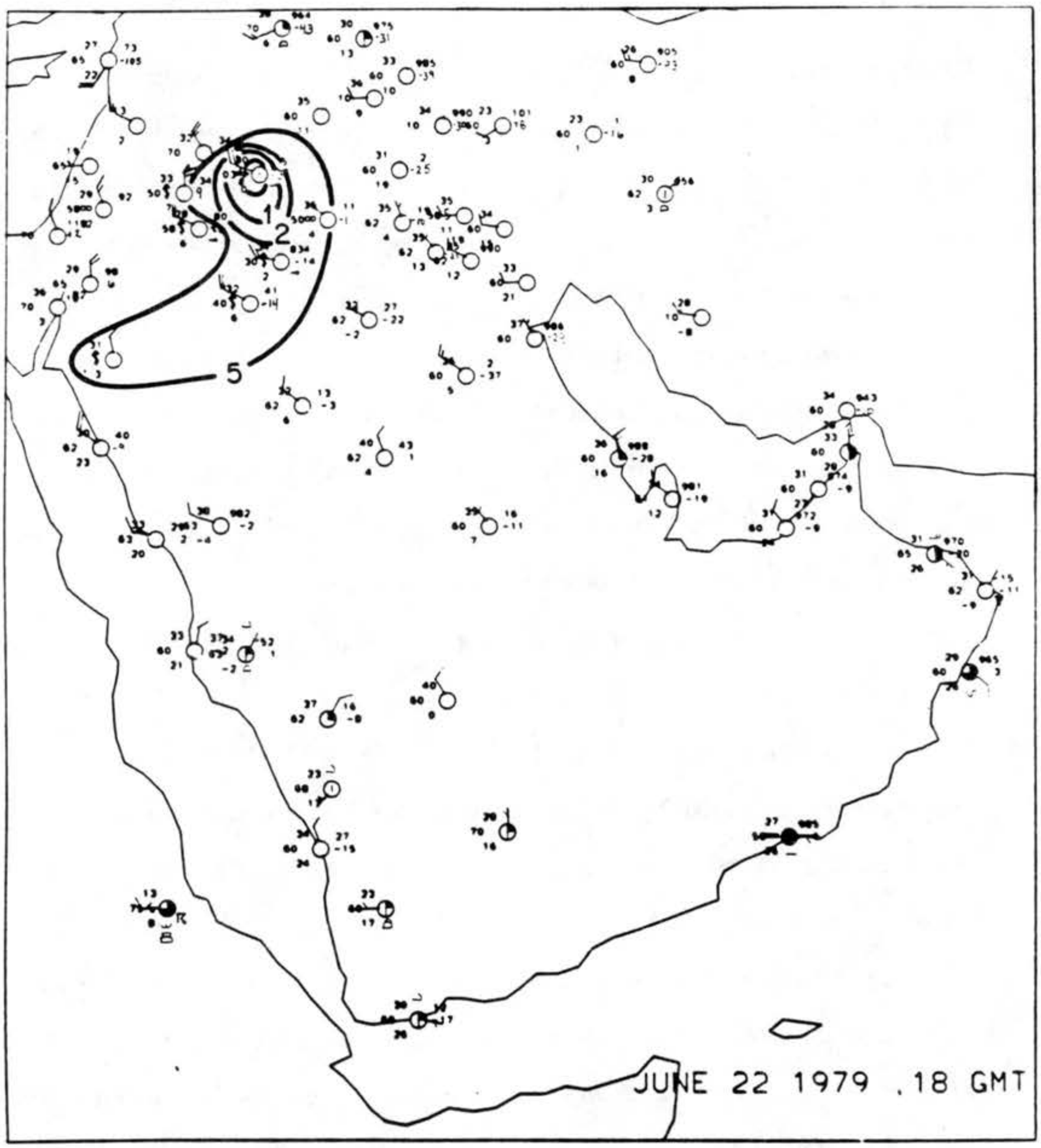


Figure B.2: Surface weather chart for 18 GMT on 22 June 1979. Isopleths of visibility are analyzed for visibilities of 5, 2, 1, and 0.5 km.

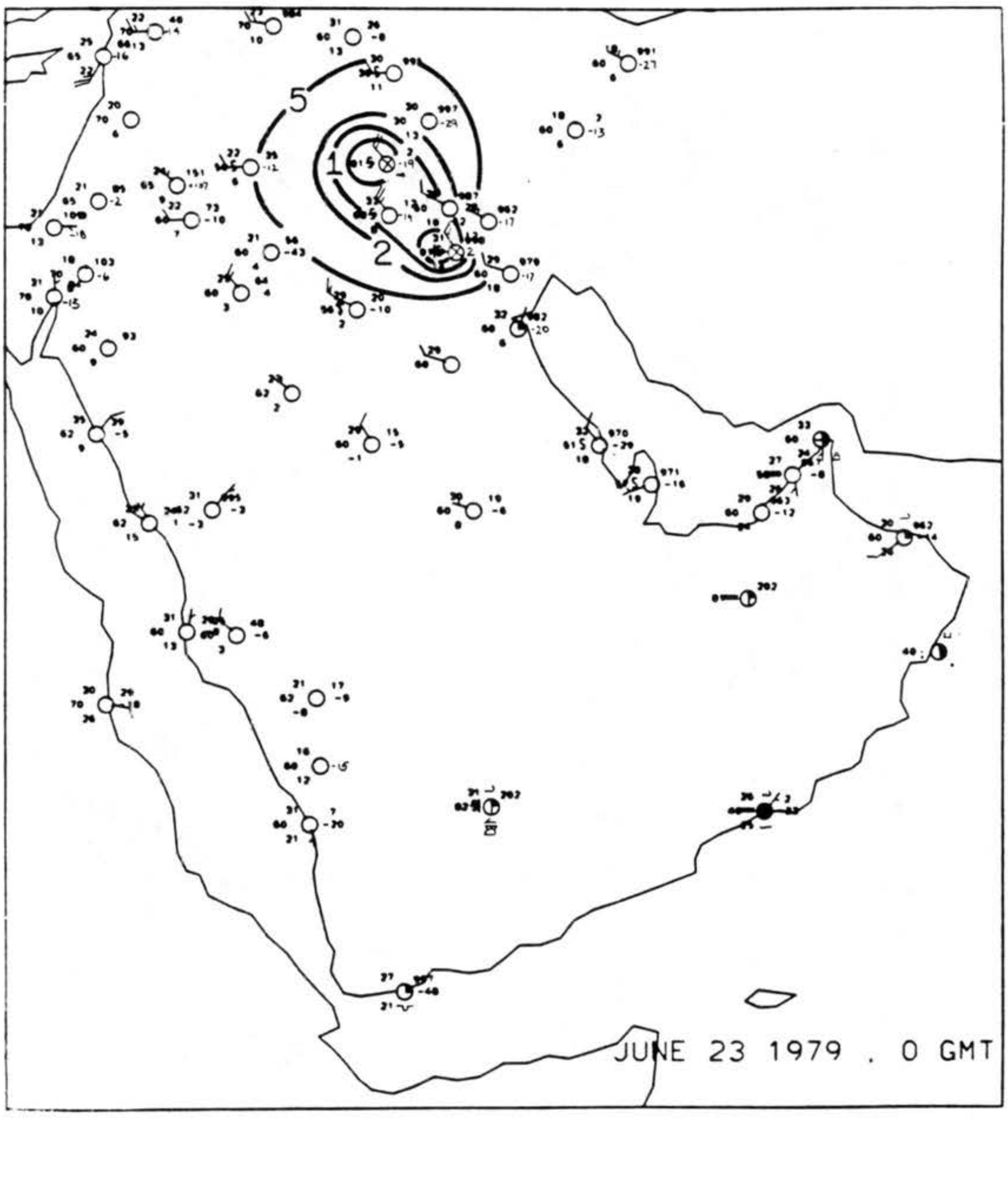


Figure B.3: Surface weather chart for 00 GMT on 23 June 1979. Isopleths of visibility are analyzed for visibilities of 5, 2, 1, and 0.5 km.

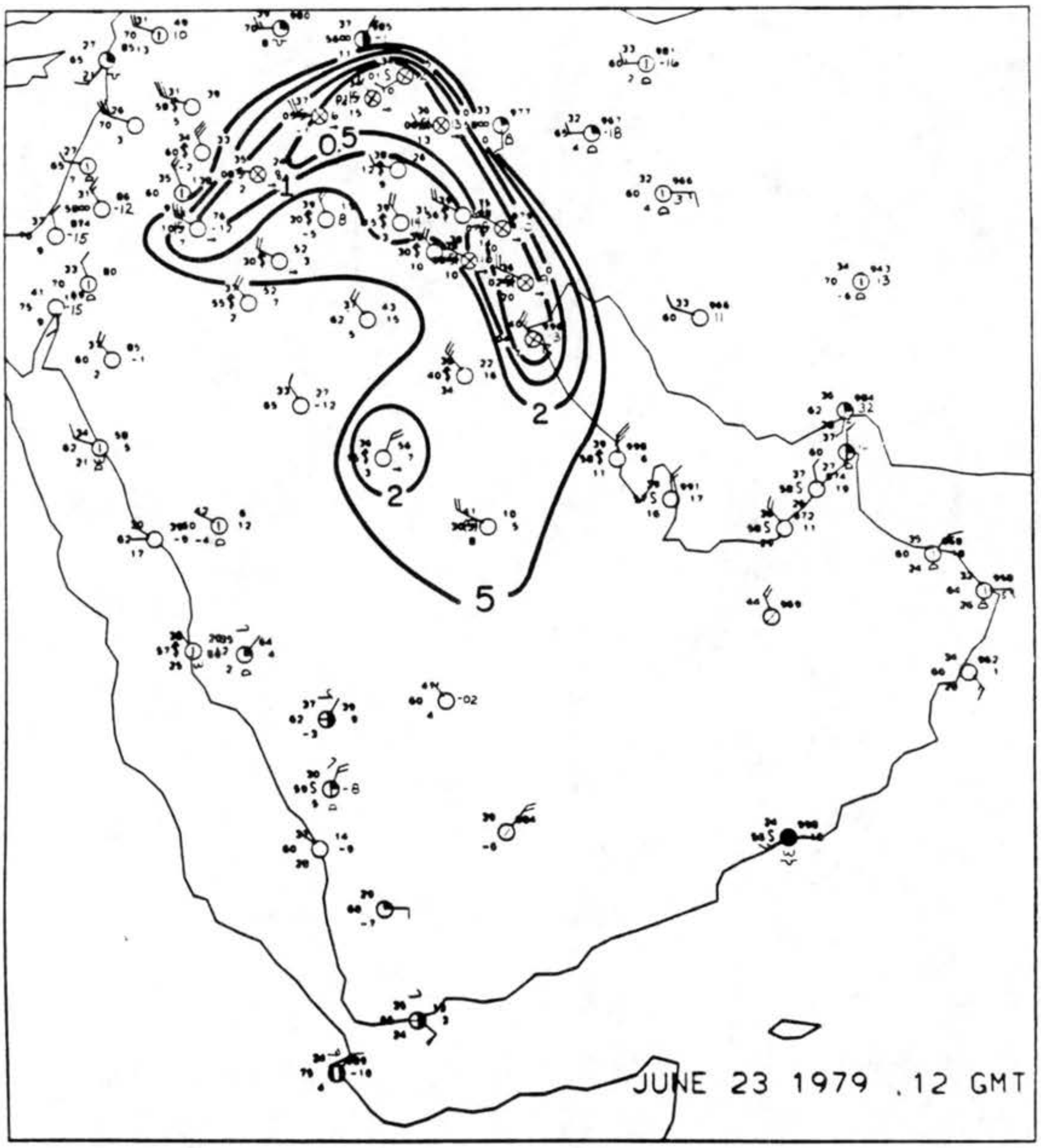


Figure B.4: Surface weather chart for 12 GMT on 23 June 1979. Isopleths of visibility are analyzed for visibilities of 5, 2, 1, and 0.5 km.

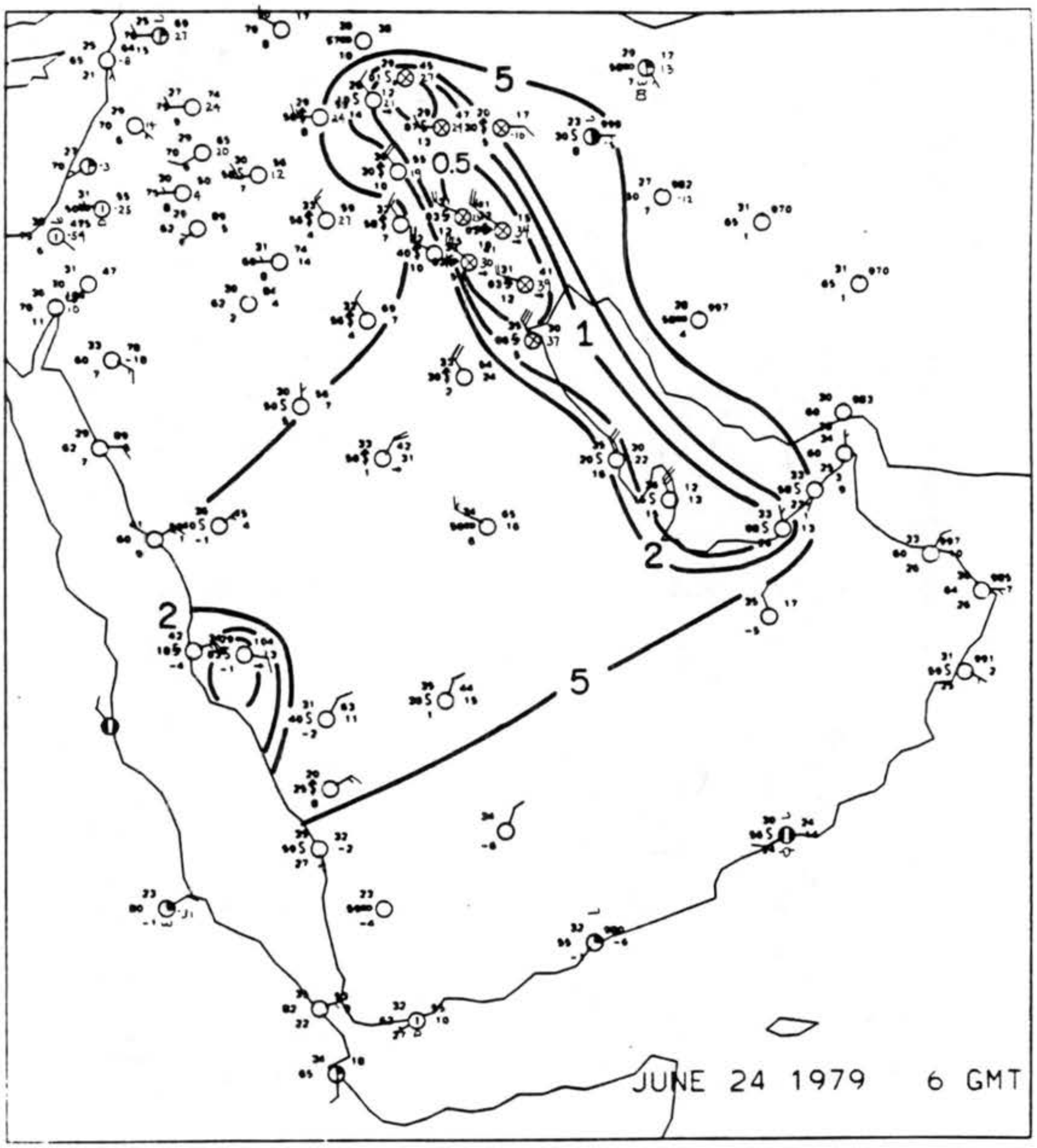


Figure B.5: Surface weather chart for 06 GMT on 24 June 1979. Isopleths of visibility are analyzed for visibilities of 5, 2, 1, and 0.5 km.

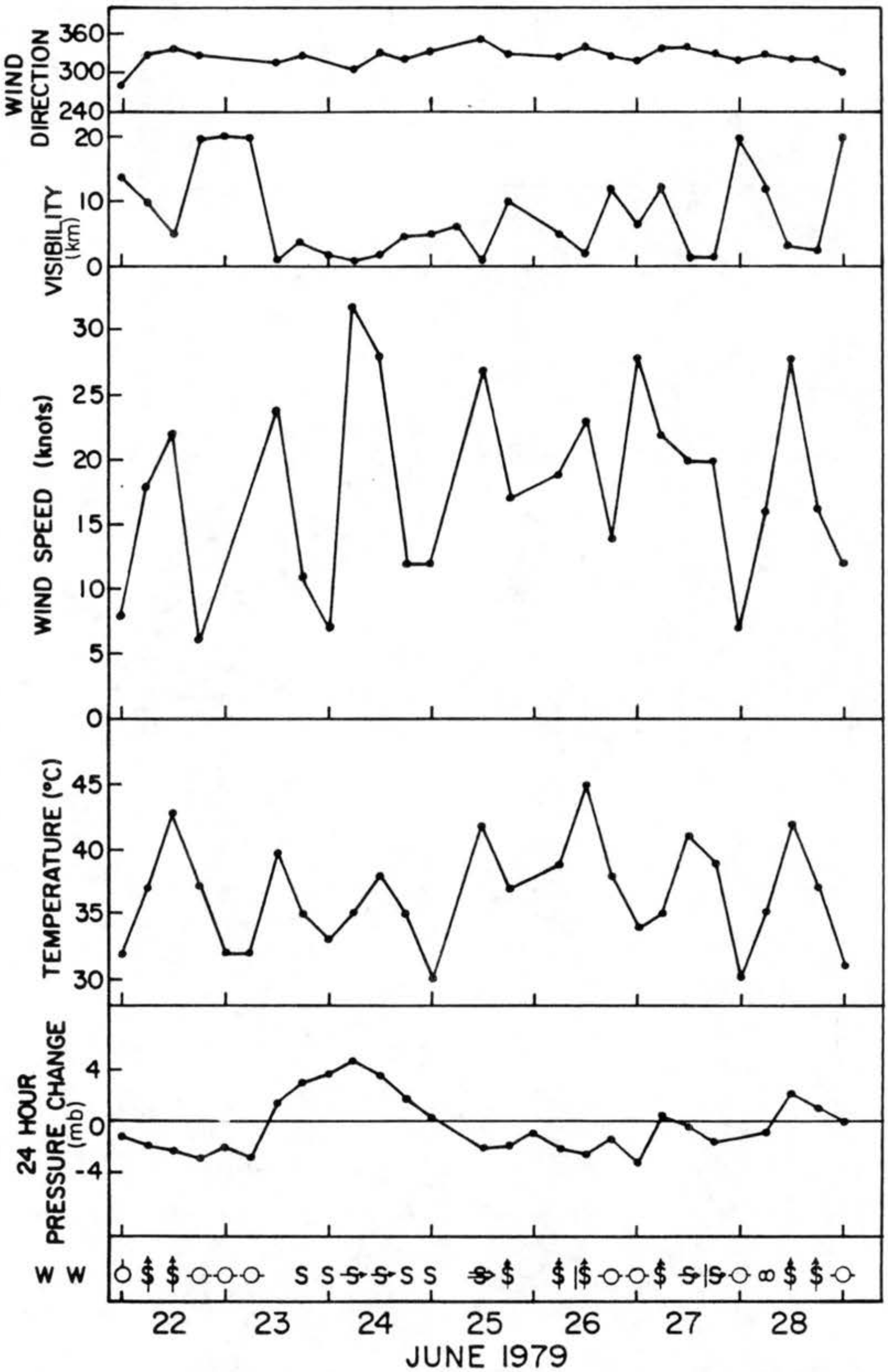


Figure B.6: Variations in weather, pressure, temperature, wind speed, visibility and wind direction observed at Kuwait, Kuwait during the period 22- 28 June, 1979.

near the surface resulting from shortwave energy extinction by the aerosol. Similar time series analysis of other stations in the region yeilded similar results.

The mobilization of dust not only depends on the meteorological conditions of the area, but is also very dependent on current surface characteristics and past history (e.g. recent precipitation, vegetation and soil particle size distribution). An important meteorological aspect of dust mobilization is the threshold wind speed at which dust would be raised off the surface and injected into the atmosphere. Surface observations can be used to estimate the threshold velocity for a given surface type by analysis of the frequency distribution of wind speed as a function of present weather condition. Figure B7 presents such an analysis where the number of occurrences of a given wind speed (3 knot intervals) was composited as a function of present weather conditions. Three types of weather situations were considered 1) no suspended aerosols (WMO codes 0-3), 2) dust suspended in the atmosphere but not raised off the surface by the wind (WMO code 6), and 3) dust or sand raised off the surface by the wind (WMO codes 7-9 and 30-35). This type of analysis can give a representative threshold velocity for the production of dust which has the potential to be carried great distances. Results for the Saudi Arabian desert stations Riyadh and Dhahan are shown in figures B7a and b. The profiles of the aerosol free atmosphere and that of weather code 6 are very similar suggesting the importance of past weather conditions in specifying the dust loading of the atmosphere. The critical wind speed for dust mobilization can be estimated as the wind speed at which there is a sharp increase in the frequency of observations of dust raised by the wind and a corresponding decrease in the frequency of the other observations. For these two stations this threshold appears to be between 10-15 knots. Since the threshold velocity is the minimum velocity at which the aerodynamic forces exceed the soil forces holding the particles together, this type of analysis is very dependent on a given region. This is demonstrated in figures B7c and d where a similar analysis was performed for New Delhi and Bikanar. It is impossible to pick a critical wind speed for these two stations and it is likely that dust transport, past weather conditions and surface characteristics play a more dominant role than in

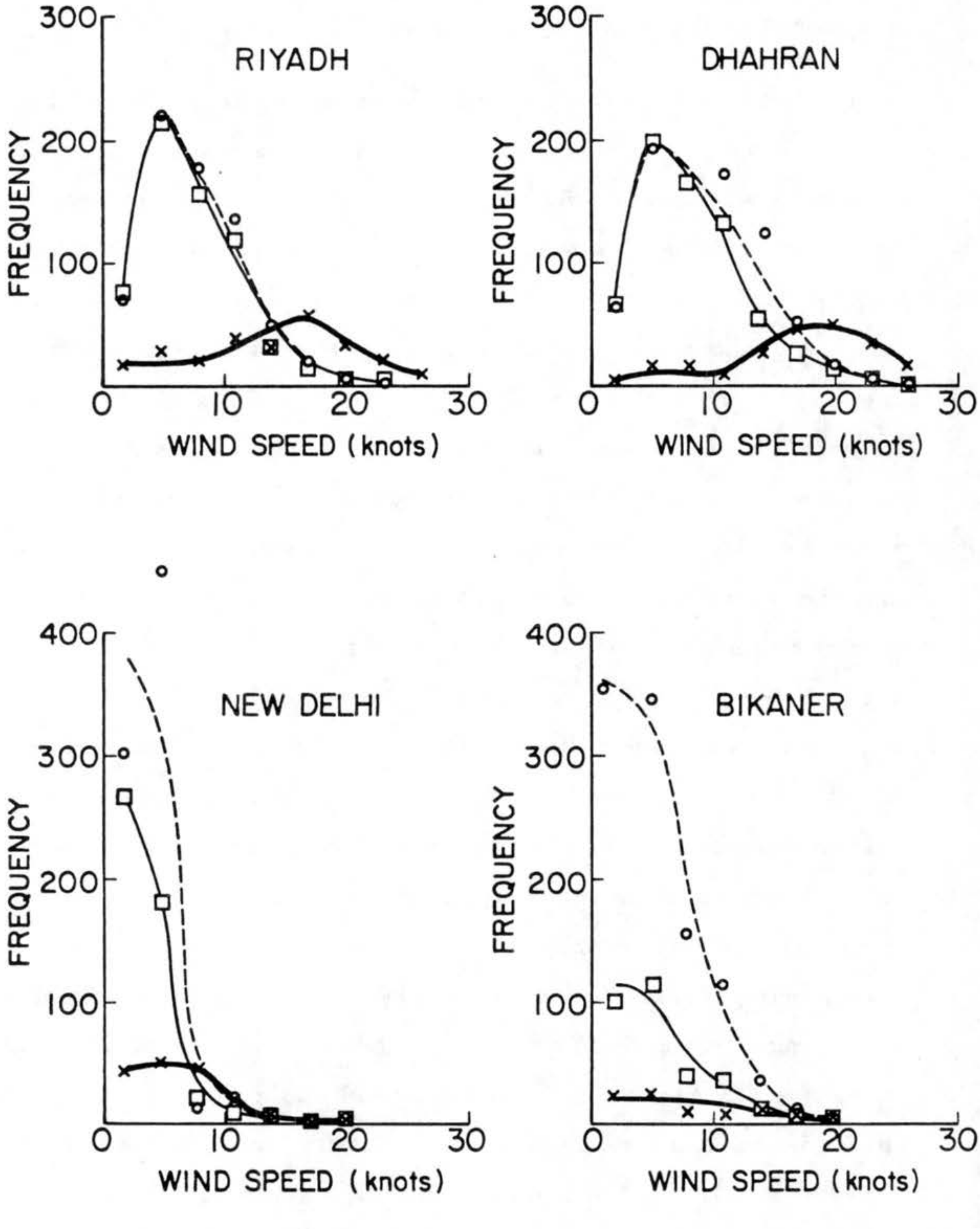


Figure B.7: Number of occurrances of a given wind speed as a function of dust loading for four stations. Circles- no aerosols suspended in the atmosphere; squares - dust in the atmosphere but not raised by the wind; x's - dust raised off the surface by the wind.

the two previous desert stations. This type of analysis will also be a function of season, particularly if there is a pronounced seasonal variation in precipitation.

## Appendix C

## IMPLICATIONS FOR REMOTE SENSING

One method for monitoring dust optical thickness is to measure the extinction of direct solar radiation. The aerosol spectral optical depth, $\tau_\lambda$, is then determined from

$$\tau_\lambda = \ln\left(\frac{I_{0\lambda}}{I_\lambda}\right)\sec\theta_0 - \tau_R - \tau_{O_3} \qquad (B1)$$

where

- $I_\lambda$ - transmissometer measurement
- $I_{0\lambda}$ - transmissometer measurement at the top of the atmosphere
- $\theta_0$ - solar zenith angle
- $\tau_R$ - Rayleigh optical depth
- $\tau_{O_3}$ - Optical depth of $O_3$

The simplcity of the above Beer-Lambert (B-L) law has led to its wide use in moinitoring atmospheric turbidity, however there are certain atmospheric conditions under which the B-L law breaks down. One such condition occurs when large amounts of diffuse radiation enter the detector's field of view along with the direct beam. To reduce the amount of spurious light most Volz type sunphotometers have small field of views (FOV), generally less than $1^0$. However such a small FOV makes it difficult to track the sun accurately in an automated mode. Thus, in the automated mode the FOV is generally on the order of $5^0$.

For such a FOV contributions to the recieved power from forward scattered radiation can be large and should be corrected for in order to get a true extinction measurement. Under relatively clear skies the total diffuse contribution represents approximate 1% of the total intensity (Box and Deepak, 1979). However in the presence of an atmospheric aerosol the effects of scattered light should be considered in extinction measurements of atmospheric turdidity (Box, 1982). Such corrections have been addressed in several studies. Deepak and Box (1978a and b) discuss forward scattering corrections assumming single scattering. The effects of second and third order scattering have been discussed by Deepak and Green (1970). Deviations from the B-L law due to the effects of multiple scattering have been discussed by Tam and Zardecki (1982), Zardecki and Tam (1982) and Zardecki and Deepak (1983).

Rather than use empirical corrections, one may employ measurements of the scattered energy to deduce aerosol optical depth. Such was the philosophy behind the multiple field of view radiometer discussed by Raschke and Cox (1983). In this section we shall explore the use of such an instrument in deducing the optical depth of a dust layer. We shall consider the case of a zero solar zenith angle and a homogeneous dust layer with no gaseous absorption. The incident solar flux, $I_{0\lambda}$, is assigned a relative value of 1. The dust single scattering albedoes and asymmetry parameters are typical of the $0.4 - 0.6\mu m$ spectral interval.

The effect of multiple scattering on inferring dust optical depth from solar transmission measurements is demonstrated in figure C1 which shows the cumulative flux (or transmittance since $I_{0\lambda} = 1$) as a function of the half angle of the 'instrument' for two different optical depths and three representative dust single scattering properties. The effect of multiple scattering on transmittance is a function of $\tau_\lambda$, $\omega_0$ and $g$, thus empirical corrections must also be a function of these parameters. In the case of a dust layer, these parameters change as the dust outbreak undergoes its life history making empirical corrections difficult. In addition, this extinction method is only good up to an optical depth of approximately 3 (D'Almeida et al., 1983).

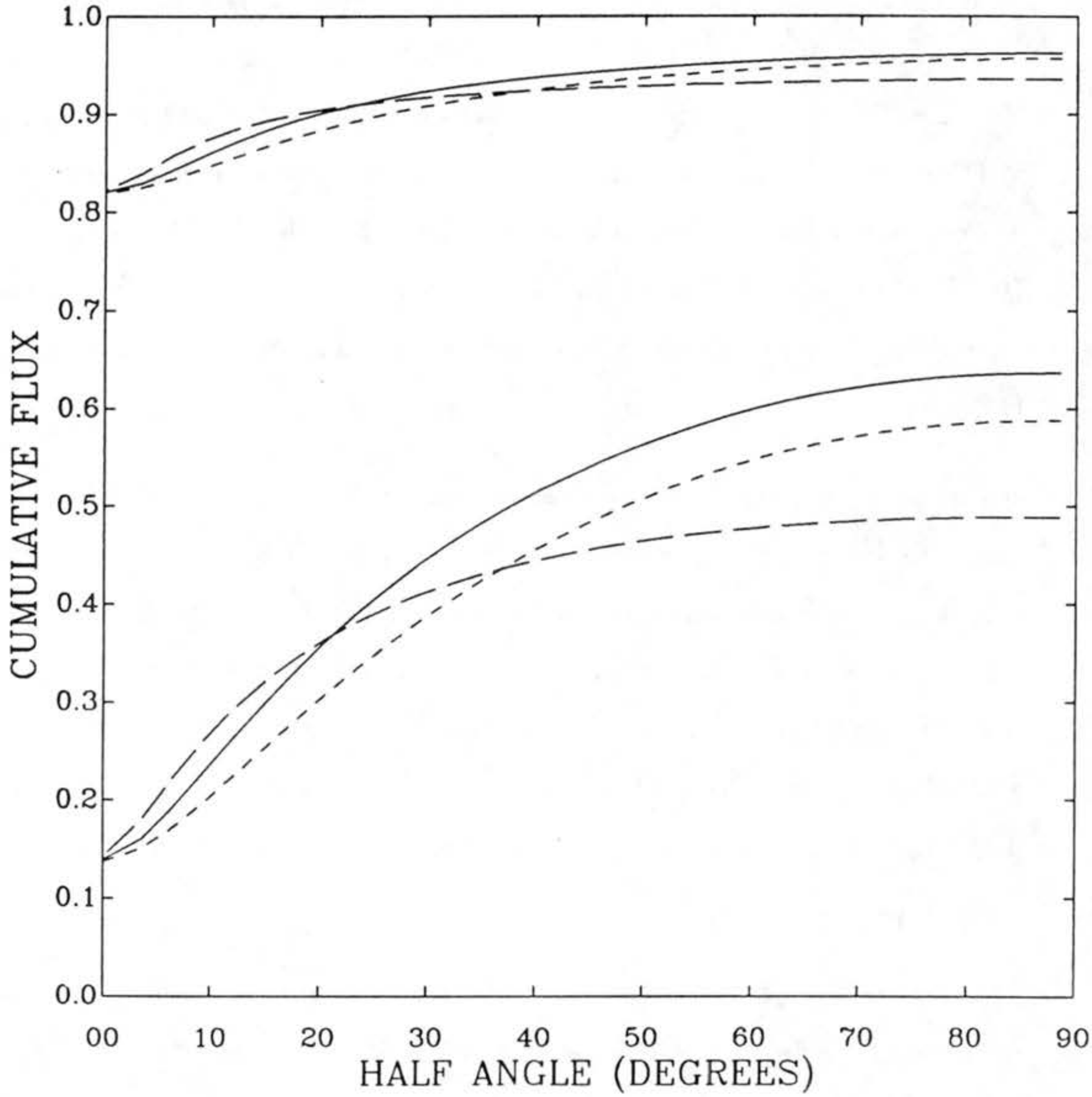


Figure C.1: Cumulative flux as a function of the instrument half angle for optical depths of 0.2 (top set) and 2 (bottom set) at a wavelength of $0.55\mu m$ for the Saharan (solid line), SW Asian (broken line) and Saharan with $r_{eff} = 5\mu m$.

To overcome some of these difficulties consider a radiometer similar in design to that of Rachke and Cox (1983). Figure C2 depicts the ratio of the measured irradiance of the $30^0$ FOV minus the $5^0$ ($10^0$) FOV to the $30^0$ FOV measured irradiance $[\frac{P_{30}-P_N}{P_{30}}]$ as a function of turbidity. The shaded regions represent the variations resulting from changes in $\omega_0$ and $g$ of the dust due to different $r_{eff}$ over the wavelength region $0.5 - 0.6\mu m$. While this type of measurement does not explicitly account for the variations resulting from different types of dust, it immediatly gives a range of optical depths appropiate to the measurements. This range increases as turbidity increases and is larger for the $10^0$ FOV than for the $5^0$ FOV. This type of instrument also has the advantage over the more standard extinction observations in that estimates of the dust loading can be obtained for turbidities as large as 6.

In addition to affecting surface radiation measurements, the presence of a dust layer will affect satellite measurements as well. This may be of concern in monitoring desertification from a satellite. On such viable technique may be the vegetation index (Tucker et al., 1985) defined as the ratio $\frac{B_2-B_1}{B_2+B_1}$ where

- $B_1$ - Reflectance measured by Channel 1 ($.55 - 0.68\mu m$) of the advanced very high resolution radiometer (AVHRR)
- $B_2$ - Reflectance measured by Channel 2 ($0.73 - 1.10\mu m$) of the AVHRR

The effect of a dust layer on the vegetation index (VI) as a function of turbidity is shown in figure C3 for solar zenith angle of $0^0$ and a nadir viewing angle. These values were determined from a doubling model with surface spectral reflectances and dust single scattering properties as given in Table C1. The presence of a dust layer has very little effect on the VI for the desert case. Only for large turbidities (greater than 0.5) over vegatation does the presence of the dust layer have any noticable effect, where it results in a decrease in VI.

Figure C3 is an example of the problems associated with attempting to monitor dust outbreaks over land using satellite visible data; it is difficult to detect the dust over a bright

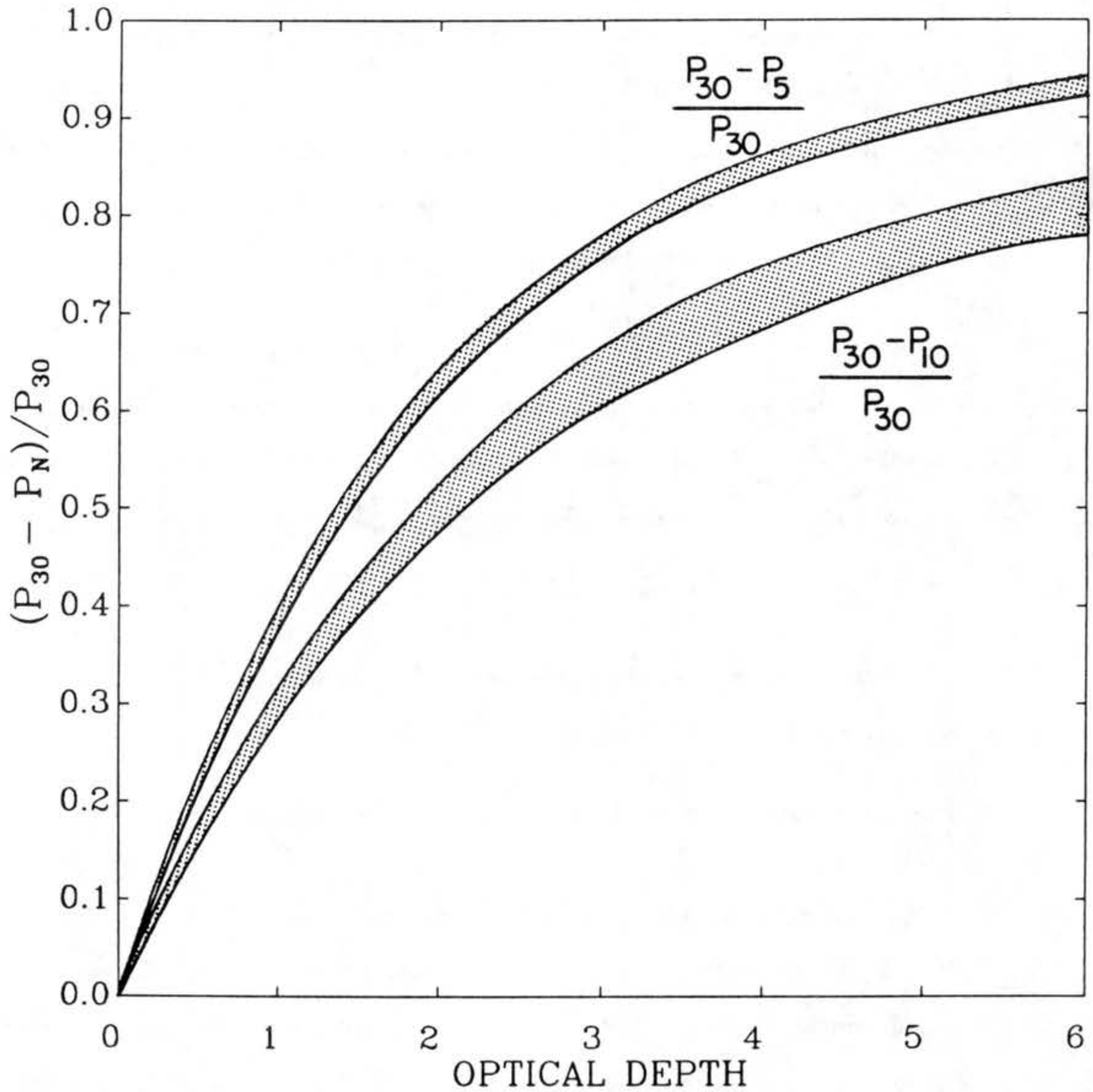


Figure C.2: Ratio of the irradiances of the $30^0$ FOV minus the $5^0$ ($10^0$) FOV to the $30^0$ FOV as a function of turbidity.

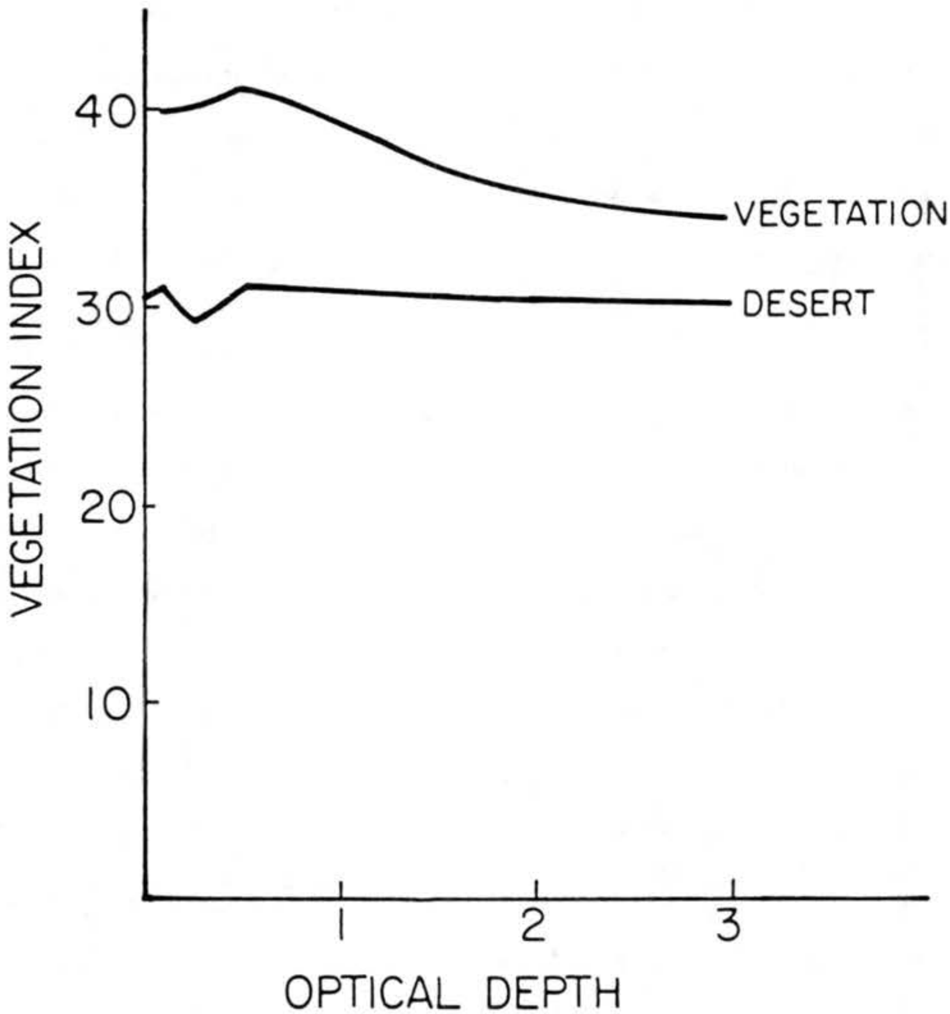


Figure C.3: Vegetation index as a function of turbidity for a solar zenith angle of $0^0$ and a nadir viewing angle.

surface. While surface observations suggest that large quantities of dust are transported out of the deserts of the world, most dust outbreaks are confined to land surfaces. These dust outbreaks can produce environmental hazards, especially along major transportation routes. Since surface observations are generally sparce, it is often difficult to locate the orgin as well as the movement of a dust outbreak. The disadvantage of surface observation horizontal resolution can be overcome with the aid of satellite data. For example, Carlson and Wendling (1977) and Norton et al., (1979) have incorported satelliete measurements in the visible to monitor dust outbreaks as well as to estimate dust optical depth over oceanic regions. We now present a technique which uses IR satellite measurements to track a dust outbreak and to derive values of the dust optical depth.

The methodology uses the radiative temperature difference between $3.7\mu m$ and $11\mu m$ in the presence of a dust layer. The single scattering albedo ($\omega_0$), and asymmetry parameter ($g$) were calculated (Table C2) from Mie theory assuming the size distribution given by Norton et al. (1980) and an index of refraction of Patterson (1981). These parameters were then used in a doubling model and the upwelling radiances were converted to brightness temperatures. The difference between these temperatures ($\Delta T = T_{3.7} - T_{11}$) is shown in figure C4 as a function of turbidity for a satellite viewing angle of $8^0$. Since optical depth is a function of wavelength, results are given as a function of optical depth at $\lambda = 0.5\mu m$. This is the most common wavelength for measuring atmospheric dust loading. The ratio of $\sigma_{ext}$ at 3.7 and $11\mu m$ to $\sigma_{ext}$ at $0.5\mu m$ is given in Table C2. For simplicity water vapor absorption has been neglected; due to the dry atmospheres involved this neglect of water vapor absorption should not affect the conclusions. To aid in the interpretation of the results dust layer reflectance, transmittance and emittance at the two wavelengths are shown in figure C5.

Figure C4 represents the case of a dust layer overlying a desert surface with a surface temperature of $315^0$K, the solid line includes solar reflectance (solar zenith angle of $0^0$) while the dashed does not. The upwelling $3.7\mu m$ radiation is significantly augmented by reflection of solar energy by the dust layer. Even without the inclusion of solar reflection

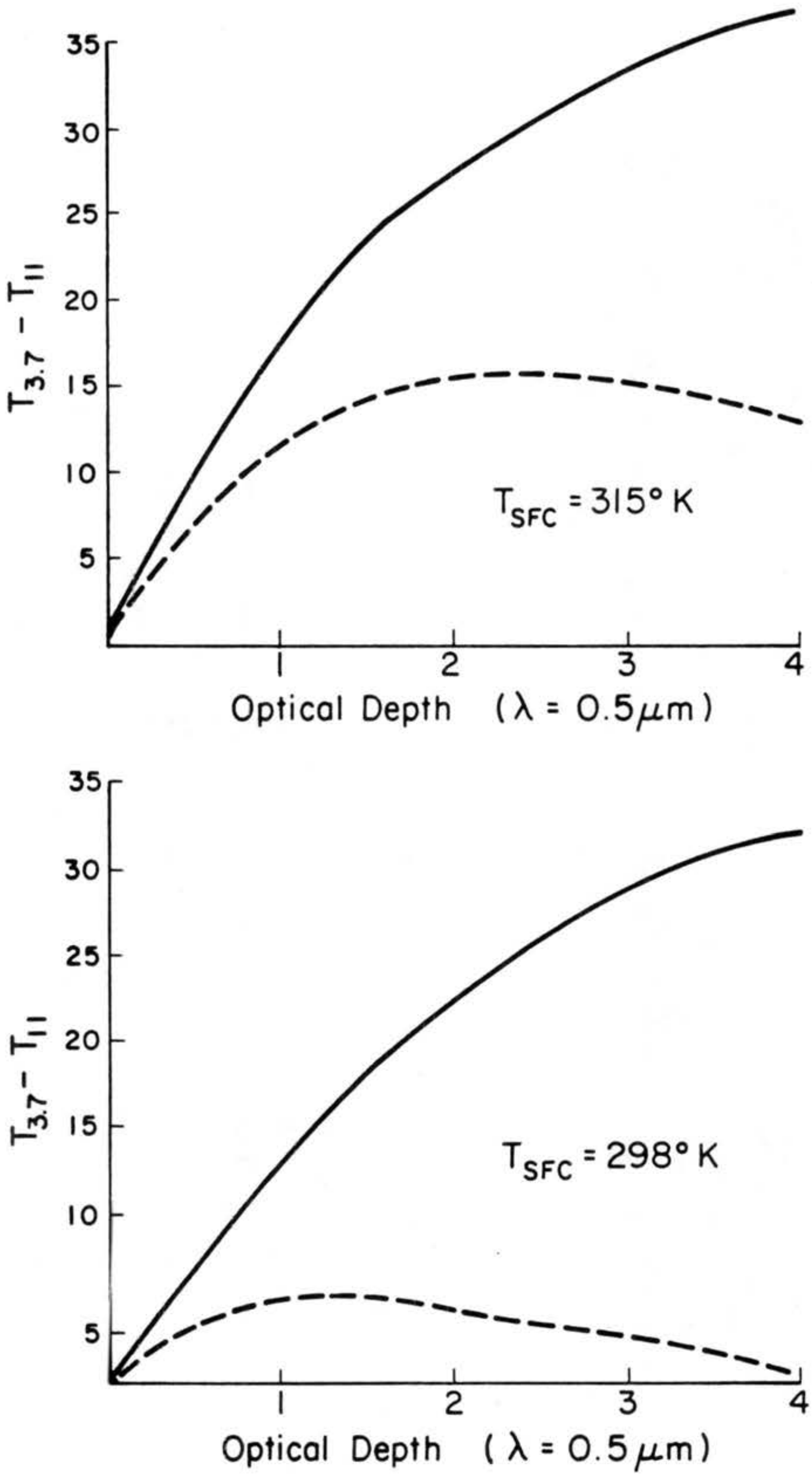


Figure C.4: Radiative temperature difference ($\Delta T = T_{3.7} - T_{11}$) as a function of turbidity for a satellite viewing angle of $8^0$ and a solar zenith angle of $0^0$.

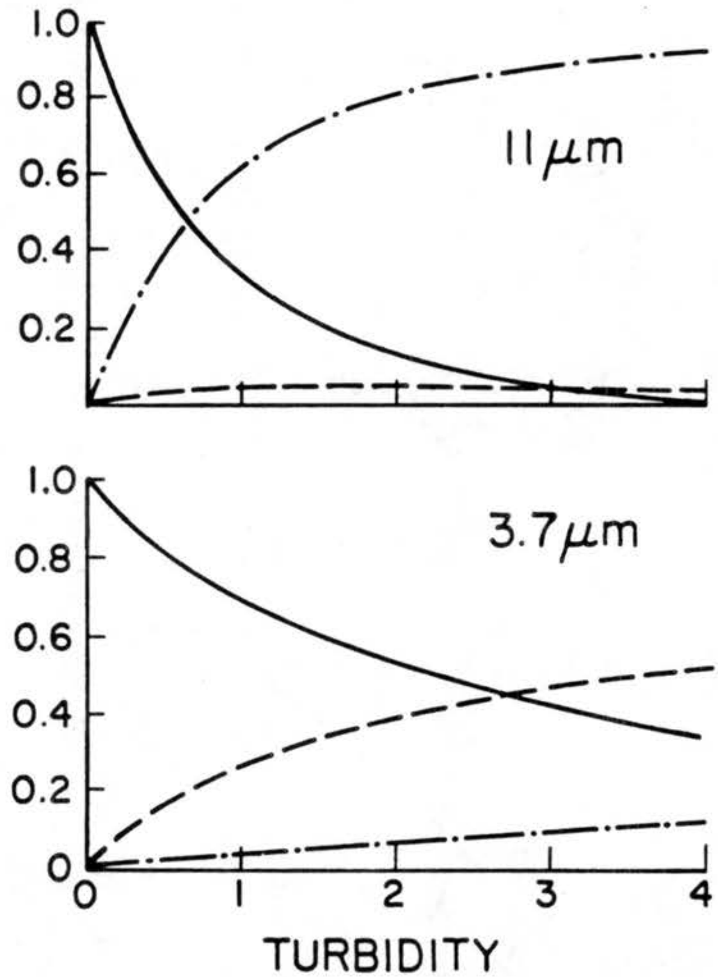


Figure C.5: Dust layer transmittance (solid), reflectance (dashed) and emittance (dot-dashed) at wavelengths of 3.7 and $11\mu m$.

the $3.7\mu m$ temperature is still larger than the $11\mu m$ temperature, despite reflection of the surface upwelling radiance at the dust layer base. The $3.7\mu m$ emittance is small even for large optical depth, thus the upward radiance is largely determined by the transmittance of the surface radiance and reflection of the downward solar component. In the $11\mu m$ radiance, the reflectance is always small. Thus for small dust optical depths the major contribution is from the surface and as the dust layer optical thickness increases, emission by the dust layer itself becomes important. The transmission is always greater at $3.7\mu m$, thus $\Delta T$ is, for this case, always positive. For the case of a surface inversion (e.g. over the desert at night) one may expect negative $\Delta T$.

Figure C4 represents the case of a dust layer overlying an ocean surface with a surface temperature of $298^0$K. The dashed line excludes the solar component and can be considered the nighttime case. Again there is a large contribution from solar reflectance. For the night case the maximum $\Delta T \approx 5^0$, which peaks at $\tau \approx 1.3$. For optical depths greater than 1.3 $\Delta T$ decreases with increasing $\tau$. The $3.7\mu m$ radiance decreases with increased $\tau$ due to the decrease in the transmitted surface radiance; while the $11\mu m$ radiance also decreases with increasing $\tau$ the rate of decrease changes as the dust layer emittance increases. This nightime curve suggests that retrieval of dust optical depth using these two wavelengths would be least sensitive at night. Given the indices of refraction of dust, it may be more appropriate to chose two wavelengths in the $8 - 12\mu m$ window where there are still large variations in complex index of refraction.

Before investigating the effects of atmospheric temperature and moisture profiles, the vertical distribution of the dust loading and the surface radiative properties on $\Delta T$, it is instructive to compare satellite measurements with surface observations. Unfortunately, coincident satellite and sun-photometer measurements were not available to demonstrate the method. However since visibilty is often related to mass concentration for airborne soil particles (Patterson and Gillete, 1977), surface observations of visibilty were compared with the satellite measurements. Observations of the TIROS-N AVHRR's channel 3 ($3.58-3.97\mu m$) and channel 4 ($10.53 - 11.45\mu m$) were used in the study. The equatorial crossing times of the TIROS-N are 0300 (descending) and 1500 (ascending) LT. The data was mapped by Smith and Graffy (1982) onto a uniform grid with a resolution of 15 points per degree latitude or longitude. The scheme of Lauritson et al. (1979) was used to convert raw digital data to window temperatures.

Figure C6 depicts a large scale dust outbreak observed over the Saudi Arabian Peninsula in late June 1979. Each station plot includes information on wind speed and direction, temperature, dew point depression, cloud cover, present and past weather, visibility, pressure and 24 hour pressure tendency (WMO,1974). Further discussion of this dust outbreak is contained in appendix B. Regions of low visibility are generally associated with large optical depths. Figure C6 also depicts the satellite radiative temperature differences (solid lines) as well as the surface observations. The dust outbreak region is cloud free. Large temperature differences measured by the satellite are well correlated with regions of low visibility. The feasibilty of tracking dust outbreaks, as well as inferring the dust layer optical depth, is demonstrated by comparing satellite observations with surface estimates of visibility.

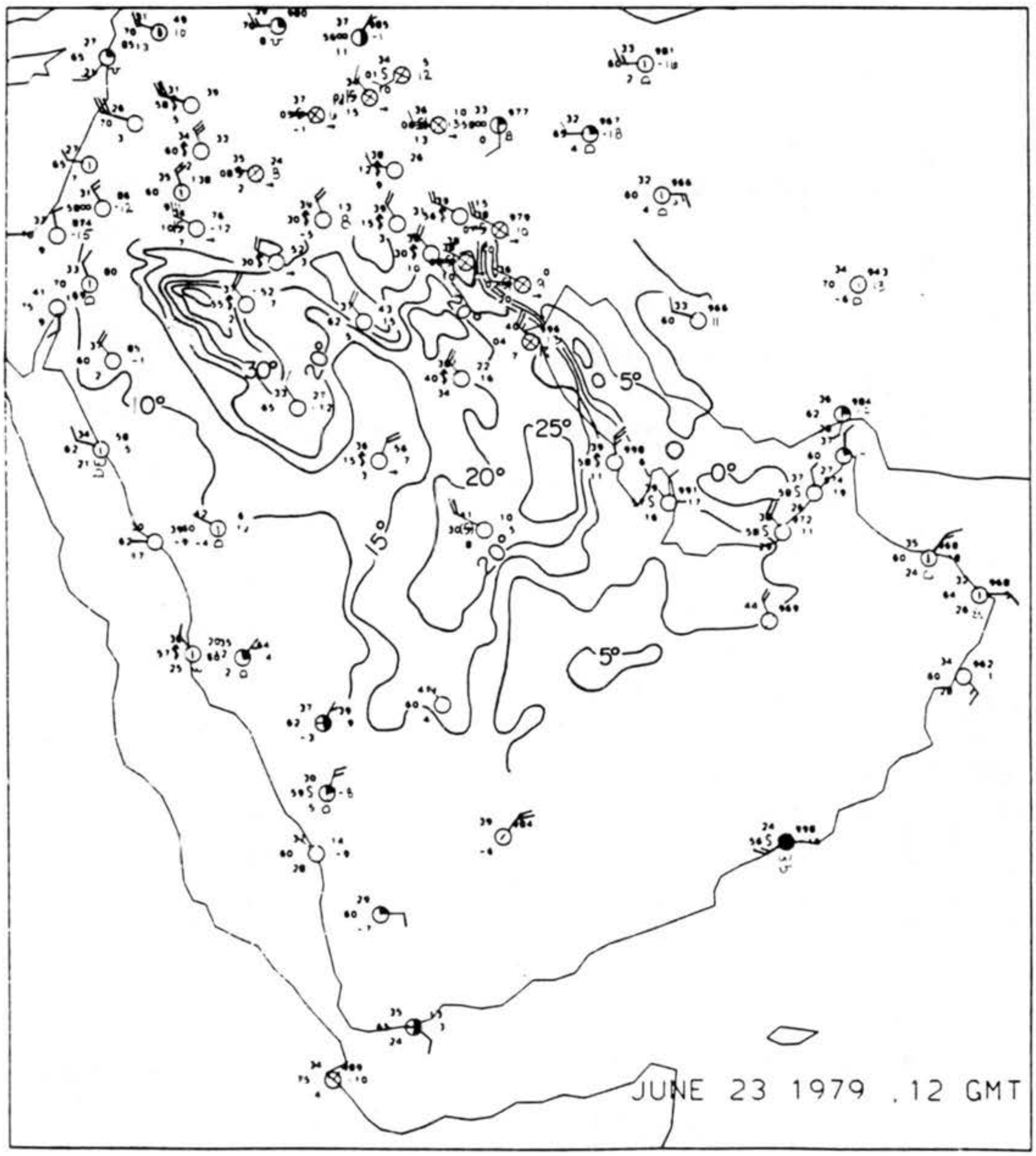


Figure C.6: Large scale dust outbreak observed over the Saudi Arabian Peninsula in late June 1979. Each station plot includes weather information (WMO,1974). Satellite radiative temperature differences (solid line) are also shown.

Table C.1: Spectral characteristics for the determination of the vegetation index.

| | $0.55 - 0.68 \mu m$ | $0.73 - 1.1 \mu m$ |
|---|---|---|
| $\omega_0$ | .8714 | .9258 |
| $g$ | .7352 | .6956 |
| Spectral reflectance | | |
| Desert | 0.8 | 0.15 |
| Vegetation | 0.9 | 0.21 |

Table C.2: Single scattering properties of the dust layer at 3.7 and $11 \mu m$.

| | $3.7 \mu m$ | $11 \mu m$ |
|---|---|---|
| $\omega_0$ | .9869 | .4162 |
| $g$ | .6507 | .5038 |
| $\sigma_\lambda / \sigma_{0.5}$ | .77 | 1.07 |